MANCHESTER
1824
The University of Manchester

Numerical simulation of liquid crystalline flows

A thesis submitted to the University of Manchester for the degree of
Doctor of Philosophy
in the Faculty of Science and Engineering

2022

Kamil M. Fedorowicz
Department of Mechanical Aerospace and Civil Engineering

Contents

List of figures **6**

List of tables **14**

List of publications **15**

Abstract **16**

Declaration of originality **17**

Copyright statement **18**

Acknowledgements **19**

Nomenclature **20**

1 Introduction **22**

1.1 Aims and objectives 24

1.2 Outline of the thesis 25

2 Literature review **27**

2.1 The structure of liquid crystals 27

2.2 Director and the order parameter 29

2.3 Wall anchoring 32

2.4 Rheology of liquid crystals 33

2.4.1 Region I 35

2.4.2 Region II 36

2.4.3 Region III 36

2.4.4 Normal stresses 37

2.4.5 Scaling rules 38

2.5 Equations of motion 41

2.6 Newtonian model 42

2.7 Generalised Newtonian Fluid models 43

2.7.1 Power-law model 44

2.7.2 Carreau-Yasuda (CY) model 46

2.7.3 Bingham model 46

2.7.4 Herschel-Bulkley model 47

2.7.5 Summary of the GNF models 47

2.8 Nematodynamics 48

2.8.1 Transversely isotropic fluid (TIF) model . . . 48
2.8.2 Thermodynamic potential . . . 52
2.8.3 Hamiltonian description of complex fluids . . . 54
2.8.4 Leslie-Ericksen (LE) model . . . 57
2.8.5 Order parameter tensor . . . 59
2.8.6 Nematic energy (order parameter tensor) . . . 61
2.8.7 Beris-Edwards (BE) model . . . 63
2.8.8 Dimensional groups and relevant scales . . . 65
2.8.9 Other models . . . 69
2.9 Computational fluid dynamics . . . 70

3 Numerical solver **71**
3.1 Implementation . . . 71
3.2 Director evolution upon a pure rotation . . . 72
3.2.1 Analytical solution . . . 72
3.2.2 Solution with the explicit Euler scheme . . . 73
3.2.3 Solution with the implicit Euler scheme . . . 74
3.2.4 Crank-Nicholson scheme . . . 75
3.3 Director normalisation . . . 75
3.4 Solver validation . . . 76
3.4.1 Analytical solution . . . 76
3.4.2 Verification of the numerical solution . . . 81
3.4.3 Convergence rate . . . 82
3.4.4 Alternative validation approaches . . . 83

4 Flow of liquid crystals in straight pipes **85**
4.1 Transversely isotropic fluid . . . 85
4.2 Leslie-Ericksen and Beris-Edwards models . . . 86
4.2.1 Homeotropic anchoring . . . 89
4.2.2 Wall-parallel anchoring . . . 101
4.3 Summary . . . 102

5 Flow of transversely isotropic fluid in curved pipes **104**
5.1 Problem formulation . . . 105
5.1.1 Geometry . . . 105
5.1.2 Equations of motion . . . 105
5.1.3 Constitutive equation . . . 106
5.1.4 Non-dimensionalization . . . 106
5.1.5 Stream function . . . 108
5.1.6 Perturbation method . . . 108
5.1.7 Boundary conditions . . . 109
5.2 Solution . . . 109
5.2.1 Solution procedure . . . 109

5.2.2 Leading order ($O(1)$) solution . . . 110
5.2.3 First order ($O(\delta)$) solution . . . 111
5.2.4 Second order ($O(\delta^2)$) solution . . . 114
5.3 Results . . . 115
5.3.1 Sources of the secondary flow . . . 115
5.3.2 Magnitude of the secondary flow at the pipe axis . . . 120
5.3.3 Structure of the secondary flow . . . 123
5.3.4 Non-uniqueness of the shear viscosity and the effect on the secondary motion . . . 124
5.3.5 Streamwise flow . . . 125
5.3.6 Validity of the perturbation method . . . 129
5.4 Summary . . . 129

6 Flow of Leslie-Ericksen fluids through 90^o bends **131**
6.1 Geometry . . . 131
6.2 Methodology . . . 131
6.2.1 Governing equations . . . 131
6.2.2 Boundary conditions . . . 132
6.2.3 Material parameters . . . 133
6.2.4 Computational domain and solution details . . . 133
6.3 Results . . . 134
6.3.1 Director field in a bend . . . 134
6.3.2 Stream-wise velocity . . . 137
6.3.3 Secondary flow . . . 138
6.3.4 Entrance and exit velocity effects . . . 142
6.3.5 Director development downstream of the bend . . . 147
6.3.6 Pressure drop . . . 151
6.4 Summary . . . 151

7 Flow of liquid crystals through a 4:1 planar contraction **153**
7.1 Geometry . . . 153
7.2 Methodology . . . 154
7.2.1 Governing equations . . . 154
7.2.2 Boundary conditions . . . 156
7.2.3 Computational domain and solution details . . . 159
7.3 Results . . . 161
7.3.1 Wall-parallel anchoring . . . 161
7.3.2 Homeotropic anchoring . . . 167
7.3.3 Pressure losses . . . 175
7.4 Summary . . . 180

8 Conclusions and future work **182**
8.1 Conclusions . . . 182

8.1.1 Flow of liquid crystals in curved pipes 182
8.1.2 Flow of liquid crystals through a planar contraction 183
8.2 Future work 183
8.2.1 Addition of yield stress term 184
8.2.2 Defect dynamics 184
8.2.3 Smectic liquid crystals 184

References **185**

Appendices **198**

A Source codes **200**

B Supplementary material of chapter 5 **211**

C Supplementary material of chapter 6 **219**

D Contraction mesh code **227**

Word Count: 68 068

List of figures

1.1 A schematic visualisation of the structure of a complex fluid based on the structure of soap. Long, anisotropic particles (bricks) are distributed within a lamellar phase that consists of sheets of rod-like molecules [23]. Reprinted with permission from [24]. Copyright Elsevier 2022. 23
1.2 Response of a generic complex fluid to small amplitude periodic straining. . 23
1.3 A schematic description of the soap extrusion process. 25

2.1 Due to the high aspect ratio, particles of p-azoxyanisole (PAA) and other liquid crystals often resemble rods. 28
2.2 Comparison of the distribution of particles in crystal, liquid crystal and isotropic fluid. 29
2.3 Schematic representation of alignment of particles in cholesterics. 29
2.4 A biaxial liquid crystal consisting of planks with the medium axis aligned in a preferential direction. 30
2.5 Example of a biaxial liquid crystal field. The director (red rods) aligns on average along the $z-$direction (the long axis), but there is also a preferential ordering along the $x-$direction (medium axis) represented by an ellipse with $r_x > r_y$. 31
2.6 Comparison of a smectic A and a smectic C. 31
2.7 Schematic illustration of columnar phases, where individual disks represent disk-shaped molecules. The distance between layers may vary. 32
2.8 Example distribution functions of nematic liquid crystal with a horizontal and vertical director fields. θ measures the angle between a single liquid crystal particle and vertical direction. Due to the head-tail symmetry, only the range $-\pi/2 \leq \theta \leq \pi/2$ is shown. 32
2.9 Schematic visualisation of a nematic field with a constant director orientation and varying order parameter. Red, orange and green colours denote high, medium and low order parameters, respectively. 33
2.10 Schematic illustration of a surface imposing a wall-parallel anchoring. The surface was rubbed along the $y-$ direction, which created microscopic rows, hence imposing alignment in the parallel direction. 34
2.11 Head of a detergent molecule is attracted to the solid surface, which imposes a wall normal orientation. 34
2.12 Schematic representation of director orientations considered by Mięsowicz in his experiment. 35

2.13 Qualitative behaviour of liquid crystal samples as a function of temperature with different director orientation in the ordered state. The vertical black line represents a nematic-isotropic transition temperature. 35
2.14 Three-region viscosity curve proposed by Onogi [76]. 36
2.15 Schematic illustration of material microstructure in different shear regimes [76]. 37
2.16 Viscosity as a function of shear rate ($\dot{\gamma} \propto \frac{4Q}{\pi R^3}$) for a set of pipes with different diameter [86]. Higher numbers indicate larger diameters. Reprinted with permission from [86]. Copyright 2022 Taylor & Francis Group. . . . 38
2.17 When the viscosity is plotted against $\dot{\gamma}L^2 \propto \frac{4Q}{\pi R}$ data points measured at different diameters collapse on the same curve [86]. Reprinted with permission from [86]. Copyright 2022 Taylor & Francis Group. 39
2.18 Schematic depiction of the setup used in the experiment. 39
2.19 a) Variation of recovered strain with time for a PBLG solution with 30% liquid crystal content. The imposed stresses (from left to right were) 25, 50, 100, 200 and 450 $^{dyn}/_{cm^2}$; b) the same variation plotted as a function of dimensionless time $\dot{\gamma}_0 t$. Reprinted with permission from [88]. Copyright 2022, The Society of Rheology. 40
2.20 Equilibrium values of G' and G'' as a function of shear rate. Reprinted with permission from [89]. Copyright 2022, The Society of Rheology. 42
2.21 Schematic representation of the effect of deformation on the microstructure. The structure of a Newtonian fluid remains unaltered (for industrially-relevant timescales), while the internal structure of fluids with a complex microstructure is deformed, affecting material properties. 43
2.22 Viscosity variation predicted by the power-law model. 45
2.23 Typical viscosity variation of a shear-thinning fluid. The viscosity changes between $\dot{\gamma}_1$ and $\dot{\gamma}_2$ and remains constant outside this region. 45
2.24 Increasing the yield stress τ_0 increases the width of the plug region. 47
2.25 Coupling between stress, flow and the director orientation. 48
2.26 Schematic visualisation of angles θ and ϕ. 51
2.27 Possible static configurations (well ordered nematic (a) and isotropic (b) allowed by the TIF model in the absence of flow. In both cases the stress field is zero. 52
2.28 Possible modes of distortion for a liquid crystal. 54
2.29 Schematic depiction of the a) Lagrangian and b) Eulerian description of the flow. 56
2.30 Some examples of the homeotropic anchoring in the vectorial framework, each representing the same physical state. 60
2.31 Director field with a pair of defects enclosed by red lines. 60
2.32 Schematic illustration of the director field polluted with defects in a contraction. Further details on the flow of liquid crystals in a contraction will be presented later in the thesis. 61

2.33 Left: a pair of parallel plates with the homeotropic anchoring on both boundaries. Right: distribution of the order parameter dependent on the defect size. 69

3.1 Rotation of the director field in a channel flow. 72
3.2 Comparison of the evolution of n_1 predicted analytically and numerically with the first order forward Euler scheme. The variation of n_2 is analogous and thus not shown here. 74
3.3 Comparison of the evolution of n_1 predicted analytically and numerically with the first order backward Euler scheme. The variation of n_2 is analogous and thus not shown here. 75
3.4 Fully developed, steady-state, straight pipe flow is considered in this section. 76
3.5 Variation of radial and axial components of the director. 77
3.6 Director field in the limit of zero Ericksen number. 78
3.7 Distribution of dimensionless effective viscosity for a range of α_2. 79
3.8 Velocity profile for a range of α_2. $\bar{v_s}$ represents the mean streamwise velocity. 80
3.9 Effective viscosity as a function of α_2 in a capillary and channel flows in the limit of $Er \rightarrow 0$. The effective viscosity in a channel flow is given by $\eta_{eff} = \frac{-\alpha_2+\alpha_4+\alpha_5}{2}$. 80
3.10 Distribution of the viscous component of the first normal stress difference for a range of α_2. 81
3.11 Grid used for the mesh refinement study. 83
3.12 Convergence of the relative velocity error. 84

4.1 Geometry considered in this chapter: a straight pipe with no-slip boundary condition on the wall. Homeotropic and wall-parallel director boundary conditions are considered. Throughout the simulations we employ a fixed pipe radius $R = 1$ mm. 85
4.2 Distribution of eigenvalues for flows with different defect sizes. Red labels correspond to a uniaxial state, while at $\xi_N/R = 3.9 \cdot 10^{-1}$, the liquid crystal has three distinct eigenvalues and the system is in a biaxial state. 90
4.3 Biaxiality at different ξ_N/R 90
4.4 Order parameter $S = \sqrt{\frac{3}{2}}\sqrt{\lambda_1^2 + \lambda_2^2 + \lambda_3^2}$ at different ξ_N. Due to a decreasing shear rate near the pipe axis, the order parameter is governed by the bulk effects, which elevate the order parameter at $r = 0$. 91
4.5 Predictions of the axial component of the director field at $Er = 0.05$. For $\xi_N/R = 3.9e - 1$ only the near wall director field can be represented as a vector and hence n_s near the axis is not shown. 91
4.6 The planar-radial solution predicted in the nearly static configuration. The order parameter at the axis is negative meaning that the director lines in a plane normal to the pipe axis. Reprinted with permission from [135]. . . . 92

4.7 Predictions of the axial velocity at $Er = 0.05$. 93
4.8 Variation of the viscous component of N_1. 94
4.9 Biaxiality at $Er = 2.5$ for different $\frac{\xi_N}{R}$. Compared to fig. 4.3 the region of biaxial behaviour shrinks. 95
4.10 Comparison of the director field at $Er = 5$ 96
4.11 Comparison of the distribution of order parameter at $Er = 5$. 96
4.12 Comparison of the velocity field at $Er = 5$ 97
4.13 Comparison of normal stress difference profiles at $Er = 5$. 97
4.14 Comparison of the axial component of the director field at $Er = 100$. . . . 98
4.15 Order parameter $S = \sqrt{\frac{3}{2}}\sqrt{\lambda_1^2 + \lambda_2^2 + \lambda_3^2}$ for different ξ_N at $Er = 100$. . . 99
4.16 Comparison of the velocity field at $Er = 100$ 99
4.17 Variation of order parameter at infinite Ericksen number with different Deborah numbers. Ratios $\frac{a}{b} = -0.05$ and $\frac{c}{b} = 1$ are constant in all cases; a, b, c are parameters of the bulk-free energy density (eq. 2.64) in the BE model. . 100
4.18 Comparison of the director field at $Er = 2.5$ with wall parallel anchoring. Note that the x-axis scale starts at 0.92, so the director is nearly aligned with the flow. 101
4.19 Comparison of the velocity field at $Er = 2.5$ with wall parallel anchoring. 102
4.20 Comparison of the shear curves produced by LE and BE model with different defect length-scales. The effective viscosity is normalised by the viscosity scale $\frac{\alpha_4}{2}$. Letters h and p refer to homeotropic and wall-parallel anchoring, respectively. 103

5.1 Toroidal geometry used in the analysis. Reprinted with permission from [24]. Copyright Elsevier 2022. 105
5.2 Contour of the director magnitude and the projection of the director field onto the $r - \phi$ plane for 5CB, $\delta = 0.2$. Director magnitude increases near the pipe axis, which is caused by a singularity in $n_\phi^{(1)}$. The region of pipe axis is blanked out for visualisation purposes. 114
5.3 Schematic illustration of the action of normal stress differences in the $r - \phi$ plane. Reprinted with permission from [24]. Copyright Elsevier 2022. . . . 115
5.4 Schematic illustration of a vortex driven only by the normal stress difference. 117
5.5 The pressure gradient is balanced by normal stresses in the core of a bend. 117
5.6 Schematic illustration of the effect of microstructure tension on the direction of the secondary motion. The red line represents a flow streamline, whose strain produces a secondary motion. Blue arrows denote the direction of the secondary motion. 118
5.7 Schematic depiction of a secondary flow driven by a pair of defects [171]. Dashed black lines denote director field and the red lines indicate the direction of rotation. 119

5.8 Schematic illustration of u_0. When u_0, the secondary flow on the symmetry line is directed towards the bend axis and the fluid rotates in the clockwise direction in the upper half of the pipe. 121
5.9 Cross-pipe velocity magnitude at the pipe axis as a function of μ_1 and μ_2 for $\lambda \to 1$. Inset: location where u_0 is evaluated. Reprinted with permission from [24]. Copyright Elsevier 2022. 122
5.10 Magnitude of the secondary flow as a function of $\mu_1 + \mu_2$. 123
5.11 Contours of the stream function for 5CB. Positive stream function implies that the flow is rotating clockwise, which is opposite to the direction of a secondary flow driven by inertia. The left side of the plot is closer to the bend axis. Reprinted with permission from [24]. Copyright Elsevier 2022. 124
5.12 The first normal stress viscosity η_{N1} need not be constant for materials with a fixed shear viscosity. Reprinted with permission from [24]. Copyright Elsevier 2022. 125
5.13 The magnitude and direction of the secondary motion in materials with fixed η_{nN} can vary significantly. The plot was obtained for $\eta_{nN} = 1$. Reprinted with permission from [24]. Copyright Elsevier 2022. 125
5.14 Contours of the streamwise velocity field $w = w^{(0)} + \delta w^{(1)}$ and the projection of the director field $\boldsymbol{n} = \boldsymbol{n}^{(0)} + \delta \boldsymbol{n}^{(1)}$ onto the $r - \phi$ plane. A shift in the director field is caused by the shift in the stream-wise velocity field. Inset: the director field in a straight pipe. Reprinted with permission from [24]. Copyright Elsevier 2022. 126
5.15 Comparison of stream-wise velocity in a curved pipe predicted for a Newtonian and 5CB fluids. 127
5.16 Contours of viscous dissipation in the bend cross-section for 5CB. Dissipation is normalised with respect to the maximum value, $\delta = 0.2$. Reprinted with permission from [24]. Copyright Elsevier 2022. 128
5.17 Change in the flow rate and the dissipation (at a fixed pressure gradient) compared with the straight pipe flow. The green curve represents dissipation changes, while the blue dashed curve denotes flow rate changes. Reprinted with permission from [24]. Copyright Elsevier 2022. 128

6.1 Schematic depiction of a 90^o pipe bend and the pipe cross-section at the inlet. The red dot denotes the centre of the coordinate system, which is located at the axis of inlet. 132
6.2 Computational domain of the bend used for simulations. For visualisation purposes only the coarse grid M_1 is shown. The grid is refined in the near-wall region to capture sharp gradients of the director field, as the size of flow-elastic layer scales with $Er^{-0.5}$. 134
6.3 Variation of the director orientation at the centre of the bend predicted for fluid 1; distributions for fluids 2 and 3 are similar and therefore not shown. θ denotes an angle between director and flow direction. 136

6.4 Due to the geometry curvature, the director field at $Er = 0$ moves towards the bend axis to minimise the Helmholtz free energy. 136
6.5 Director profile for $Er = 10$ at the symmetry plane of the bend for fluid 3. The red colour represents orientation for homeotropic anchoring and the black colour is the result for a wall-parallel anchoring. 137
6.6 Stream-wise velocity profile in the bend centre predicted for 5CB. Letters h and p refer to homeotropic and wall-parallel respectively. 138
6.7 Variation of the curvature effect (dimensionless) at the symmetry line for the fluid 1. Stresses are normalised by the shear scale $\frac{w_0\alpha_4}{r_0^*}$. 139
6.8 Variation of the imbalance effect (dimensionless) at the symmetry line for the fluid 1. 140
6.9 Effect of the Ericksen number on the magnitude of the secondary flow. For $u_{sec}^* > 0$ the secondary velocity at the symmetry line is directed towards the bend axis, similarly to fig. 5.8. 141
6.10 Variation of the curvature effect at the symmetry line for fluid 2. 142
6.11 Variation of the imbalance effect at the symmetry line for fluid 2. 142
6.12 Comparison of Newtonian velocity profiles in a straight pipe and a bend. . 143
6.13 Transverse velocity of a Newtonian fluid as it travels across the bend for $\delta = \frac{r_0^*}{R_0^*} = 0.2$. s denotes the distance downstream the bend entrance and is schematically illustrated in the inset. 144
6.14 Transverse velocity of fluid 1 across the bend. $s = 0$ corresponds to the location of the bend entrance. $\delta = \frac{r_0}{R} = 0.2$. Vertical black lines denote the location of bend inlet and outlet. 145
6.15 Transverse velocity of fluid 2 across the bend. $s = 0$ corresponds to the location of the bend entrance. $\delta = \frac{r_0^*}{R^*} = 0.2$. Vertical black lines denote the location of bend inlet and outlet. The variation of u_{tr} for fluid 3 is qualitatively the same and thus not shown. 145
6.16 Streamwise variation of normal and shear stresses for fluid 1. N_2 is small in comparison to τ_{sr} and thus have a limited impact on the velocity spike. . . 146
6.17 Streamwise variation of normal and shear stresses for fluid 2. N_2 is small in comparison to τ_{sr} and thus have a limited impact on the velocity spike. . . 146
6.18 Mean spike magnitude vs the shear stress τ_{sr} normalised by $(\alpha_2 + \alpha_4 + \alpha_5)\frac{w_0^*}{r_0^*}$. 147
6.19 Distorted director field entering a straight channel. 148
6.20 Evolution of the director angle downstream the bend exit for fluids 2 and 3 according to eq. (6.6). 149
6.21 Director development on the centerline with homeotropic anchoring for $\delta = \frac{r_0}{R} = 0.2$. y_d denotes the distance downstream the bend exit. Results for wall-parallel anchoring are qualitatively similar and hence not shown. . . . 149
6.22 Director variation normalised by the entrance director angle. 150

6.23 Schematic visualisation of a director (red rods) layer Δw with a uniform director orientation. The layer size increases as the Ericksen number decreases. 150
6.24 Additional pressure gradient relative to the straight pipe solution $\delta = 0.2$. . 151

7.1 Schematic illustration of the contraction geometry considered in this chapter. 154
7.2 Director orientation in a channel flow when a) $\boldsymbol{n}$ points in the same direction on both boundaries; b) $\boldsymbol{n}$ points in the opposite direction on both boundaries. Anderson [169] found that at low Er configuration a) is preferred and configuration b) is favourable at higher Er. 158
7.3 Some examples of wall-parallel boundary conditions in the vectorial framework, each representing notionally the same physical state. 158
7.4 Some examples of homeotropic anchoring in the vectorial framework, each representing the same notional physical state. 159
7.5 Mesh M_1 used in this study. The figure shows a coarsened (by a factor of 2) version of the M_1 grid for presentation purposes. Only a part of the inlet and outlet channel is included. 160
7.6 Director field with wall-parallel boundary conditions at $Er = 1.73$ a) Beris-Edwards model, b) Leslie-Ericksen model, configuration A, c) Leslie-Ericksen model, configuration B. 162
7.7 Director field with wall-parallel boundary conditions at $Er = 173$ a) Beris-Edwards model, b) Leslie-Ericksen model, configuration A, c) Leslie-Ericksen model, configuration B. 163
7.8 Comparison of the velocity fields predicted by BE and LE models at a distance $2h$ upstream of the contraction for the wall-parallel anchoring at $Er = 1.73$. 164
7.9 Distribution of N_1 and τ_{yx} predicted by BE and LE models at at a distance $2h$ upstream of the contraction for the wall-parallel anchoring at $Er = 1.73$. All stresses are normalised by the stress scale $\frac{\alpha_4 u_0}{H}$. 165
7.10 Comparison of the velocity fields predicted by BE and LE models at a distance $2h$ upstream of the contraction for the wall-parallel anchoring at $Er = 173$. 165
7.11 Distribution of N_1 and τ_{yx} predicted by BE and LE models at at a distance $2h$ upstream of the contraction for the wall-parallel anchoring at $Er = 173$. All stresses are normalised by the stress scale $\frac{\alpha_4 u_0}{H}$. 166
7.12 Variation of the director angle at $y = 0.4h$, wall-parallel anchoring. At $Er = 1.73$, the prediction of the LE theory (config. A) nearly coincides with the prediction of the BE model. 167
7.13 Director field with homeotropic boundary conditions at $Er = 1.73$ a) Beris-Edwards model, b) Leslie-Ericksen model, configuration A, c) Leslie-Ericksen model, configuration B, d) Leslie-Ericksen model, configuration D (due to the asymmetry of the director field, a whole contraction is shown). . 169

7.14 Comparison of the velocity fields predicted by BE and LE models at a distance $2h$ upstream of the contraction with the homeotropic anchoring at $Er = 1.73$. Note that the velocity distribution for configuration C is not symmetric about the centreline. 170
7.15 Distribution of N_1 and τ_{yx} predicted by BE and LE models at at a distance $2h$ upstream of the contraction with the homeotropic anchoring at $Er = 1.73$. Note that the stress distribution for configuration C is not symmetric about the centreline. All stresses are normalised by the stress scale $\frac{\alpha_4 u_0}{H}$. The shear stress in the BE model (blue dashed line) is falls onto τ_{yx} predicted by the LE theory (red dashed line) and hence the former is hardly visible. 170
7.16 Comparison of vortex sizes obtained with configurations A and B ($Er = 1.73$). 171
7.17 Director field with homeotropic boundary conditions at $Er = 173$ a) Beris-Edwards model, b) Leslie-Ericksen model, configuration A, c) Leslie-Ericksen model, configuration B, d) Leslie-Ericksen model, configuration D (due to the asymmetry of the director field, a whole contraction is shown). . 173
7.18 Comparison of the velocity fields predicted by BE and LE models at a distance $2h$ upstream of the contraction ($Er = 173$). 174
7.19 Distribution of N_1 and τ_{yx} predicted by BE and LE models at at a distance $2h$ upstream of the contraction ($Er = 173$). All stresses are normalised by the stress scale $\frac{\alpha_4 u_0}{H}$. 174
7.20 Variation of the director angle at $y = 0.4h$, homeotropic anchoring. 175
7.21 Director development at $Er = 173$ for configuration C. 175
7.22 Pressure drop across a contraction. 176
7.23 Couette criterion for the BE and LE models with homeotropic and wall-parallel boundary conditions. 177
7.24 Distribution of dissipation at a distance h upstream of the contraction. . . . 178
7.25 Budget of dissipation in configurations with wall-parallel anchoring. 178
7.26 Budget of dissipation in configurations with homeotropic anchoring. 179
7.27 Graphical interpretation of the Couette correction. 180

C.1 Schematic illustration of a curved duct. The director is pointing in the opposite direction to mimic the situation in a curved pipe. 221
C.2 Comparison of curved and straight duct solutions. Negative x-axis is closer to the centre of curvature. 222
C.3 Due to the geometry curvature, the director field at $Er = 0$ moves towards the bend axis to minimise the Helmholtz free energy. 223

List of tables

3.1 Relative errors obtained on meshes $M_1 - M_3$ for $\alpha_2 = -0.5$. 82

5.1 Coefficients a and b for different liquid crystals. 113
5.2 Nematic viscosities converted to match the TIF model [43], the imbalance ratio χ, analytical predictions of horizontal velocities at the pipe axis. . . . 120
5.3 The relative magnitude of first order terms with respect to the leading order solution for $\delta = 0.2$. Red values indicate a singular behaviour, where radial and axial director components diverge. 129

6.1 Boundary conditions for the velocity, director and pressure fields. 133
6.2 Nematic viscosities of the fluids considered in this chapter. 133
6.3 Change in the strength of a given effect with respect to the infinite Ericksen number limit for fluid 1. 140

7.1 Boundary conditions for the velocity, pressure, $\boldsymbol{Q}$-tensor and director fields in the wall-parallel anchoring configuration. Superscripts A, B refer to configurations shown in fig. 7.3. The off-diagonal components of $\boldsymbol{Q}$ on the boundaries are zero. 157
7.2 Boundary conditions for the velocity, pressure, $\boldsymbol{Q}$-tensor and director fields in the homeotropic configuration. The off-diagonal components of $\boldsymbol{Q}$ on the boundaries are zero. Superscripts A-D refer to configurations shown in fig. 7.4. 157
7.3 Normalised 2-norm of the LE prediction with respect to the BE result $\frac{|N_{LE}-N_{BE}||_2}{||N_{BE}||_2}$ for flows with the wall-parallel anchoring. N represents either the velocity or stress component. 166
7.4 Normalised 2-norm of the LE prediction with respect to the BE result $\frac{|N_{LE}-N_{BE}||_2}{||N_{BE}||_2}$ for flows with the homeotropic anchoring. N represents either the velocity or stress component. 171

List of publications

K. Fedorowicz and R. Prosser, “Flow of transversely isotropic fluid in curved pipes,” *Journal of Non-Newtonian Fluid Mechanics*, p. 104 716, 2022.

Abstract

Numerical simulation of liquid crystalline flows in complex geometries.
Kamil Fedorowicz
A thesis submitted to the University of Manchester
for the degree of Doctor of Philosophy, 2022

The term complex fluids refers to a group of materials whose behaviour is intermediate between solids and liquids. They have found applications in numerous areas and are used to manufacture foods, cosmetics and medicines. With the rise of computer power over the last few decades and in the spirit of the Fourth Industrial Revolution (Industry 4.0), there is an increased tendency for in-silico product development. Physical experiments are reduced to the minimum and substituted with computer simulation in order to decrease the roll-out time of new formulations. Numerical calculations can provide an insight into the microstructure behaviour, however computations are only as good as the physics embedded in the constitutive equation. This project aims to assess the suitability of some of the existing governing equations of liquid crystals to model soap behaviour.

In the thesis, we aim to examine the impact of the non-Newtonian microstructure on the material behaviour in complex geometries. The flow of liquid crystals through a curved pipe in the limit of infinite Ericksen number is analysed. The governing equations are solved analytically and reveal that the secondary flow arises at zero Reynolds number due to the misalignment between the microstructure orientation (director) and flow. Different mechanisms driving the secondary flow are distinguished: 1) the combination of normal stresses and geometry curvature and; 2) non-axisymmetric stress distribution caused by the flow curvature. Depending on material properties, those effects may act in the opposite direction, so the rotation of the secondary flow can vary. Additionally, the geometry curvature shifts the velocity field towards the bend axis, which results in the re-orientation of the internal microstructure. Analytical estimations are complemented with numerical simulations to give an insight into the flow behaviour at finite Ericksen numbers. The direction and intensity of the secondary motion depend on the director orientation on boundaries and the Ericksen number that quantifies the strength of viscous to elastic effects; for liquid crystals with specific material properties, a flow reversal is possible. Numerical simulations show that the pipe curvature manifests its presence outside the elbow. There is a spike in the velocity field as the fluid enters/leaves the elbow, while the director development length downstream of the bend is affected by the Ericksen number and material properties.

In the last part of the thesis, a planar contraction geometry is used to compare director and $\boldsymbol{Q}$-tensor frameworks of simulating liquid crystals. The vectorial approach cannot model the head-tail symmetry and predicts different flow fields for boundary conditions with the same physical meaning; a drawback that is particularly evident at low Ericksen number flows with homeotropic anchoring. There is less ambiguity with wall-parallel anchoring, where vectorial and tensorial frameworks produce similar results, provided that the correct set of boundary conditions is chosen.

Declaration of originality

I hereby confirm that no portion of the work referred to in the thesis has been submitted in support of an application for another degree or qualification of this or any other university or other institute of learning.

Copyright statement

i The author of this thesis (including any appendices and/or schedules to this thesis) owns certain copyright or related rights in it (the "Copyright") and s/he has given The University of Manchester certain rights to use such Copyright, including for administrative purposes.

ii Copies of this thesis, either in full or in extracts and whether in hard or electronic copy, may be made *only* in accordance with the Copyright, Designs and Patents Act 1988 (as amended) and regulations issued under it or, where appropriate, in accordance with licensing agreements which the University has from time to time. This page must form part of any such copies made.

iii The ownership of certain Copyright, patents, designs, trademarks and other intellectual property (the "Intellectual Property") and any reproductions of copyright works in the thesis, for example graphs and tables ("Reproductions"), which may be described in this thesis, may not be owned by the author and may be owned by third parties. Such Intellectual Property and Reproductions cannot and must not be made available for use without the prior written permission of the owner(s) of the relevant Intellectual Property and/or Reproductions.

iv Further information on the conditions under which disclosure, publication and commercialisation of this thesis, the Copyright and any Intellectual Property and/or Reproductions described in it may take place is available in the University IP Policy (see `http://documents.manchester.ac.uk/DocuInfo.aspx?DocID=24420`), in any relevant Thesis restriction declarations deposited in the University Library, The University Library's regulations
(see `http://www.library.manchester.ac.uk/about/regulations/`) and in The University's policy on Presentation of Theses.

Acknowledgements

Firstly, I would like to thank my supervisor Dr Robert Prosser for his immense support and patience during the last six years of my undergraduate and postgraduate studies. He is a great mentor, and his honest advice was crucial for my development as an academic and a person.

I am extremely grateful to Dr Ioannis Bagkeris and Dr Vipin Michael for helping me throughout my PhD journey. Their help was invaluable during the initial stages of my research when everything was new and mysterious to me. I could not have progressed without your support.

I would like to acknowledge the Unilever (Grant No. EP/R00482X/1) for funding my research and the CAFE4DM group for helpful discussions and team meetings. I am particularly grateful to my industrial supervisors: Dr Simon Watson, Yury Yarovoy and Prof. Adam Kowalski for introducing me to the world of material characterisation and helping to understand the soap production process when experimental facilities were unavailable. Special thanks go to Elliott Sutton and Dr Claudio Pereira Da Fonte, who helped me to better understand the nature of yield stress fluids. I would also like to acknowledge Andrew Masters and Carlos Avendaño for their help and discussions about liquid crystals.

I would also like to mention my closest friends: Diego del Cura, James Hack and Mate Vida, for providing me with much-needed distractions and incredible memories during the first four years of my studies in Manchester. I would also like to thank Hongru Li, who taught me a lot about Chinese cuisine - you have significantly enriched my cooking skills. Special thanks go to the whole George Begg crew, who have been so hospitable during pastry mornings and PGR events.

Last but not least, I would like to thank my loving parents, who are always ready to support me in all possible aspects and encourage me to challenge myself. They had dedicated an enormous amount of effort to support the development of my interests when I was younger; from sacrificing their weekends to watch me swim or attend science exhibitions to spending evenings and helping with my schoolwork.

Nomenclature

Roman symbols

$\boldsymbol{h}$	molecular field in the vectorial framework
$\boldsymbol{n}$	director
$\boldsymbol{v}$	velocity
p	pressure
$\boldsymbol{D}$	symmetric part of the velocity gradient tensor
Er	Ericksen number
f_d	distortion energy in vectorial models
f_d^Q	distortion energy in tensorial models
$f_{nematic}$	nematic bulk energy
f_{LdG}	Landau-de Gennes energy
$\boldsymbol{H}$	molecular field in the tensorial framework
K_i	Frank constants in vectorial models
K_i^Q	Frank constants in tensorial models
$\boldsymbol{N}$	corotational time derivative of the director
$\boldsymbol{Q}$	order parameter tensor
S	order parameter (scalar)
$\boldsymbol{S}$	hydrodynamic torque acting on the order parameter tensor

Greek symbols

α_i	Leslie viscosities
β	biaxiality of the order parameter tensor
$\dot{\boldsymbol{\gamma}}$	strain rate tensor
δ	bend curvature
η_0	zero-shear viscosity
η_∞	viscosity at an infinite shear rate
η_{eff}	effective viscosity
λ	tumbling parameter (transversely isotropic fluid model)
λ_i	eigenvalues of $\boldsymbol{Q}$
ξ	tumbling parameter (Beris-Edwards model)
ξ_N	defect size
ρ	density
$\boldsymbol{\tau}$	total stress tensor
τ_0	yield stress
ψ	stream function
$\boldsymbol{\omega}$	antisymmetric part of the velocity gradient tensor
θ_L	Leslie angle
Γ	rotational diffusivity in the Beris-Edwards model

Chapter 1

Introduction

The term Fast Moving Consumer Goods (FMCG) describes a vast range of cheap products that are purchased in high quantities such as medicines, cosmetics, foods, and drinks [1]. The worth of the FMCG market was estimated to be over $10 000 billion in 2017 with an expected 50% rise by 2025 [2]. The last number can increase even further due to the impact of COVID-19, which caused a 500% spike in demand on cleaning products [3]. The abundance of the FMCG sector and the potential for significant financial benefits results in a highly competitive environment. In order to increase market share and gain an advantage over other contenders, FMCG companies aim to develop high-quality products in the shortest possible time - releasing a new brand seven months before competitors generates 60% higher sales [4]. The traditional development consists of a series of iterative tests of sample products, which ends upon obtaining a satisfactory formulation [5]. The method is time-consuming, generates much waste, and therefore companies search for alternative techniques of product development. The reduction of the roll-out time and waste can be achieved through the use of computer-aided engineering (CAE) [6, 7], which is one of the concepts of the Fourth Industrial Revolution that aims to substitute physical experiments with computer simulations [8].

Seemingly simple and cheap FMCG articles are usually required to have multiple features that ensure the handiness of the product [9]. Toothpaste should not only have a cleaning function, but it must flow when squeezed and stay put on the toothbrush [10, 11]. A shampoo should easily spill out of the container but be viscous enough to not leak through a hand [12, 13]. Ice creams are kept in low temperatures to remain solid, but the impression of excessive cold should be eliminated or delayed in order to improve the customer experience [9, 14]. The above characteristics can be achieved by exploiting the properties complex fluids, whose microstructure may consist of multiple phases or contain solid-like objects, and is therefore more intricate than the microstructure of simple fluids (water or oil) [15]. The functionality of the FMCG products is predicated on their complex properties, such as variable viscosity or solid-like behaviour, and the exploitation of complex fluids is necessary for further development of the FMCG industry [16].

Newtonian fluids (water, oil, air) consist of such small particles that they instantaneously respond to any deformation [17]. In contrast, complex fluids are made up of larger molecules (fig. 1.1); in the case of soap, the microstructure is a mixture of high aspect ratio particles, called bricks and the lyotropic liquid crystal phase. The material's relaxation time is

comparable to the flow time-scale [15, 18] induced upon material processing. As a result, the deformation response of many complex fluids is intermediate between solids and simple liquids; so-called non-Newtonian behaviour [16–18] with an example shown in fig. 1.2. Depending on the structure of molecules and their arrangement, complex fluids are grouped into emulsions (one fluid dispersed in another [19]), polymeric liquids (large molecular chains that consist of repeating units [20]) and liquid crystals (anisotropic molecules dispersed in a solvent [21, 22]).

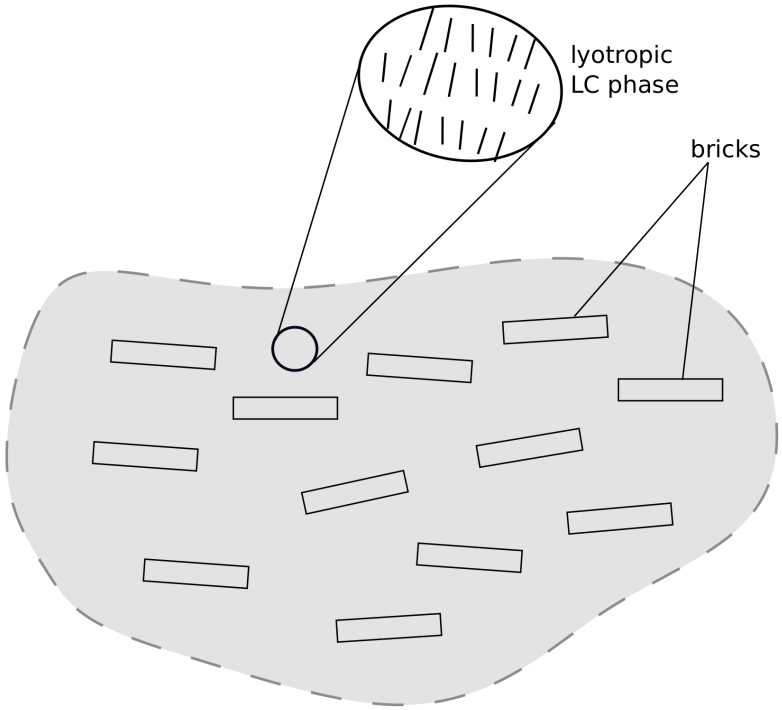

Figure 1.1. A schematic visualisation of the structure of a complex fluid based on the structure of soap. Long, anisotropic particles (bricks) are distributed within a lamellar phase that consists of sheets of rod-like molecules [23]. Reprinted with permission from [24]. Copyright Elsevier 2022.

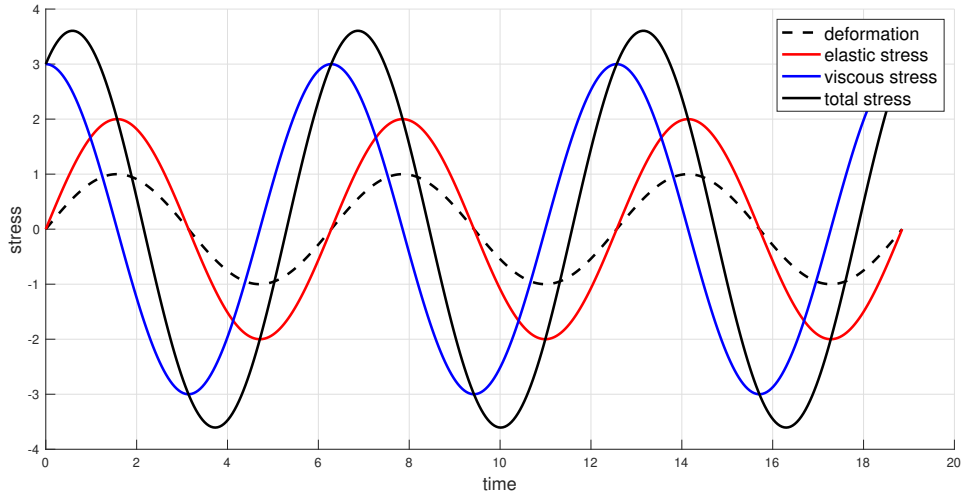

Figure 1.2. Response of a generic complex fluid to small amplitude periodic straining. The elastic response (—) is proportional to the deformation (– –), while the viscous (—) response is proportional to the rate of deformation. A typical non-Newtonian fluids has both viscous and elastic components, so the net response is intermediate between those two.

The intricate structure of non-Newtonian fluids is both a desirable and daunting characteristic. It provides the functionality of the FMCG products (e.g. the solid-like behaviour of a toothpaste) but also makes the manufacturing process highly challenging [25, 26]. In contrast to Newtonian liquids, the viscosity of complex fluids varies and may depend on internal (solvent concentration, shear rate, deformation history) and external factors (magnetic and electric fields) [15, 18, 27]. Additionally, the interaction of stretching molecules with the flow complicates scaling [17], so flows with the same Reynolds number (which itself cannot be unambiguously defined because of a variable viscosity) need not be dynamically similar [28, 29]. The process of scaling from laboratory to industrial scales is often further complicated by material elasticity, whose importance can be quantified by Ericksen or Weisenberg numbers [15].

Significant progress was made in the last century in the development of non-Newtonian constitutive relations. The early models were based on empirical observations, thus capable of describing a wide range of fluids [18, 30, 31]. With an advance in mathematical techniques, more recent constitutive relations focused on describing the materials stress as a result of the applied deformation. Each constitutive equation aims to model the microstructure dependent physics; for example, governing equations of entangled polymers concentrate on their stretching and deformation [32, 33], while those of liquid crystals focus on the orientation of anisotropic molecules and their interaction with the flow [34, 35]. Numerous constitutive equations have been proposed, but the majority of them are capable of replicating only some of the behaviour observed in experiments [15, 18, 27]. With increases in the computing power and the development of numerical techniques, it is possible to simulate the most complex constitutive behaviours [36]. However, the simulation can only replicate the physics that is embedded in the model [37], so understanding the constitutive relations and their limitations is necessary to accelerate the transition to virtual product development.

1.1 Aims and objectives

This project aims to improve the understanding of the rheological properties of soap by taking into account its liquid-crystalline structure. Soap bars are produced in a screw extruder (plodder) where a noodle material (granular molecules consisting of fatty acids [23]) mixed with perfumes and dyes is compressed and blended into a uniform mass, as shown in fig. 1.3. Soap is classified as a viscoplastic material [5] - it is solid-like at low shear rates and liquid-like as the deformation rate increases [38]. Experiments suggest that it also experiences wall slip [39]. Origins of the wall slip are not clear; some studies associate it with fluid separation and the migration of less viscous phase towards the wall [40].

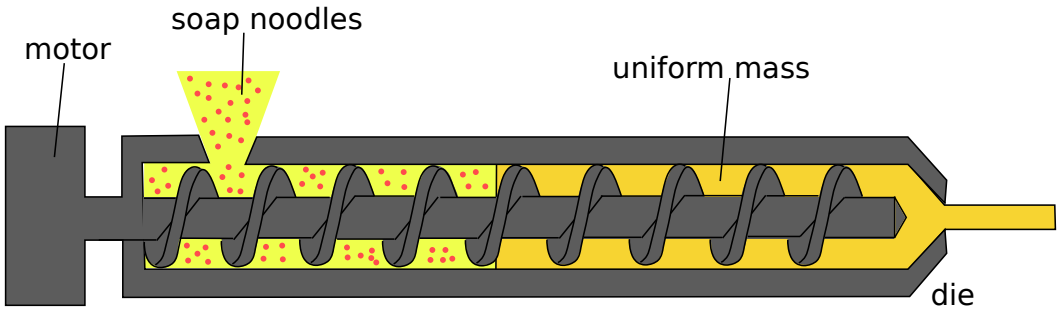

Figure 1.3. A schematic description of the soap extrusion process.

For industrial purposes, soap is modelled through empirical relations, where the viscosity depends on the applied shear rate only [41]. The models are simple, robust and easy to use in commercial codes [42]; however, they fail to describe the evolution of microstructure in any detail. The assumption of a shear dependent viscosity generates a significant error associated with parameter fit [41] because the flow curve (the curve describing the relation between stress and strain) strongly depends on other factors such as the characteristic dimension of the geometry [41]. This length-scale is easily chosen in pipes or channels, but the situation complicates as the geometry becomes more complex, e.g. the extruder used to produce soap bars. Furthermore, empirical models assume that the physics of shear and elongation is the identical, so the effective viscosity changes in the same fashion irrespective of deformation mode. That flaw does not impact predictions in shear dominated flows (pipes, channels); however, it causes a significant discrepancy between experiments and simulations in geometries where the extensional component is significant (contractions, T-junctions). Thus, this project aims to explore more advanced constitutive equations as an alternative to modelling the soap flow.

This project examines the performance of constitutive equations dedicated to liquid crystals as a precursor of soap. The majority of rheological descriptions were developed to understand phase transitions and near-static flows and they tend to perform well in simple flow geometries [21, 43]. However, since typical industrial configurations are more complex than straight pipes, the work presented in this thesis explores the behaviour of currently available liquid crystal models in industry-relevant domains such as bends and contractions.

1.2 Outline of the thesis

This thesis summarises the research overtaken during the PhD project. Chapter 2 introduces liquid crystals, describes their structure and basic concepts used in modelling. Non-Newtonian rheology and the flow behaviour of liquid crystals is discussed. Different approaches of modelling the fluid flow are presented; we first introduce the Newtonian approximation and then present more advanced constitutive behaviours (generalised Newtonian fluid models and nematodynamic equations). Chapter 3 introduces the novel OpenFOAM solver dedicated to modelling the flow of nematic liquid crystals. The solver is used throughout the thesis to investigate the behaviour of liquid crystals in complex geometries. Chapter 4 presents the results of capillary simulations and quantifies the effect of wall anchoring on the rheology.

Perturbation analysis is used in chapter 5 and provides an insight into the physics governing the flow of nematic liquid crystals in a fully curved pipe flow at an infinite Ericksen number. The work is extended in chapter 6 where numerical solutions of finite Ericksen number flows are presented. The effect of wall anchoring and director development downstream/upstream of the bend is discussed. Chapter 7 analyses the flow of liquid crystals through a 4:1 planar contraction and a comparison of vectorial and tensorial frameworks to modelling the director and flow field is made. Chapter 8 summarises the findings and provides suggestions for future work.

Chapter 2

Literature review

This chapter establishes the background material for discussions presented later in the thesis. Firstly, the structure of liquid crystals is discussed, and the *director* and *order parameter tensor* approaches of representing liquid crystal microstructure are introduced. Later sections describe the rheology of liquid crystals and the consequences of the anisotropic structure on the material behaviour. Foundations of the *Hamiltonian formulation* are presented as an alternative of developing the governing equations. Finally, we present a ladder of solution techniques available to model the fluid flow: the Newtonian model with the non-Newtonian empirical extensions (Generalised Newtonian Fluid models) are discussed first; later, liquid crystal theories are introduced as an alternative that allows for a more accurate description of the microstructure.

2.1 The structure of liquid crystals

Molecules of a crystal form a regular, three-dimensional lattice [44]. Small inter-molecular distances combined with strong bonds result in rigid materials that are highly resistant to deformation. In contrast, there are no long-range positional correlations in the arrangement of fluid molecules [45]; the structure cannot resist forces and flows arise when stress is applied. Liquid crystals are an intermediate state of matter whose behaviour shares characteristics common to fluids and solids. They consist of anisotropic elements (rods (fig. 2.1) or disks) that, on average, align in the same direction. The liquid crystalline state can be achieved over a wide spectrum of materials, ranging from elongated organic molecules (e.g. p-azoxyanisole, fig. 2.1) with typical length $O(20\ \text{Å})$ to large, synthetic polymeric fibres whose length is $O(100\ \mu\text{m})$ [21]. Due to the orientational ordering within their structure, liquid crystals share some properties with solid materials, e.g. birefringence, anisotropic thermal and electrical conductivity [21]. Similarly to isotropic fluids, liquid crystals cannot resist stresses and are easily deformable; however, their flow properties are strongly dependent on the orientation of the microstructure, providing another link to solids. Additionally, the interaction of anisotropic objects in a flow results in normal stresses. Normal stresses are insignificant in simple shear flows, but they have a crucial effect on material behaviour in industrially relevant geometries, such as extruders or mixers [18, 46].

An external electric or magnetic field can easily control the orientation of the long axis of a liquid crystal. Therefore, liquid crystals were originally exploited in the production of opto-

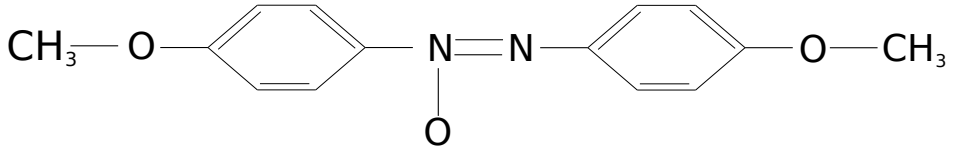

Figure 2.1. Due to the high aspect ratio, particles of p-azoxyanisole (PAA) and other liquid crystals often resemble rods.

electronic devices such as watches and portable calculators [47, 48]. Continuous progress in the electronics industry allowed for extending the applications of liquid crystals to lasers and liquid crystal display (LCD) devices [49, 50]. The traditional manufacturing method relied on filling a thin gap with a nematic material [51]. The procedure is time consuming, and alternative approaches of LCD production are investigated [52]. Faster methods allow for an increased throughput; however, they introduce more strain on the nematic microstructure, which can decrease the display quality. Therefore, modelling the flow-director interaction plays a crucial role in the product development [53]. Further improvements in the quality of LCD devices are more possible by the exploitation of liquid crystals with non-axisymmetric molecules [54]. Liquid crystals are also used in the detergent industry to produce soaps, which consists of amphiphilic molecules, whose hydrophobic part provides the cleaning action. Amphiphiles assemble into larger structures, and the final shape of the macromolecules is predicated on the amphiphile concentration [55]. At intermediate concentrations, amphiphiles form rod-like particles, while at high concentrations the structure resembles sheets of elongated cylinders. Both structures are characterised by a high degree of orientational alignment, therefore resulting in anisotropic properties [21].

In the case of simple materials (water, oil), the liquid-solid transition occurs by decreasing temperature, which strengthens molecular interactions, resulting in rigid solids. For liquid crystals, the transition involves several intermediate stages [56] and can be driven either by changing temperature (thermotropic LC) or the concentration of anisotropic particles (lyotropic LC). As the liquid-solid transition occurs, the degree of orientational alignment between neighbouring macromolecules increases and the centres of gravity of anisotropic particles tend to exhibit a long-range ordering in one or two directions. The latter characteristic is the basis for distinguishing different types of liquid crystals:

- Nematics - these consist of rod-like molecules oriented on average in the same direction, and there is a short range ordering between their centres of mass (fig. 2.2 b) [57]. The susceptibility of nematic particles to the electric field is exploited in the optoelectronic industry to produce watches and portable calculators.

  Cholesterics are a subgroup of nematics whose chiral structure lacks a mirror symmetry (fig. 2.3) and resembles the shape of some cholesterol esters (hence the name cholesterics [58]). Similarly to nematics, cholesterics have also been predominantly exploited in the display industry.

  A subgroup of nematics can be identified with different degrees of orientational order along three distinct axes, called biaxial liquid crystals [57]. The biaxial state can be formed either by planks with both long and medium axes having common orientations

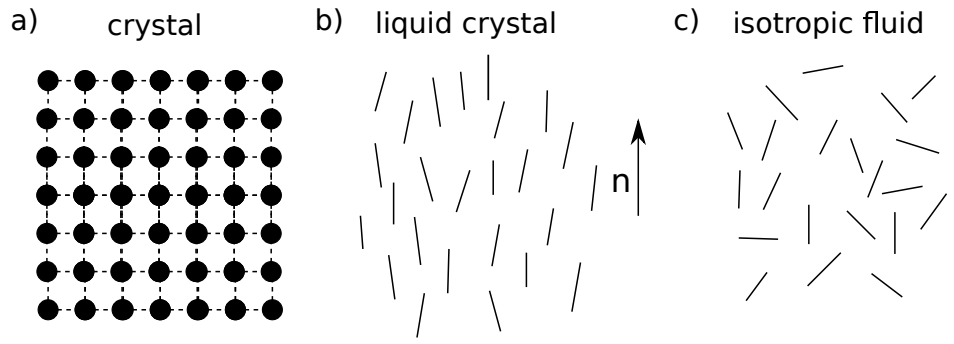

Figure 2.2. Schematic depiction of the structure of a a) crystal, b) liquid crystal, c) isotropic fluid consisting of anisotropic objects.

(fig. 2.4) or by axi-symmetric rods whose rotation is constrained along a certain direction, giving an impression of a secondary alignment direction (fig. 2.5). Biaxial nematics were discovered relatively recently, in 2004 [59, 60], over forty years after their existence was predicted theoretically [61].

- Smectics have a lamellar structure, where the molecules in each layer point on average in the same direction. We distinguish different types of smectics, depending on the molecule orientation within each layer (smectic A and C [62, 63], fig. 2.6) [21, 64], or the arrangement of their centres of gravity. The properties of smectic liquid crystals are primarily exploited in the cleaning industry, as at high concentrations micelles tend to form sheets of elongated cylinders [55].

- Columnar phase - is the phase with the highest positional order; each layer consists of discotic elements arranged in a two-dimensional lattice, pointing in the same direction (fig. 2.7) [65]. The fluid-like behaviour arises from the lack of positional order in each column, as the distances between particles vary [21].

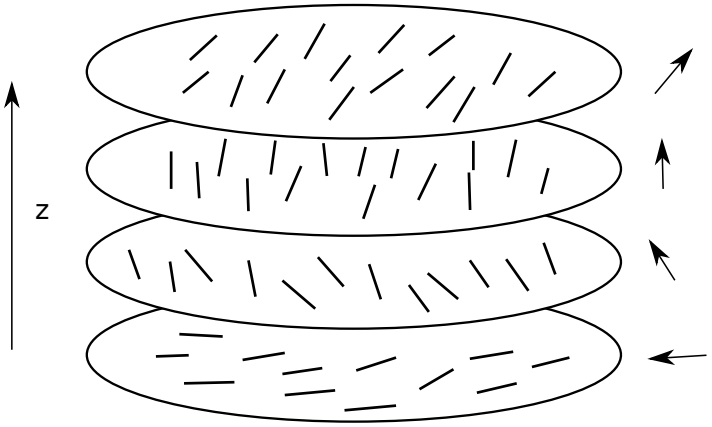

Figure 2.3. Schematic representation of alignment of particles in cholesterics.

2.2 Director and the order parameter

The complete information about the orientational distribution of rod-like molecules within a nematic is provided by the orientational distribution function $p(\boldsymbol{a})$ that describes the chance

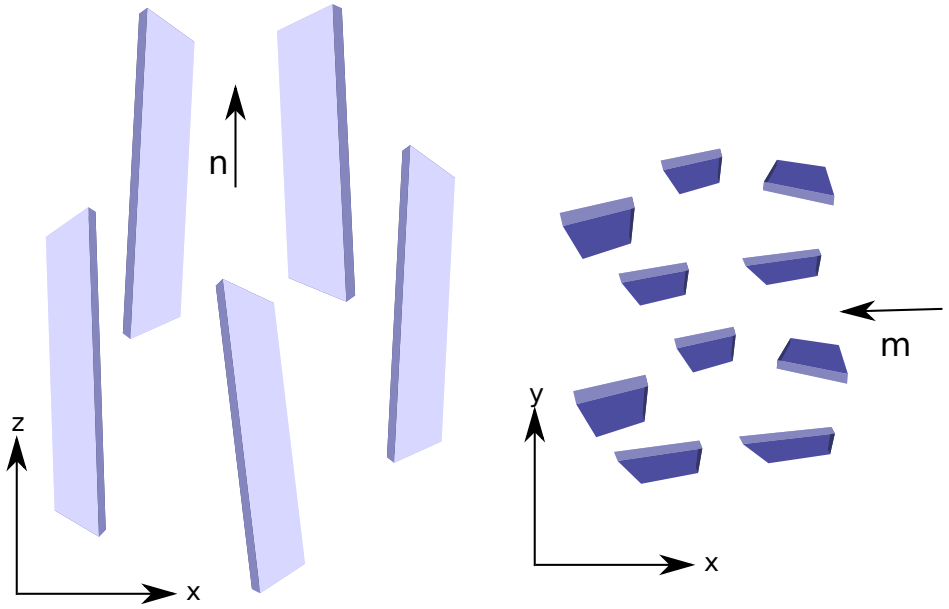

Figure 2.4. A biaxial liquid crystal consisting of planks with the medium axis aligned in a preferential direction.

of finding a particle, whose main axis points in the direction $\boldsymbol{a}$ [21]. Since liquid crystal particles are represented by headless rods, a pair of vectors with the opposite signs represents the same state $p(\boldsymbol{a}) = p(-\boldsymbol{a})$. For isotropic systems, the orientational distribution function is independent of $\boldsymbol{a}$ and $p = {}^1\!/_{4\pi}$ [15]. This is not the case for nematic liquid crystals, in which the long axis of rod-like particles points on average in a common direction. The description of the microstructure via the orientational distribution function is computationally expensive and thus rarely used for industrial purposes [66]. Instead, the structure is characterised via the *director field* $\boldsymbol{n}$, defined as the average molecular direction of an assembly of rod-like particles [57] (fig. 2.8). $\boldsymbol{n}$ is a unit vector, which represents only the orientation of rod-like particles and its length does not change. Due to the head-tail symmetry of nematics, vectors $\boldsymbol{n}$ and $-\boldsymbol{n}$ represent the same physical state.

The director field describes only the average local orientation of rod-like particles, however $\boldsymbol{n}$ does not provide any information on the degree of alignment, which can vary between systems described by the same director field (fig. 2.9). The first approach to quantify the degree of alignment is to use the first moment of the orientational distribution function

$$\langle \boldsymbol{n} \cdot \boldsymbol{a} \rangle = \langle \cos\theta \rangle, \tag{2.1}$$

where $\langle \cdot \rangle$ is the average operator and θ measures the misalignment between director and a single particle. Since liquid crystal particles are headless ($p(\boldsymbol{a}) = p(-\boldsymbol{a})$), for each molecule misaligned by θ with respect to the director field, there is a particle misaligned by $\theta + \pi$, so $\langle \cos\theta \rangle = 0$. Therefore, the degree of molecular alignment is measured by the second moment of the distribution function

$$S = \frac{1}{2}\langle 3\cos^2\theta - 1 \rangle, \tag{2.2}$$

referred to as the *order parameter*. In nematic systems, $-0.5 \leq S \leq 1$ [67]; when all

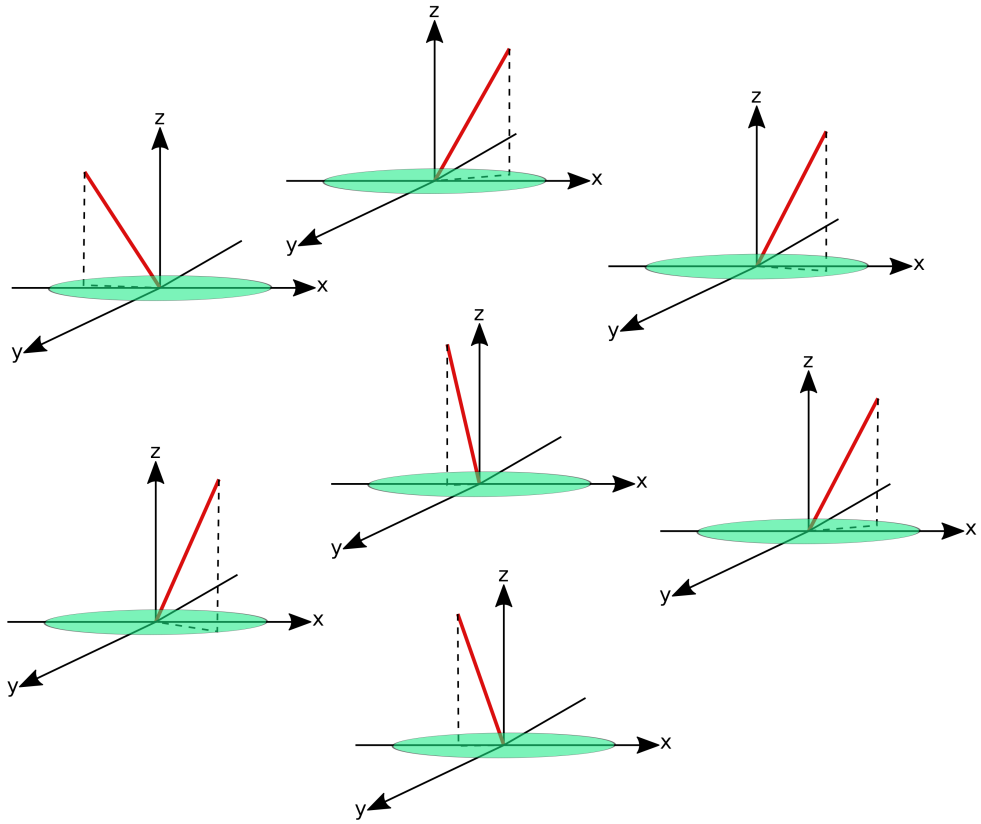

Figure 2.5. Example of a biaxial liquid crystal field. The director (red rods) aligns on average along the $z-$direction (the long axis), but there is also a preferential ordering along the $x-$direction (medium axis) represented by an ellipse with $r_x > r_y$.

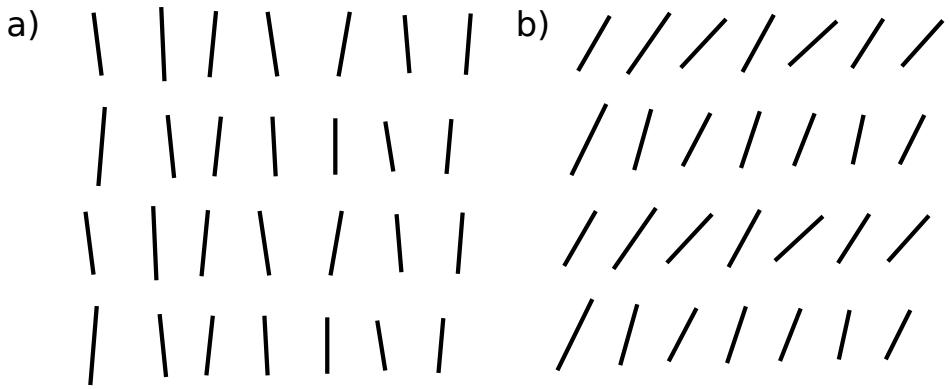

Figure 2.6. Comparison of a smectic A (a) and a smectic C (b). Particles in smectics A are aligned (on average) in the direction normal to the layer, and are tilted in case of a smectic C.

particles are perfectly aligned with $\boldsymbol{n}$, $S = 1$, while for isotropic systems the director cannot be defined and $S = 0$ [21]. The order parameter is a molecular quantity and changes in S occur over distances significantly smaller than the mean director orientation. For that reason, the majority of liquid crystal theories based on the director framework describe only the mean orientation of rod-like particles and fails to provide any information on the order parameter.

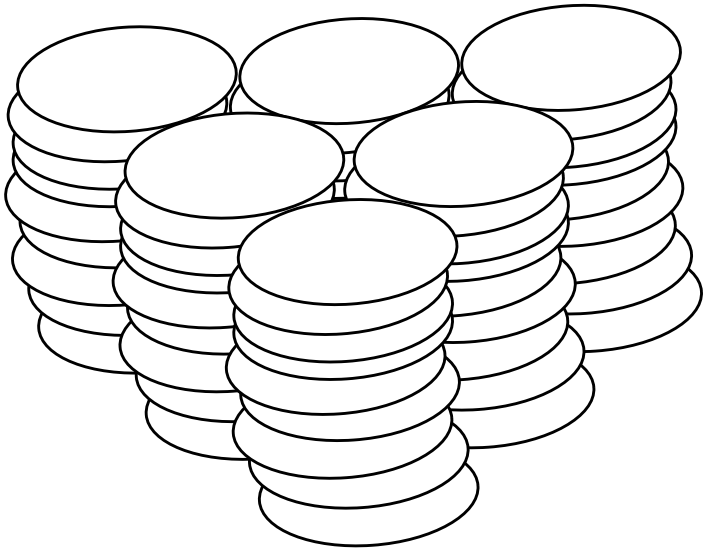

Figure 2.7. Schematic illustration of columnar phases, where individual disks represent disk-shaped molecules. The distance between layers may vary.

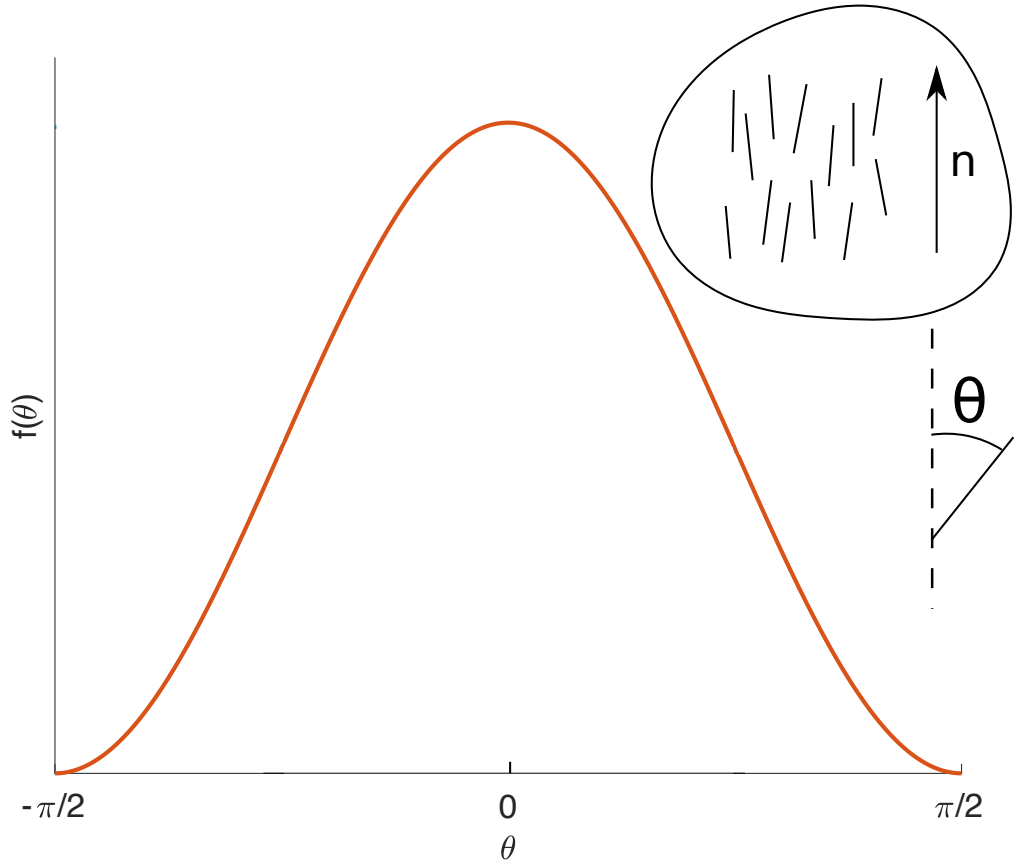

Figure 2.8. Example distribution functions of nematic liquid crystal with a horizontal and vertical director fields. θ measures the angle between a single liquid crystal particle and vertical direction. Due to the head-tail symmetry, only the range $-\pi/2 \leq \theta \leq \pi/2$ is shown.

2.3 Wall anchoring

Liquid crystals are characterised by the long-range orientational order that has a substantial effect on their mechanical, electrical and optical properties [21]. In static cases, the direction of $\boldsymbol{n}$ can be controlled on solid boundaries through surface treatment [68]. Rubbing a surface along a certain direction produces microscopic rows (fig. 2.10) and the director is more likely

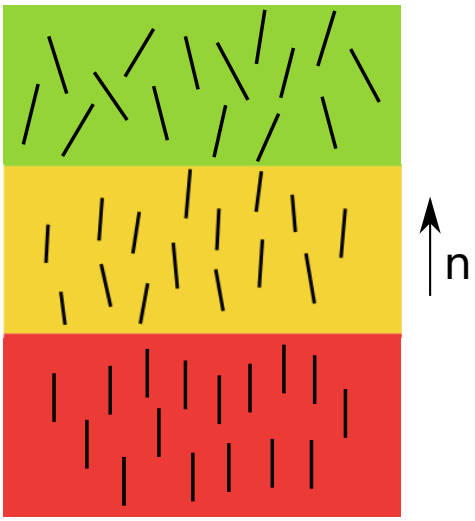

Figure 2.9. Schematic visualisation of a nematic field with a constant director orientation and varying order parameter. Red, orange and green colours denote high, medium and low order parameters, respectively.

to align along them, in the *wall-parallel* direction [21, 69]. On the other hand, an application of detergents with high aspect ratio particles (polyamides and lipids) attaches a polar head to the surface, imposing a wall-normal (*homeotropic*) orientation (fig. 2.11) [21]. Depending on the strength of wall effects, the boundary conditions may be grouped into [43]:

- Strong anchoring (Dirichlet boundary condition) - the wall interaction is strong enough to fix the director orientation irrespective of other fields (i.e. magnetic or flow-induced).
- No anchoring (Neumann boundary condition) - when the wall exerts no effect on the director, it aligns in the same direction as nearby particles to minimise the director distortion.
- Weak anchoring (Robin type boundary condition) - intermediate condition. The director has a preferred orientation at the wall, but if the contribution from other fields (such as the flow or magnetic fields) is strong enough, the anchoring deviates from the preferred direction [70]. This generates an additional surface energy [43, 71]

$$f_s = \frac{1}{2} a_0 (1 + \phi(\boldsymbol{n} \cdot \boldsymbol{\nu})^2), \tag{2.3}$$

where a_0 controls the resistance to deviation from the preferred orientation, $\boldsymbol{\nu}$ is the wall-normal vector. If $-1 < \phi < 0$, the director favours alignment parallel to ν (homeotropic), while for $\phi > 0$, a surface-aligned orientation minimises the additional surface energy. In the limit of $a_0 \to 0$ and $a_0 \to \infty$ zero-gradient and fixed value boundary conditions are restored respectively.

2.4 Rheology of liquid crystals

Some of the liquid crystal applications (display devices) exploit the optical properties of liquid crystals and typically involve static configurations, where significant director distor-

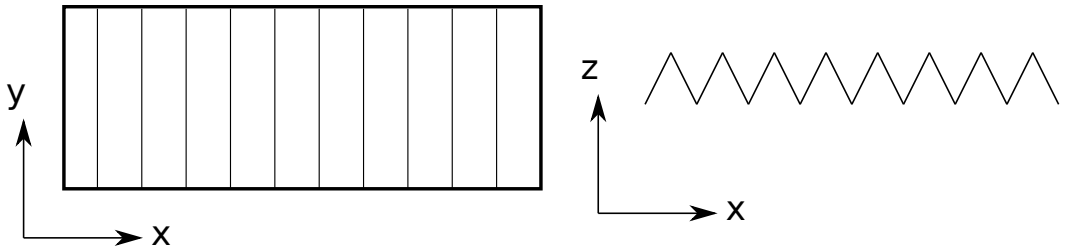

Figure 2.10. Schematic illustration of a surface imposing a wall-parallel anchoring. The surface was rubbed along the $y-$ direction, which created microscopic rows, hence imposing alignment in the parallel direction.

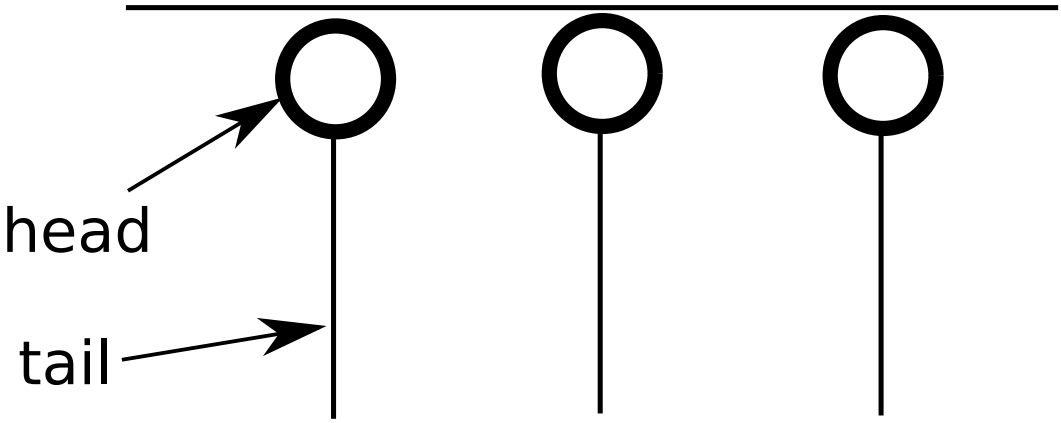

Figure 2.11. Head of a detergent molecule is attracted to the solid surface, which imposes a wall normal orientation.

tions can be caused by electric fields. That is not the case in injection moulding, where anisotropic properties of liquid crystal polymers are utilised to produce high strength, light materials (e.g. Kevlar) with numerous applications including medicine, sports equipment and manufacturing of automotive parts [72]. Rheological characteristics of liquid crystals not only determine the power expenditure required to pump the fluid but also, depending on the orientation of the long axis, control the material strength [73]. Despite the importance of liquid crystal polymers, their rheology is not completely understood. Mięsowicz demonstrated that by restraining the orientation of the long axis through an external field (fig. 2.12), the shear viscosity could differ by a factor of four; when the director lies parallel to the velocity gradient, particles have limited freedom to travel as they frequently collide with each other, increasing the flow resistance. On the other hand, particles aligned in the flow direction can easily slide past each other, which results in the smallest viscosity [74]. The viscosity of a liquid crystal can also be controlled through temperature [75]; at low temperatures, the viscosity displays a strong orientational dependence, as shown in fig. 2.13. However, above the nematic to isotropic transition temperature, the long-range ordering is lost, the director distribution is isotropic, thus erasing all effects of previous ordering [75].

Apart from external factors (temperature, magnetic field), the mechanical properties of liquid crystals also depend on shear rate and deformation history. For that reason, their rheology is complex and not fully understood. Based on experimental measurements, Onogi and Asada [76] proposed a three region curve (fig. 2.14) consisting of a pair of shear-thinning regimes separated by a Newtonian regime. The curve is not fixed for all materials with some liquid crystals experiencing monotonic shear thinning in the range $10^{-3}\ \mathrm{s}^{-1} < \dot{\gamma} < 10^{3}\ \mathrm{s}^{-1}$,

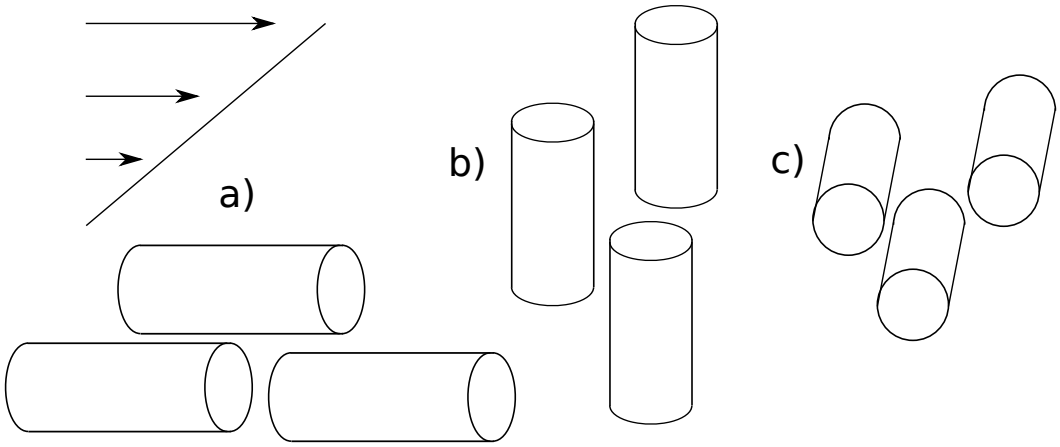

Figure 2.12. Schematic representation of director orientations considered by Mięsowicz in his experiment.

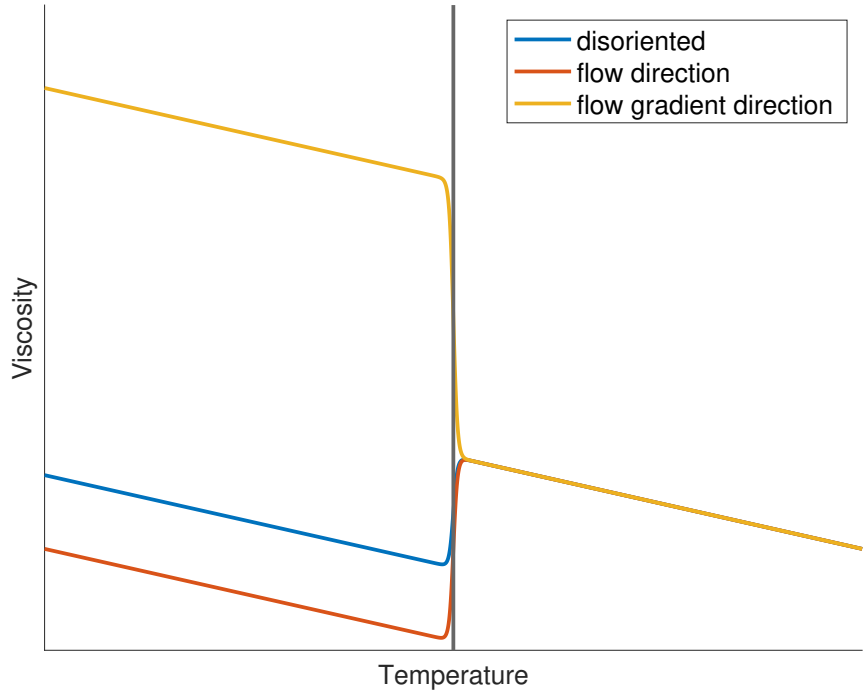

Figure 2.13. Qualitative behaviour of liquid crystal samples as a function of temperature with different director orientation in the ordered state. The vertical black line represents a nematic-isotropic transition temperature.

which makes the distinction between region I and III hard or impossible [27]. Despite those complications, there is a reasonable agreement on the mechanisms governing the material behaviour in each regime.

2.4.1 Region I

The low shear rate region I was understood the latest and stimulated the most academic discussion [27]. The currently accepted explanation for shear-thinning stems from rheo-optical measurement, wherein the system is seen to be an assembly of jammed domains (fig. 2.15 I), each with a different orientation [77]. The structured morphology results in high viscosity understood as the yield stress. As the shearing progresses, liquid crystal domains align

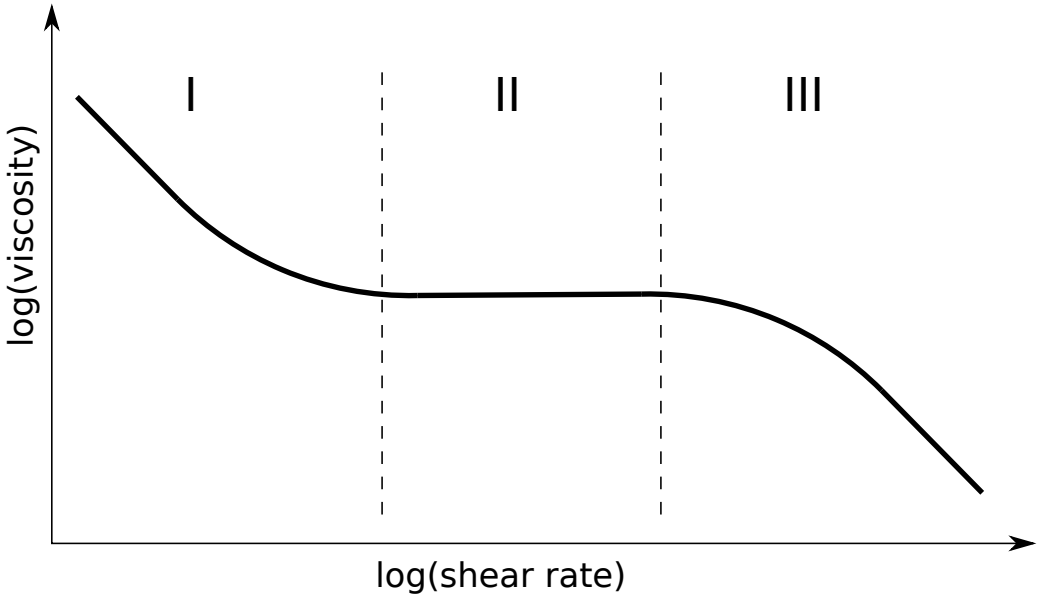

Figure 2.14. Three-region viscosity curve proposed by Onogi [76].

with the flow, and the viscosity decreases [76, 78]. Other mechanisms explaining the shear thinning in region I have been suggested: 1) flow induced phase transition (however this is more likely to be significant at higher shear rates) [27]; 2) mechanical stress arising from the homeotropic boundary condition resisting the director deformation [79] (this only accounts for a small fraction of the yield stress measured in experiments).

The rheology in the region I is strongly affected by mechanical, chemical or thermal histories; for example, the poly-domain network can be partially destroyed by shearing, so the effect of the previous deformation must be considered as it affects the current viscosity [80]. Similarly, the defect structure melts upon heating (thermotropic phase transition), reducing or eliminating the yield stress and changing the flow behaviour to a constant viscosity region II [81].

2.4.2 Region II

Region II is well understood and describes the behaviour of both isotropic and anisotropic liquid crystals. The structure is not as jammed as in region I (fig. 2.15 II), however, elastic effects are strong enough to maintain a fixed director orientation. This results in a constant viscosity, which is strongly dependent on the molecular weight [82] and concentration. When a concentration is increased beyond the threshold value, a lyotropic phase transition occurs, decreasing viscosity by a factor of two compared to the isotropic state [83].

2.4.3 Region III

Region III is the simplest part of the flow curve to describe - the shear rate and stresses are large, so any poly-domains are destroyed (fig. 2.15); the director aligns in the flow direction resulting in a shear-thinning behaviour [78].

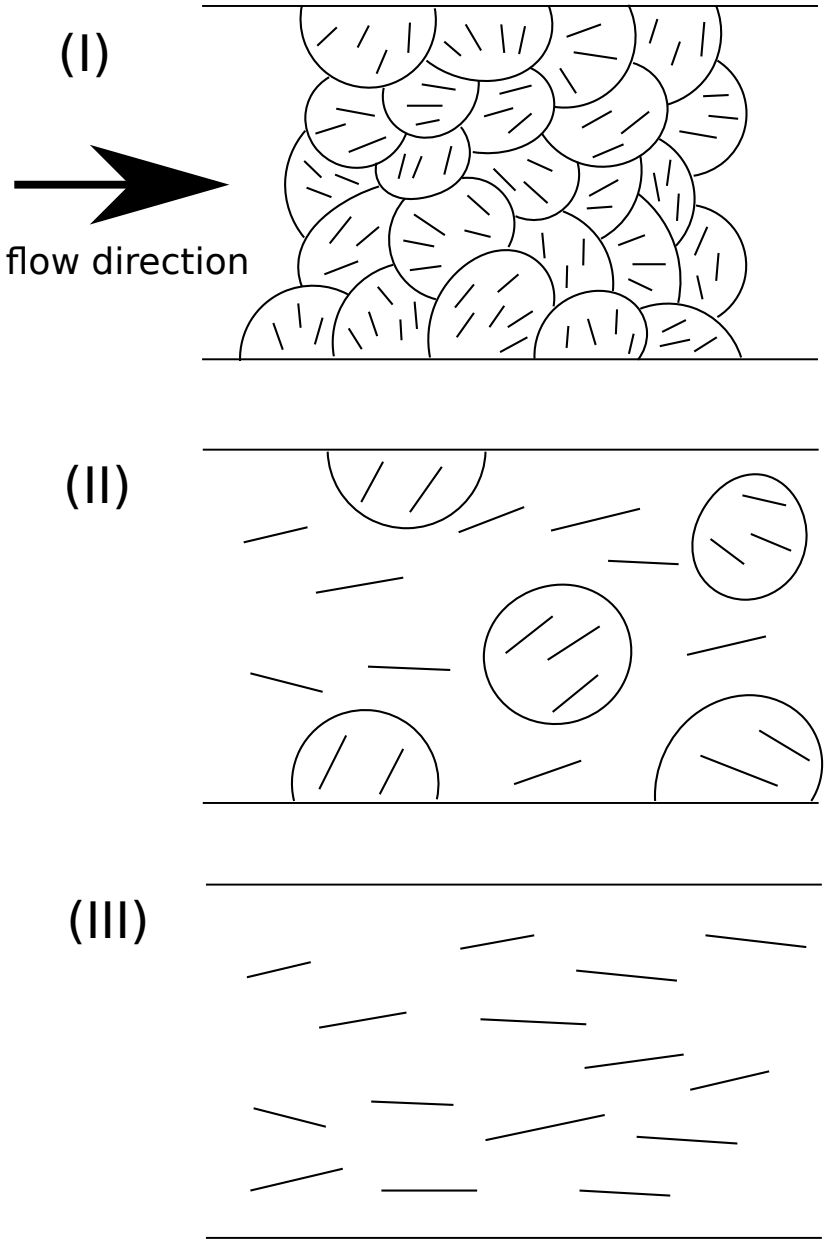

Figure 2.15. Schematic illustration of material microstructure in different shear regimes [76].

2.4.4 Normal stresses

The long-range orientational order has a significant effect on normal stresses, where the first normal stress difference $N_1 = \tau_{11} - \tau_{22}$ (numbers 1 and 2 denote the flow and flow gradient directions, respectively) in ordered systems can be an order of magnitude larger than in isotropic solutions with the same shear viscosity [73]. There is a significant disparity in the normal stress behaviour of many liquid crystals; some of them only exhibit positive N_1, similarly to entangled polymers [20], while in others, regions of positive and negative normal stresses exist. The range of shear rates with negative N_1 depends on polymer concentration and molecular weight [84]; however, it is most frequently encountered at the onset of region III [15]. Negative normal stresses were observed in nematic and cholesteric states, but not isotropic, suggesting that the phenomenon is related with long-range orientational effects [84]. The hypothesis is confirmed by the theoretical calculations, which show that $N_1 < 0$ occurs when the long axis of a liquid crystal is oriented at $45^o - 135^o$ to the flow direction

[85]. Transient normal stresses were observed even for a larger group of materials, but they are related with yield stress, and the flow reversal [81].

2.4.5 Scaling rules

Steady state viscosity

Liquid crystals also possess distinct scaling properties, which was demonstrated by Fishers and Fredrickson [86]. They pumped p-azoxyanisole (PAA) through a set of pipes of different sizes with homeotropic boundary conditions in the absence of external fields. It was observed that the material is shear thinning, as predicted in the three region curve. The decrease in viscosity is caused by the re-orientation of the director to a flow aligned state (fig. 2.16), resulting in less resistance to the motion of rod-like molecules. The data points, however, collapse onto a single curve when plotted against $\dot{\gamma}L^2$ (fig. 2.17), as opposed to polymeric melts whose viscosity scales with the shear rate $\dot{\gamma}$ [20, 87].

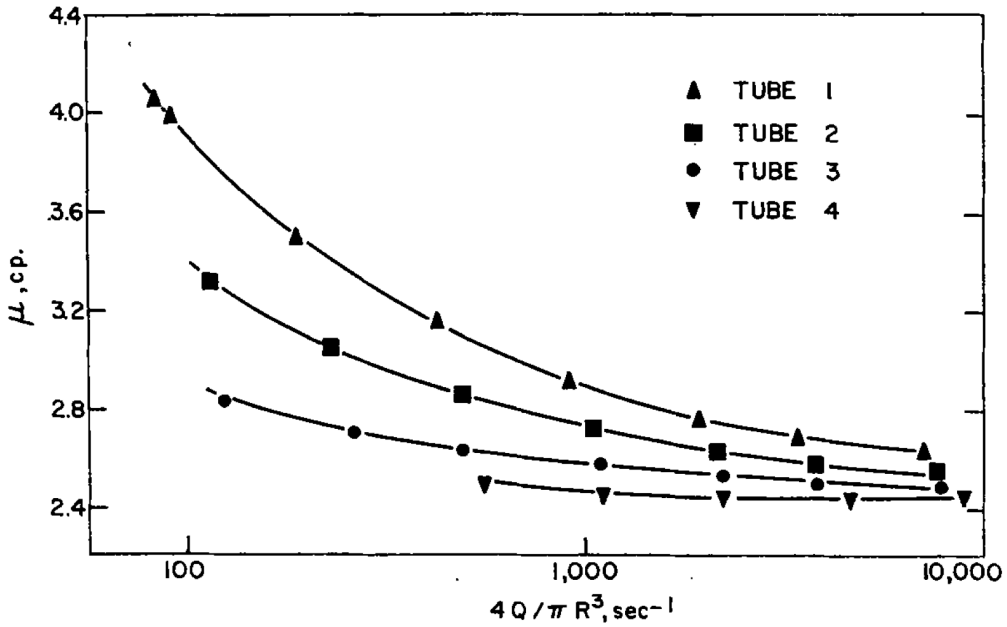

Figure 2.16. Viscosity as a function of shear rate ($\dot{\gamma} \propto \frac{4Q}{\pi R^3}$) for a set of pipes with different diameter [86]. Higher numbers indicate larger diameters. Reprinted with permission from [86]. Copyright 2022 Taylor & Francis Group.

Strain recovery

Larson and Mead [88] experimentally measured the strain relaxation upon the cessation of torque in a Couette flow (fig. 2.18). In their experiment, a constant torque T is applied on the inner cylinder and the fluid rotates until a steady state is reached. The torque is then removed and material recoils. For a Newtonian fluid the strain relaxes exponentially [88]

$$\gamma_{relaxed} = \dot{\gamma}_0 \exp(-t/t_I), \tag{2.4}$$

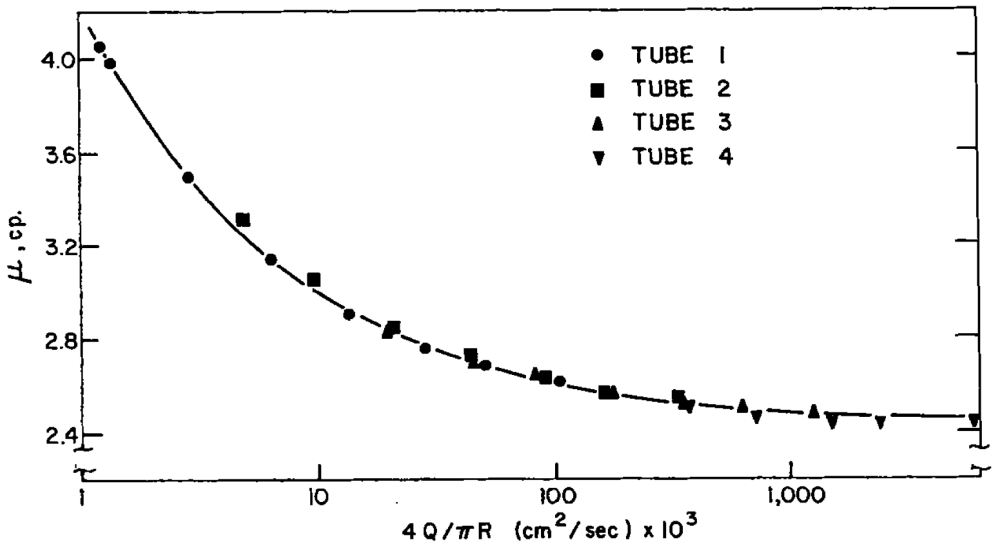

Figure 2.17. When the viscosity is plotted against $\dot{\gamma}L^2 \propto \frac{4Q}{\pi R}$ data points measured at different diameters collapse on the same curve [86]. Reprinted with permission from [86]. Copyright 2022 Taylor & Francis Group.

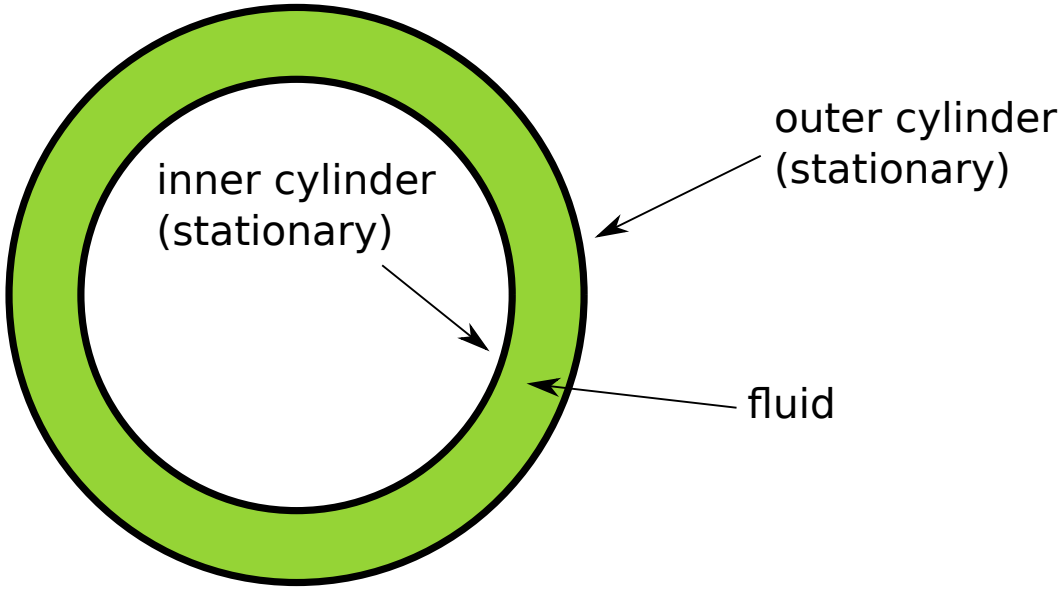

Figure 2.18. Schematic depiction of the setup used in the experiment.

where $\dot{\gamma}_0$ is the steady state shear rate and $t_I = \frac{T}{J\delta}$ is the relaxation time, J is the moment of inertia of the inner cylinder and δ is the gap size. Thus the total strain is given by

$$\Delta\gamma = \int_0^\infty \dot{\gamma}_0 \exp(-t/t_I)dt = \dot{\gamma}_0 t_I, \tag{2.5}$$

so upon the cessation of torque the strain scales linearly with the shear rate $\dot{\gamma}_0$. That is not the case for liquid crystals, where the recovered strain is not a function of the $\dot{\gamma}_0$ (fig. 2.19a), even in the low shear rate, constant viscosity region [88]. The strain relaxation history nearly collapses when plotted as a function of $\dot{\gamma}_0 t$ (fig. 2.19b), suggesting that the deformation rate imposes a characteristic time-scale of the process.

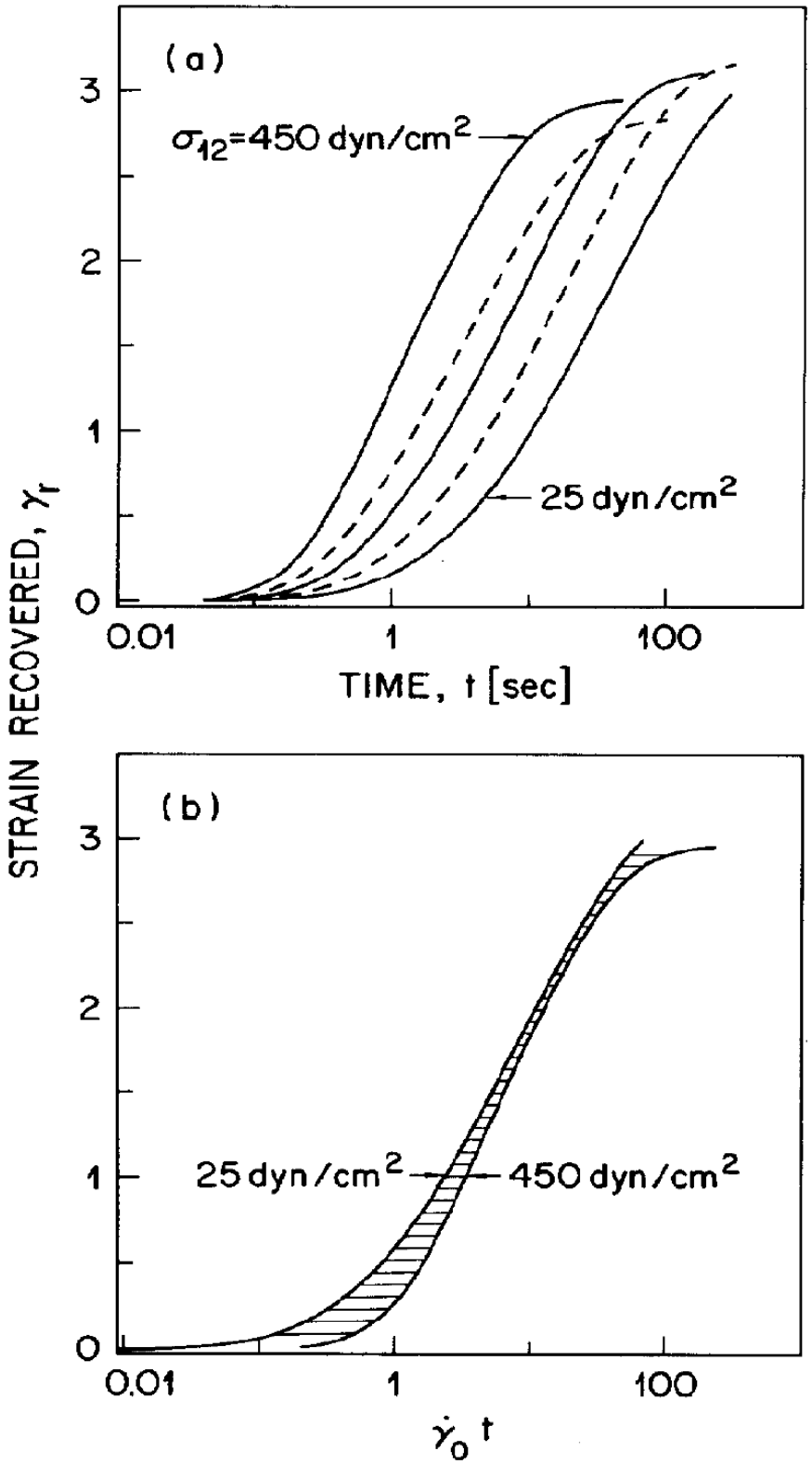

Figure 2.19. a) Variation of recovered strain with time for a PBLG solution with 30% liquid crystal content. The imposed stresses (from left to right were) 25, 50, 100, 200 and 450 $^{dyn}/_{cm^2}$; b) the same variation plotted as a function of dimensionless time $\dot{\gamma}_0 t$. Reprinted with permission from [88]. Copyright 2022, The Society of Rheology.

Small amplitude oscillatory shear

The transient response of a complex fluid can be investigated in the small amplitude oscillatory shear (SAOS) test, which indicates the relative importance of liquid- and solid-like stresses [18]. Applying a small, periodic deformation $\gamma(t) = \gamma_0 \sin(\omega t)$, the fluid responds with stress that can be decomposed into components proportional to the strain (viscous) and the strain rate (elastic):

$$\tau_{12} = G' \sin(\omega t) + G'' \cos(\omega t), \tag{2.6}$$

where G' and G'' are called storage and loss moduli. A Newtonian fluid can respond with a shear stress only, so $G' = 0$, while an elastic solid behaves like a spring and $G'' = 0$.

Moldenaers and Mewis [89] experimentally measured the response of liquid crystals to a periodic deformation. Their results show that the reaction strongly depends on the shear rate; the microstructure is hardly distorted at low frequencies, so $G'' >> G'$, indicating a Newtonian behaviour. As the deformation rate increases, the loss and storage moduli tend to the same value (fig. 2.20), so viscous and elastic components are equally important. As shown by Fishers and Fredrickson, the geometry size also affects the fluid rheology. For that reason, Moldenaers and Mewis used a domain with a gap large enough to erase any wall induced effect. Their insight provides important information on the scaling properties; industrial geometries need not be large enough, and wall anchoring may play a role.

It would be valuable to measure the storage and loss moduli in situations where the effect of boundary conditions is significant. The loss modulus is expected to be larger in the flow with homeotropic anchoring due to the higher viscosity, but the behaviour of the storage modulus is unknown. Homeotropic anchoring typically results in higher elastic stresses [15, 43], so G', would presumably increase, but in order to assess the effect of wall anchoring better, more experiments must be undertaken.

2.5 Equations of motion

The motion of a fluid is governed by a set of partial differential equations describing the conservation of mass and momentum. Fluids considered in this thesis are isothermal and incompressible ($\frac{\partial \rho}{\partial t} = 0$) and the mass balance equation becomes a velocity constraint

$$\boldsymbol{\nabla} \cdot \boldsymbol{v} = 0, \tag{2.7}$$

where $\boldsymbol{v}$ is the velocity vector. Additionally, the linear momentum balance provides the velocity evolution equation, which in the most general form is given by

$$\rho \frac{D\boldsymbol{v}}{Dt} = -\boldsymbol{\nabla} p + \boldsymbol{\nabla} \cdot \boldsymbol{\tau}, \tag{2.8}$$

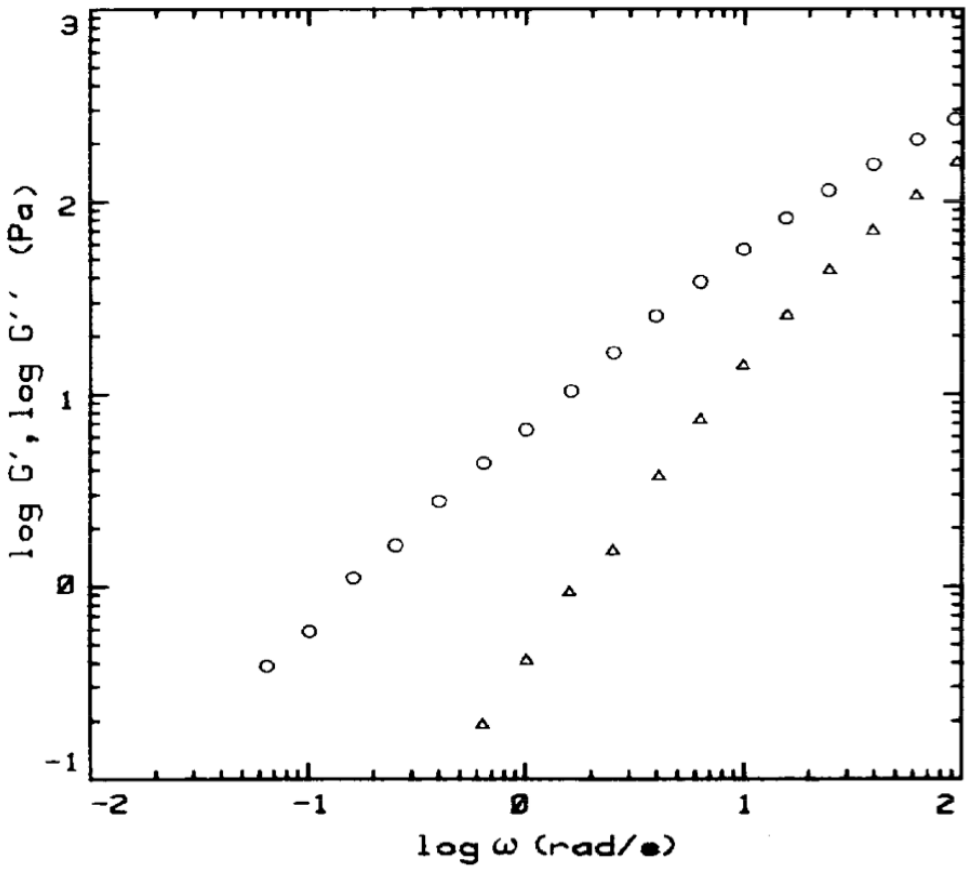

Figure 2.20. Equilibrium values of G' and G'' as a function of shear rate. Reprinted with permission from [89]. Copyright 2022, The Society of Rheology.

where $\frac{D}{Dt} = \frac{\partial}{\partial t} + \boldsymbol{v} \cdot \boldsymbol{\nabla}$ is the material derivative, p is pressure and $\boldsymbol{\tau}$ is the stress tensor, which includes viscous and elastic components. The stress may depend on the state of microstructure; therefore, it is often necessary to provide an additional equation of the form

$$\frac{D\boldsymbol{c}}{Dt} = f(...), \tag{2.9}$$

where $\boldsymbol{c}$ denotes the microstructure-related variable and $f(...)$ is a material-dependent function.

2.6 Newtonian model

The Newtonian approximation is the simplest approach to model the stress tensor. The building blocks of a fluid (atoms/molecules) are assumed to be infinitely small compared with the characteristic size of the flow, so the pressure and density change continuously on the macroscopic scale [17]. Upon deformation, the system returns to the equilibrium state within $O(10^{-12})$ s [90]. This is negligibly small compared to industrial time-scales, typically in the range $O(10^{-3}) - O(10^{3})$ s [17]. Therefore, as far as the industrial flow times scales are concerned, the microstructure of a Newtonian flow responds instantaneously to imposed deformation (fig. 2.21); equilibrium of the microstructure is thus always maintained, and the

stress tensor is linearly proportional to the strain rate

$$\boldsymbol{\tau} = \eta\dot{\boldsymbol{\gamma}} = 2\eta\boldsymbol{D}, \tag{2.10}$$

where

$$\dot{\boldsymbol{\gamma}} = \boldsymbol{\nabla v} + \boldsymbol{\nabla v}^T = 2\boldsymbol{D}. \tag{2.11}$$

The assumption of constant viscosity η works well for commonly encountered Newtonian fluids such as water, oil and air (at low speeds) [45, 91, 92]. Their relaxation time is very small, so an enormous deformation rate (either impossible or impractical to achieve) is needed to alter the fluid microstructure. That is not the case for complex fluids (emulsions, polymers or liquid crystals), whose relaxation and deformation time-scales are much closer and often of a similar order of magnitude [17]. The microstructure of a non-Newtonian fluid at low shear rates remains unaltered (similarly to a Newtonian fluid), but as the deformation rate increases, the structure cannot fully relax, which results in a complex stress-strain response with variable viscosity or history effects [18, 93–95]. None of these characteristics can be represented by the Newtonian approximation, so another approach is needed to model the behaviour of complex fluids [17, 18].

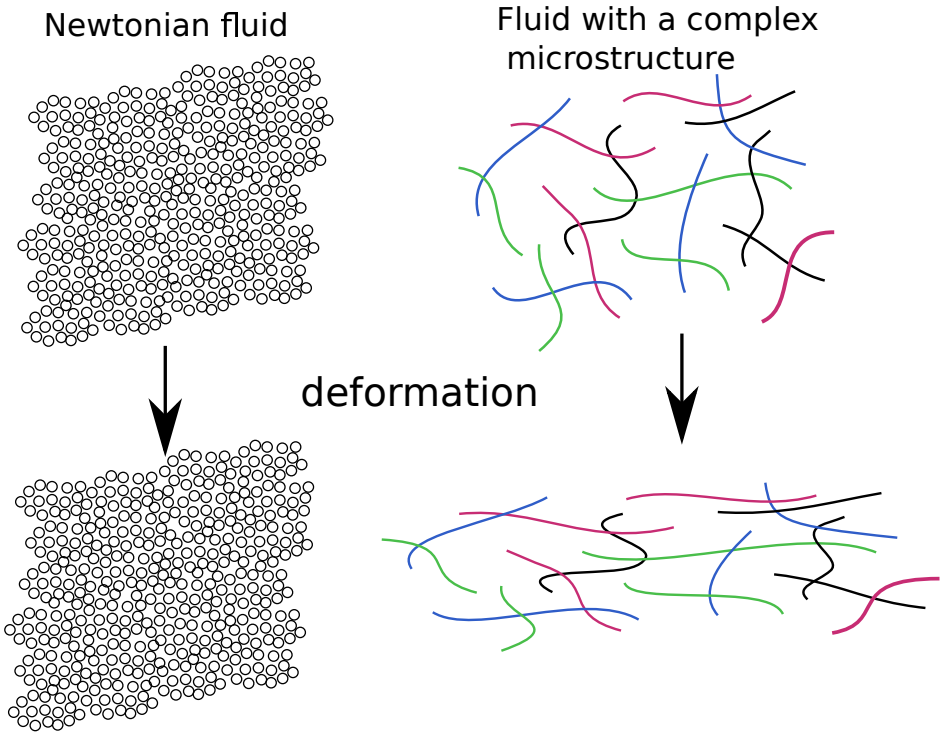

Figure 2.21. Schematic representation of the effect of deformation on the microstructure. The structure of a Newtonian fluid remains unaltered (for industrially-relevant timescales), while the internal structure of fluids with a complex microstructure is deformed, affecting material properties.

2.7 Generalised Newtonian Fluid models

The drawback of the constant-viscosity Newtonian approach is addressed by the Generalised Newtonian Fluid (GNF) models, which are derived based on the observation that

the viscosity changes with the shear rate. They represent only a phenomenological behaviour without providing any insight into the physics of material deformation. The stress in the GNF relations maintains the same structure as in the Newtonian fluid (eq. 2.10), but the viscosity becomes a shear rate-dependent variable [17]

$$\eta = \eta(\dot{\boldsymbol{\gamma}}). \tag{2.12}$$

GNF models are versatile - the viscosity definition (2.12) can represent many non-Newtonian characteristics such as shear thinning (viscosity decreases as the shear rate increases), shear thickening (viscosity increases as the shear rate increases), or a yield stress [17].

Viscosity is a scalar quantity, and thus, its value should be independent of the reference frame. Assuming that the effective viscosity depends on the rate of strain tensor, η must be a function of the invariants of $\dot{\boldsymbol{\gamma}}$ to remain frame indifferent [18]. The first invariant is [17]:

$$I_{\dot{\gamma}} = \sum_{i=1}^{3} \dot{\gamma}_{ii} = \boldsymbol{\nabla} \cdot \boldsymbol{v}. \tag{2.13}$$

$I_{\dot{\gamma}}$ equals zero for an incompressible fluid and therefore is not suitable to model η. The second invariant of $\dot{\boldsymbol{\gamma}}$ is

$$II_{\dot{\gamma}} = \dot{\boldsymbol{\gamma}} : \dot{\boldsymbol{\gamma}} = \sum_{i=1}^{3} \sum_{j=1}^{3} \dot{\gamma}_{ij} \dot{\gamma}_{ji}, \tag{2.14}$$

and the third invariant is

$$III_{\dot{\gamma}} = \text{tr}(\dot{\boldsymbol{\gamma}} \cdot \dot{\boldsymbol{\gamma}} \cdot \dot{\boldsymbol{\gamma}}) = \sum_{i=1}^{3} \sum_{j=1}^{3} \sum_{k=1}^{3} \dot{\gamma}_{ij} \dot{\gamma}_{jk} \dot{\gamma}_{ki}. \tag{2.15}$$

For two-dimensional flows, one of the components of eq. (2.15) is always zero. Thus, $III_{\dot{\gamma}}$ cannot be used in the viscosity function. The only non-zero invariant is then $II_{\dot{\gamma}}$ [18] whose magnitude:

$$|\dot{\gamma}| = \sqrt{\frac{II_{\dot{\gamma}}}{2}}, \tag{2.16}$$

is used as a basis to calculate the shear-dependent viscosity.

2.7.1 Power-law model

The power-law model is the simplest of the GNF models, where η is a power function of the shear rate [18]

$$\eta(\dot{\boldsymbol{\gamma}}) = m|\dot{\gamma}|^{n-1}, \tag{2.17}$$

where m is the consistency index (it can be understood as the viscosity at $\dot{\gamma} = 1\ \mathrm{s}^{-1}$ [18]) and n determines the type of non-Newtonian behaviour (fig. 2.22):

- $n = 1$ produces a constant viscosity $\eta = m$.
- $n < 1$ describes the shear thinning behaviour.
- $n > 1$ describes the shear thickening behaviour.

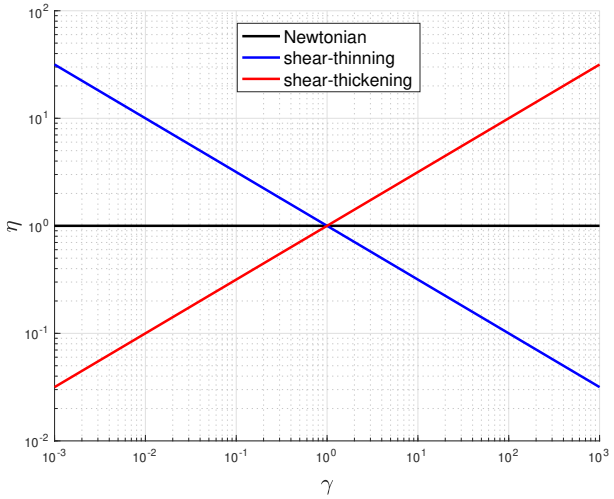

Figure 2.22. Viscosity variation predicted by the power-law model.

The power-law model predicts that in a shear-thinning fluid, the viscosity becomes infinite at low shear rates and tends to zero for large $\dot{\gamma}$ [18, 96, 97]. This feature is unphysical and computationally expensive - higher viscosity enforces smaller time steps, thus increasing the simulation time [37]. Experiments show that in those limiting scenarios, the viscosity plateaus [17] (fig. 2.23), which is not accounted for in the power-law model; thus, its applicability is limited to flows where $\dot{\gamma}$ falls in the variable viscosity regime (between γ_1 and γ_2 in fig. 2.23).

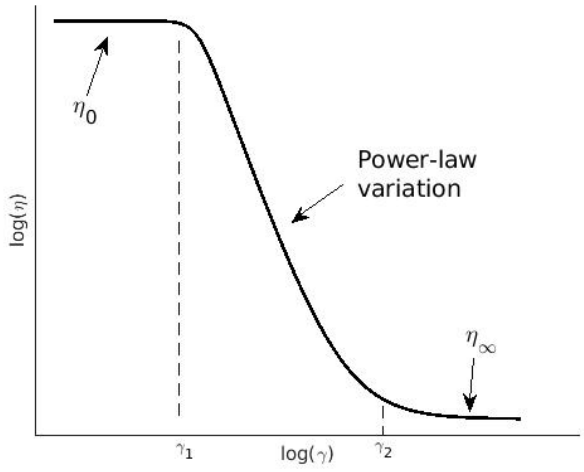

Figure 2.23. Typical viscosity variation of a shear-thinning fluid. The viscosity changes between $\dot{\gamma}_1$ and $\dot{\gamma}_2$ and remains constant outside this region.

2.7.2 Carreau-Yasuda (CY) model

The problem of unbounded viscosity is eliminated in the Carreau - Yasuda model which expresses the effective viscosity as [17]:

$$\eta(\dot{\gamma}) = \eta_\infty + (\eta_0 - \eta_\infty)[1 + |\dot{\gamma}\lambda|^a]^{\frac{n-1}{a}}, \tag{2.18}$$

η_0 and η_∞ are zero and infinite shear limits, $n < 1$ and $a > 0$ control the viscosity variation in the shear-thinning/shear-thickening region. λ does not have a physical meaning, but since it has units of time, it can be understood as the fluid relaxation time-scale and thus $\lambda\dot{\gamma}$ describes the ratio of fluid relaxation to flow time-scales. For $\lambda\dot{\gamma} << 1$, the fluid relaxes more quickly than the strain rate perturbation; the second term in eq. (2.18) approaches $\eta_0 - \eta_\infty$, and the viscosity reaches the low strain rate plateau η_0. As $\lambda\dot{\gamma} \to O(1)$ and larger, the strain rate deforms the flow faster than it can relax; the stress increases, and this is manifested by the power-law dependence in the square bracket, which initially causes the viscosity to decrease (for a shear-thinning fluid), before reaching the high strain rate plateau. For fluids with a large difference between limiting viscosities $\eta_0 >> \eta_\infty$, the Carreau-Yasuda model at large strain rates $\lambda\dot{\gamma} >> 1$ simplifies to [17]

$$\eta(\dot{\gamma}) = \eta_0|\dot{\gamma}\lambda|^{n-1}, \tag{2.19}$$

which is the power-law behaviour.

The shear curve of the CY model (fig. 2.23) displays a similarity to many non-Newtonian fluids. For that reason, the relation has been successfully applied to model non-Newtonian flows in shear dominated geometries such as arteries [98–100] and microchannels [101–103].

2.7.3 Bingham model

There is a special class of materials that are solid-like at low shear rates and liquid-like at higher shear rates, for example toothpaste, mayonnaise and drilling muds [104]. The first model to capture this behaviour of fluids was suggested by Bingham [105], who proposed modelling the viscosity according to

$$\eta = \begin{cases} \infty, & |\dot{\gamma}| \leq \dot{\gamma}_0. \\ \eta_0 + \tau_0|\dot{\gamma}|^{-1}, & |\dot{\gamma}| > \dot{\gamma}_0. \end{cases} \tag{2.20}$$

$\dot{\gamma}$ and $\dot{\gamma}_0$ denote the applied shear rate and the critical shear rate above which the material yields, respectively. The Bingham model is suitable for viscoplastic [106] fluids, where the yield stress has an effect on the flow. In the limit of high shear rate, the Bingham model predicts a constant Newtonian viscosity, which need not be the case for complex fluids such as gels and soaps [40, 41].

2.7.4 Herschel-Bulkley model

A correction to the Bingham model, allowing shear thinning/thickening behviour at high shear rates is provided by the Herschel-Bulkley model, where the effective viscosity is given by [30]

$$\eta = \begin{cases} \infty, & |\dot{\gamma}| \leq \dot{\gamma}_0. \\ \eta_0 |\dot{\gamma}|^{n-1} + \tau_0 \dot{\gamma}^{-1}, & |\dot{\gamma}| > \dot{\gamma}_0. \end{cases} \tag{2.21}$$

n is a material parameter that controls the viscosity variation in the shear thinning region. In a pipe flow, the HB equation predicts the existence of a plug flow near the axis (the size of which depends on the magnitude of the yield stress τ_0 (fig. 2.24)) and for that reason the model is used to analyse the flow of soap [5].

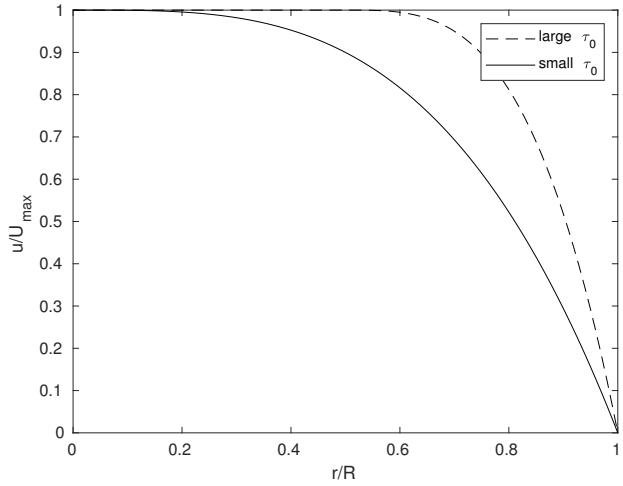

Figure 2.24. Increasing the yield stress τ_0 increases the width of the plug region.

2.7.5 Summary of the GNF models

Because of the similarity to the Newtonian model, GNF relations are simple to use or implement in numerical solvers [107]. They have been successful in predicting the pressure drop of polymeric flows [108] in shear dominated geometries. On the other hand, there are some drawbacks of the GNF models that limit their reliability:

- Experimental measurements of complex fluids (such as polymeric melts or liquid crystals) indicate non-zero normal stress differences in simple shear flows [15, 18, 27]. Normal stresses are a manifestation of elasticity of the internal microstructure; they cannot be captured by GNF relations, which have Newtonian characteristics, and therefore fail to account for stresses unrelated with the mode of deformation (e.g. shearing produces only shear stresses, extension results only in normal stresses). The incorrect prediction of normal stresses is not an issue in simple geometries, e.g. straight pipes, where the pressure drop comes from shearing only [18]. However, as the geometry complexity increases (which is typical in FMCG processing), the improper technique of modelling

normal stresses is detrimental, particularly with flows where the extensional component is significant, e.g. the screw extruder.

- The viscosity of complex fluids depends on the deformation history [27]; in the case of liquid crystals, the previous shearing can destroy some of the existing defects, hence reducing the viscosity. On the other hand, GNF fluids model the viscosity as a function of the instantaneous deformation rate, so incorporating history effects is impossible.
- As discussed in section 2.4, the effective viscosity of liquid crystals depends on the orientation of the director. Particles aligned in the direction of the velocity gradient result in a higher viscosity compared to the flow aligned state [109]. The presence of walls can control the director/velocity alignment. Therefore, since GNF models assume that the deformation rate is the only variable that can affect the viscosity, they cannot replicate the effect of wall anchoring.

2.8 Nematodynamics

Generalised Newtonian Fluid models address some drawbacks of the Newtonian approximation; however, they fail to account for the anisotropic properties of liquid crystals, which is the motivation to introduce nematodynamic equations. The theories covered in this section treat the nematic fluid as an assembly of rod-like particles, and the state of the system is governed by the interaction of anisotropic particles with the flow (fig. 2.25). In addition to continuity and linear momentum equations, the system is described by the angular momentum balance governing the director orientation.

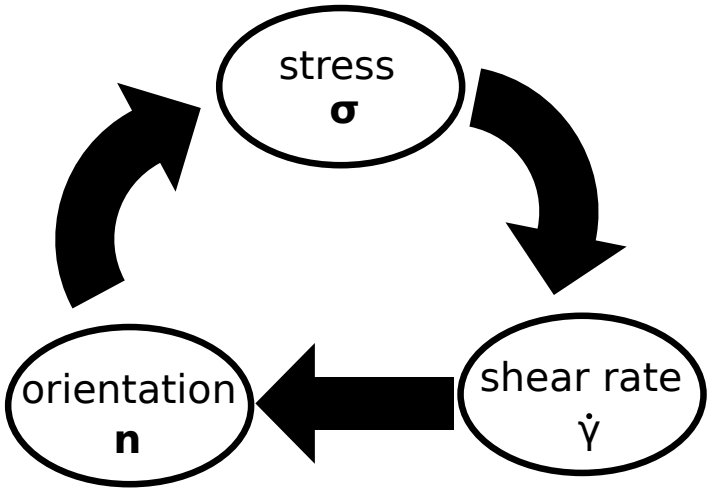

Figure 2.25. Coupling between stress, flow and the director orientation.

2.8.1 Transversely isotropic fluid (TIF) model

The first constitutive equation devoted to liquid crystals was introduced by Ericksen [110], who considered an assembly of ellipsoidal particles with preferred orientation described by the director $\boldsymbol{n}$. Ericksen assumed that the stress has only a viscous component, which depends

on the interaction between flow and microstructure

$$\boldsymbol{\tau} = \boldsymbol{\tau}(\boldsymbol{n}, \boldsymbol{D}). \tag{2.22}$$

Additionally, in the absence of elasticity, Ericksen proposed that the director orientation evolves according to

$$\boldsymbol{N} = \dot{\boldsymbol{n}} - \boldsymbol{n} \cdot \boldsymbol{\omega} = \boldsymbol{g}(\boldsymbol{n}, \boldsymbol{D}), \tag{2.23}$$

where the superscripted dot denotes the material derivative and $\boldsymbol{g}$ is an unknown function describing effect of material deformation on director evolution. $\boldsymbol{D} = \frac{1}{2}(\boldsymbol{\nabla v} + (\boldsymbol{\nabla v})^T)$ and $\boldsymbol{\omega} = \frac{1}{2}(\boldsymbol{\nabla v} - (\boldsymbol{\nabla v})^T)$ are symmetric and anti-symmetric components of the velocity gradient. Hence, the corotational time derivative of the director $\boldsymbol{N}$ measures the relative rotation of $\boldsymbol{n}$ with respect to the surrounding fluid. The evolution equations are formulated in terms $\boldsymbol{N}$ and $\boldsymbol{D}$ instead of $\dot{\boldsymbol{n}}$ and $\boldsymbol{\nabla v}$ to ensure frame indifference [111]. Ericksen then made the following assumptions about the stress and director fields [110]

- $\boldsymbol{n}$ and$-\boldsymbol{n}$ represent the same orientation, so $\boldsymbol{\tau}(\boldsymbol{n}, \boldsymbol{D}) = \boldsymbol{\tau}(-\boldsymbol{n}, \boldsymbol{D})$.
- $\boldsymbol{\tau}$ and $\boldsymbol{g}$ depend linearly on the strain rate tensor $\boldsymbol{D}$.
- The director remains a unit vector $|\boldsymbol{n}|^2 = 1$, so $\frac{\partial(|\boldsymbol{n}|^2)}{\partial t} = 2\boldsymbol{n} \cdot \dot{\boldsymbol{n}} = 0$.
- The stress tensor is symmetric.

Therefore, the most general forms of $\boldsymbol{\tau}$ and $\boldsymbol{g}$ satisfying the above requirements are given by [110]

$$\boldsymbol{\tau} = \boldsymbol{A}^0 + \boldsymbol{A}^1 \cdot \boldsymbol{D} + \boldsymbol{D} \cdot \boldsymbol{A}^1, \tag{2.24}$$

$$\boldsymbol{g} = \boldsymbol{B}^1 \cdot \boldsymbol{D} + \boldsymbol{D} \cdot \boldsymbol{B}^1, \tag{2.25}$$

where $\boldsymbol{A}^i$ and $\boldsymbol{B}^i$ are constant matrices. In order to ensure frame invariance, each matrix must be a linear combination of $\boldsymbol{nn}$ and the identity tensor $\boldsymbol{\delta}$ [110], which in index notation can be written as

$$A^0_{ij} = \beta_1 \delta_{ij} + \beta_2 n_i n_j, \tag{2.26a}$$

$$\begin{aligned} A^1_{ijkp} = \beta_3 \delta_{ij}\delta_{kp} + \beta_4 \delta_{ij}\delta_{jp} + \beta_5 \delta_{ip}\delta_{jk} + \beta_6 \delta_{ij} n_k n_p + \beta_7 \delta_{jk} n_i n_p + \beta_8 \delta_{ik} n_j n_p \\ + \beta_9 \delta_{ip} n_j n_k + \beta_{10} \delta_{jp} n_i n_k + \beta_{11} \delta_{kp} n_i n_j + \beta_{12} n_i n_j n_k n_p, \end{aligned} \tag{2.26b}$$

$$B^1_{ijk} = \beta_{13} n_i \delta_{jk} + \beta_{14} n_j \delta_{ik} + \beta_{15} n_k \delta_{ij} + \beta_{16} n_i n_j n_k, \tag{2.26c}$$

Combining eq. (2.24) with (2.26) gives the most general form of the stress tensor

$$\boldsymbol{\tau} = 2\mu \boldsymbol{D} + \mu_y \boldsymbol{nn} + 2\mu_1 \boldsymbol{D} : \boldsymbol{nnnn} + \mu_2 (\boldsymbol{nn} \cdot \boldsymbol{D} + \boldsymbol{D} \cdot \boldsymbol{nn}), \tag{2.27}$$

where $2\mu \boldsymbol{D}$ is a Newtonian contribution, while $2\mu_1 \boldsymbol{D} : \boldsymbol{nnnn}$ and $\mu_2(\boldsymbol{nn} \cdot \boldsymbol{D} + \boldsymbol{nn} \cdot \boldsymbol{D})$

can be understood as stresses oriented along the director and straining axis [112], respectively. The second term in eq. (2.27), $\mu_y \boldsymbol{nn}$, represents an orientation-dependent yield stress, which is often omitted [15]. Since the stress (2.27) was derived from purely formal arguments [110], the last two terms are not easy to interpret physically.

The derivation of the angular momentum equation follows the same procedure as for the stress tensor, and the angular momentum balance reads

$$\dot{\boldsymbol{n}} - \boldsymbol{n} \cdot \boldsymbol{\omega} + \lambda \boldsymbol{n} \cdot \boldsymbol{D} = \kappa \boldsymbol{n}, \tag{2.28}$$

where $\boldsymbol{\omega}$ is the vorticity tensor and λ is the tumbling parameter, which quantifies the relative importance of extensional and rotational effects acting on the director. κ is a Lagrange multiplier that enforces a constant director magnitude; κ can be calculated by taking the scalar product of eq. (2.28) with $\boldsymbol{n}$, and the angular momentum balance can be re-written as

$$\dot{\boldsymbol{n}} - \boldsymbol{n} \cdot \boldsymbol{\omega} + \lambda(\boldsymbol{n} \cdot \boldsymbol{D} - \boldsymbol{nnn} : \boldsymbol{D}) = 0. \tag{2.29}$$

Equations (2.27) and (2.29) combined with the momentum and continuity equations constitute the transversely isotropic fluid model.

Interpretation of the angular momentum equation

The angular momentum equation indicates that the director orientation is governed by the competition of rotational and extensional flows. In the limit of $\lambda \to 0$, the director only feels the action of rotational flow; therefore $\boldsymbol{n}$ spins as long as $\boldsymbol{\omega} \neq 0$. On the other hand, when $\lambda \to \infty$, the contribution of vorticity is negligible and a steady-state director orientation is given by the solution of

$$\boldsymbol{n} \cdot \boldsymbol{D} - \boldsymbol{nnn} : \boldsymbol{D} = 0. \tag{2.30}$$

In a two-dimensional flow, the director can be represented in terms of the polar angle θ (fig. 2.26)

$$\boldsymbol{n} = \begin{bmatrix} n_x & n_y \end{bmatrix} = \begin{bmatrix} \cos\theta & \sin\theta \end{bmatrix}, \tag{2.31}$$

and the symmetric strain rate tensor in the most general form is given by

$$\boldsymbol{D} = \begin{bmatrix} A & \frac{1}{2} \\ \frac{1}{2} & -A \end{bmatrix} \dot{\gamma}, \tag{2.32}$$

where A quantifies the ratio of extensional to shear flows. For $|A| >> 1$ the flow is dominated by the extensional component, while $A \to 0$ corresponds to shear flow. Substituting the simplified definitions of $\boldsymbol{n}$ (2.31) and $\boldsymbol{D}$ (2.32) into eq. (2.30) and solving for the steady state

angle gives

$$\tan(2\theta) = \frac{1}{2A}. \tag{2.33}$$

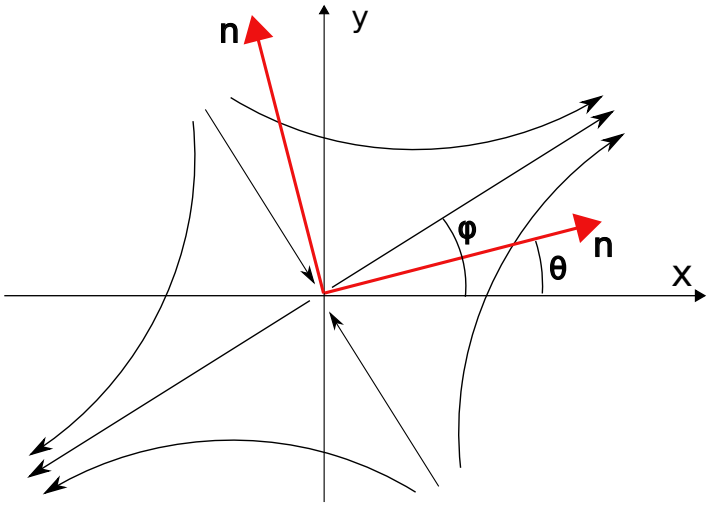

Figure 2.26. Schematic visualisation of angles θ and ϕ.

By decomposing the strain rate tensor (2.32), the eigenvector corresponding to the positive eigenvalue lies along the direction prescribed by the vector

$$\begin{bmatrix}\cos\phi & \sin\phi\end{bmatrix} = \left[-\frac{1}{(\sqrt{4A^2+1}+2A)\sqrt{(\sqrt{4A^2+1}+2A)^2+1}} \quad \frac{1}{\sqrt{(\sqrt{4A^2+1}+2A)^2+1}}\right], \tag{2.34}$$

where ϕ is the angle between the eigenvector corresponding to the positive eigenvalue and the horizontal direction (fig. 2.26). Some algebraic manipulation reveals that ϕ satisfies

$$\tan(2\phi) = \frac{1}{2A} = \tan(2\theta). \tag{2.35}$$

Therefore, the term $\boldsymbol{n}\cdot\boldsymbol{D}-\boldsymbol{nnn}:\boldsymbol{D}$ acts to align the director along the extension direction. Thus, λ describes the relative importance of rotational effects (that continuously rotate the director) and extensional effects (acting to align the director along the extension direction). In a shear flow, for $0 < |\lambda| < 1$ the director rotates continuously with a period $P = \frac{2\pi}{\dot{\gamma}\sqrt{1-\lambda^2}}$ [113] (tumbling), while when $|\lambda| \geq 1$, $\boldsymbol{n}$ aligns at an angle θ_L to the flow direction:

$$\tan\theta_L = \pm\sqrt{\frac{\lambda-1}{\lambda+1}}. \tag{2.36}$$

For the liquid crystals considered in this thesis, the tumbling parameter $\lambda > 1$, characteristic for flow aligning materials [15].

Limitations of the TIF model

The TIF model performs well in strong flows where the director orientation is only affected by the flow. However, in the absence of flow, the angular momentum equation (2.29)

simplifies to

$$\frac{\partial \boldsymbol{n}}{\partial t} = 0, \tag{2.37}$$

which effectively allows for any director configuration. The TIF model fails to account for microstructure elasticity and therefore permits arbitrary long-range orientational distortions; two example configurations allowed by the TIF model are shown in fig. 2.27.

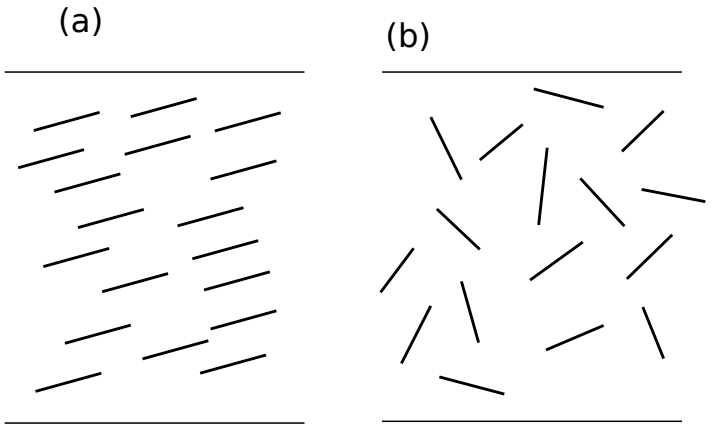

Figure 2.27. Possible static configurations (well ordered nematic (a) and isotropic (b) allowed by the TIF model in the absence of flow. In both cases the stress field is zero.

The drawbacks of the TIF model can be eliminated by introducing elastic effects, which act to minimise distortions of the director field.

2.8.2 Thermodynamic potential

When complex fluids are deformed, they respond with a viscoelastic stress [18]. The elastic contribution has entropic origins and represents the effects of reversible changes in the configuration of macromolecules. In the absence of external forces, the microstructure of a complex fluid evolves towards the equilibrium state, which maximises the entropy of the universe [114, 115]. Since the entropic effects are absent in the TIF model, the theory fails to account for non-zero elastic stresses that would otherwise drive the system towards the equilibrium state; this failure allows for arbitrary director distortions (fig. 2.27), which have no entropic consequences.

More generally, the thermodynamic state of the system can be considered as a potential (in an analogy with mechanical or electrostatic potentials), which reaches its minimum value in the stable equilibrium [115]. Depending on the nature of the process, different potential definitions can be provided, e.g. *Gibbs and Helmholtz free energies* [114]. For a system at constant volume and temperature, the maximisation of universe's entropy is equivalent to the minimum system's Helmholtz free energy, which is defined as [64, 116]

$$dF = dU - TdS = 0, \tag{2.38}$$

where U is the internal energy of the system, T is the temperature and S represents system's

entropy. The exact form of S and thus F is determined by the physics of the microstructure and modelling assumptions. This thesis focuses on liquid crystals, where the Helmholtz free energy density $f = f(\boldsymbol{n}, \nabla \boldsymbol{n})$ depends on the distortion of the director field [35]. The total energy of the system is thus given by

$$F(\boldsymbol{n}, \boldsymbol{\nabla n}) = \int_\Omega f(\boldsymbol{n}, \boldsymbol{\nabla n}) d\Omega, \tag{2.39}$$

where Ω is the control volume enclosing the liquid crystal and the director orientation is known on the boundary $\partial\Omega$. Introducing a variation $\delta\boldsymbol{n}$ to the director field in the bulk of the fluid, the corresponding variation of the total system's energy density is

$$\begin{aligned} \delta F &= \int_\Omega \left(\frac{\partial f}{\partial \boldsymbol{n}} \cdot \delta \boldsymbol{n} + \frac{\partial f}{\partial \boldsymbol{\nabla n}} \cdot \delta(\boldsymbol{\nabla n}) \right) d\Omega \\ &= \int_\Omega \left(\frac{\partial f}{\partial \boldsymbol{n}} - \boldsymbol{\nabla} \cdot \left(\frac{\partial f}{\partial \boldsymbol{\nabla n}} \right) \right) \cdot \delta \boldsymbol{n} \, d\Omega + \cancel{\int_\Omega \boldsymbol{\nabla} \cdot \left(\frac{\partial f}{\partial \boldsymbol{\nabla n}} \cdot \delta \boldsymbol{n} \right) d\Omega}, \end{aligned} \tag{2.40}$$

where the crossed-out term can be transformed into a surface integral and vanishes because $\delta\boldsymbol{n} = 0$ on the boundary. Hence, the *functional derivative* of F with respect to $\boldsymbol{n}$ can be defined as

$$\frac{\delta F}{\delta \boldsymbol{n}} \equiv \frac{\partial f}{\partial \boldsymbol{n}} - \boldsymbol{\nabla} \cdot \left(\frac{\partial f}{\partial \boldsymbol{\nabla n}} \right), \tag{2.41}$$

and measures the deviation of the system from the minimum energy state. The system is in equilibrium when $\frac{\delta F}{\delta \boldsymbol{n}} = 0$, which is known as the *Euler-Lagrange equation*.

Nematic energy (director)

Nematic liquid crystals act like elastic materials when their microstructure is distorted. Ideally, the director field is uniform throughout the whole domain, which corresponds to the state of no distortion. However, perfect alignment is not always possible, as the presence of walls may enforce spatial variation in the director field, producing a long-range orientational distortion. When the director orientation imposed by the walls varies across in the domain, liquid crystals have less freedom to rotate, which introduces a free energy density penalty predicted by the Frank-Oseen theory [35, 43, 117]

$$\begin{aligned} f_d = \underbrace{\frac{1}{2} K_1 (\boldsymbol{\nabla} \cdot \boldsymbol{n})^2}_{\text{splay}} + \underbrace{\frac{1}{2} K_2 (\boldsymbol{n} \cdot \boldsymbol{\nabla} \times \boldsymbol{n})^2}_{\text{twist}} + \underbrace{\frac{1}{2} K_3 (\boldsymbol{n} \times \boldsymbol{\nabla} \times \boldsymbol{n})^2}_{\text{bend}} \\ + \underbrace{\frac{1}{2} K_{24} \nabla \cdot [(\boldsymbol{n} \cdot \nabla)\boldsymbol{n} - (\nabla \cdot \boldsymbol{n})\boldsymbol{n}]}_{\text{saddle-splay}}, \end{aligned} \tag{2.42}$$

where K_i are Frank constants quantifying the strength of each effect (fig. 2.28) and the saddle-splay contribution can be neglected in confugurations with the strong anchoring boundary condition. Experimental measurements suggest that K_i are of the same order of magnitude

[118–120], so it is often assumed that

$$K_1 = K_2 = K_3 = K, \tag{2.43}$$

which simplifies eq. (2.42) to

$$f_d = \frac{1}{2} K (\boldsymbol{\nabla n}) : (\boldsymbol{\nabla n})^T, \tag{2.44}$$

(known as the one-constant approximation).

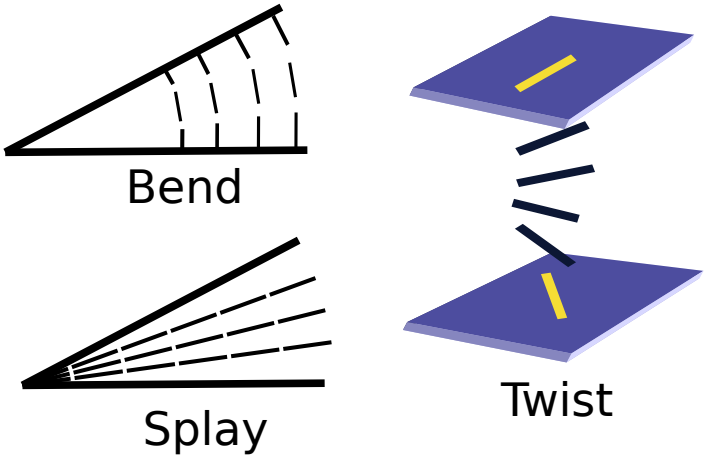

Figure 2.28. Possible modes of distortion for a liquid crystal [15].

2.8.3 Hamiltonian description of complex fluids

The content presented in the following sections gives the framework for deriving new constitutive equations, and shows how the nematodynamic theories can be unified by the Poisson bracket approach.

Lagrangian

The exact evolution of a single particle can be calculated from Hamilton's principle of least action, which states that the integral

$$I = \int_{t_1}^{t_2} L(\boldsymbol{q}, \dot{\boldsymbol{q}}) dt \tag{2.45}$$

is extremum [121]. t_1 and t_2 are the initial and final times at which the state of the system is known, $L = T - V$ is the *Lagrangian*, which measures the difference between kinetic ($T = \frac{1}{2} m \dot{\boldsymbol{q}}^2$) and potential ($V = V(\boldsymbol{q})$) energies, m is the particle mass, $\boldsymbol{q}$ and $\dot{\boldsymbol{q}}$ are position and velocity vectors, respectively. The minimisation of the Lagrangian over time and space requires a variational formulation, leading to the Euler-Lagrange equation:

$$\frac{\partial L}{\partial \boldsymbol{q}} - \frac{\mathrm{d}}{\mathrm{d}t}\left(\frac{\partial L}{\partial \dot{\boldsymbol{q}}}\right) = 0, \tag{2.46}$$

which enables to find the actual evolution of a point particle.

Hamiltonian

The motion of a particle can be alternatively described in terms of its position $\boldsymbol{q}$ and generalised momentum $\boldsymbol{p} = \frac{\partial L}{\partial \dot{\boldsymbol{q}}}$. Since the Lagrangian uses $\boldsymbol{q}$ and $\dot{\boldsymbol{q}}$ as the arguments, it is necessary to employ another function that describes the system in terms of position and momentum [121]. The *Hamiltonian* is obtained through the Legendre transform of the Lagrangian

$$H(\boldsymbol{q}, \boldsymbol{p}) = \boldsymbol{p} \cdot \dot{\boldsymbol{q}} - L(\boldsymbol{q}, \dot{\boldsymbol{q}}), \tag{2.47}$$

and measures the total energy of a particle $H = T + V$. In the Hamiltonian framework, the system's evolution is described by a pair of first order differential equations [122]

$$\frac{\mathrm{d}\boldsymbol{q}}{\mathrm{d}t} = \frac{\partial H}{\partial \boldsymbol{p}}, \qquad \frac{\mathrm{d}\boldsymbol{p}}{\mathrm{d}t} = -\frac{\partial H}{\partial \boldsymbol{q}}. \tag{2.48}$$

Hence, L and H provide different techniques for modelling the motion of solid bodies.

Properties of the Hamiltonian can be further exploited to describe the time evolution of functionals, whose value depends on the generalised position and momentum $F = F(\boldsymbol{q}, \boldsymbol{p})$. The time derivative of F is given by

$$\frac{\mathrm{d}}{\mathrm{d}t} F(\boldsymbol{q}, \boldsymbol{p}) = \frac{\partial F}{\partial \boldsymbol{q}} \frac{\mathrm{d}\boldsymbol{q}}{\mathrm{d}t} + \frac{\partial F}{\partial \boldsymbol{p}} \frac{\mathrm{d}\boldsymbol{p}}{\mathrm{d}t} = \frac{\partial F}{\partial \boldsymbol{q}} \frac{\partial H}{\partial \boldsymbol{p}} - \frac{\partial F}{\partial \boldsymbol{p}} \frac{\partial H}{\partial \boldsymbol{q}} = \{F, H\}, \tag{2.49}$$

where $\{F, H\}$ is the *Poisson bracket*. Hence, we can model the time evolution of any functional of $\boldsymbol{q}$ and $\boldsymbol{p}$, provided that the Hamiltonian is specified. In the special case when F represents the total energy of a particle, $F = H$, $\frac{\mathrm{d}H}{\mathrm{d}t} = \{H, H\} = 0$, indicating that the system's energy is conserved.

Lagrangian and Eulerian description of the flow

So far, the analyses were concerned with single-particle systems, whose evolution can be expressed through a Poisson bracket. The approach can be generalised to fluids by monitoring the evolution of position and velocity of each particle (fig. 2.29a). Particles are labelled with their coordinates at a reference time t_0, and as the flow progresses, the position $\boldsymbol{q}$ and velocity $\dot{\boldsymbol{q}}$ are specified as a function of the initial coordinate [122]. This approach to describing the fluid flow is called the Lagrangian description; it is rarely used in fluid mechanics since fluids consist of many particles, and tracking each element's evolution is impossible.

Alternatively, the fluid flow can be described by the Eulerian framework, where instead of following each particle, properties of the flow field (mass density, momentum density) are monitored in control volumes, whose position is fixed in time (fig. 2.29b). The transformation from Lagrangian to Eulerian reference frame is done by the mapping function $\boldsymbol{R}$, which

converts the particle label (position at a reference time t_0) into a position at an arbitrary time t' [123]. The Eulerian-Lagrangian transformation is performed analogously by using the inverse of the mapping function. The Poisson bracket for a fluid element enclosed in the control volume Ω is analogous to eq. (2.49) [64]

$$\{F, H\} = \int_\Omega \left[\frac{\delta F}{\delta \boldsymbol{q}} \frac{\delta H}{\delta \boldsymbol{p}} - \frac{\delta F}{\delta \boldsymbol{p}} \frac{\delta H}{\delta \boldsymbol{q}} \right] d\Omega. \tag{2.50}$$

The bracket formulation provides a systematic mathematical framework for introducing new phenomenon to the problem. Any physical quantity (for example, velocity or director field) can be included in the Poisson bracket by assuming that $F = F[\boldsymbol{v}(\boldsymbol{q}, \boldsymbol{p}), \boldsymbol{n}(\boldsymbol{q}, \boldsymbol{p})]$, which appropriately modifies the definition of functional derivatives

$$\frac{\delta F}{\delta \boldsymbol{q}} = \frac{\delta F}{\delta \boldsymbol{v}} \frac{\delta \boldsymbol{v}}{\delta \boldsymbol{q}} + \frac{\delta F}{\delta \boldsymbol{n}} \frac{\delta \boldsymbol{n}}{\delta \boldsymbol{q}}, \qquad \frac{\delta F}{\delta \boldsymbol{p}} = \frac{\delta F}{\delta \boldsymbol{v}} \frac{\delta \boldsymbol{v}}{\delta \boldsymbol{p}} + \frac{\delta F}{\delta \boldsymbol{n}} \frac{\delta \boldsymbol{n}}{\delta \boldsymbol{p}}. \tag{2.51}$$

Evolution equations are obtained by converting variables between Lagrangian and Eulerian frames and replacing the Hamiltonian with the Helmholtz free energy describing material deformation and kinetic energy. In the case of liquid crystals, whose microstructure is represented by the director field, the $\boldsymbol{n}$-dependent part of Hamiltonian represents the Frank-Oseen distortion energy density (2.42) described in the previous subsection.

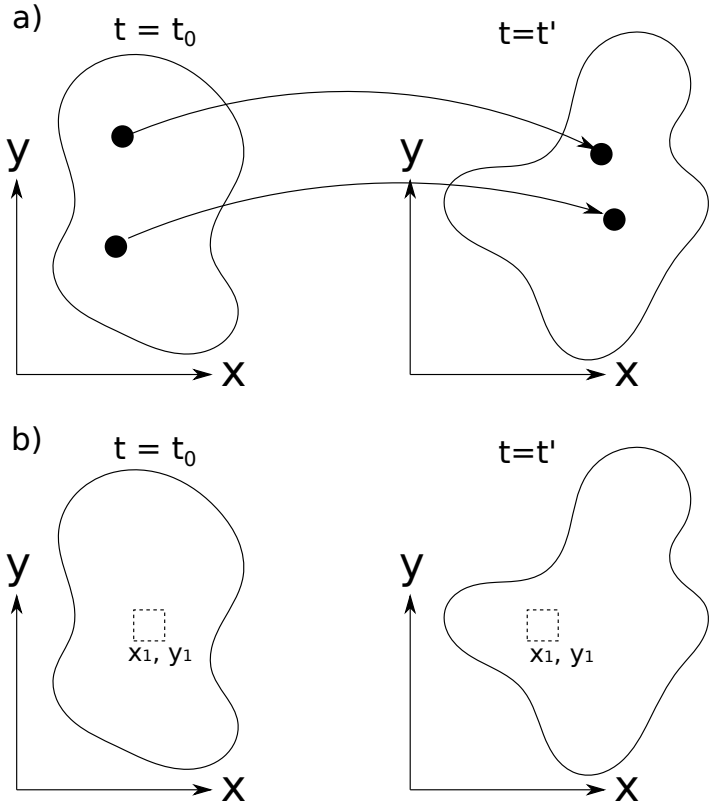

Figure 2.29. Schematic depiction of the a) Lagrangian and b) Eulerian description of the flow.

Dissipaton bracket

The Poisson bracket describes non-dissipative processes which conserve the system's energy; hence the approach is suitable to modelling systems where reversible, elastic stresses arise due to the deformation of the microstructure. The drawback of the Poisson bracket formulation is that it cannot describe dissipative processes, which are also important in fluid flow. Therefore, it is a common practice to supplement the Poisson bracket with a *dissipation bracket* $[F, H]$, whose purpose is to model fully phenomenological processes, e.g. diffusion, or flow-director interaction [64]. The dissipation bracket can have an arbitrary form and contain several phenomenological coefficients, provided that $[F, H]$ does not violate the laws of thermodynamics [124]. By combining the dissipative and Poisson brackets, we obtain a set of constitutive equations describing the evolution of the system's variables (e.g. momentum, microstructure).

2.8.4 Leslie-Ericksen (LE) model

Drawbacks of the transversely isotropic fluid model are addressed by the Leslie-Ericksen theory, which takes into account director elasticity. Materials considered in this thesis are incompressible, so the state of the system is described in terms of the velocity and director fields. The Hamiltonian has kinetic ($\frac{1}{2}\boldsymbol{v}^2$) and elastic ($f_d$) components with the latter describing effects of the distortion of director field on the Helmholtz free energy. The Poisson bracket, which depends on $\boldsymbol{v}$ and $\boldsymbol{n}$, is supplemented with a fully phenomenological dissipation bracket describing the flow-director interaction [64]. The combination of Poisson and dissipation brackets enables one to obtain the velocity and director evolution equations. The momentum balance has the standard form (2.8) with the non-Newtonian stress given by

$$\boldsymbol{\tau} = \underbrace{\alpha_1 \boldsymbol{nnnn} : \boldsymbol{D} + \alpha_2 \boldsymbol{nN} + \alpha_3 \boldsymbol{Nn} + \alpha_4 \boldsymbol{D} + \alpha_5 \boldsymbol{nn} \cdot \boldsymbol{D} + \alpha_6 \boldsymbol{D} \cdot \boldsymbol{nn}}_{\text{viscous stress}} - \underbrace{\frac{\partial f_d}{\partial \boldsymbol{\nabla n}} \cdot (\boldsymbol{\nabla n})^T}_{\text{elastic stress}}. \tag{2.52}$$

The elastic stress comes from the Poisson bracket and describes the reversible effects of material deformation. The viscous stress tensor arises from the dissipation bracket, and therefore is purely phenomenological. Apart from $\alpha_4 \boldsymbol{D}$, individual stress components do not have a clear physical interpretation, however their combinations have a clear physical meaning. Depending on the relative orientations of flow and director, we distinguish three Miesowicz viscosities: $\eta_1 = \frac{\alpha_3+\alpha_4+\alpha_6}{2}$ corresponds to a flow, where the director aligns with the velocity; $\eta_2 = \frac{-\alpha_2+\alpha_4+\alpha_5}{2}$ describes the case when the director aligns in the velocity gradient direction and $\eta_3 = \frac{\alpha_4}{2}$ is the viscosity when the director aligns in the vorticity direction. Calculation of the total stress tensor requires the specification of the director field, for which the evolution equation is given by

$$\frac{\boldsymbol{h} - \boldsymbol{nn} \cdot \boldsymbol{h}}{\gamma_1} - \frac{\gamma_2}{\gamma_1}(\boldsymbol{n} \cdot \boldsymbol{D} - \boldsymbol{nnn} : \boldsymbol{D}) - \boldsymbol{N} = 0, \tag{2.53}$$

where $\gamma_1 = \alpha_3 - \alpha_2$, $\gamma_2 = \alpha_6 - \alpha_5 = \alpha_2 + \alpha_3$ [125]. Equation (2.53) resembles the angular momentum balance in the transversely isotropic fluid model (2.29) with the addition of the molecular field

$$\boldsymbol{h} = -\frac{\delta f_d}{\delta \boldsymbol{n}}, \tag{2.54}$$

which expresses the contribution of elastic effects to the director orientation. The constant magnitude of the director field is ensured by the inclusion of $\boldsymbol{nn} \cdot \boldsymbol{h}$ and $\boldsymbol{nnn} : \boldsymbol{D}$.

Static limit

In the static limit, the flow-related terms in eq. (2.53) vanish and the steady-state director orientation satisfies

$$\boldsymbol{h} - \boldsymbol{nn} \cdot \boldsymbol{h} = 0, \tag{2.55}$$

indicating that in the absence of flow the director aligns to minimise the Helmholtz free energy with the constraint $|\boldsymbol{n}|^2 = 1$.

Zero elasticity limit

In the limit of negligible elasticity, the distortion effect $\boldsymbol{h}$ can be neglected and the angular momentum balance (2.53) reduces to

$$\boldsymbol{N} + \frac{\gamma_2}{\gamma_1}(\boldsymbol{n} \cdot \boldsymbol{D} - \boldsymbol{n} \cdot \boldsymbol{D}) = 0, \tag{2.56}$$

which is identical to the director transport equation of the TIF model (2.29) with $\lambda = -\frac{\gamma_2}{\gamma_1} = -\frac{\alpha_3+\alpha_2}{\alpha_3-\alpha_2}$ [125]. Substituting eq. (2.56) into the stress definition (2.52) recovers the stress tensor of the transversely isotropic fluid (2.27) with the modified coefficients μ_i

$$\mu = \frac{\alpha_4}{2}, \qquad \mu_1 = \frac{1}{2}\left(\alpha_1 + \gamma_2 + \frac{2\gamma_2\alpha_2}{\gamma_1}\right), \qquad \mu_2 = \alpha_5 - \frac{\gamma_2\alpha_2}{\gamma_1}, \tag{2.57}$$

indicating that the TIF model is a zero elasticity limit of the Leslie-Ericksen theory.

Summary of the LE model

The Leslie-Ericksen model is the most frequently used constitutive equation in nemato-dynamic simulations [126, 127]. It is relatively simple yet capable of coupling the effects of flow and material elasticity controlling the director orientation [128]. In the limiting case of small elasticity, the LE theory accurately captures flow alignment, while for nearly static cases, the flows induced by director rotation (backflow effect) can be modelled [129]. The latter property is important even in static cases, where an unwanted rotation of the director

field may reduce the contrast in optical devices [53, 130]; backflow effects can also be used in microfluidic devices as an alternative for mechanical pumps, where an external field rotates the director and induces flow [131].

2.8.5 Order parameter tensor

Despite the number of advantages of the LE theory, its main drawback is the vectorial nature of the director and the assumption of a constant order parameter. The model does not perform well in the presence of significant variations of the order parameter [126], or when the geometry has discontinuities in the director orientation. If the director orientation changes discontinuously over a small distance, say, in corner bounded flows, the Frank-Oseen theory predicts infinite distortion energy density [35]. These problems can be solved by describing the microstructure via the *tensor-based order parameter* $\boldsymbol{Q}$, which has the following advantages over the vectorial approach

- Apolarity of the director field [57]. Even though vectors $\boldsymbol{n}$ and $-\boldsymbol{n}$ represent the same state, the vectorial framework enforces director polarity. As will be shown in the next chapters, the sign of $\boldsymbol{n}$ does affect the flow field in vectorial based models, which is unphysical. The problem becomes particularly important in more complex, industrial geometries, where the simulation outcome depends on the boundary conditions. For a planar contraction consisting of six walls joined by sharp corners, the wall-normal boundary condition can be prescribed in 64 ways; some examples are shown in fig. 2.30. The situation becomes even more problematic for mixers or manifolds with more degrees of freedom. The orientability issue is resolved by employing the $\boldsymbol{Q}$-tensor approach [132], where the orientation of the nematic element is represented as a directionless line, and each boundary condition can be uniquely defined.
- Varying order parameter [64] - the Leslie-Ericksen theory models only the director orientation and fails to provide any information on the degree of molecular alignment. Material characteristics (viscosity, normal stresses) depend on the ordering within the system [133]; therefore, taking into account the order parameter enables a more accurate microstructure description.
- Defects - these are discontinuities in the orientation of rod-like particles (fig. 2.31) with a lower order parameter, and where the uniaxial director is not well defined [134, 135]. Defects arise in locations where a purely vectorial based description is not well defined, for example, in corners (fig. 2.32). In addition, defects introduce local biaxiality in the state of a liquid crystal, which cannot be captured in the director framework due to the uniaxial symmetry of $\boldsymbol{n}$.

$\boldsymbol{Q}$ is a traceless, symmetric second order tensor whose eigenvector corresponding to the largest eigenvalue determines the mean orientation of the long axis of $\boldsymbol{n}$. For biaxial liquid

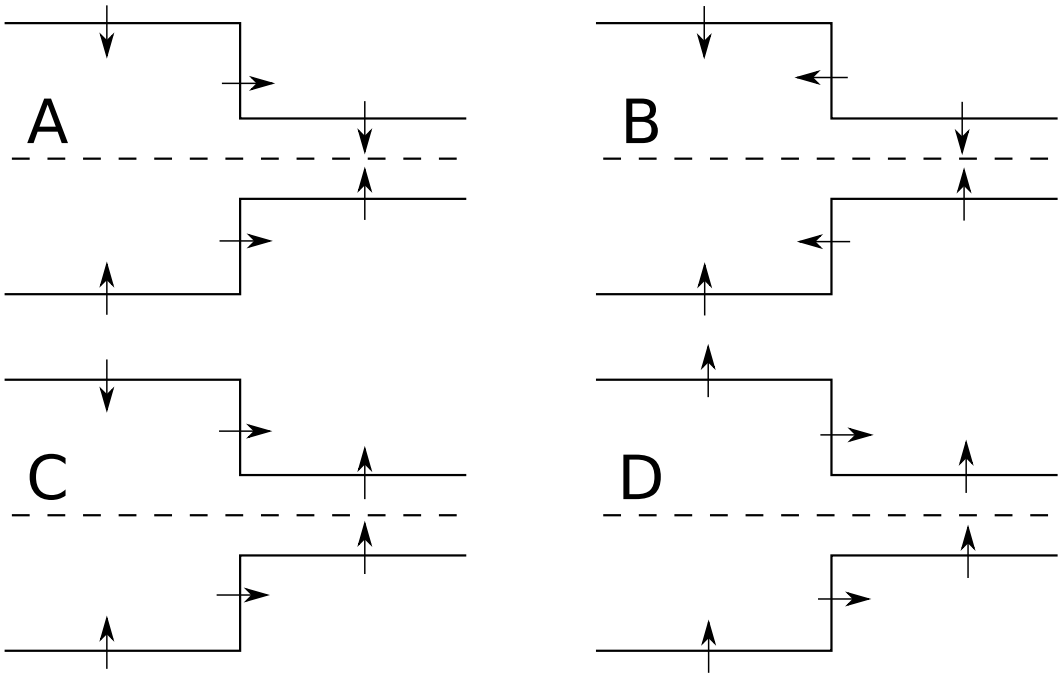

Figure 2.30. Some examples of the homeotropic anchoring in the vectorial framework, each representing the same physical state.

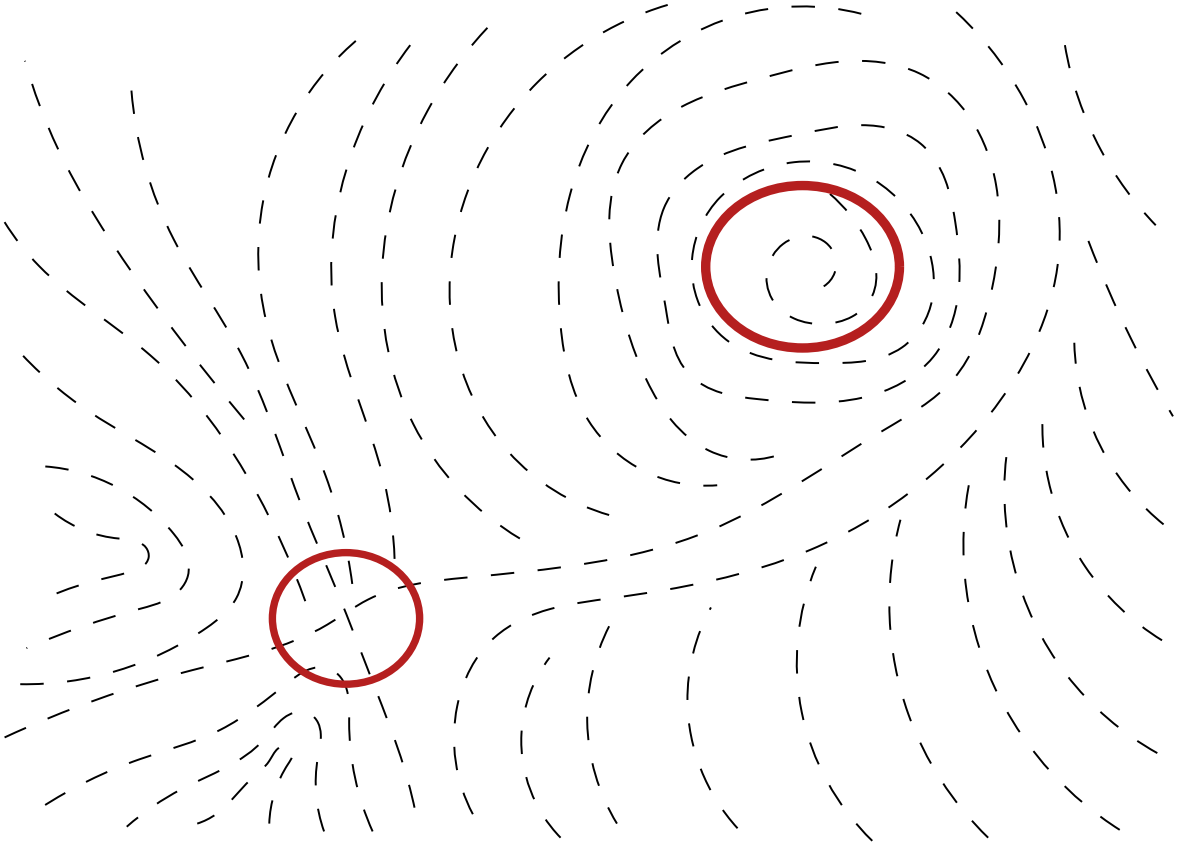

Figure 2.31. Director field with a pair of defects enclosed by red lines.

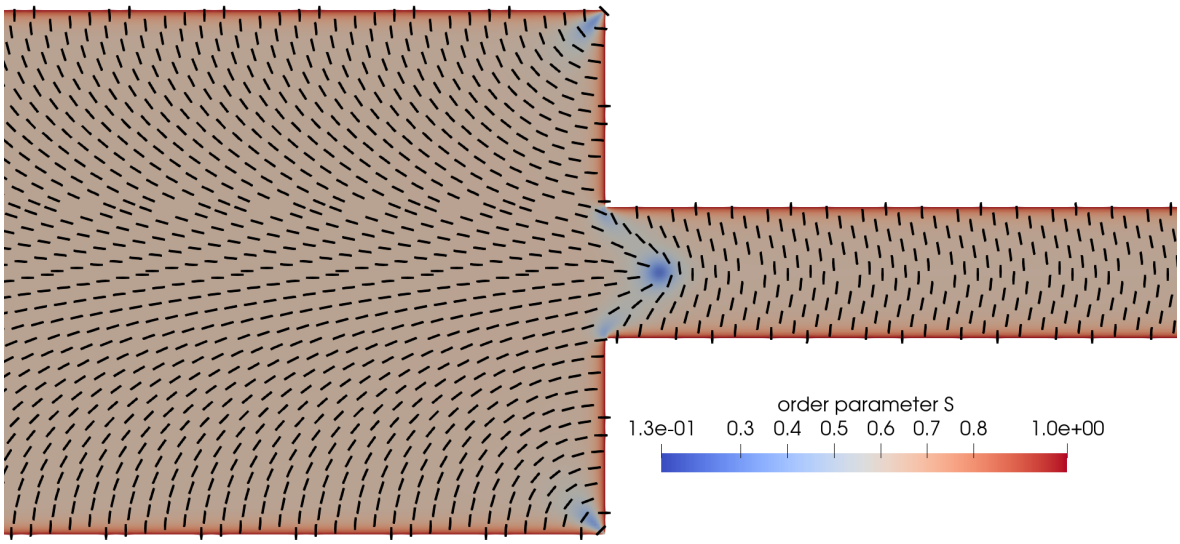

Figure 2.32. Schematic illustration of the director field polluted with defects in a contraction. Further details on the flow of liquid crystals in a contraction will be presented later in the thesis.

crystals, the eigenvector corresponding to the second largest eigenvalue describes the direction of the medium axis $\boldsymbol{m}$. Thus, in the most general form, $\boldsymbol{Q}$ can be written as [57]

$$\boldsymbol{Q} = S_1 \boldsymbol{nn} + S_2 \boldsymbol{mm} - (S_1 + S_2)\frac{\boldsymbol{\delta}}{3}, \tag{2.58}$$

where S_1 and S_2 describe the ordering of the system along the long and medium axis and $\boldsymbol{\delta}$ is the identity tensor. The degree of alignment S_i can be found from the eigenvalues of $\boldsymbol{Q}$ [67]:

$$S_1 = \lambda_1 + \lambda_2, \qquad S_2 = \lambda_3 - \lambda_2, \tag{2.59}$$

where $\lambda_1 > \lambda_2 > \lambda_3$ are the eigenvalues of the order parameter tensor.

2.8.6 Nematic energy (order parameter tensor)

Elastic energy

The Frank-Oseen theory (section 2.8.2) was developed to model uniaxial, constant order parameter systems and was exploited in the design of display devices [136, 137]. However, it fails when the order parameter varies significantly; in such cases, the $\boldsymbol{Q}$-tensor may be used to describe the liquid crystal field.

The physics described by the earlier Frank-Oseen theory can be formulated through the $\boldsymbol{Q}$-tensor framework, since a constant order parameter, uniaxial director field $\boldsymbol{n}$ is a limiting case of $\boldsymbol{Q}$. Assuming that the distortion energy density depends only on quadratic and cubic variations of $\boldsymbol{\nabla Q}$, a possible, frame indifferent form for the free energy density of a distorting

liquid crystal is given by [138]

$$f_d^Q = \frac{1}{2}\left[K_2^Q Q_{ik,j}Q_{ik,j} + K_3^Q Q_{ik,i}Q_{jk,j} + K_5^Q Q_{ij}Q_{lk,i}Q_{ik,j}\right], \tag{2.60}$$

where $Q_{ik,j} \equiv \frac{\partial Q_{ik}}{\partial x_j}$ and K_i^Q are Frank constants in the $\boldsymbol{Q}$ tensor framework. Other choices of the cubic terms are possible; however, the inclusion of the term $K_3^Q Q_{ik,i}Q_{jk,j}$ ensures that in the uniaxial, constant order parameter limit, eq. (2.60) expresses the same physics as the Frank-Oseen theory in the vectorial framework. The phenomenological constants in the tensorial framework K_i^Q can be expressed in terms of the Frank constants K_i [138]

$$K_2^Q = \frac{3K_2 - K_1 + K_3}{6S^2}, \qquad K_3^Q = \frac{K_1 - K_2}{S^2}, \qquad K_5^Q = \frac{K_3 - K_1}{2S^2}, \tag{2.61}$$

where S is the order parameter. In the limit of the one constant approximation with $K_1 = K_2 = K_3$, the constants K_i^Q simplify to

$$K_2^Q = \frac{K}{2S^2}, \qquad K_3^Q = K_5^Q = 0, \tag{2.62}$$

which simplifies the energy density (2.60) to

$$f_d^Q = \frac{1}{2}K_2 Q_{ik,j}Q_{ik,j} \tag{2.63}$$

Bulk free-energy

In the absence of director distortions, the degree of molecular alignment within a liquid crystal is controlled either by the concentration of anisotropic particles (lyotropic LC), or by the temperature (thermotropic LC). In thermotropic liquid crystals, the additional bulk free-energy density can be modelled by an empirical theory provided by Landau, where the order-dependent bulk potential is expanded in terms of invariants of $\boldsymbol{Q}$ around the isotropic state [139]

$$f_{nematic} = \frac{a}{2}\,\mathrm{tr}(\boldsymbol{Q}\cdot\boldsymbol{Q}) - \frac{b}{3}\,\mathrm{tr}(\boldsymbol{Q}\cdot\boldsymbol{Q}\cdot\boldsymbol{Q}) + \frac{c}{4}\,\mathrm{tr}^2(\boldsymbol{Q}\cdot\boldsymbol{Q}), \tag{2.64}$$

where $a = \alpha(T - T^*)$, T^* is a critical temperature, below which the isotropic state is unstable and $\alpha, b, c > 0$ [57, 140] are material parameters. For uniaxial systems, $\boldsymbol{Q} = S(\boldsymbol{nn} - \frac{\boldsymbol{\delta}}{3})$ and the bulk energy density can be represented solely in terms of the order parameter S

$$f_{nematic} = \frac{1}{3}aS^2 - \frac{2}{27}bS^3 + \frac{1}{9}cS^4. \tag{2.65}$$

In equilibrium, the nematic energy density of the uniaxial system is extremized with respect to variations in the order parameter tensor

$$\frac{\delta f_{nematic}}{\delta \boldsymbol{Q}} = \frac{\partial f_{nematic}}{\partial \boldsymbol{Q}} = \frac{\partial f_{nematic}}{\partial S}\frac{\partial S}{\partial \boldsymbol{Q}} = 0, \tag{2.66}$$

which is satisfied by three different order parameters

$$S_1 = 0, \tag{2.67a}$$

$$S_2 = \frac{b + \sqrt{b^2 - 24ac}}{4c}, \tag{2.67b}$$

$$S_3 = -\frac{-b + \sqrt{b^2 - 24ac}}{4c}. \tag{2.67c}$$

S_1 corresponds to the isotropic ordering, S_2 represents a nematic state which is stable for sufficiently low temperatures ($T < T^* + \frac{b^2}{27ac}$) [57] and S_3 is a nematic state, whose stability depends on the temperature. S_3 is unstable at high temperatures ($T > T^* + \frac{b^2}{24ac}$), while for lower T, S_3 represents a metastable state with a negative order parameter [57]. For systems considered in this thesis, material parameters a, b, c are chosen such that the minimum of $f_{nematic}$ is in the nematic state with order parameter S_2.

Landau-de Gennes energy

In the $\boldsymbol{Q}$-tensor framework, the Helmholtz free energy has two contributions: the elastic component acting to minimise the distortion of $\boldsymbol{Q}$ and the bulk free energy density driving the system to the equilibrium order parameter S_2. Therefore, for the systems described by the order parameter tensor, the Helmholtz free energy requires the specification of both elastic (2.60) and bulk (2.64) components. Their sum is called the Landau-de Gennes energy density [140]

$$f_{LdG} = f_d^Q + f_{nematic}, \tag{2.68}$$

and similarly to the vectorial framework, the system is in equilibrium when the Landau-de Gennes energy density is minimum with respect to variations in the order parameter tensor $\frac{\delta f_{LdG}}{\delta \boldsymbol{Q}} = 0$.

2.8.7 Beris-Edwards (BE) model

The drawbacks of the Leslie-Ericksen theory have been addressed by the constitutive equation proposed by Beris and Edwards [64, 141], which models the evolution of the $\boldsymbol{Q}$-tensor. It is assumed that the state of an incompressible, liquid crystalline material is described by the velocity $\boldsymbol{v}$ and the order parameter tensor $\boldsymbol{Q}$, where the latter represents the mean orientation and alignment of the microstructure. Similarly to the Leslie-Ericksen theory, the Hamiltonian contains the kinetic $\frac{1}{2}\boldsymbol{v}^2$ and a configuration-dependent components. However, the microstructure contribution is expressed in terms of the order parameter tensor and is quantified through the Landau-de Gennes free energy density (eq. (2.68)). The Poisson bracket is supplemented with a phenomenological dissipation bracket. The linear momentum balance

has the standard form (2.8) with the viscoelastic stress tensor now given by [64, 131]

$$\boldsymbol{\tau} = \underbrace{\mu\boldsymbol{D} - \xi\left[(\boldsymbol{Q}+\frac{\boldsymbol{\delta}}{3})\cdot\boldsymbol{H} + \boldsymbol{H}\cdot(\boldsymbol{Q}+\frac{\boldsymbol{\delta}}{3}) - 2(\boldsymbol{Q}+\frac{\boldsymbol{\delta}}{3})(\boldsymbol{H}:\boldsymbol{Q})\right] + \boldsymbol{H}\cdot\boldsymbol{Q} - \boldsymbol{Q}\cdot\boldsymbol{H}}_{\text{viscous stress}} \underbrace{- \frac{\partial f_{LdG}}{\partial Q_{ij,\alpha}} Q_{ij,\beta}}_{\text{elastic stress}}, \quad (2.69)$$

where

$$\boldsymbol{H} = -\frac{\delta f_{LdG}}{\delta \boldsymbol{Q}} + \underline{\frac{1}{3}\,\mathrm{tr}\frac{\delta f_{LdG}}{\delta \boldsymbol{Q}}}, \quad (2.70)$$

measures the deviation of the microstructure from the minimum Helmholtz free energy. The momentum equation is supplemented with the $\boldsymbol{Q}$-tensor evolution equation, which models the competition of static and hydrodynamic effects acting on the microstructure [64, 126]

$$\frac{D\boldsymbol{Q}}{Dt} = \boldsymbol{S} + \Gamma\boldsymbol{H}, \quad (2.71)$$

where $\boldsymbol{S}$ represents the action of hydrodynamic torques on the $\boldsymbol{Q}$-tensor and is defined as [64]

$$\boldsymbol{S} = (\xi\boldsymbol{D} - \boldsymbol{\Omega})(\boldsymbol{Q}+\frac{\boldsymbol{\delta}}{3}) + (\boldsymbol{Q}+\frac{\boldsymbol{\delta}}{3})(\xi\boldsymbol{D}+\boldsymbol{\Omega}) - \underline{2\xi(\boldsymbol{Q}+\frac{\boldsymbol{\delta}}{3})\,\mathrm{tr}(\boldsymbol{Q}\cdot\boldsymbol{\nabla u})}. \quad (2.72)$$

The underlined terms in equations (2.70) and (2.72) are included to ensure that $\boldsymbol{Q}$ is traceless. The Beris-Edwards model contains three phenomenological parameters Γ, μ, ξ, whose meaning is clearer than in the LE theory; Γ controls the relaxation towards the state of minimum Helmholtz free energy [142], μ is the Newtonian viscosity, and ξ controls the misalignment between the flow and director, analogous to the tumbling parameter in the TIF model [64].

Reduction to the Leslie-Ericksen theory

Let us consider a uniaxial, constant order parameter nematic that does not contain defects. In such case, the Beris-Edwards model represents the same physics as the Leslie-Ericksen model: competition of viscous and elastic effects that can only affect the director orientation. The uniaxial, constant order parameter tensor is then given by

$$\boldsymbol{Q} = S\left(\boldsymbol{nn} - \frac{\boldsymbol{\delta}}{3}\right), \quad (2.73)$$

and the viscous stress tensor can be formulated solely in terms of $\boldsymbol{n}$ in the Leslie-Ericksen form [142]

$$\boldsymbol{\tau}^{visc} = \alpha_1\boldsymbol{nnnn} : \boldsymbol{D} + \alpha_2\boldsymbol{nN} + \alpha_3\boldsymbol{Nn} + \alpha_4\boldsymbol{D} + \alpha_5\boldsymbol{nn}\cdot\boldsymbol{D} + \alpha_6\boldsymbol{D}\cdot\boldsymbol{nn}, \quad (2.74)$$

where α_i are Leslie viscosities, that can be expressed solely in terms of the parameters of the BE model [142]

$$\alpha_1 = -\frac{2}{3}S_1^2(3+4S-4S^2)\xi^2\frac{1}{\Gamma}, \tag{2.75a}$$

$$\alpha_2 = \left[-\frac{1}{3}S(2+S)\xi - S^2\right]\frac{1}{\Gamma}, \tag{2.75b}$$

$$\alpha_3 = \left[-\frac{1}{3}S(2+S)\xi + S^2\right]\frac{1}{\Gamma}, \tag{2.75c}$$

$$\alpha_4 = \mu + \frac{4}{9}(1-S)^2\xi^2\frac{1}{\Gamma}, \tag{2.75d}$$

$$\alpha_5 = \left[\frac{1}{3}S(4-S)\xi^2 + \frac{1}{3}S(2+S)\xi\right]\frac{1}{\Gamma}, \tag{2.75e}$$

$$\alpha_6 = \left[\frac{1}{3}S(4-S)\xi^2 - \frac{1}{3}S(2+S)\xi\right]\frac{1}{\Gamma}. \tag{2.75f}$$

A quick inspection of eq. (2.75) indicates that apart from α_4, the magnitude of α_i rises as the order parameter S increases, indicating a larger microstructure contribution to the stress tensor. On the other hand, in the isotropic limit, $S = 0$ and $\alpha_{i=1:6, i\neq 4} = 0$ removing orientational dependence from the stress tensor.

2.8.8 Dimensional groups and relevant scales

The nematodynamic equations describe a multiphysics problem, with several mechanisms controlling the director orientation and thus flow behaviour. Below are described the relevant length scales and dimensionless numbers, whose properties will be used in the following chapters.

Reynolds number

The linear momentum balance (2.8) is an example of a convection-diffusion equation, which can be written as

$$\rho\frac{\partial \boldsymbol{v}}{\partial t} + \rho\underbrace{\boldsymbol{v}\cdot\boldsymbol{\nabla}\boldsymbol{v}}_{\text{convection}} = -\boldsymbol{\nabla}p + \underbrace{\boldsymbol{\nabla}\cdot\boldsymbol{\tau}}_{\text{diffusion}}. \tag{2.76}$$

For a Newtonian fluid, the stress tensor is linear with the shear rate $\dot{\gamma}$. Introducing the following scaled variables

$$\boldsymbol{\nabla} = \frac{1}{L}\boldsymbol{\nabla}^*, \qquad \boldsymbol{v} = V\boldsymbol{v}^*, \qquad p = \rho V^2 p^*, \qquad \boldsymbol{\tau} = \mu\frac{V}{L}\boldsymbol{\tau}^*, \qquad t = \frac{L}{V}t^*, \tag{2.77}$$

enables to re-write the momentum balance (2.76) in a dimensionless form

$$\frac{\partial \boldsymbol{V}^*}{\partial t^*} + \boldsymbol{V}^*\cdot\boldsymbol{\nabla}^*\boldsymbol{V}^* = -\boldsymbol{\nabla}^* p^* + \frac{\mu}{\rho V L}\boldsymbol{\nabla}^*\cdot\boldsymbol{\tau}^* \tag{2.78}$$

where V, L, μ are velocity-, length- and viscosity-scales and starred variables denote dimensionless quantities. Thus, eq. (2.78) indicates that the relative importance of convective to diffusive effects is quantified by

$$Re = \frac{VL\rho}{\mu}, \tag{2.79}$$

called the Reynolds number [45]. The interpretation of the Reynolds number becomes more ambiguous for non-Newtonian fluids, as their viscosity is not constant. Therefore, in order to keep the analysis consistent, a particular viscosity limit is chosen as the representative value of viscosity, for example, the zero shear-rate viscosity [18]. The typical flows considered in this thesis focus on the motion of highly viscous fluids, which take place in small geometries ($O(\text{mm})$) at low speeds. Therefore, the Reynolds number is significantly smaller than unity, so the importance of inertial effects is negligible.

Ericksen number

The total stress tensor in the Leslie-Ericksen theory has both viscous and elastic components and is given by

$$\boldsymbol{\tau} = \alpha_1 \boldsymbol{nnnn} : \boldsymbol{D} + \alpha_2 \boldsymbol{nN} + \alpha_3 \boldsymbol{Nn} + \alpha_4 \boldsymbol{D} + \alpha_5 \boldsymbol{nn}\cdot\boldsymbol{D} + \alpha_6 \boldsymbol{D}\cdot\boldsymbol{nn} - \frac{\partial f_d}{\partial \boldsymbol{\nabla n}}\cdot(\boldsymbol{\nabla n})^T. \tag{2.52}$$

Let us use the following scaled variables

$$\begin{aligned} \boldsymbol{\nabla} = \frac{1}{L}\boldsymbol{\nabla}^*, \qquad \boldsymbol{D} = \frac{V}{L}\boldsymbol{D}^*, \qquad \boldsymbol{N} = \frac{V}{L}\boldsymbol{N}^*, \\ \alpha_i = \alpha_4 \alpha_i^*, \qquad f_d = K\left(\frac{\boldsymbol{\nabla}^* \boldsymbol{n}}{L}\right)^2, \qquad \boldsymbol{\tau} = \alpha_4 \frac{U}{L}\boldsymbol{\tau}^*, \end{aligned} \tag{2.80}$$

where starred variables represent dimensionless quantities and the Newtonian viscosity was chosen for the viscosity-scale. The stress can be written in a dimensionless form

$$\boldsymbol{\tau}^* = \alpha_1^* \boldsymbol{nnnn} : \boldsymbol{D}^* + \alpha_2^* \boldsymbol{nN}^* + \alpha_3^* \boldsymbol{N}^* \boldsymbol{n} + \boldsymbol{D}^* + \alpha_5^* \boldsymbol{nn}\cdot\boldsymbol{D}^* + \alpha_6^* \boldsymbol{D}\cdot\boldsymbol{nn} - \tfrac{K}{VL\alpha_4^*}\boldsymbol{\nabla}^*\boldsymbol{n}\cdot(\boldsymbol{\nabla}^*\boldsymbol{n})^T, \tag{2.81}$$

indicating that the relative importance viscous to elastic stresses is described by

$$Er = \frac{VL\alpha_4^*}{K}, \tag{2.82}$$

called the Ericksen number. With the same scaling, the director transport equation becomes

$$\frac{1}{Er}\frac{\boldsymbol{h}^* - \boldsymbol{nn}\cdot\boldsymbol{h}^*}{\gamma_1^*} - \frac{\gamma_2^*}{\gamma_1^*}(\boldsymbol{n}\cdot\boldsymbol{D} - \boldsymbol{nnn}:\boldsymbol{D}^*) - \boldsymbol{N}^* = 0, \tag{2.83}$$

indicating that for $Er \to 0$, the stress and director fields are controlled by elastic contribution, while when $Er \to \infty$, flow effects govern the stress and director orientation [15, 43].

In order to make a direct comparison between the LE and BE models, the Ericksen number

in the Beris-Edwards framework is defined through eq. (2.82). The corresponding Newtonian viscosity α_4 and the Frank elastic constant K are expressed via eq. (2.75d) and (2.62) to ensure a consistent definition of Er

$$Er_{BE} = \left[\mu + \frac{4}{9}(1-S)^2\xi^2\frac{1}{\Gamma}\right]\frac{VL}{2K^Q S_{eq}^2}. \tag{2.84}$$

Flow elastic length-scale

For moderate Ericksen number flows, the director orientation in the bulk of the fluid is controlled by viscous torques; close to the wall, the fluid is nearly static, particles align in the direction prescribed by the wall anchoring, so the Helmholtz free energy is minimum with respect to the geometry induced distortions. The changeover from wall dominated to flow dominated dynamics occurs across a boundary layer whose thickness can be estimated from [21]

$$w = \sqrt{\frac{K}{\mu\dot{\gamma}_w}}, \tag{2.85}$$

where $\dot{\gamma}_w$ is the shear rate at the wall. In a simple shear flow, assuming that $\dot{\gamma}$ is uniform and given by $\dot{\gamma}_w = \frac{V}{L}$ eq. (2.85) yields

$$\frac{w}{L} = \frac{1}{\sqrt{Er}}, \tag{2.86}$$

so the thickness of the near-wall layer dominated by elastic effects decreases as the Ericksen number increases. Thus, to resolve the near-wall director transition, the computational domain must be appropriately refined in the locations where steep director gradients occur.

Deborah number

The Beris-Edwards theory accounts for three distinct contributions to the $\boldsymbol{Q}$-tensor evolution: 1) hydrodynamic effects quantified by $\boldsymbol{S}$; 2) material elasticity $-\frac{\delta f_d^Q}{\delta \boldsymbol{Q}}$ acting to maintain the uniform $\boldsymbol{Q}$ field across the domain; 3) molecular ordering $-\frac{\delta f_{nematic}^Q}{\delta \boldsymbol{Q}}$, which drives $\boldsymbol{Q}$ towards the equilibrium order parameter. Hence, the $\boldsymbol{Q}$-tensor evolution equation (2.71) can be written as

$$\frac{D\boldsymbol{Q}}{Dt} = \boldsymbol{S} - \Gamma\frac{\delta f_{nematic}^Q}{\delta \boldsymbol{Q}} - \Gamma\frac{\delta f_d^Q}{\delta \boldsymbol{Q}}. \tag{2.87}$$

We introduce the following scaling

$$\frac{D}{Dt} = \frac{V}{L}\frac{D^*}{Dt^*}, \qquad \boldsymbol{S} = \frac{V}{L}\boldsymbol{S}^*, \qquad f_{nematic}^Q = \frac{a+b+c}{3}f_{nematic}^{Q*}, f_d^Q = \frac{K^Q}{L^2}f_d^{Q*}, \tag{2.88}$$

where the starred variables refer to dimensionless quantities, V and L are the velocity- and length scales respectively, a, b, c are parameters of the nematic bulk energy density and K^Q is the Frank constant. Hence, the $\boldsymbol{Q}$-tensor evolution equation (2.87) can be written in the dimensionless form as

$$\frac{D^*\boldsymbol{Q}}{Dt^*} = \boldsymbol{S}^* - \frac{\Gamma K}{VL}\frac{\delta f_d^{Q*}}{\delta \boldsymbol{Q}} - \frac{(a+b+c)L\Gamma}{3V}\frac{\delta f_{nematic}^{Q*}}{\delta \boldsymbol{Q}}. \tag{2.89}$$

Since Γ has the units of reciprocal viscosity, the term $\frac{VL}{\Gamma K}$ is related to the Ericksen number, which quantifies the relative strength to hydrodynamic and elastic effects. The coefficient of the last term on the right-hand side of eq. (2.89) is defined as the Deborah number

$$De = \frac{3V}{(a+b+c)L\Gamma}, \tag{2.90}$$

and quantifies the relative strength of nematic and hydrodynamic effects acting on the order parameter [143]. When $De \to 0$, nematic effects are strong enough to maintain a constant order parameter. Only in the limit of strong flows, $De >> 1$ and deformation effects are strong enough to affect the order parameter [143].

Defect size

Consider a static liquid crystal sample constrained in a one-dimensional domain with the same anchoring on both walls (fig. 2.33). In such a system, the director is horizontal across the whole domain and only the order parameter changes. In the one-constant approximation, the Landau-de Gennes energy density is given by

$$f_{LdG} = f_d^Q + f_{nematic} = \frac{1}{3}K(\boldsymbol{\nabla}S)^2 + \frac{1}{3}aS^2 - \frac{2}{27}bS^3 + \frac{1}{9}cS^4. \tag{2.68}$$

Using the scaling

$$a = \frac{a+b+c}{3}a*, \qquad b = \frac{a+b+c}{3}b*, \qquad c = \frac{a+b+c}{3}c*, \qquad f_{LdG} = \frac{K}{L^2}f^*_{LdG}, \tag{2.91}$$

the dimensionless Landau-de Gennes energy density becomes

$$f^*_{LdG} = \underbrace{\frac{1}{3}(\boldsymbol{\nabla}^*S)^2}_{\text{elasticity}} + \frac{a+b+c}{3}\frac{L^2}{K}\underbrace{\left(\frac{1}{3}a^*S^2 - \frac{2}{27}b^*S^3 + \frac{1}{9}c^*S^4\right)}_{\text{bulk energy}}, \tag{2.92}$$

which shows that the term $\frac{a+b+c}{3}\frac{L^2}{K} = (\frac{L}{\xi_N})^2$ controls the relative importance of elastic and bulk effects and

$$\xi_N = \sqrt{\frac{3K}{a+b+c}} \tag{2.93}$$

provides the length-scale over which the elastic and bulk contributions are of a equal importance. Elasticity drives system to the state with a uniform order parameter imposed by the boundaries, while the bulk energy density term acts to minimise $f_{nematic}$; for typical liquid crystal parameters, $S \approx 0.5$ [57, 140]. In small geometries (with respect to the geometry size) $\xi_N >> L$ (fig. 2.33, blue line), the equilibrium value of the order parameter is governed by the elastic contribution and $S = 1$, as imposed by the boundaries. On the other hand, for large domain sizes, $\xi_N << L$, so apart from the near-wall locations (with the order parameter imposed by the wall orientation), S takes the value which minimises $f_{nematic}$ (fig. 2.33, yellow curve). Hence, material elasticity imposes a characteristic length-scale over which the order parameter varies, and ξ_N can be understood as a measure of the defect size. Therefore, to capture potential defects in numerical simulations, the grid spacing should be small enough to resolve any rapid variations of the order parameter; for example, ten nodes for each defect dimension ξ_N.

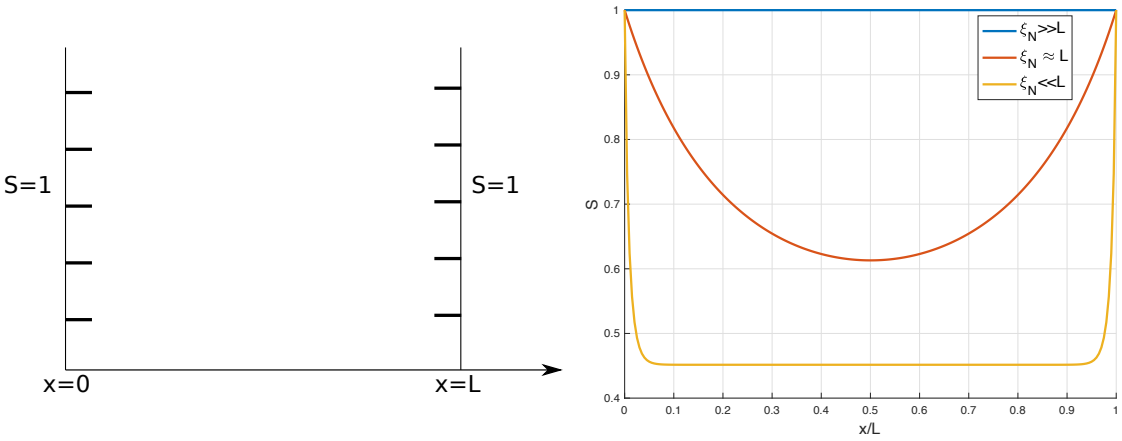

Figure 2.33. Left: a pair of parallel plates with the homeotropic anchoring on both boundaries. Right: distribution of the order parameter dependent on the defect size.

2.8.9 Other models

Several other nematodynamic theories have been proposed to model the flow of liquid crystals. Ericksen [144] suggested an extension of the Leslie-Ericksen theory, which provides an additional transport equation for the variable order parameter S. However, the same model can be obtained from the Beris-Edwards equation by assuming a uniaxial director field [141]. Doi [83] introduced a constitutive equation that models the orientation and distribution of rod-like particles based on the probability distribution function; this approach requires significant computational efforts to solve, even in the simplest geometries; therefore, it is impractical to use in industry-relevant domains. Doi's theory can be simplified to model the evolution of the order parameter tensor. The model has no elasticity in the original form and can be recovered from the BE theory by neglecting elastic effects. The extended Doi theory [133] includes elastic effects; however, the model can also be recovered from the bracket formulation by altering the dissipative contribution $[F, H]$ [64]. The expanded dissipation bracket requires even more phenomenological coefficients without a clear physical meaning. For that reason,

in the remainder of the thesis, we limit the attention to the baseline theories: the transversely isotropic fluid, the Leslie-Ericksen model and the Beris-Edwards model.

2.9 Computational fluid dynamics

The fluid motion is described by a system of nonlinear, partial differential equations. Due to the complexity of the governing equations, obtaining analytical solutions of flow problems may be possible in basic geometries (channel, pipe flows). That is of limited use from the industrial point of view since the industrially relevant flows occur in manifolds, contractions and mixers. The increase of available computing power in the last fifty years have given rise to a new area of fluid mechanics - computational fluid dynamics (CFD) [36]. A typical CFD solution is based on dividing the domain of interest (e.g. mixer, extruder) into a large number of smaller sub-domains, discretising the governing relations and solving the resultant system of equations for the unknown variables such as the velocity and pressure. For more complex materials, information about the microstructure orientation and deformation can be obtained by solving additional transport equations. Numerical calculations presented in this thesis are solved with the finite volume method; a detailed description is provided in [36, 37].

Chapter 3

Numerical solver

This chapter presents details of the implementation and validation of the solver used to conduct the simulations, whose results are discussed in subsequent chapters.

3.1 Implementation

Numerical simulations described in further chapters of the thesis are performed in *rheoTool* - the open-source OpenFOAM toolbox dedicated to modelling non-Newtonian and electrically driven flows [145]. OpenFOAM is an object-oriented, unstructured, finite volume solver used for numerical simulations of both laminar and turbulent flows [107]. The code employs the SIMPLEC pressure-velocity coupling scheme to solve the Navier-Stokes equations supplemented with the non-Newtonian stress tensor [145].

RheoTool and, more specifically, one of its solvers *rheoFoam* has been frequently used by the non-Newtonian fluid mechanics community to model viscoelastic flows [46, 146, 147] with a symmetric stress tensor. The stress tensor in the models considered in this thesis (transversely isotropic fluid, Leslie-Ericksen and Beris-Edwards) need not be symmetric [43, 64], so *rheoFoam* is not suitable to model the flow of liquid crystals. One of the major contributions from the research in this thesis is the development of the solver *rheoFoam2*, which is capable of simulating constitutive equations with a non-symmetric stress tensor; the source code of the solver is presented in the appendix A. *rheoFoam2* can simulate any constitutive behaviour, however in this thesis we limit our attention to nematodynamic equations. OpenFOAM provides a consistent framework for the implementation of new models, where the physics introduced by each model is described in a single file. In case of the Leslie-Ericksen and Beris-Edwards models the solution algorithm follows the same procedure

1. Solution of the microstructure evolution equation: director transport equation in the LE theory or the $\boldsymbol{Q}$-tensor transport equation in the BE model.
2. Calculation of the non-Newtonian stress contribution based on the director/$\boldsymbol{Q}$-tensor field.
3. Solution of the Navier-Stokes equation with both Newtonian and non-Newtonian contributions to the stress tensor.

Source codes of the Leslie-Ericksen and Beris-Edwards models are presented in the appendix A.

3.2 Director evolution upon a pure rotation

Analytical solutions of the Leslie-Ericksen and Beris-Edwards models are possible only in the limiting cases of simple geometries (e.g. channel flow at an infinite Ericksen number). For more complex flow geometries (bends, contractions, mixers), numerical solutions only are achievable. In this section, we consider the evolution of a single director element subject to a pure rotation (fig. 3.1). The suitability of time discretisation schemes is examined by comparing analytical and numerical predictions. Simulations of viscoelastic flows with *rheoTool* employ either the first-order Euler (forward and backward) or the second-order Crank-Nicholson schemes [46, 107, 147]; hence, the performance of these discretisation techniques is examined and compared with the analytical solution.

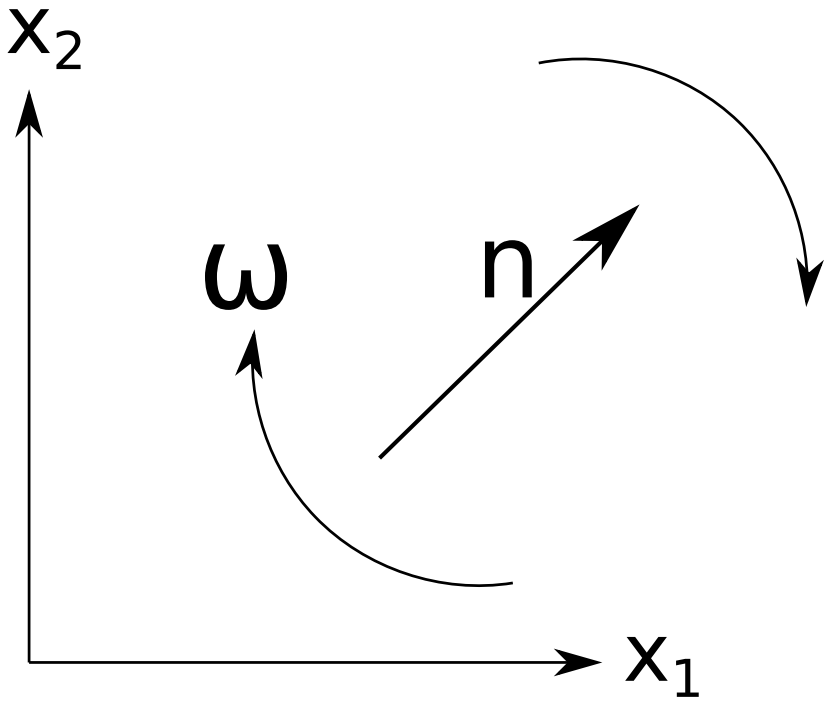

Figure 3.1. Rotation of the director field in a channel flow.

3.2.1 Analytical solution

Consider a simplified version of the Leslie-Ericksen equation (2.53) with $\boldsymbol{D} = 0$, $K = 0$, that reduces the angular momentum balance to

$$\boldsymbol{N} = \dot{\boldsymbol{n}} - \boldsymbol{n} \cdot \boldsymbol{\omega} = 0, \tag{3.1}$$

and represents a pure rotation of nematic molecules. If the flow and director are confined to the same plane (fig. 3.1), the director and vorticity tensor are defined as

$$\boldsymbol{n} = [n_1,\ n_2], \tag{3.2}$$

$$\boldsymbol{\omega} = \frac{\boldsymbol{\nabla v} - (\boldsymbol{\nabla v})^T}{2} = \begin{bmatrix} 0 & -1 \\ 1 & 0 \end{bmatrix} \frac{\dot{\gamma}}{2},$$

where $\boldsymbol{v}$ is the fluid velocity and $\dot{\gamma} = \frac{\partial v_1}{\partial x_2} - \frac{\partial v_2}{\partial x_1}$ is assumed constant. Re-writing the vorticity tensor via a similarity transform, equation (3.1) can be diagonalised to give

$$\frac{\partial}{\partial t} \begin{bmatrix} \nu_1 \\ \nu_2 \end{bmatrix} + \begin{bmatrix} i & 0 \\ 0 & -i \end{bmatrix} \begin{bmatrix} \nu_1 \\ \nu_2 \end{bmatrix} \frac{\dot{\gamma}}{2} = 0. \tag{3.3}$$

The analytical solution of eq. (3.3) is:

$$\nu_1 = \cos\left(\frac{\dot{\gamma}}{2}t + c_1\right) + i \sin\left(\frac{\dot{\gamma}}{2}t + c_1\right), \tag{3.4a}$$

$$\nu_2 = \cos\left(-\frac{\dot{\gamma}}{2}t + c_2\right) + i \sin\left(-\frac{\dot{\gamma}}{2}t + c_2\right), \tag{3.4b}$$

where c_1 and c_2 are integration constants. Inverting the similarity transform and assuming that at $t = 0$, $\boldsymbol{n} = [\cos(\theta_0),\ \sin(\theta_0)]^T$, the director evolves as

$$n_1 = \cos\left(\frac{\dot{\gamma}}{2}t - \theta_0\right), \tag{3.5a}$$

$$n_2 = -\sin\left(\frac{\dot{\gamma}}{2}t - \theta_0\right), \tag{3.5b}$$

which thus satisfies $|\boldsymbol{n}|^2 = 1$.

3.2.2 Solution with the explicit Euler scheme

In order to solve the simplified director evolution equation (3.1) numerically, we limit our attention to a single grid point. Assuming that the orientation of $\boldsymbol{n}$ is known at the kth time level, the director orientation at the $(k+1)$th time level can be calculated by applying the explicit Euler scheme [148]

$$n_1^{k+1} = n_1^k - n_2^k a, \tag{3.6a}$$

$$n_2^{k+1} = n_2^k + n_1^k a, \tag{3.6b}$$

where $a = \frac{\dot{\gamma}}{2}\Delta t$. The magnitude of $\boldsymbol{n}$ is then $|\boldsymbol{n}^{k+1}|^2 = |\boldsymbol{n}^k|^2(1 + a^2)$; hence, for $|\dot{\gamma}| \neq 0$, $\boldsymbol{n}$ grows unbounded as shown in fig. 3.2.

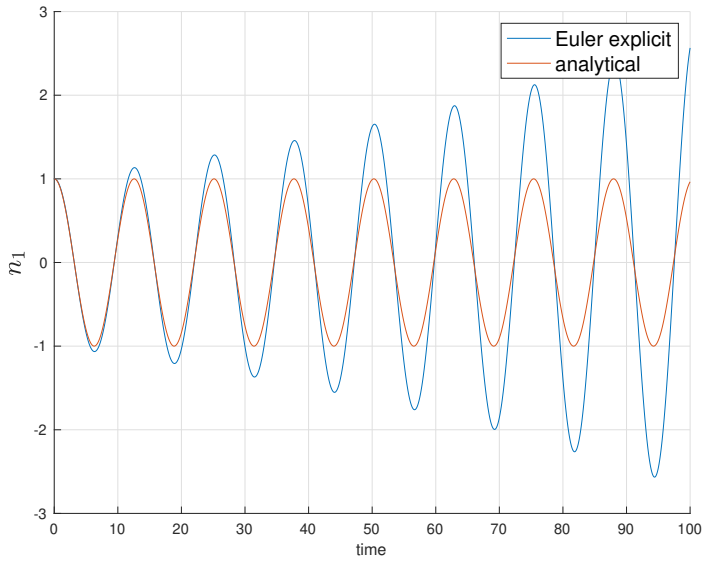

Figure 3.2. Comparison of the evolution of n_1 predicted analytically and numerically with the first order forward Euler scheme. The variation of n_2 is analogous and thus not shown here.

3.2.3 Solution with the implicit Euler scheme

The director evolution at a fixed grid point can be numerically modelled through the implicit Euler scheme [148]. If the components of $\boldsymbol{n}$ are known at the kth time level, then the director orientation at the next time step is calculated as

$$n_1^{k+1} = \frac{n_1^n - a n_2^n}{1 + a^2}, \tag{3.7a}$$

$$n_2^{k+1} = \frac{a n_1^n + n_2^n}{1 + a^2}, \tag{3.7b}$$

where $a = \frac{\dot{\gamma}}{2}\Delta t$. Thus $|\boldsymbol{n}^{k+1}|^2 = \frac{1+a^2}{(1+a^2)^2}|\boldsymbol{n}^k|^2$ and the magnitude of director decreases with each time step as shown in fig. 3.3.

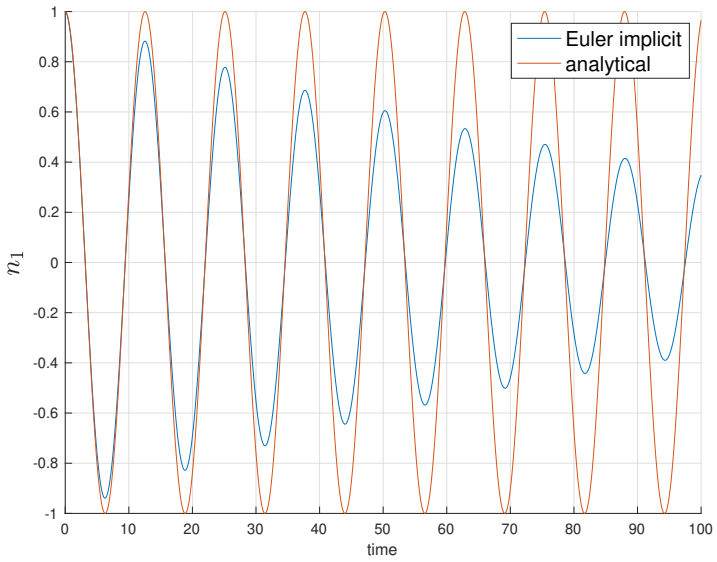

Figure 3.3. Comparison of the evolution of n_1 predicted analytically and numerically with the first order backward Euler scheme. The variation of n_2 is analogous and thus not shown here.

3.2.4 Crank-Nicholson scheme

As shown in the previous sections, the first order Euler schemes are inappropriate to model the evolution of the director field, since these approaches cannot maintain $|\boldsymbol{n}|^2 = 1$. Therefore, we investigate the performance of the second-order Crank-Nicholson scheme [148]. If the components of $\boldsymbol{n}$ are known at the kth time level, then the director orientation at the next time step is calculated as

$$n_1^{k+1} = \frac{(4-a^2)n_1^k + 4an_2^k}{4+a^2}, \tag{3.8a}$$

$$n_2^{k+1} = \frac{(4-a^2)n_2^k - 4an_1^k}{4+a^2}, \tag{3.8b}$$

where $a = \frac{\dot{\gamma}}{2}\Delta t$. Therefore, $(n_1^{k+1})^2 + (n_2^{k+1})^2 = (n_1^k)^2 + (n_2^k)^2$, so the Crank-Nicholson scheme maintains a constant director magnitude in a pure rotation.

3.3 Director normalisation

Examples above illustrate that among the time discretisation techniques available in OpenFOAM, only the Crank-Nicholson scheme maintains the constant director magnitude when $\boldsymbol{n}$ is subject to a pure rotation. In real flows, an accurate modelling of the director field requires to incorporate both extensional and elastic effects and $\boldsymbol{n}$ evolves as

$$\dot{\boldsymbol{n}} = \frac{\boldsymbol{h} - \boldsymbol{nn}\cdot\boldsymbol{h}}{\gamma_1} - \frac{\gamma_2}{\gamma_1}(\boldsymbol{n}\cdot\boldsymbol{D} - \boldsymbol{nnn}:\boldsymbol{D}) + \boldsymbol{n}\cdot\boldsymbol{\omega}. \tag{3.9}$$

By taking the scalar product of the above equation with $\boldsymbol{n}$, we obtain the evolution equation for the director magnitude

$$\frac{1}{2}\frac{D|\boldsymbol{n}|^2}{Dt} = (1-|\boldsymbol{n}|^2)\left[\frac{\boldsymbol{n}\cdot\boldsymbol{h}}{\gamma_1} - \frac{\gamma_2}{\gamma_1}\boldsymbol{n}\cdot\boldsymbol{D}\right]. \tag{3.10}$$

Provided that the initial director field is of unit magnitude everywhere in the domain, the inclusion of $\boldsymbol{nnn}\cdot\boldsymbol{D}$ and $\boldsymbol{nn}\cdot\boldsymbol{h}$ is supposed to ensure that $|\boldsymbol{n}|^2 = 1$. However, due to the finite computer precision, the director magnitude need not be identically one after each time step, and the term $(1-|\boldsymbol{n}|^2)\left[\frac{\boldsymbol{n}\cdot\boldsymbol{h}}{\gamma_1} - \frac{\gamma_2}{\gamma_1}\boldsymbol{n}\cdot\boldsymbol{D}\right]$ can alter the director's magnitude. The round-off errors may propagate further, violating the requirement of a unit-length director field. For that reason, the OpenFOAM solver described in section 3.1 re-normalises the magnitude of the director field after each iteration.

3.4 Solver validation

Validation of the full Leslie-Ericksen model is undertaken by analysing the steady-state flow of nematic liquid crystal through a straight pipe with homeotropic boundary conditions (fig. 3.4). The analytical solution at $Er << 1$ is compared with the numerical predictions.

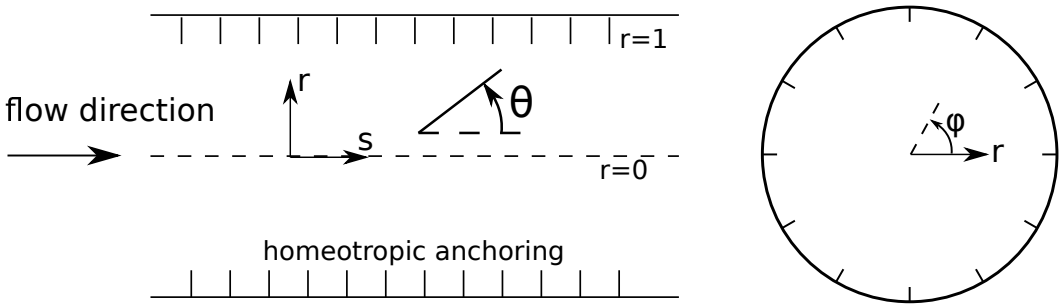

Figure 3.4. Fully developed, steady-state, straight pipe flow is considered in this section.

3.4.1 Analytical solution

Angular momentum

The director orientation is governed by the angular momentum balance in the Leslie-Ericksen theory

$$\frac{\boldsymbol{h}-\boldsymbol{nn}\cdot\boldsymbol{h}}{\gamma_1} - Er\left(\frac{\gamma_2}{\gamma_1}(\boldsymbol{n}\cdot\boldsymbol{D}-\boldsymbol{nnn}:\boldsymbol{D}) - \boldsymbol{N}\right) = 0, \tag{2.83}$$

where γ_i are dimensionless coefficients and $\boldsymbol{h}$, $\boldsymbol{D}$ represent dimensionless molecular field and strain rate tensors respectively. At finite Ericksen numbers, the system is fully non-linear and intractable. Therefore, we focus on the $Er << 1$ limit (the director orientation is not affected by the flow and the steady-state director configuration minimises the free energy),

where the steady-state director balance simplifies to

$$\boldsymbol{h} - \boldsymbol{n}\boldsymbol{n} \cdot \boldsymbol{h} = 0. \tag{3.11}$$

In the one-constant approximation, the dimensionless molecular field reads

$$\boldsymbol{h} = \nabla^2 \boldsymbol{n}. \tag{3.12}$$

At the boundary ($r = \frac{r^*}{R^*} = 1$), the director is anchored normal to the wall direction

$$\boldsymbol{n} = [n_r,\ n_\phi,\ n_s] = [-1,\ 0,\ 0], \tag{3.13}$$

where n_r, n_ϕ, n_s are radial, tangential and axial components of the director respectively. We assume that the steady-state solution is axisymmetric, so the $n_\phi = 0$. The solution of eq. (3.11) was presented in [149, 150] and reads

$$[n_r,\ n_\phi,\ n_s] = [-\sin\theta,\ 0,\ \cos\theta], \tag{3.14}$$

where

$$\theta = \pi - 2\tan^{-1}\left(\frac{R^*}{r^*}\right), \tag{3.15}$$

is schematically denoted in fig. 3.4. Components of the director field are plotted in fig. 3.5. The director escapes from the radial direction at the wall into the axial direction at the pipe axis, hence the configuration shown in fig. 3.6 is called an escaped solution [43].

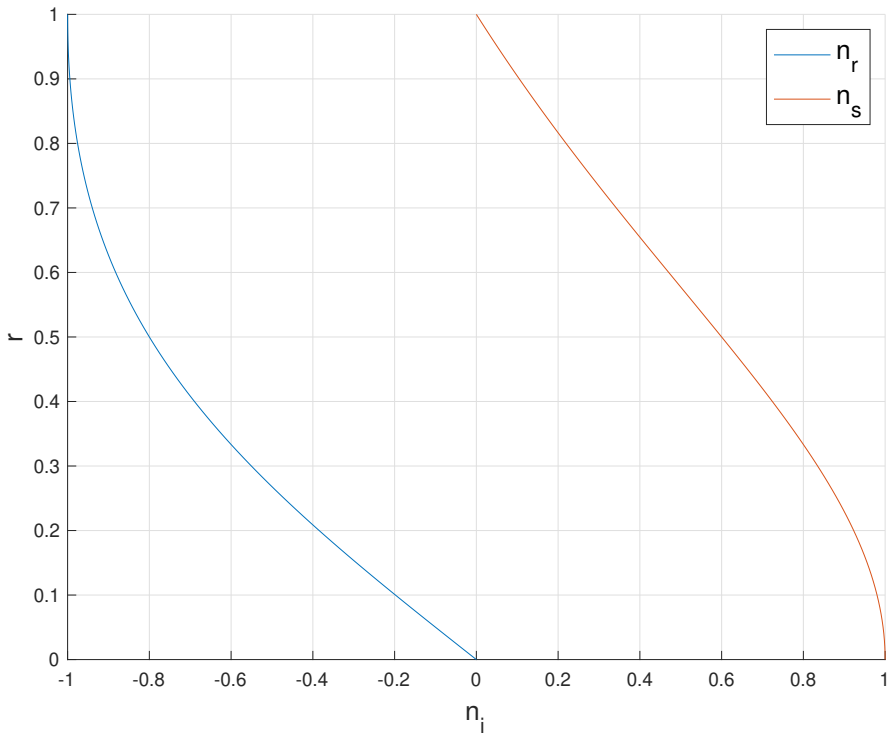

Figure 3.5. Variation of radial and axial components of the director.

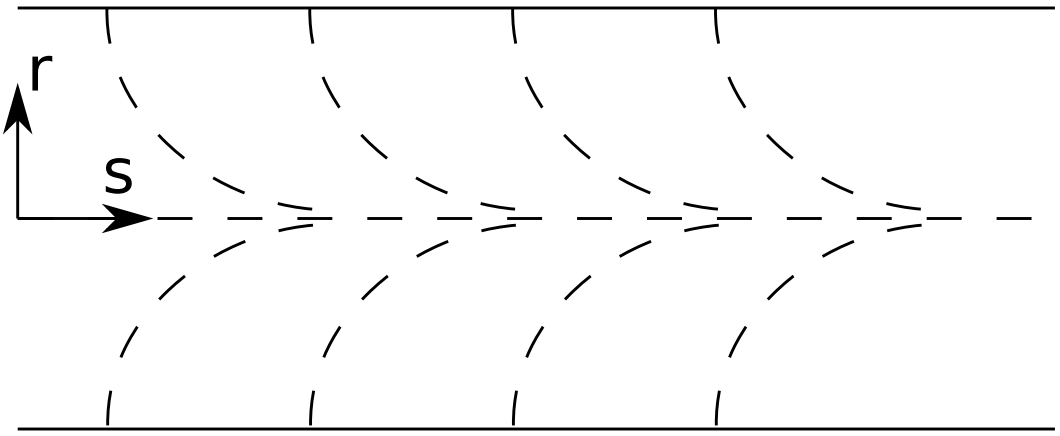

Figure 3.6. Director field in the limit of zero Ericksen number.

Linear momentum

Even in the limit of $Er << 1$, the analytical solution of the momentum balance is not obtainable for an arbitrary set of Leslie viscosities α_i. For typical liquid crystals [21, 43]

$$|\alpha_1| \approx |\alpha_3| \approx |\alpha_6| << |\alpha_2| \approx |\alpha_5| = O(1), \tag{3.16}$$

so in order to obtain the analytical solutions we assume that

$$\alpha_1 = \alpha_3 = \alpha_6 = 0, \qquad \alpha_2 = -\alpha_5. \tag{3.17}$$

The above assumption enables to obtain an analytical solution for the flow of the Leslie-Ericksen fluid at a low Ericksen number, and the velocity profile is given by

$$\begin{aligned}\frac{v_s^*}{2\frac{\partial p^*}{\partial s^*}\frac{(r_0^*)^2}{\alpha_4^*}} &= \frac{1-r^2}{4} - \frac{1}{2}\alpha_2 \ln\left(1 + r^4 + (-4\alpha_2 + 2)r^2\right) \\ &+ \tanh^{-1}\left(\frac{r^2 - 2\alpha_2 + 1}{2\sqrt{\alpha_2(\alpha_2 - 1)}}\right)\frac{\alpha_2^2 - \frac{1}{2}\alpha_2}{\sqrt{\alpha_2(\alpha_2 - 1)}} \\ &+ \tanh^{-1}\left(\frac{\alpha_2 - 1}{\sqrt{\alpha_2(\alpha_2 - 1)}}\right)\frac{\alpha_2^2 - \frac{1}{2}\alpha_2}{\sqrt{\alpha_2(\alpha_2 - 1)}} + \frac{\alpha_2[2\ln(2) + \ln(-\alpha_2 + 1)]}{2}\end{aligned} \tag{3.18}$$

where the full derivation of eq. (3.18) is presented in the appendix A.2 and the starred variables refer to dimensional quantities, $\alpha_i = 2\frac{\alpha_i^*}{\alpha_4^*}$ are dimensionless viscosities. The inclusion of the non-Newtonian contribution makes the material more viscous in the regions where the director is parallel to the velocity gradient direction. Hence, the effective viscosity is the largest at the wall and the smallest at the pipe axis (fig. 3.7). The difference between maximum and minimum viscosities depends on α_2; as $|\alpha_2|$ increases, the shear-thinning effects are more pronounced and the peak velocity is higher (fig. 3.8). For low Ericksen number

flows, the effective viscosity can be calculated from the analytical velocity profile

$$\eta_{eff} = \frac{2\eta^*_{eff}}{\alpha_4} = -\frac{8}{\bar{v^*_s} R^{*2}} \frac{\partial p^*}{\partial s^*}, \tag{3.19}$$

where

$$\bar{v^*} = \frac{1}{\pi R^2} \int_{\phi=0}^{2\pi} \int_{r=0}^{R} v^*_s(r) r dr, \tag{3.20}$$

is the mean velocity. The effective viscosity as a function of α_2 is plotted in fig. 3.9 and indicates that η_{eff} increases linearly with $|\alpha_2|$. That is also the case in a channel flow with homeotropic anchoring; however, since the director aligns with the velocity gradient everywhere in the domain, the increase in the effective viscosity is more significant than in a pipe flow (fig. 3.9).

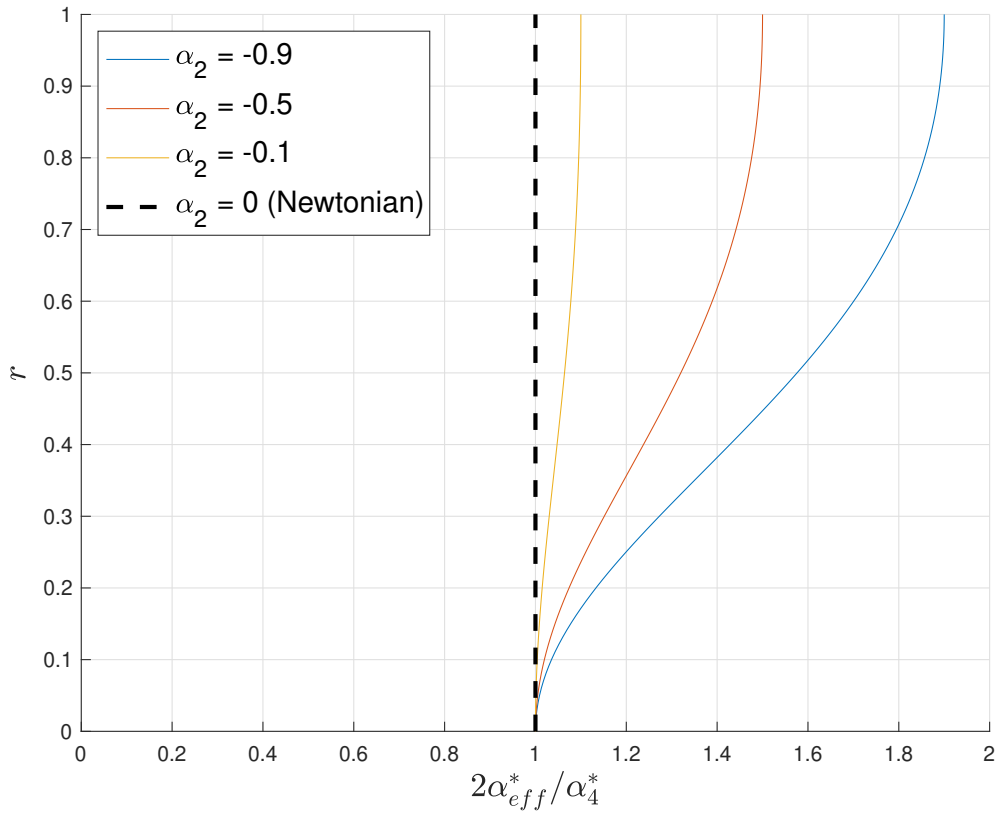

Figure 3.7. Distribution of dimensionless effective viscosity for a range of α_2.

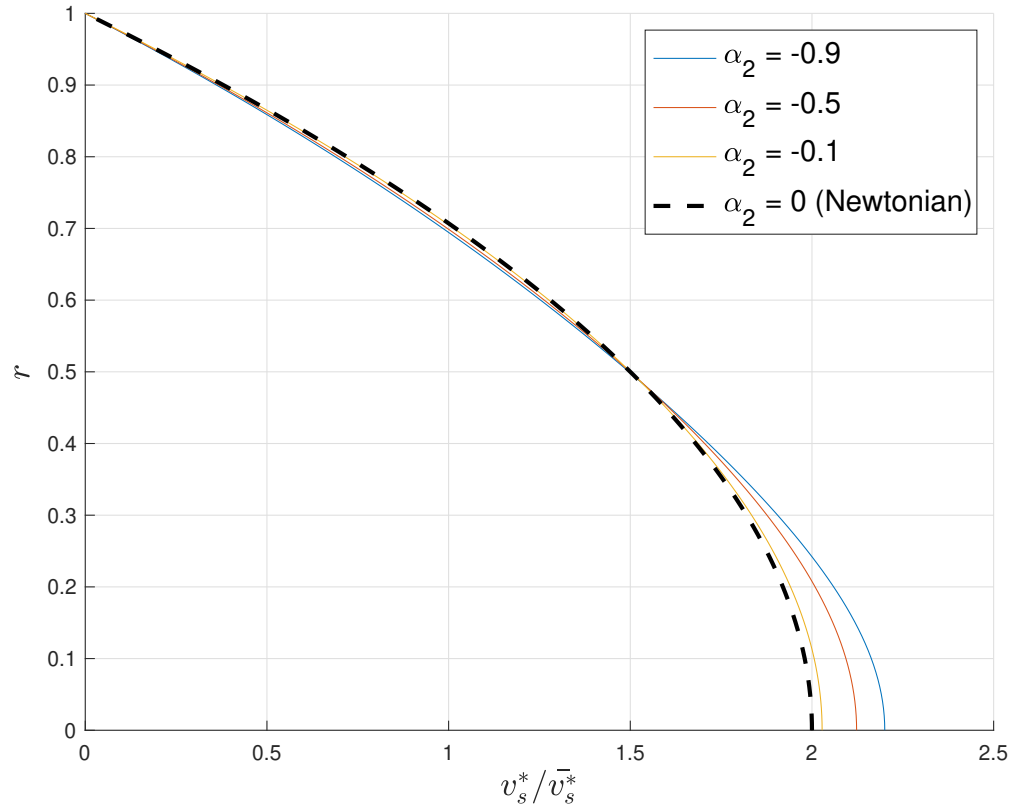

Figure 3.8. Velocity profile for a range of α_2. $\bar{v_s}$ represents the mean streamwise velocity.

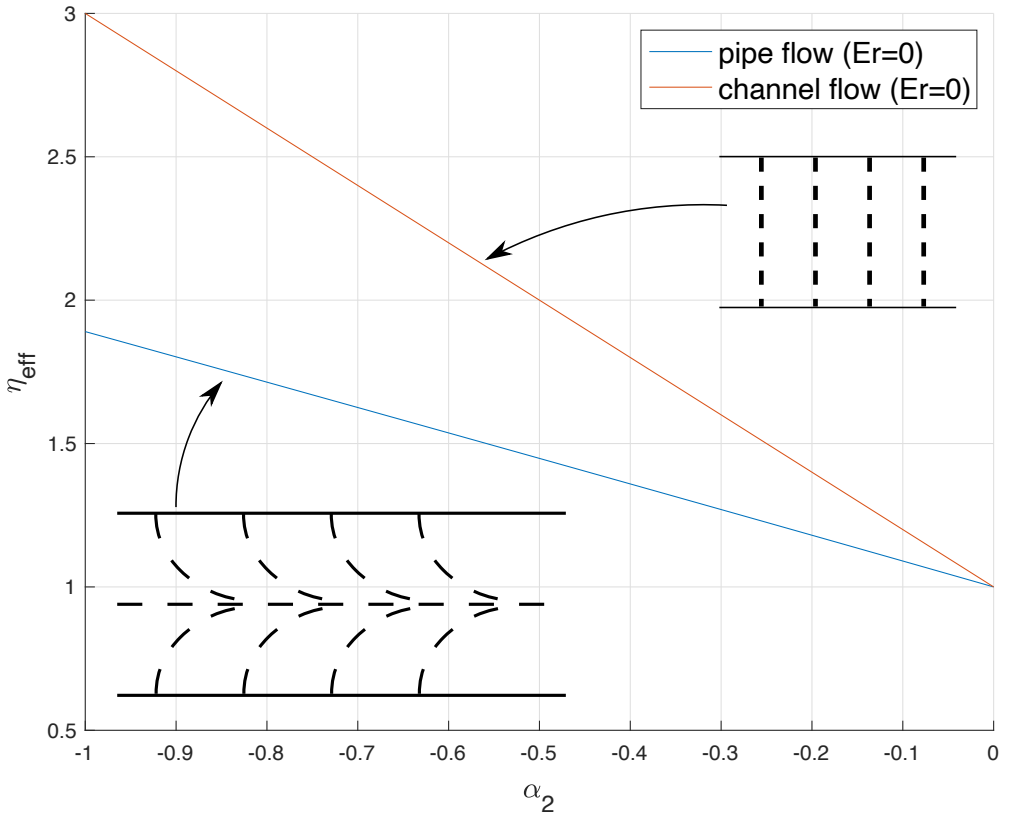

Figure 3.9. Effective viscosity as a function of α_2 in a capillary and channel flows in the limit of $Er \rightarrow 0$. The effective viscosity in a channel flow is given by $\eta_{eff} = \frac{-\alpha_2+\alpha_4+\alpha_5}{2}$.

The non-Newtonian contribution also affects the distribution of normal stresses. The viscous component of the first normal stress difference is given by

$$N_1 = -\alpha_2 n_r n_s \frac{\partial v_s}{\partial r}. \tag{A.8}$$

In the low Er limit $\boldsymbol{n}$ is independent of α_2 and the velocity profile depends at most only weakly on α_2, so the peak of N_1 is predominantly determined by the magnitude of α_2, as shown in fig. 3.10. The second normal stress difference is given by

$$N_2 = \frac{2\alpha_1 n_r^2 + \alpha_2 + \alpha_3 + \alpha_5 + \alpha_6}{2} \frac{\partial v_s}{\partial r} \tag{3.21}$$

and therefore due to the simplification (3.17), $N_2 = 0$ for the set of parameters chosen in this section. For materials where eq. (3.17) is not satisfied, the second normal stress difference need not be zero, but its magnitude is usually much smaller than N_1 [15].

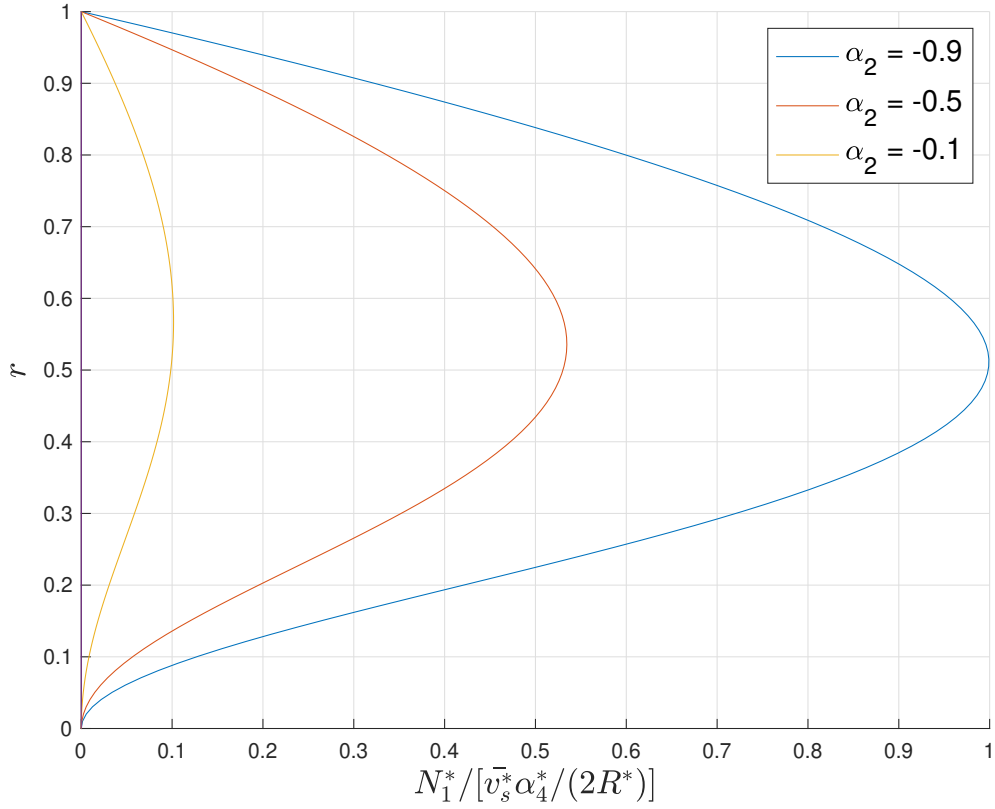

Figure 3.10. Distribution of the viscous component of the first normal stress difference for a range of α_2.

3.4.2 Verification of the numerical solution

The solver described in section (3.1) is verified by comparing the numerical results with the benchmark analytical solution. We assume that the fluid is stationary and use homeotropic anchoring for the director field. A cyclic boundary condition is implemented at the inlet and outlet by neglecting the director and velocity gradients in the stream-wise direction. The fixed pressure gradient is chosen to set $Er = 0.001$, as a representative case for the low Ericksen

number limit. The cyclic boundary condition enables us to use a mesh with a single unit cell in the flow direction, as shown in fig. 3.11. Spatial gradients are discretised through a second-order central differencing scheme with an absolute convergence criteria for velocity, pressure and director set to 10^{-6}. Computations are initialised with zero velocity and the director field oriented in the axial direction $\boldsymbol{n} = [n_r,\ n_\phi,\ n_s] = [0,\ 0,\ 1]$

Grid refinement study

The mesh refinement of the capillary geometry considered in this section is controlled by the parameters c_1 and c_2, schematically depicted in fig. 3.11. We conduct the grid refinement study by considering three meshes with different cell densities:

- M_1 with $c_1 = 8$ and $c_2 = 16$, giving $N = 576$ cells in total;
- M_2 with $c_1 = 16$ and $c_2 = 32$, giving $N = 2304$ cells in total;
- M_3 with $c_1 = 32$ and $c_2 = 64$, giving $N = 9216$ cells in total.

Numerical predictions of director, velocity and normal stress profiles collapse on the same curve as the corresponding analytical solutions (fig. 3.5, 3.8 and 3.10) even on the coarse M_1 mesh. We quantify the convergence of the numerical solution through the normalised l^2-norm [151]

$$E(\text{Sol}_{\text{numerical}}) = \sqrt{\frac{\sum(\text{Sol}_{\text{analytical}} - \text{Sol}_{\text{numerical}})^2}{\sum(\text{Sol}_{\text{analytical}})^2}}. \tag{3.22}$$

The relative errors in the prediction of θ, v_s and N_1 are compared in table 3.1 and indicate that as the mesh density increases, the numerical solution is closer to the reference analytical solution. Therefore, we conclude that the solver was implemented correctly.

Table 3.1. Relative errors obtained on meshes $M_1 - M_3$ for $\alpha_2 = -0.5$.

	Relative error M_1	Relative error M_2	Relative error M_3
θ	$5.6 \cdot 10^{-3}$	$1.6 \cdot 10^{-3}$	$9.2 \cdot 10^{-4}$
v_s	$8.1 \cdot 10^{-3}$	$6.4 \cdot 10^{-3}$	$2.4 \cdot 10^{-3}$
N_1	$6.3 \cdot 10^{-2}$	$3.9 \cdot 10^{-3}$	$3.1 \cdot 10^{-3}$

3.4.3 Convergence rate

The convergence time varies depending on the mesh refinement. When the computations run on four cores in parallel, the simulation converges in around 30 minutes, three hours, and 16 hours for the M_1, M_2 and M_3 grids. The calculation requires about $60 \cdot 10^{12}$ floating point operations on the M_1 mesh. The convergence history of v_s and θ in the M_1 grid is shown in fig. 3.12 and the convergence plots for M_2 and M_3 meshes are qualitatively similar and not shown. The computation time on M_2 and M_3 meshes can be reduced by employing the *mapFields* utility [107], which allows to map inputs (velocity, pressure, director fields)

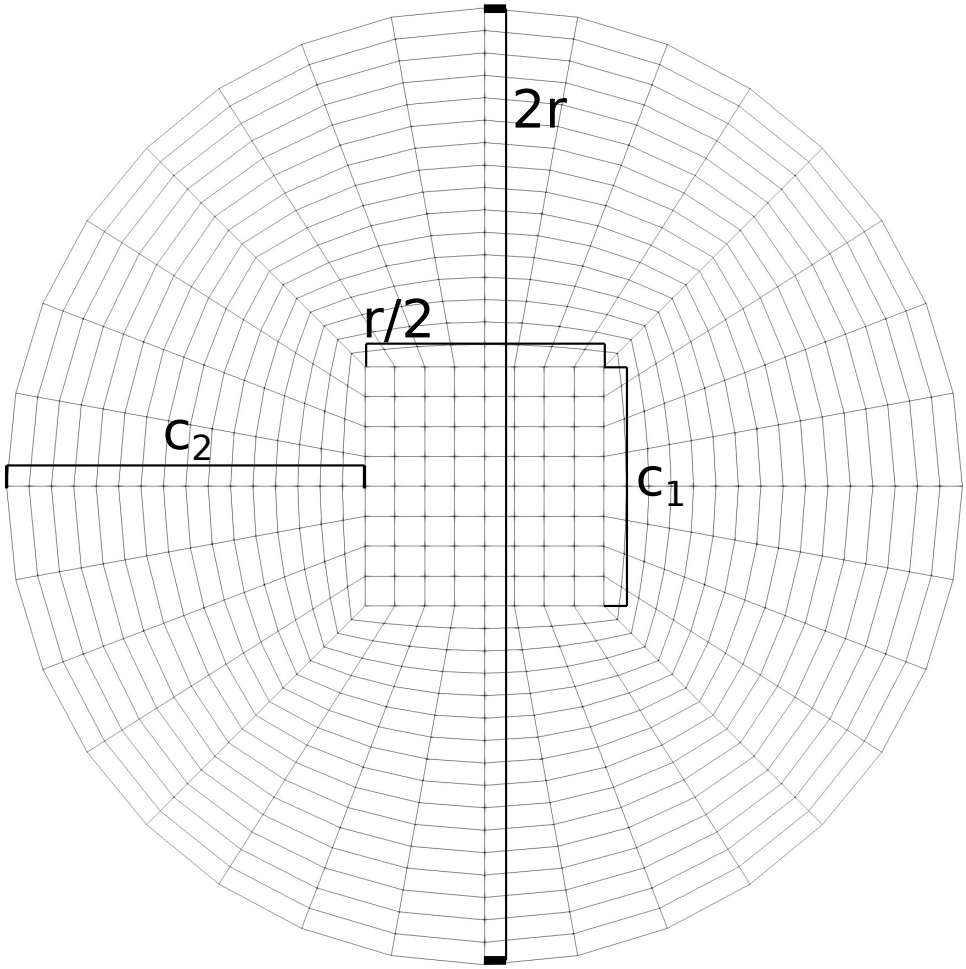

Figure 3.11. Grid used for the mesh refinement study.

between different meshes. The computational cost of the simulation on the M_2 mesh can be decreased by initialising the relevant variables with the solution obtained on the coarse M_1 grid. An analogous procedure can be repeated on the most refined grid. The *mapFields* utility will be exploited in further chapters when dealing with more complex geometries.

3.4.4 Alternative validation approaches

The solver presented in this chapter was validated in the limit of weak flow, where the director orientation is only affected by elastic effects, and hence the director-flow cross-coupling has not been tested. Therefore, a further solver validation could involve other potential test cases:

- High Ericksen number shear flow to examine whether the director aligns at a Leslie angle to the flow direction.
- Low Ericksen number channel flow with a wall-parallel anchoring. Since the director is nearly horizontal, the velocity profile remains parabolic, while the flow causes minor director distortions. This method of solver validation was presented in [151].
- Comparison with analytical solutions for the backflow effect [43].

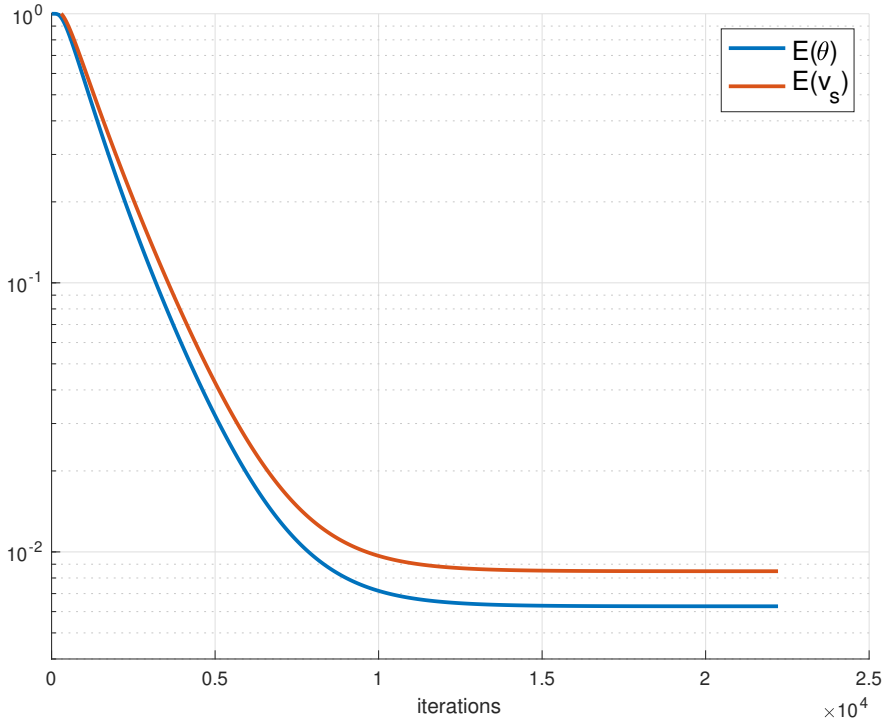

Figure 3.12. Convergence of the relative velocity error.

- Comparison with other solvers, which use alternative solution techniques, for example the lattice Boltzmann [142], or the finite element method [152].

Chapter 4

Flow of liquid crystals in straight pipes

Straight pipes are the fundamental element of any piping system. Their presence has a gross effect on the pressure drops encountered in process equipment, based on which pipework is chosen. Understanding the fluid rheology in this simple configuration is the first step towards validating model predictions against experiments. In this chapter, we examine the predictions of the nematodynamic equations (TIF, LE, BE models) in straight pipes (fig. 4.1) with wall parallel and homeotropic boundary conditions. The straight pipe configuration is also a precursor for the curved pipe flow, which is discussed in the next chapter; some of the conclusions made in subsequent sections of this chapter are also applicable to more complex geometries.

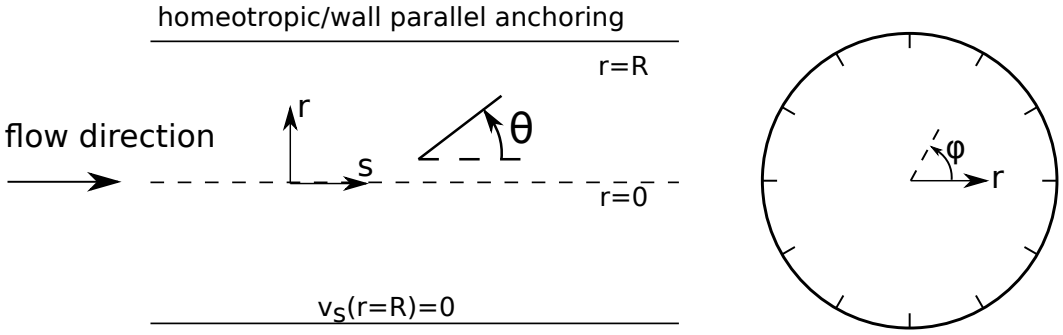

Figure 4.1. Geometry considered in this chapter: a straight pipe with no-slip boundary condition on the wall. Homeotropic and wall-parallel director boundary conditions are considered. Throughout the simulations we employ a fixed pipe radius $R = 1$ mm.

4.1 Transversely isotropic fluid

Since the TIF model does not contain an elasticity contribution, its predictions are independent of the anchoring type. In steady-state capillary flow, the stress field is axisymmetric, the secondary motion vanishes so we are interested in the streamwise component of the momentum balance [18]

$$\frac{\partial p}{\partial s} = \frac{\partial \tau_{rs}}{\partial r} + \frac{\tau_{rs}}{r}, \tag{4.1}$$

where $\frac{\partial p}{\partial s}$ is the streamwise pressure gradient and τ_{rs} is the shear component of the stress tensor. The TIF model neglects elastic stresses, so $\boldsymbol{\tau}$ has only a viscous contribution and is

given by

$$\boldsymbol{\tau} = 2\mu\boldsymbol{D} + 2\mu_1\boldsymbol{D} : \boldsymbol{nnnn} + \mu_2(\boldsymbol{nn}\cdot\boldsymbol{D} + \boldsymbol{D}\cdot\boldsymbol{nn}), \tag{2.27}$$

where μ_i are material viscosities. The director orientation $\boldsymbol{n}$ is calculated from the angular momentum equation

$$\dot{\boldsymbol{n}} - \boldsymbol{n}\cdot\boldsymbol{\omega} + \lambda(\boldsymbol{n}\cdot\boldsymbol{D} - \boldsymbol{nnn} : \boldsymbol{D}) = 0, \tag{2.29}$$

where λ is a tumbling parameter. The solution of the angular momentum equation (2.29) is given by [15]

$$\boldsymbol{n}(r \neq 0, \phi) = [n_r, n_\phi, n_s] = \left[-\sqrt{\frac{\lambda-1}{2\lambda}}, 0, \sqrt{\frac{\lambda+1}{2\lambda}}\right], \tag{4.2}$$

hence, the shear component of the stress reads

$$\tau_{rs} = \left(\mu + 2\mu_1 \left(n_r n_s\right)^2 + \frac{\mu_2}{2}\right)\frac{\partial v_s}{\partial r}. \tag{4.3}$$

Since the director orientation does not change, the term $\mu + 2\mu_1 \left(n_r n_s\right)^2 + \frac{\mu_2}{2}$ is constant and can be treated as a modified Newtonian viscosity. Implementing the no-slip boundary condition $v_s(r = R) = 0$, the velocity profile is given by

$$v_s = \left(\mu + 2\mu_1 \left(n_r n_s\right)^2 + \frac{\mu_2}{2}\right)\frac{\partial p}{\partial s}\frac{R^2}{4}\left[\left(\frac{r}{R}\right)^2 - 1\right], \tag{4.4}$$

which is the same as for isotropic, constant viscosity fluids. However, in contrast to the Newtonian approximation, the TIF model introduces non-zero normal stress differences

$$N_1 = -2\mu_1 n_r n_s (n_r^2 - n_s^2)\frac{\partial v_s}{\partial r}, \tag{4.5a}$$

$$N_2 = (2\mu_1 n_r^2 + \mu_2) n_r n_s \frac{\partial v_s}{\partial r}. \tag{4.5b}$$

The presence of normal stresses does not affect the flow in a straight pipe, however as will be shown in the next chapter, N_1 and N_2 control the secondary motion in curved pipes [24, 153, 154].

4.2 Leslie-Ericksen and Beris-Edwards models

In contrast to the transversely isotropic fluid model, the Leslie-Ericksen and Beris-Edwards theories account for microstructure elasticity, and the orientation of rod-like particles is governed by the competition of static and hydrodynamic effects. Each of the models introduces

a viscoelastic stress

$$\begin{aligned}\boldsymbol{\tau}^{LE} = \alpha_1 \boldsymbol{nnnn} : \boldsymbol{D} + \alpha_2 \boldsymbol{nN} + \alpha_3 \boldsymbol{Nn} + \alpha_4 \boldsymbol{D} + \alpha_5 \boldsymbol{nn} \cdot \boldsymbol{D} + \alpha_6 \boldsymbol{D} \cdot \boldsymbol{nn} \\ -K \nabla \boldsymbol{n} \cdot (\nabla \boldsymbol{n})^T,\end{aligned} \tag{4.6}$$

$$\begin{aligned}\boldsymbol{\tau}^{BE} = \mu \boldsymbol{D} - \xi \left[(\boldsymbol{Q} + \frac{\boldsymbol{I}}{3}) \cdot \boldsymbol{H} + \boldsymbol{H} \cdot (\boldsymbol{Q} + \frac{\boldsymbol{I}}{3}) - 2(\boldsymbol{Q} + \frac{\boldsymbol{I}}{3})(\boldsymbol{H} : \boldsymbol{Q}) \right] \\ + \boldsymbol{H} \cdot \boldsymbol{Q} - \boldsymbol{Q} \cdot \boldsymbol{H} - K^Q \frac{\partial Q_{kl}}{\partial x_i} \frac{\partial Q_{kl}}{\partial x_j},\end{aligned} \tag{4.7}$$

which is computed from the solution of the angular momentum equation describing the orientation and degree of alignment within the microstructure:

$$\frac{\boldsymbol{h} - \boldsymbol{nn} \cdot \boldsymbol{h}}{\gamma_1} - \frac{\gamma_2}{\gamma_1} (\boldsymbol{n} \cdot \boldsymbol{D} - \boldsymbol{nnn} : \boldsymbol{D}) - \boldsymbol{N} = 0, \tag{4.8a}$$

$$\frac{D\boldsymbol{Q}}{Dt} = \boldsymbol{S} + \Gamma \boldsymbol{H}, \tag{4.8b}$$

where $\boldsymbol{h} = -\frac{\delta f_d}{\delta \boldsymbol{n}}$ and $\boldsymbol{H} = -\frac{\delta f_{LdG}}{\delta \boldsymbol{Q}} + \underline{\frac{1}{3} \operatorname{tr} \frac{\delta f_{LdG}}{\delta \boldsymbol{Q}}}$ measure the configurational departure of $\boldsymbol{n}$ or the $\boldsymbol{Q}$ from the minimum Helmholtz free energy. We consider the one-constant approximation, with the nematic energies given by

$$f_d = \frac{1}{2} K (\boldsymbol{\nabla n}) : (\boldsymbol{\nabla n})^T, \tag{4.9}$$

$$\begin{aligned}f_{LdG} &= f_d^Q + f_{nematic} \\ &= \frac{1}{2} K^Q Q_{ik,j} Q_{ik,j} + \frac{a}{2} \operatorname{tr}(\boldsymbol{Q} \cdot \boldsymbol{Q}) - \frac{b}{3} \operatorname{tr}(\boldsymbol{Q} \cdot \boldsymbol{Q} \cdot \boldsymbol{Q}) + \frac{c}{4} \operatorname{tr}^2(\boldsymbol{Q} \cdot \boldsymbol{Q}),\end{aligned} \tag{4.10}$$

where K is the Frank elastic constant and a, b, c are coefficients in the expansion of the bulk energy density; $\boldsymbol{S}$ expresses the contribution of hydrodynamic effects acting on the $\boldsymbol{Q}$-tensor field

$$\boldsymbol{S} = (\xi \boldsymbol{D} - \boldsymbol{\Omega})(\boldsymbol{Q} + \frac{\boldsymbol{\delta}}{3}) + (\boldsymbol{Q} + \frac{\boldsymbol{\delta}}{3})(\xi \boldsymbol{D} + \boldsymbol{\Omega}) - \underline{2\xi (\boldsymbol{Q} + \frac{\boldsymbol{\delta}}{3}) \operatorname{tr}(\boldsymbol{Q} \cdot \boldsymbol{\nabla u})}. \tag{4.11}$$

Material parameters used in the Beris-Edwards model are similar to those used in [155]:

- The Frank constant $K^Q = 40$ pN.
- The tumbling parameter in the BE model $\xi = 1.02$.
- The relaxation parameter $\Gamma = 7.29\ (\text{Pa} \cdot \text{s})^{-1}$.
- The Newtonian viscosity $\mu = 0.2$ Pa $\cdot$ s.

We consider two sets of bulk free energy density coefficients

- Set 1: $a = -2 \cdot 10^{-3} \frac{\text{MJ}}{\text{m}^3}$, $b = 4 \cdot 10^{-2} \frac{\text{MJ}}{\text{m}^3}$, $c = 4 \cdot 10^{-2} \frac{\text{MJ}}{\text{m}^3} \rightarrow \xi_N \approx 3.9 \cdot 10^{-5}$ m and the equilibrium order parameter is $S_{eq} = 0.6208$ (eq. (2.67b)). These material parameters are representative for flows where the defect size is significantly smaller

than the characteristic geometry length-scale $\xi_N/R = 3.9 \cdot 10^{-2} << 1$. For thermotropic liquid crystals, the typical defect dimension is $O(\text{nm})$ [140], however this thesis aims to explore the rheology of lyotropic liquid crystals, where the defect size can be of larger magnitudes due to the inclusion of solid-like particles (bricks) that are used to provide a solid-like soap consistency.

- Set 2: $a = -2 \cdot 10^{-5} \frac{\text{MJ}}{\text{m}^3}$, $b = 4 \cdot 10^{-4} \frac{\text{MJ}}{\text{m}^3}$, $c = 4 \cdot 10^{-4} \frac{\text{MJ}}{\text{m}^3} \rightarrow \xi_N \approx 3.9 \cdot 10^{-4}$ m and $S_{eq} = 0.6208$. These parameters are representative for flows where the defect size is of a comparable magnitude as the geometry length-scale $\xi_N/R = 3.9 \cdot 10^{-1}$.

Throughout the calculations, the Ericksen number is defined as

$$Er = \frac{\bar{v} R \alpha_4}{K}, \tag{4.12}$$

where $\bar{v}$ denotes the mean stream-wise velocity and the pipe radius R is chosen as the geometry length-scale. K and α_4 are Frank constant and the Newtonian Leslie viscosity, both of which are required in the Leslie-Ericksen theory. The Frank constant can be mapped between LE and BE models through eq. (2.61) and is given by $K = 2S_{eq}^2 K^Q = 30.8$ pN. Leslie viscosities are calculated via eq. (2.75): $\alpha_1 = -0.1445$ Pa $\cdot$ s, $\alpha_2 = -0.1287$ Pa $\cdot$ s, $\alpha_3 = -0.023$ Pa $\cdot$ s, $\alpha_4 = 0.2091$ Pa $\cdot$ s, $\alpha_5 = 0.1757$ Pa $\cdot$ s, $\alpha_6 = 0.0239$ Pa $\cdot$ s.

The Ericksen number in the BE model is defined as

$$Er_{BE} = \left[\mu + \frac{4}{9}(1 - S^2)^2 \xi^2 \frac{1}{\Gamma} \right] \frac{\bar{v} R}{2 K^Q S_{eq}^2}, \tag{4.13}$$

which ensures that in the uniaxial, constant order parameter limit, the same Ericksen number represents an identical partitioning of hydrodynamic and elastic contributions, which control microstructure orientation. Additionally, in case of the Beris-Edwards model, the relative importance of flow and bulk effects acting on the order parameter is quantified through the Deborah number

$$De = \frac{3\bar{v}}{(a + b + c) R \Gamma}. \tag{4.14}$$

Analytical solutions of the Leslie-Ericksen and Beris-Edwards theories are not possible due to the high degree of nonlinearity of these equations. For that reason, the governing equations in the LE and BE models are solved numerically on the M_3 grid discussed in the previous chapter (fig. 3.11). The cyclic boundary condition on the inlet and outlet is employed, enabling use of a single cell in the axial direction, thus reducing the computational cost of simulations. Spatial gradients are discretised through a second-order central differencing scheme with absolute convergence criteria for velocity, pressure and director set to 10^{-6}. Computations are initialised with zero velocity and horizontal director fields throughout the whole domain.

4.2.1 Homeotropic anchoring

Low Ericksen numbers

Computations are undertaken to describe the flow of the LE and BE fluids, as these equations are too complex to obtain an analytical solutions for both orientation and velocity distribution. Numerical calculations indicate that at low Er, the defect size plays a key role in determining the director configuration in the BE model. In the $\xi_N/R << 1$ limit:

- The $\boldsymbol{Q}$-tensor has a pair of repeating eigenvalues (fig. 4.2), indicating that the liquid crystal is uniaxial.
- The degree of molecular ordering is predominantly governed by $f_{nematic}$, which drives the liquid crystal towards the uniaxial state, as shown in fig. 4.3 (red line).
- The order parameter is controlled by the bulk contribution $f_{nematic}$, and apart from a thin near-wall layer ($0.85 \leq r/R \leq 1$), S does not vary significantly (fig. 4.4).
- The director points in the radial direction at the wall and escapes into the axial direction at the pipe axis (fig. 4.5). The behaviour is qualitatively similar to the Leslie-Ericksen theory, which is the uniaxial, constant order parameter limit of the BE model.

The configuration of the micostructure significantly differs when the defect size is of a comparable size to the geometry length-scale:

- The $\boldsymbol{Q}$-tensor has three distinct eigenvalues (fig. 4.2), meaning that the liquid crystal is not uniaxial, as in the case for $\xi_N/R << 1$.
- There is not enough space for the director to escape into the axial direction, so the Helmholtz free energy is minimised by reducing the order parameter near the axis, as shown in fig. 4.4.
- The director is oriented in the radial direction everywhere except from the pipe axis (fig. 4.5), where the vector corresponding to the non-repeating eigenvalue is parallel to the axial direction.
- The behaviour of the microstructure is schematically illustrated in fig. 4.6, where the liquid crystal transforms from uniaxial state at the wall to fully biaxial state at $r \approx 0.5$ (fig. 4.3) and back to a planar-uniaxial field at the core.

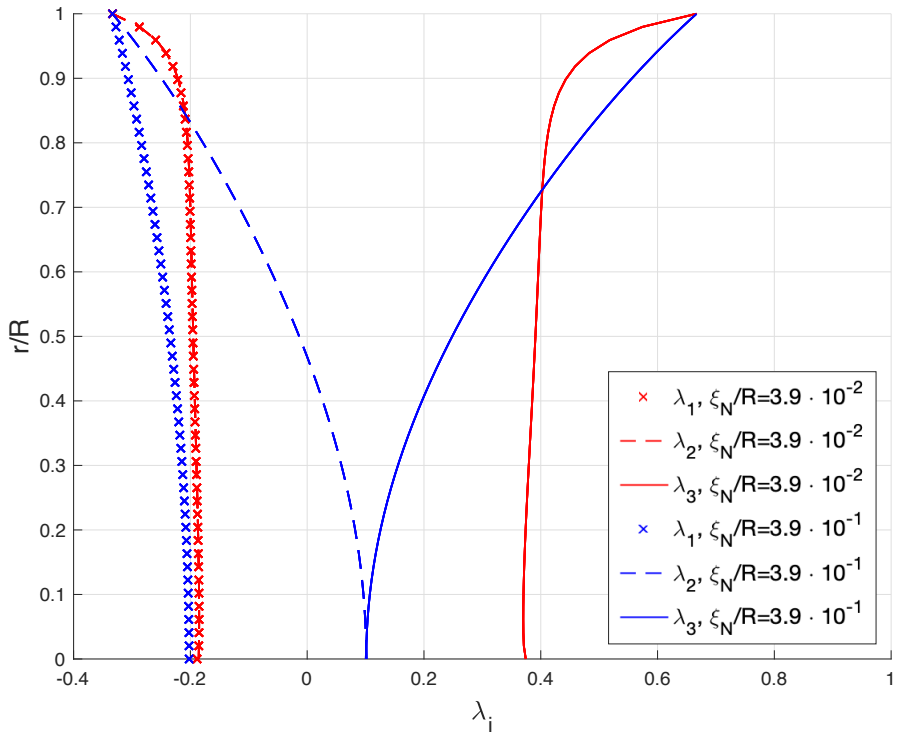

Figure 4.2. Distribution of eigenvalues for flows with different defect sizes. Red labels correspond to a uniaxial state, while at $\xi_N/R = 3.9 \cdot 10^{-1}$, the liquid crystal has three distinct eigenvalues and the system is in a biaxial state.

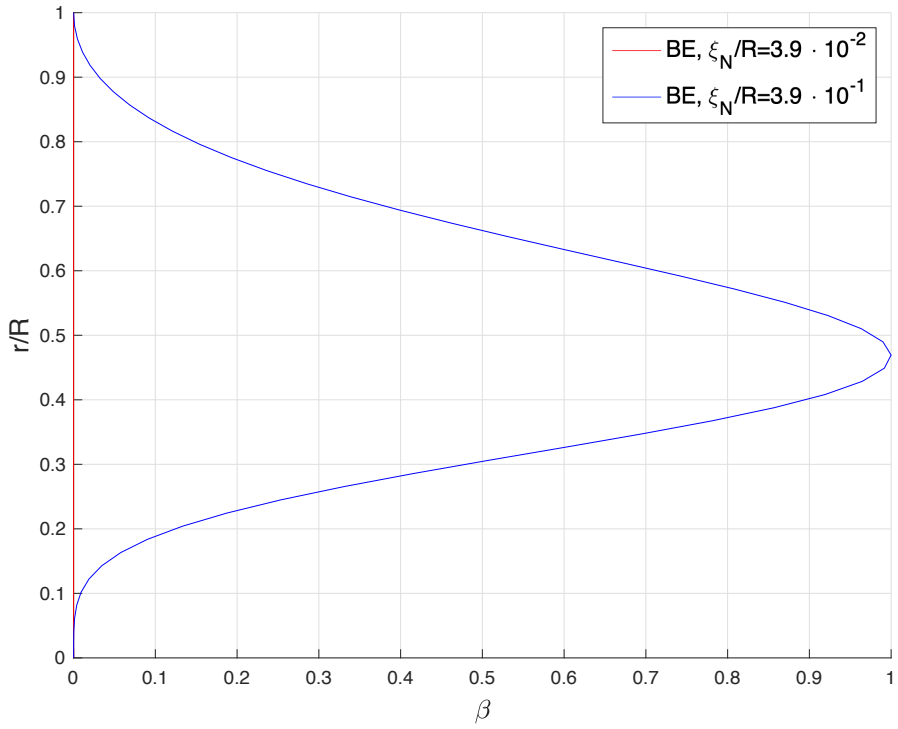

Figure 4.3. Biaxiality at different ξ_N/R

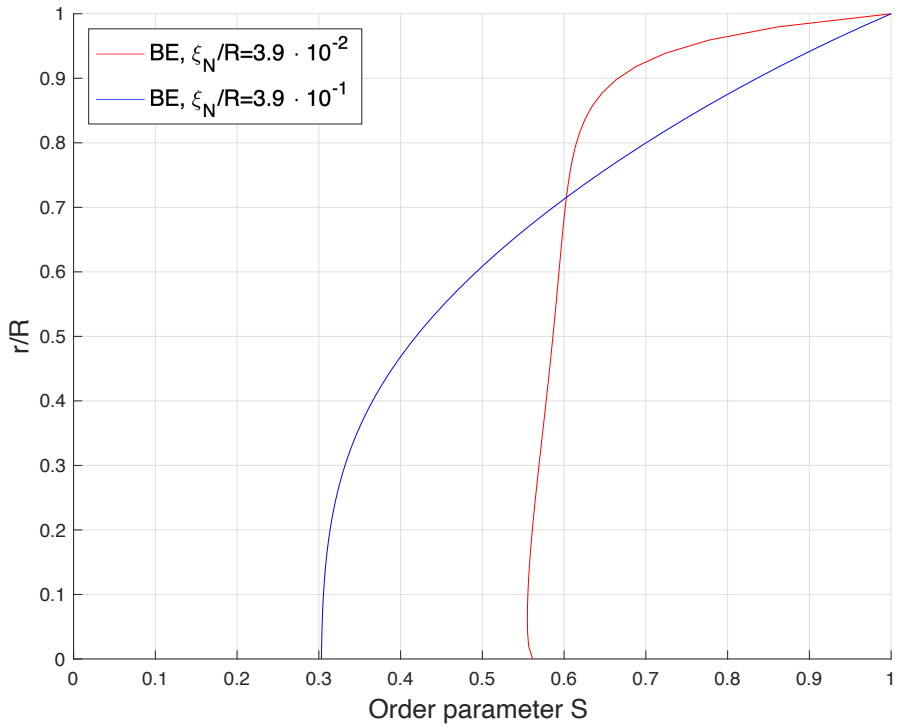

Figure 4.4. Order parameter $S = \sqrt{\frac{3}{2}}\sqrt{\lambda_1^2 + \lambda_2^2 + \lambda_3^2}$ at different ξ_N. Due to a decreasing shear rate near the pipe axis, the order parameter is governed by the bulk effects, which elevate the order parameter at $r = 0$.

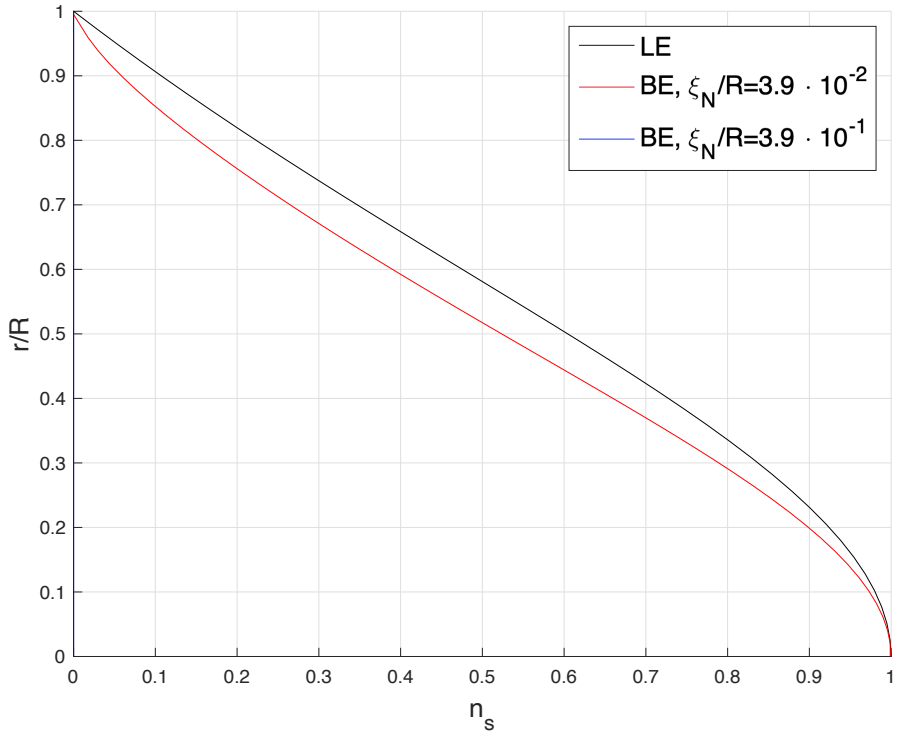

Figure 4.5. Predictions of the axial component of the director field at $Er = 0.05$. For $\xi_N/R = 3.9e - 1$ only the near wall director field can be represented as a vector and hence n_s near the axis is not shown.

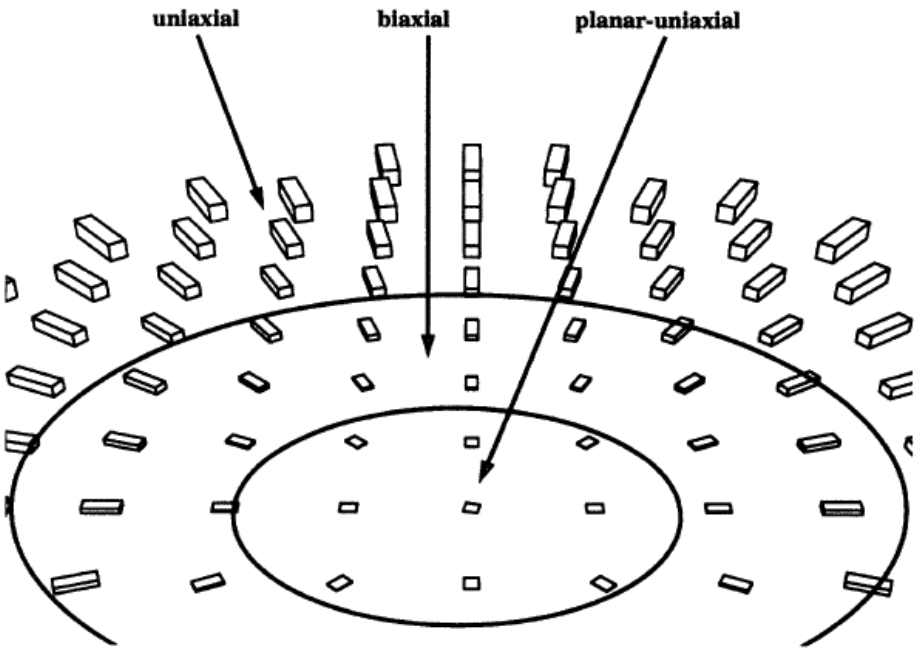

Figure 4.6. The planar-radial solution predicted in the nearly static configuration. The order parameter at the axis is negative meaning that the director lines in a plane normal to the pipe axis. Reprinted with permission from [135].

Despite the varying defect size and its implications on the microstructure, the velocity profiles are similar in all three cases analysed (fig. 4.7). The similarity between LE and BE model with $\xi_N/R << 1$ is expected since both represent a uniaxial liquid crystal with a constant (or nearly constant) order parameter. The director orientation at the wall is the same in all three cases considered: $\boldsymbol{n}$ is parallel to the velocity gradient direction, and the fluid is most viscous. However, depending on the relative magnitude of the defect size (ξ_N/R), the mechanism of shear-thinning differs; for $\xi_N/R << 1$, the shear-thinning occurs via the director reorientation and $\boldsymbol{n}$ aligns with the velocity direction at the pipe axis (fig. 4.5). In contrast, for larger ξ_N/R, the decrease in viscosity is predominantly caused by the reduction in the order parameter (fig. 4.4), which decreases the contribution of the non-Newtonian stresses.

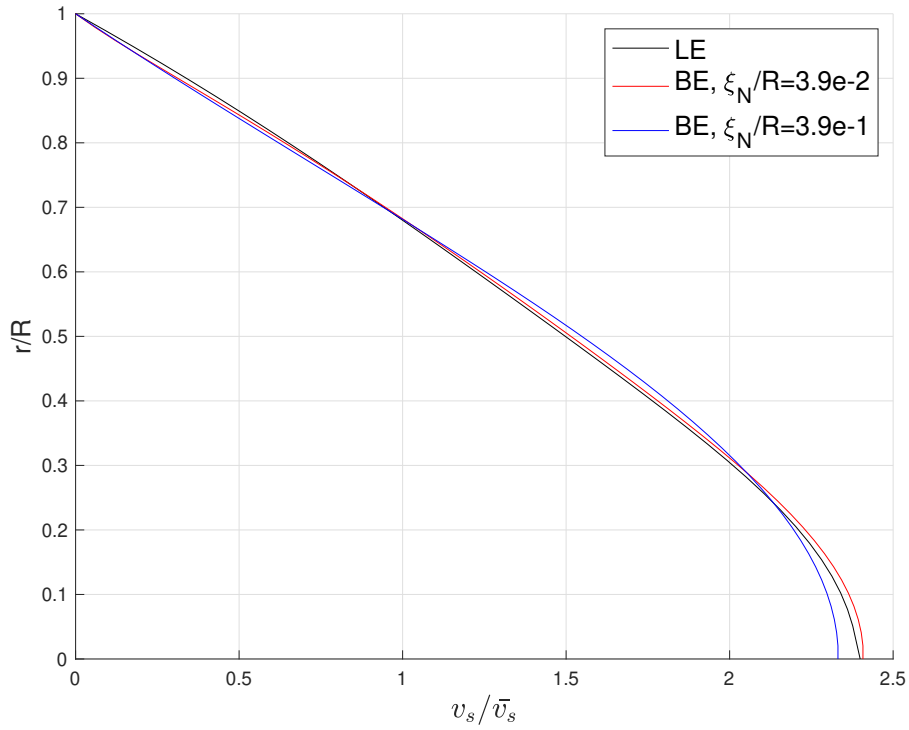

Figure 4.7. Predictions of the axial velocity at $Er = 0.05$.

The similarity of velocity profiles need not imply the similarity of normal stresses (fig. 4.8) and emphasise the complex nature of non-Newtonian fluids where normal stresses are also significant. The first normal stress difference $N_1 = \tau_{ss} - \tau_{rr}$ can be of the same order of magnitude as the shear stress, however it does not have any effect on the velocity distribution in a straight pipe [18]. The stress tensor in the LE and BE models has both viscous and elastic components and eq. (2.52) implies that the distribution of normal stresses strongly depends on the microstructure configuration, which is controlled by the defect size. When $\xi_N/R << 1$, the uniaxial limit is recovered, and the prediction of the BE model resembles the LE theory (fig. 4.8). In contrast, for larger ξ_N/R, the viscous component of the first normal stress difference is negative and much smaller in magnitude than in the escaped radial solution.

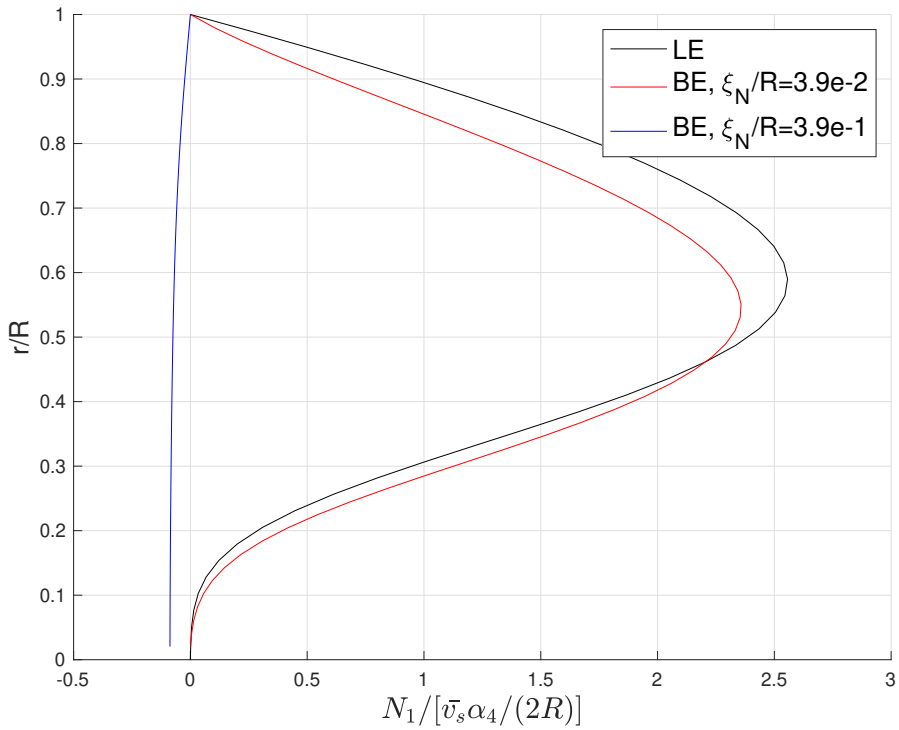

Figure 4.8. Variation of the viscous component of N_1.

Intermediate Ericksen numbers

As the Ericksen number increases, hydrodynamic effects become stronger. In the planar radial configuration ($\xi_N/R = 0.39$), the biaxial ring shrinks (fig. 4.9) and is completely destroyed at $Er \approx 5$. Above a threshold Ericksen number, the director assumes the escaped radial configuration irrespective of the relative magnitude of the defect size (fig. 4.10). The non-uniform order parameter introduces a spatial variation in the strength of elastic effects; the Frank constant is effectively smaller in the regions of lower S (eq. (2.61)), which are thus more prone to director distortions. As ξ_N increases, the order parameter at the pipe axis becomes smaller (fig. 4.11), and in effect, the resistance to director rotation is the weakest there. In contrast, the presence of walls imposes perfect alignment ($S = 1$), so the resistance to imposed distortions is the strongest there. In the case of $\xi_N/R = 0.39$, the region of the elevated order parameter is the widest, which corresponds to the smallest rotation of the director field (fig. 4.10). The Leslie-Ericksen theory is a limiting case of the Beris-Edwards model with $\xi_N/R \to 0$; as a result, the microstructure resistance to director rotation in the near-wall region is smaller than in the BE model with a spatially varying order parameter.

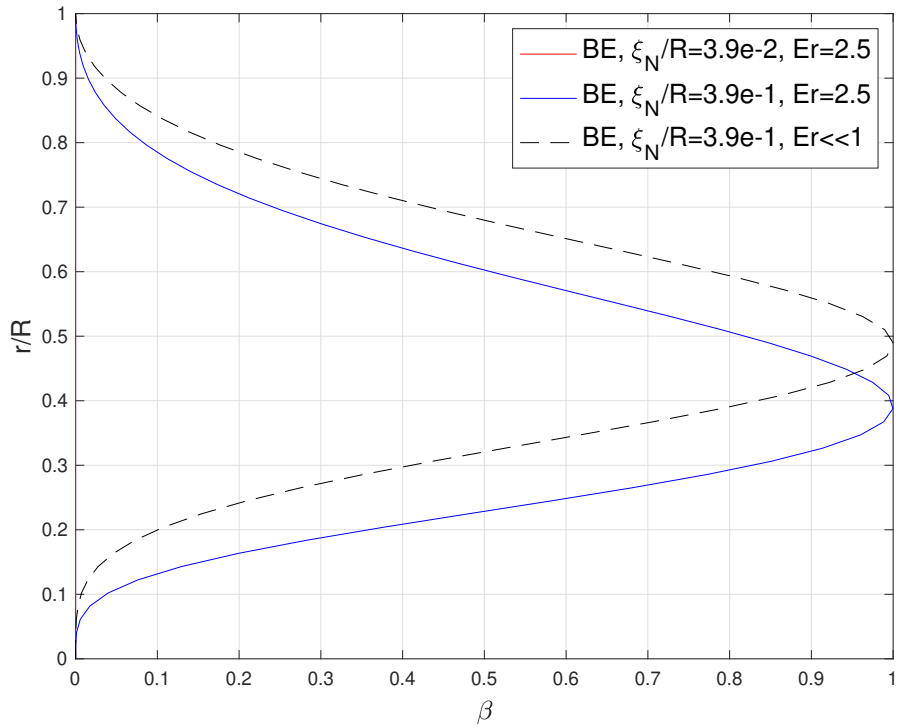

Figure 4.9. Biaxiality at $Er = 2.5$ for different $\frac{\xi_N}{R}$. Compared to fig. 4.3 the region of biaxial behaviour shrinks.

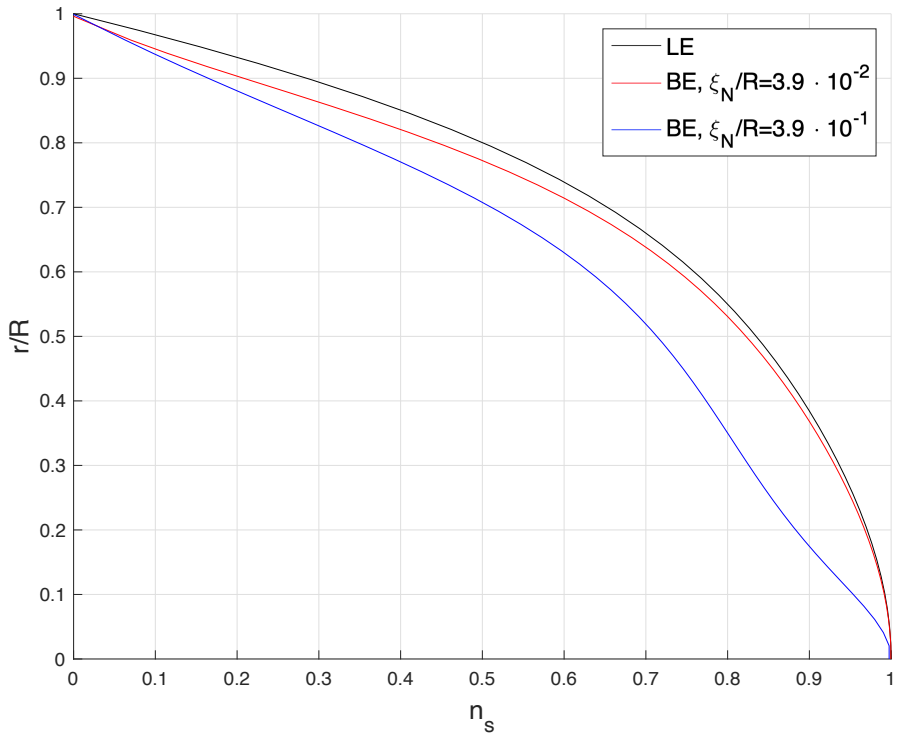

Figure 4.10. Comparison of the director field at $Er = 5$

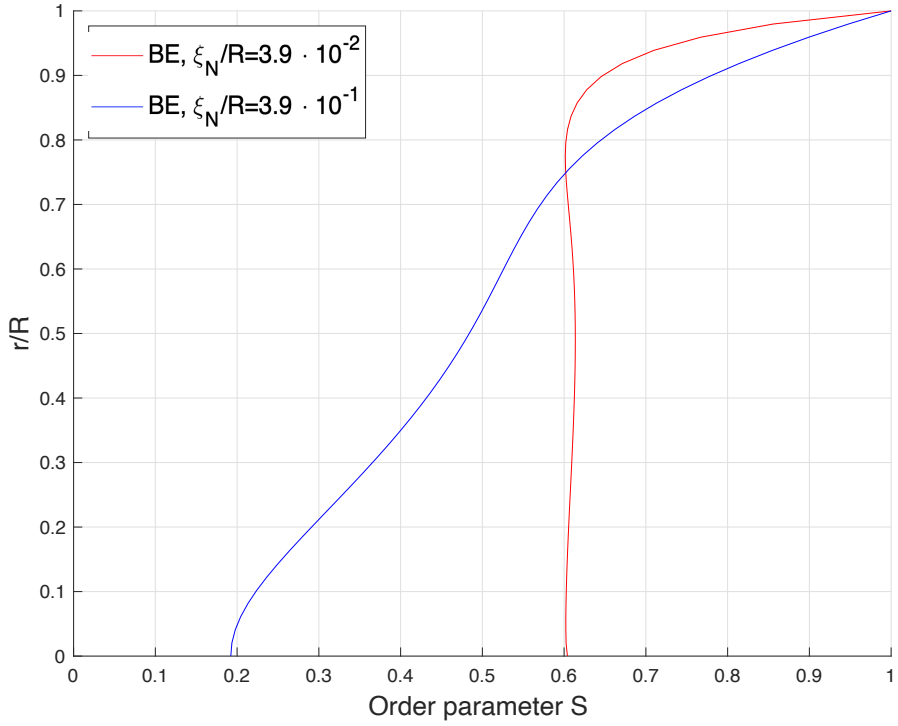

Figure 4.11. Comparison of the distribution of order parameter at $Er = 5$.

The velocity distribution is similar to the low Ericksen number regime, and the shear thinning mechanism is the same for all configurations (fig. 4.12)- the effective viscosity is largest at the wall, where the director is parallel to the velocity gradient direction and smallest at the axis, where $\boldsymbol{n}$ and $\boldsymbol{v}$ align. The varying order parameter changes the distribution of the

first normal stress difference (fig. 4.13); a high gradient in the order parameter near the wall produces significant elastic stresses, which are absent in the LE theory. The maximum normal stress is larger as the defect size decreases because the order parameter changes over a smaller distance (fig. 4.11).

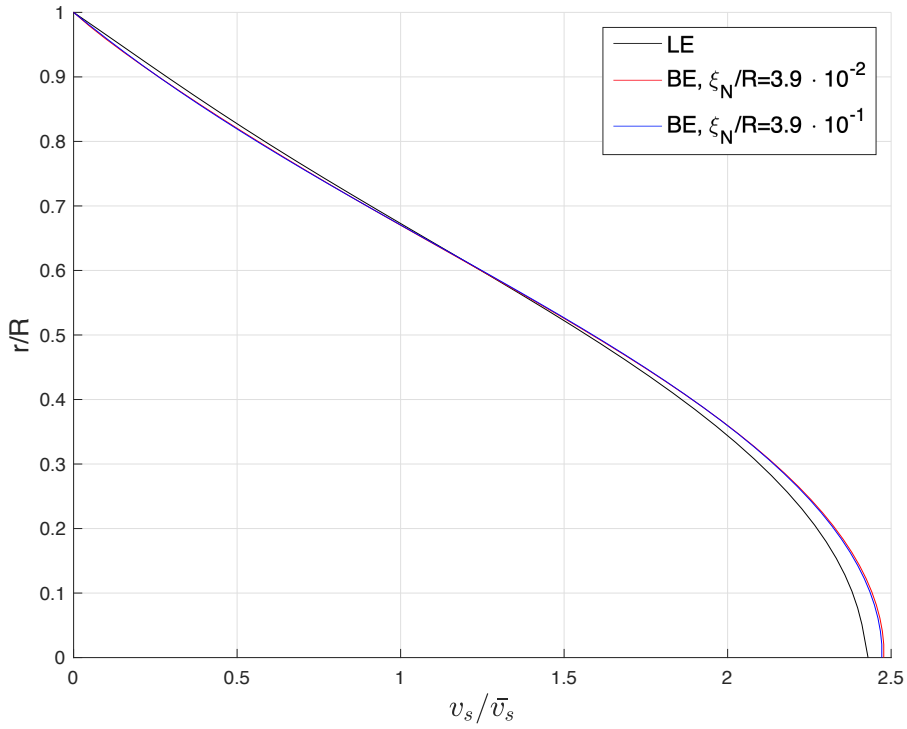

Figure 4.12. Comparison of the velocity field at $Er = 5$

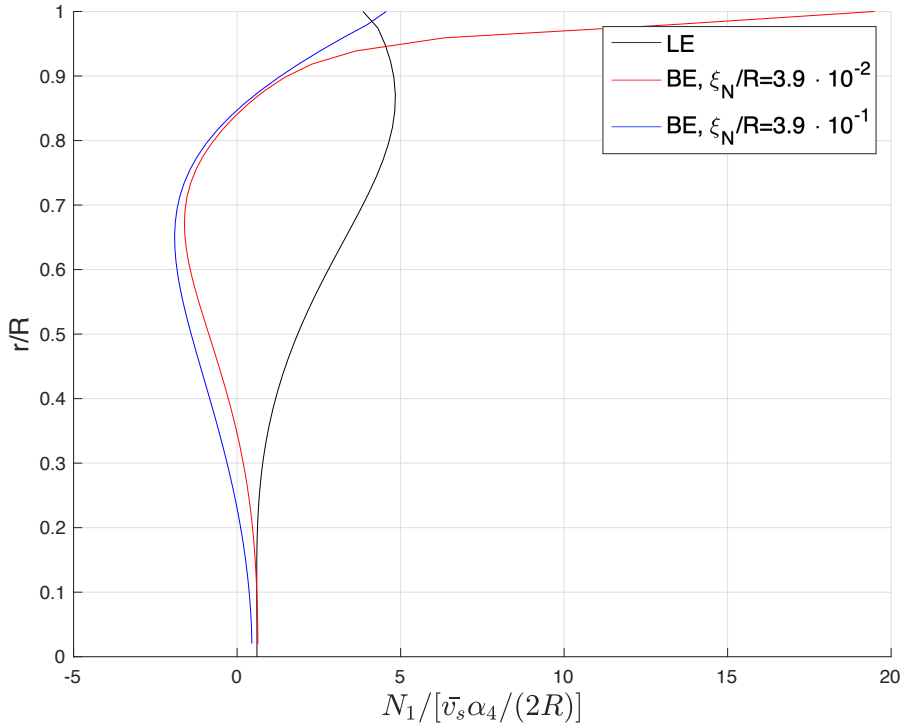

Figure 4.13. Comparison of normal stress difference profiles at $Er = 5$.

High Ericksen numbers

At higher Ericksen numbers, the director orientation is controlled by the flow effects, and apart from the near-wall layer, $\boldsymbol{n}$ aligns at a small angle to the flow direction (fig. 4.14). For the parameters employed in this chapter, the shearing motion is strong enough to affect the order parameter, as shown in fig. 4.15. The Deborah number is higher for the second set of parameters (eq. (4.14)), and hence, the dominance of flow effects causes a more significant increase in the order parameter. The degree of molecular ordering affects the Leslie angle, which for a uniaxial, constant order parameter in the $\boldsymbol{Q}$ tensor framework is given by

$$\theta_L = \frac{1}{2}\cos^{-1}\left(\frac{3S}{(2+S)\xi}\right). \tag{4.15}$$

Therefore, the elevated order parameter at higher Ericksen (and thus Deborah) numbers (fig. 4.15), results in a better director/flow alignment as shown in fig. 4.14. For typical liquid crystal parameters, $\theta_L < 10^o$, so the increased alignment has little effect on the velocity distribution, which has a Newtonian-like profile everywhere except the near-wall, highly viscous region, as shown in fig. 4.16.

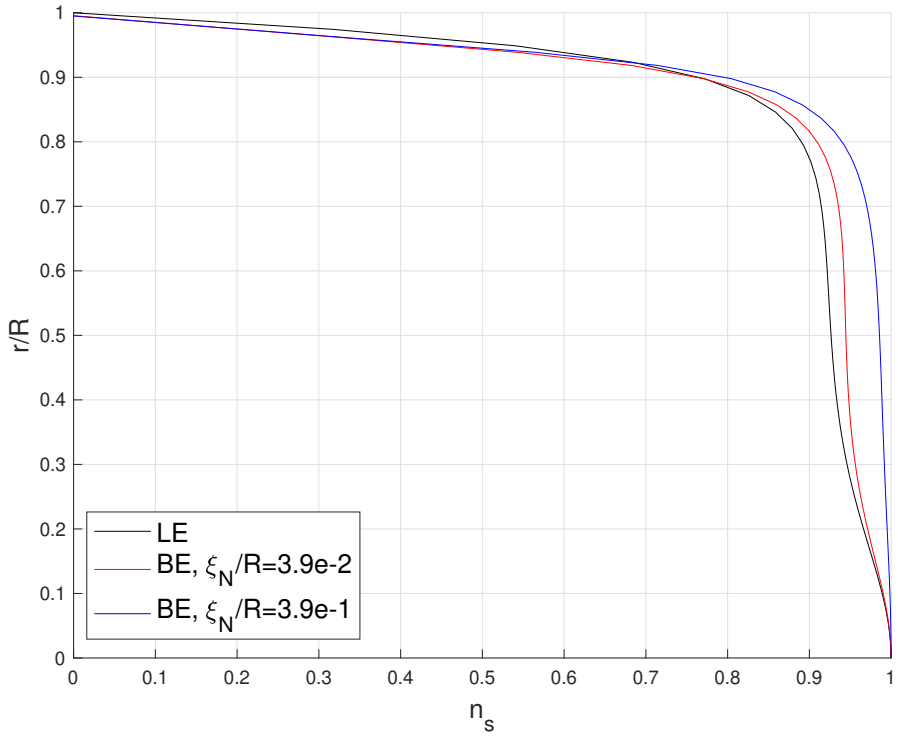

Figure 4.14. Comparison of the axial component of the director field at $Er = 100$.

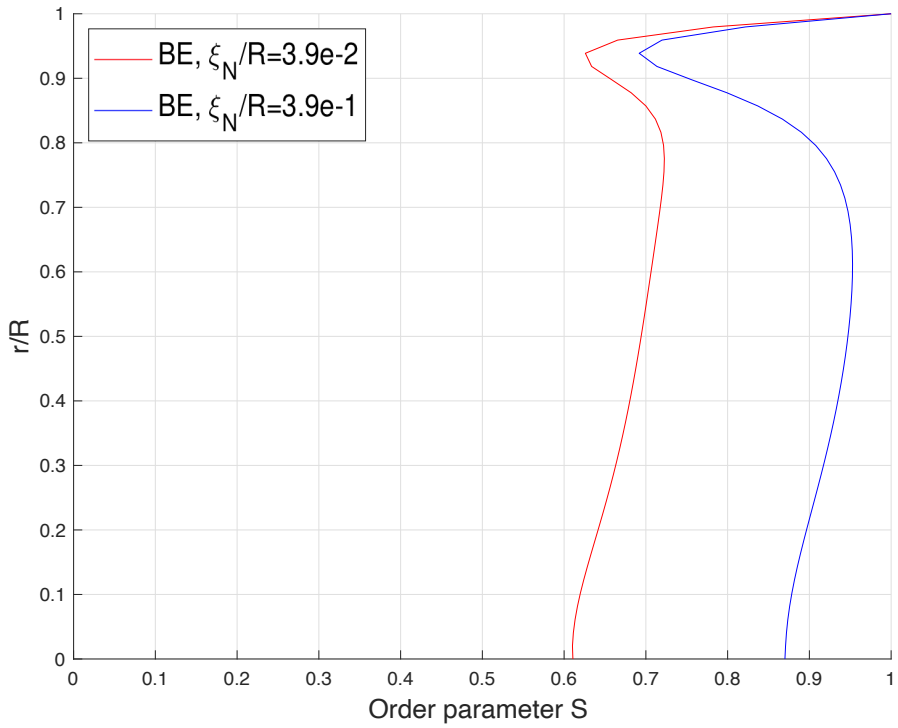

Figure 4.15. Order parameter $S = \sqrt{\frac{3}{2}}\sqrt{\lambda_1^2 + \lambda_2^2 + \lambda_3^2}$ for different ξ_N at $Er = 100$.

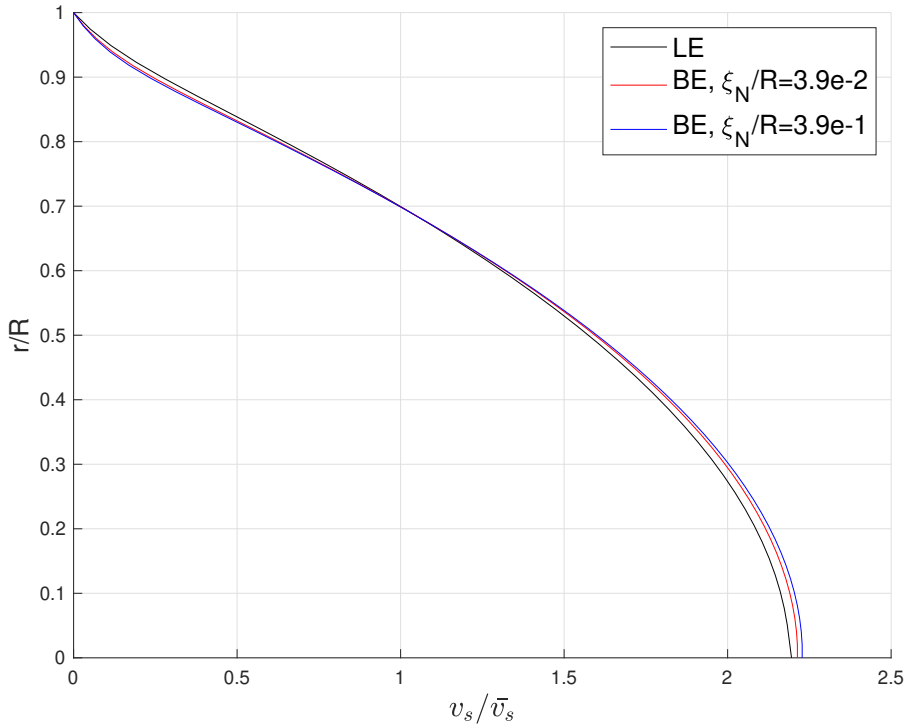

Figure 4.16. Comparison of the velocity field at $Er = 100$

Flow alignment at the infinite Ericksen number

In the Leslie-Ericksen theory with $K = 0$, the director aligns at the Leslie angle (eq. (4.15)) to the flow. The situation is more complex in the case of the Beris-Edwards model, where the alignment angle depends on the order parameter (eq. (4.15)). The alignment is controlled by the order parameter, which depends on the Deborah number; De quantifies the relative importance of flow aligning to bulk effects, thus controlling the distribution of the order parameter (fig. 4.17). For $De << 1$, bulk effects dominate, and the order parameter is only weakly affected by the flow; increasing De improves the molecular alignment. Since the shearing effects are the strongest at the wall, the order parameter is highest at $r/R \rightarrow 1$ (fig. 4.17); conversely, the increase in S is the smallest at $r/R \rightarrow 0$, where the shear rate is minimum.

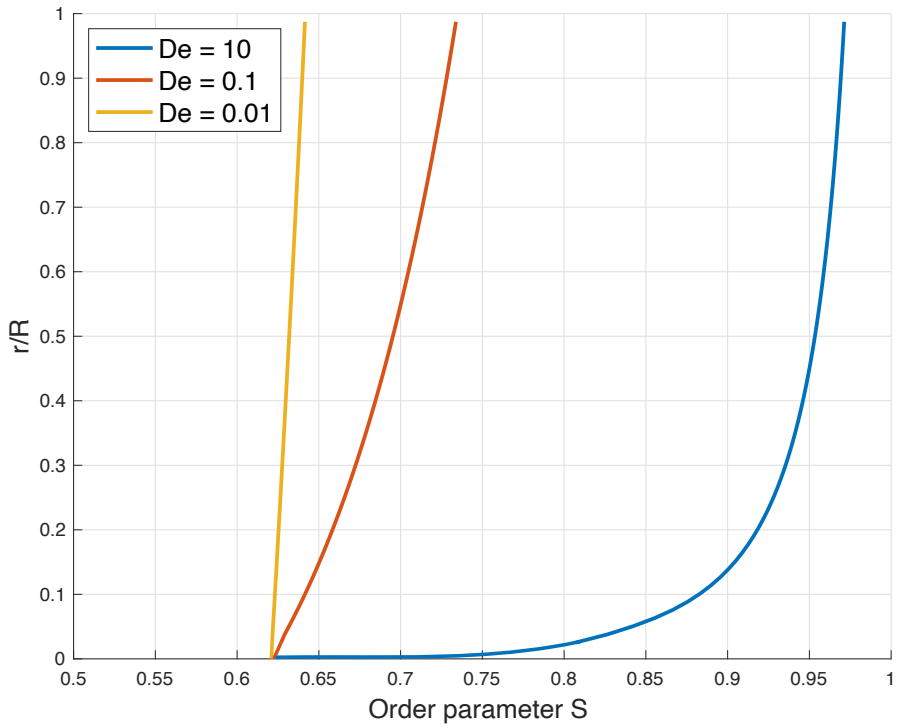

Figure 4.17. Variation of order parameter at infinite Ericksen number with different Deborah numbers. Ratios $\frac{a}{b} = -0.05$ and $\frac{c}{b} = 1$ are constant in all cases; a, b, c are parameters of the bulk-free energy density (eq. 2.64) in the BE model.

4.2.2 Wall-parallel anchoring

The wall-parallel anchoring produces less interesting rheological behaviour than the homeotropic boundary condition. The director aligns with the flow (fig. 4.18), and the viscosity is nearly constant across the pipe, which results in a Newtonian velocity profile (fig. 4.19).

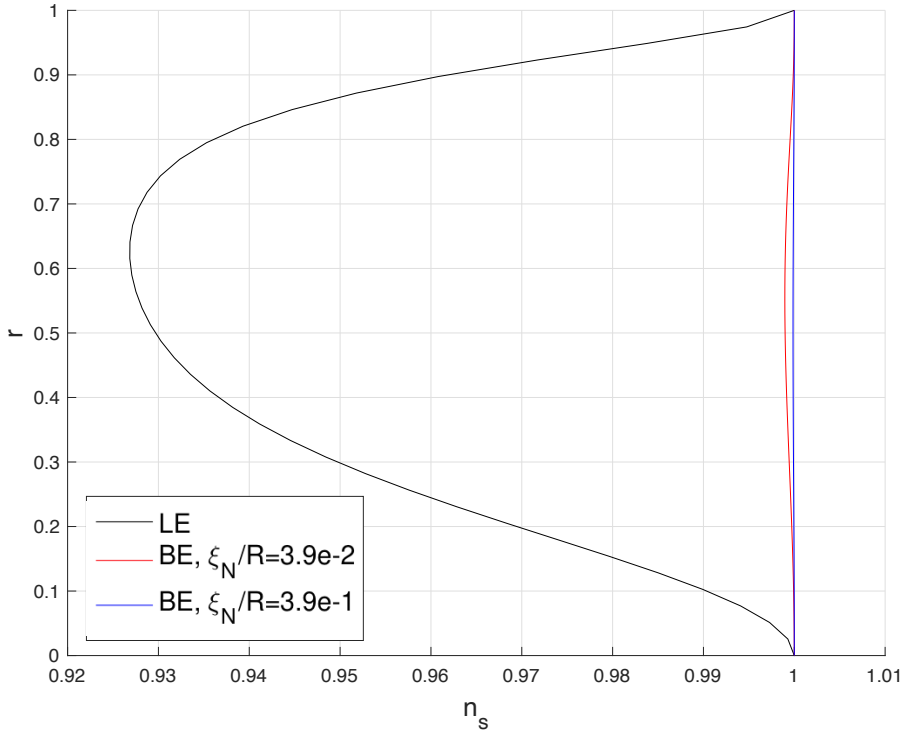

Figure 4.18. Comparison of the director field at $Er = 2.5$ with wall parallel anchoring. Note that the x-axis scale starts at 0.92, so the director is nearly aligned with the flow.

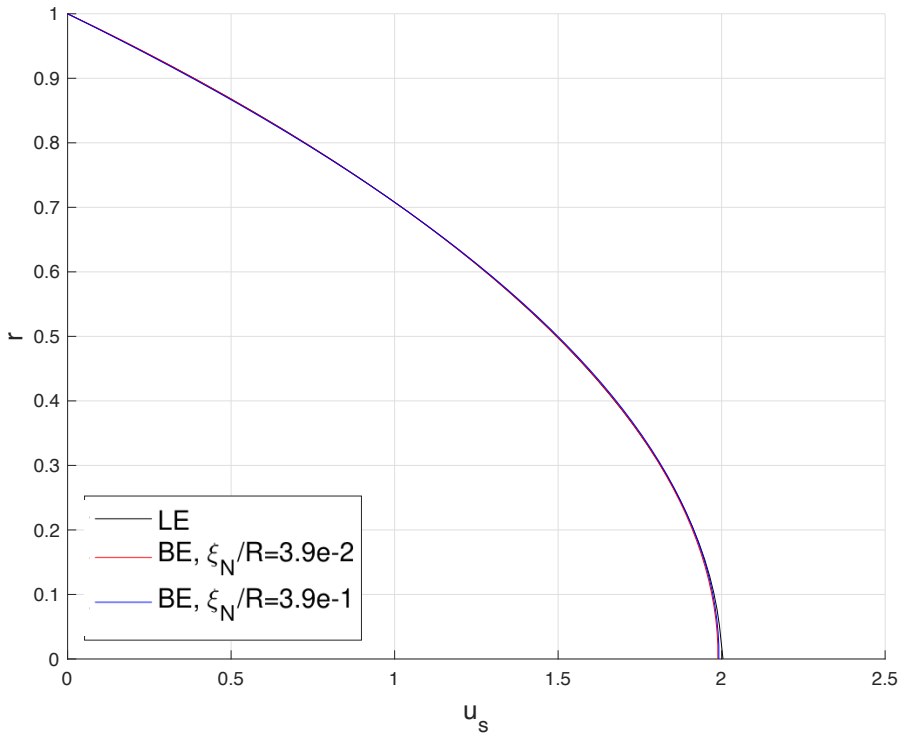

Figure 4.19. Comparison of the velocity field at $Er = 2.5$ with wall parallel anchoring.

4.3 Summary

Predictions of the Leslie-Ericksen and Beris-Edwards models were investigated in a capillary flow. Homeotropic anchoring results in a rich rheological behaviour: the effective viscosity decreases with the Ericksen number, and the zero-shear viscosity limit is controlled by the relative magnitude of the defect size ξ_N/R (fig. 4.20). At low Ericksen numbers, the director distribution is predicated on ξ_N/R; when $\xi_N/R << 1$, we recover the Leslie-Ericksen number limit and the shear-thinning occurs via director reorientation. As the capillary dimension decreases (keeping ξ_N constant), there is a phase transition in the director field; the director field changes from the uniaxial state at the wall, to the bixaial state at $r = 0.5$, and back to the uniaxial state at the pipe axis. In contrast to the $\xi_N/R << 1$ limit, shear thinning occurs via a local reduction of the order parameter. All simulations discussed in this chapter were initialised with a horizontal director field. A future investigation of other initial director configurations and a potential time variation of the imposed pressure gradient could help to reveal potential hysteresis in the selection of the steady-state.

The wall-parallel anchoring nearly aligns the director with the flow, which results in a Newtonian behaviour with a nearly constant shear viscosity $\frac{\alpha_3+\alpha_4+\alpha_6}{2} \approx \frac{\alpha_4}{2}$ [15]. At high Ericksen number ($O(10^3)$), the flow aligning effects are so strong that the wall anchoring is irrelevant, so the wall-parallel and homeotropic boundary conditions result in the same effective viscosities (high shear plateau).

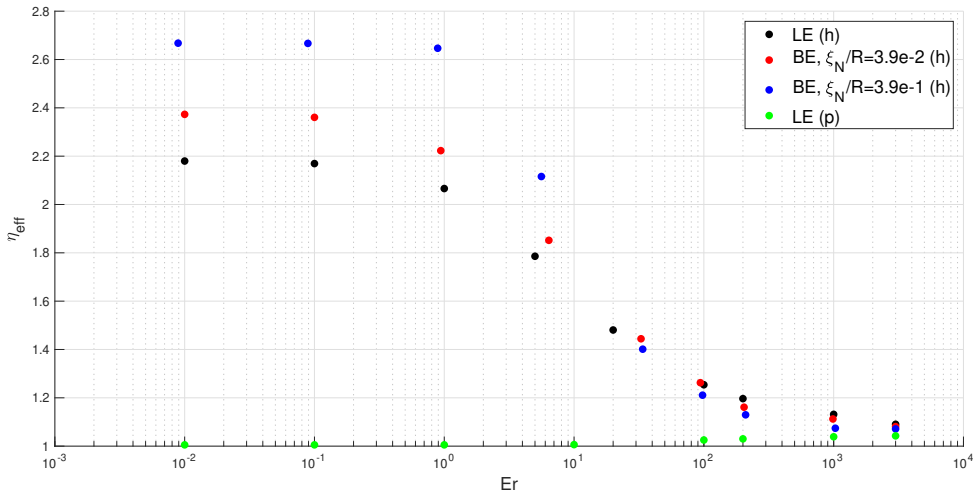

Figure 4.20. Comparison of the shear curves produced by LE and BE model with different defect length-scales. The effective viscosity is normalised by the viscosity scale $\frac{\alpha_4}{2}$. Letters h and p refer to homeotropic and wall-parallel anchoring, respectively.

Chapter 5

Flow of transversely isotropic fluid in curved pipes

The majority of liquid crystal studies present in the literature focus either on static problems [135, 156] or investigate flow of nematic liquid crystals in simple geometries, such as straight channels [66, 142, 155] and pipes [157, 158]. These studies are of limited use for industrial purposes since the manufacturing of FMCG products involves material transport through complex pipeworks, which may consist of bends, manifolds and contractions. The flow of Leslie-Ericksen fluids in a planar contraction was investigated by Cruz et al. [151]; their results demonstrate a strong dependence of the microstructure orientation and flow on the Ericksen number. Cruz's work was extended to model free surface flows [159] and indicated the key role of wall anchoring in controlling process parameters such as filling time. Kos et al. [160] analysed the behaviour of the Beris-Edwards in a junction of three perpendicular pipes and found that the number of inlet and outlets determines the flow and microstructure configuration.

One of the major undertakings of this thesis is the investigation of liquid crystal behaviour in curved pipes. Studies of flow in bends were initiated by Dean [161, 162], who has shown that for a Newtonian fluid, the combination of fluid inertia with pipe curvature is responsible for the emergence of secondary flow. Experimental measurements of complex fluids demonstrate that in the absence of inertia, secondary flow can be generated by non-zero normal stress differences [163]. The effect can be modelled through Oldroyd-B and UCM models [154, 164], where the (positive) first normal stress difference acts similar to fluid inertia. Analyses of viscoelastic flows in curved pipes were extended by Fan et al. [153], who demonstrated that the (negative) second normal stress difference in the Oldroyd 3-constant model reduces the magnitude of secondary motions. The normal stresses within liquid crystals are generated by the interaction of microstructure with the flow; they can be of any sign, depending on the material properties and the shear rate [27]. This chapter uses perturbation analysis to investigate soap flow (represented as a nematic liquid crystal) in the limit of infinite Ericksen and zero Deborah numbers. The governing equations are simple enough to yield an analytical solution, which provides insight into the behaviour of liquid crystalline materials in geometries that induce flow curvature.

5.1 Problem formulation

5.1.1 Geometry

We analyse the steady-state, fully developed flow of liquid crystals in a curved pipe. The system is schematically shown in fig. 5.1 and can be most conveniently described in toroidal coordinates (r^*, ϕ, s^*).

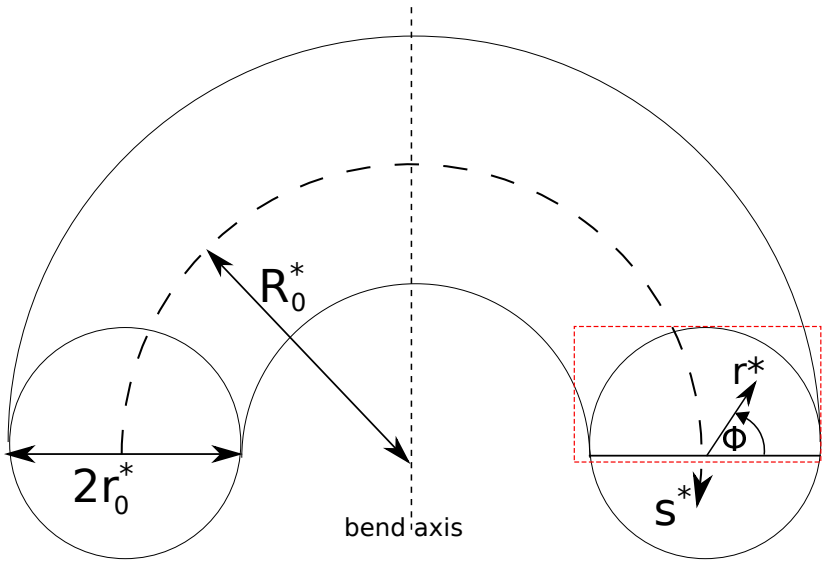

Figure 5.1. Toroidal geometry used in the analysis. Reprinted with permission from [24]. Copyright Elsevier 2022.

5.1.2 Equations of motion

The flow of a non-Newtonian fluid through a curved pipe with a constant diameter is described by a set of momentum and continuity equations [154]

$$\frac{\partial p^*}{\partial r^*} = \frac{\partial \tau^*_{rr}}{\partial r^*} + \frac{1}{r^*}\frac{\partial \tau^*_{r\phi}}{\partial \phi} + \frac{1}{r^*}N_2^* + \frac{1}{R_0^* + r^*\cos\phi}\left[-\tau^*_{r\phi}\sin\phi - N_1^*\cos\phi\right], \tag{5.1a}$$

$$\frac{1}{r^*}\frac{\partial p^*}{\partial \phi} = \frac{\partial \tau^*_{r\phi}}{\partial r^*} + \frac{1}{r^*}\frac{\partial \tau^*_{\phi\phi}}{\partial \phi} + \frac{2}{r^*}\tau^*_{r\phi} + \frac{1}{R_0^* + r^*\cos\phi}\left[\tau^*_{r\phi}\cos\phi + (N_1^* + N_2^*)\sin\phi\right], \tag{5.1b}$$

$$\frac{1}{R_0^* + r^*\cos\phi}\frac{\partial p^*}{\partial s^*} = \frac{\partial \tau^*_{rs}}{\partial r} + \frac{1}{r^*}\frac{\partial \tau^*_{\phi s}}{\partial \phi} + \frac{1}{r^*}\tau^*_{rs} + \frac{2}{R_0^* + r^*\cos\phi}\left[\tau^*_{rs}\cos\phi - \tau^*_{\phi s}\sin\phi\right], \tag{5.1c}$$

$$0 = \frac{\partial u^*}{\partial r^*} + \frac{u^*}{r^*} + \frac{u^*\cos\phi}{R_0^* + r^*\cos\phi} - \frac{v^*\sin\phi}{R_0^* + r^*\cos\phi} + \frac{1}{r^*}\frac{\partial v^*}{\partial \phi}, \tag{5.2}$$

where p^* is the pressure, τ^*_{ij} denotes the symmetric stress tensor, u^* and v^* represent dimensionless radial and tangential velocity components, respectively. The normal stress differ-

ences are defined as

$$N_1^* = \tau_{ss}^* - \tau_{rr}^*, \tag{5.3a}$$

$$N_2^* = \tau_{rr}^* - \tau_{\phi\phi}^*. \tag{5.3b}$$

Throughout this chapter, starred variables refer to dimensional quantities, while their dimensionless counterparts appear without a star.

5.1.3 Constitutive equation

Here, we treat soap as a uniaxial, constant order parameter nematic liquid crystal, where the orientation of the microstructure is represented by the director field $\boldsymbol{n}$. The behaviour of the microstructure can be described by the Leslie-Ericksen theory, which introduces a configuration-dependent stress tensor [34, 43]

$$\boldsymbol{\tau}^* = \alpha_1^* \boldsymbol{nnnn} : \boldsymbol{D^*} + \alpha_2^* \boldsymbol{n N^*} + \alpha_3^* \boldsymbol{N^* n} + \alpha_4^* \boldsymbol{D^*} + \alpha_5^* \boldsymbol{nn} \cdot \boldsymbol{D^*} + \alpha_6^* \boldsymbol{D^*} \cdot \boldsymbol{nn} - K^* \nabla^* \boldsymbol{n} (\nabla^* \boldsymbol{n})^T, \tag{2.52}$$

where $\boldsymbol{N^*}$ is the corotational derivative of the director, α_i^* are Leslie viscosities, $\boldsymbol{K}^*$ is the Frank constant and $\boldsymbol{D^*}$, $\boldsymbol{\omega^*}$ are symmetric and antisymmetric components of the velocity gradient tensor. Computation of the stress tensor requires knowledge of the microstructure orientation, which is modelled by the angular momentum balance [34]

$$\boldsymbol{h^*} - \boldsymbol{nn} \cdot \boldsymbol{h^*} - \gamma_2^* (\boldsymbol{n} \cdot \boldsymbol{D^*} - \boldsymbol{nnn} : \boldsymbol{D^*}) - \gamma_1^* \boldsymbol{N^*} = 0. \tag{2.53}$$

For the distortion energy density, we use the one constant approximation and the molecular field reads

$$\boldsymbol{h}^* = -\frac{\delta f_d}{\delta \boldsymbol{n}} = K^* \nabla^{*2} \boldsymbol{n}. \tag{5.4}$$

5.1.4 Non-dimensionalization

Throughout this chapter, we introduce the following dimensionless quantities

$$\begin{gathered} s = \frac{s^*}{r_0^*}, \qquad r = \frac{r^*}{r_0^*}, \qquad u = \frac{\boldsymbol{v}^* \cdot \boldsymbol{e_r}}{W_0^*}, \qquad v = \frac{\boldsymbol{v}^* \cdot \boldsymbol{e_\phi}}{W_0^*}, \qquad w = \frac{\boldsymbol{v}^* \cdot \boldsymbol{e_s}}{W_0^*}, \\ \boldsymbol{h} = \frac{(r_0^*)^2}{K} \boldsymbol{h^*}, \qquad \boldsymbol{\tau} = \frac{r_0^*}{\frac{\alpha_4}{2} W_0^*} \boldsymbol{\tau^*}, \qquad \alpha_i = \frac{\alpha_i^*}{\frac{\alpha_4^*}{2}}, \qquad \delta = \frac{r_0^*}{R^*}, \quad p = p^* \frac{r_0^*}{\frac{\alpha_4}{2} W_0^*}, \end{gathered} \tag{5.5}$$

where W_0^* - the maximum axial velocity - denotes the velocity scale.

Equations of motion

Substituting scaled variables (eq. (5.5)) into the momentum equation (5.1) gives the set of dimensionless momentum balance equations

$$\frac{\partial p}{\partial r} = \frac{\partial \tau_{rr}}{\partial r} + \frac{1}{r}\frac{\partial \tau_{r\phi}}{\partial \phi} + \frac{1}{r}N_2 + \frac{\delta}{B}\left[-\tau_{r\phi}\sin\phi - N_1\cos\phi\right], \tag{5.6a}$$

$$\frac{1}{r}\frac{\partial p}{\partial \phi} = \frac{\partial \tau_{r\phi}}{\partial r} + \frac{1}{r}\frac{\partial \tau_{\phi\phi}}{\partial \phi} + \frac{2}{r}\tau_{r\phi} + \frac{\delta}{B}\left[\tau_{r\phi}\cos\phi + (N_1+N_2)\sin\phi\right], \tag{5.6b}$$

$$\frac{1}{B}\frac{\partial p}{\partial s} = \frac{\partial \tau_{rs}}{\partial r} + \frac{1}{r}\frac{\partial \tau_{\phi s}}{\partial \phi} + \frac{1}{r}\tau_{rs} + \frac{2\delta}{B}\left[\tau_{rs}\cos\phi - \tau_{\phi s}\sin\phi\right], \tag{5.6c}$$

and the continuity equation reduces to

$$0 = \frac{\partial (urB)}{\partial r} + \frac{\partial (vB)}{\partial \phi}, \tag{5.7}$$

where

$$B = 1 + \delta r\cos\phi, \tag{5.8}$$

is the distance from the bend axis normalised by the bend radius. In the limiting case of a small curvature, $\delta \to 0$, and the system can be considered as a straight pipe.

Angular momentum and stress

The dimensionless stress is obtained by substituting eq. (5.5) into the stress definition: (2.52)

$$\boldsymbol{\tau} = 2\boldsymbol{D} + \alpha_1 \boldsymbol{nnnn} : \boldsymbol{D} + \alpha_2 \boldsymbol{nN} + \alpha_3 \boldsymbol{Nn} + \alpha_5 \boldsymbol{nn}\cdot\boldsymbol{D} + \alpha_6 \boldsymbol{D}\cdot\boldsymbol{nn} - \frac{1}{Er}\nabla\boldsymbol{n}(\nabla\boldsymbol{n})^T, \tag{5.9}$$

where $Er = \frac{W_0^* r_0^* \alpha_4}{K^*}$ is the Ericksen number. The non-dimensional angular momentum equation is obtained in the same manner and reads

$$\frac{\boldsymbol{h} - \boldsymbol{nn}\cdot\boldsymbol{h}}{Er} - \gamma_2(\boldsymbol{n}\cdot\boldsymbol{D} - \boldsymbol{nnn} : \boldsymbol{D}) - \gamma_1 \boldsymbol{N} = 0. \tag{5.10}$$

Based on the process parameters given by Bryan et al. [38], soap is typically manufactured at $Er >> 1$, which allows us to neglect the elastic contributions in eq. (5.9) and (5.10), therefore reducing the stress and director balance to the transversely isotropic fluid model provided by Ericksen [110]:

$$\boldsymbol{\tau} = 2\boldsymbol{D} + 2\mu_1 \boldsymbol{nnnn} : \boldsymbol{D} + \mu_2(\boldsymbol{nn}\cdot\boldsymbol{D} + \boldsymbol{D}\cdot\boldsymbol{nn}), \tag{2.27}$$

$$\dot{\boldsymbol{n}} = \lambda(\boldsymbol{n}\cdot\boldsymbol{D} - \boldsymbol{nnn} : \boldsymbol{D}) + \boldsymbol{n}\cdot\boldsymbol{\omega}, \tag{2.29}$$

where

$$\mu = \frac{\alpha_4}{2}, \qquad \mu_1 = \frac{1}{2}\left(\alpha_1 + \gamma_2 + \frac{2\gamma_2\alpha_2}{\gamma_1}\right), \qquad \mu_2 = \alpha_5 - \frac{\gamma_2\alpha_2}{\gamma_1}. \tag{2.57}$$

Stream-wise pressure gradient

Results presented in section 4.1 show that the TIF model predicts a uniform director distribution in a straight pipe with a constant viscosity. The velocity profile is parabolic with the peak value of [45]

$$W_0^* = -\frac{(r_0^*)^2}{4\eta_{eff}^*}\frac{\partial p^*}{\partial s^*}. \tag{5.11}$$

η_{eff}^* is the orientation-dependent effective viscosity given by

$$\eta_{eff}^* = \frac{\alpha_4^*}{2} + 2\mu_1^*\left(n_r^{(0)}n_s^{(0)}\right)^2 + \frac{\mu_2^*}{2}, \tag{5.12}$$

where $n_i^{(0)} = n_i^{(0)}(\lambda)$ are director components obtained from the straight pipe (zero curvature) calculation. The dimensionless pressure gradient in a straight pipe is obtained by substituting the scaling equation (5.5) into the definitions of peak velocity (5.11) and viscosity (5.12) to yield

$$\frac{\partial p}{\partial s} = -4\Big(1 + 2\mu_1\left(n_r^{(0)}n_s^{(0)}\right)^2 + \frac{\mu_2}{2}\Big). \tag{5.13}$$

5.1.5 Stream function

For a steady-state, fully developed flow in a bend, the motion in the $r-\phi$ plane can be considered separately from the stream-wise component. For that reason, we use the stream function approach [165] with $r-$ and $\phi-$ velocity components defined as [154]

$$u = -\frac{1}{rB}\frac{\partial\psi}{\partial\phi}, \tag{5.14a}$$

$$v = \frac{1}{B}\frac{\partial\psi}{\partial r}. \tag{5.14b}$$

5.1.6 Perturbation method

Solutions to the linear and angular momentum equations ((5.6) and (2.29), respectively) are obtained as perturbations to the straight pipe solution. The perturbation parameter is chosen as $\delta << 1$, and solutions are sought in the form of

$$w = \sum_{m=0}^{m=\infty}\delta^m w^{(m)}(r,\phi), \tag{5.15a}$$

$$\psi = \sum_{m=0}^{m=\infty} \delta^m \psi^{(m)}(r,\phi), \tag{5.15b}$$

$$\boldsymbol{n} = \sum_{m=0}^{m=\infty} \delta^m \boldsymbol{n}^{(m)}(r,\phi), \tag{5.15c}$$

where w is a dimensionless axial velocity.

5.1.7 Boundary conditions

We assume that the fluid is stationary at the wall. Hence, the no-slip boundary conditions impose the following restrictions on the $s-$, $r-$, $\phi-$ velocity components:

$$w^{(m)}(r=1)=0, \qquad \psi^{(m)}(r=1)=0, \qquad \frac{\partial \psi^{(m)}}{\partial r}(r=1)=0. \tag{5.16}$$

There is no long range ordering of the director field because of the absence of elasticity, so the director orientation on the boundaries need not be specified.

Perturbation equations were solved with the mathematical manipulation software Maple 2020 [166].

5.2 Solution

5.2.1 Solution procedure

The flow of a transversely isotropic fluid in a curved pipe is described by the solution of the linear and angular momentum equations (5.6) and (2.29), respectively. Substituting the definition of dimensionless pressure gradient (5.13) into the $s-$ component momentum equation (5.6c) enables us to eliminate the axial pressure gradient:

$$0 = -\frac{\partial p}{\partial s}\frac{1}{B} + \frac{\partial \tau_{rs}}{\partial r} + \frac{1}{r}\frac{\partial \tau_{\phi s}}{\partial \phi} + \frac{1}{r}\tau_{rs} + 2\frac{\delta}{B}\left[\tau_{rs}\cos\phi - \tau_{\phi s}\,\sin\phi\right], \tag{5.17}$$

where $\frac{\partial p}{\partial s}$ is specified by eq. (5.13). The steady-state momentum balance equation (5.6) can be written in the form $\nabla p = \nabla \cdot \boldsymbol{\tau}$, expressing the pressure-stress balance. Hence, the curl of the pressure gradient describes the rotational force balance within the fluid; the ith component of $\nabla \times \nabla p$ represents the force balance in a plane normal to the ith coordinate. The radial and azimuthal components of the pressure gradient terms are eliminated, and the momentum balance in the $r-\phi$ plane reads

$$(\nabla \times \nabla p)_s = 0 = \left[-\frac{1}{r}\frac{\partial^2 N_2}{\partial r \partial \phi} - \frac{1}{r^2}\frac{\partial N_2}{\partial \phi} + \frac{\partial^2 \tau_{r\phi}}{\partial r^2} + \frac{3}{r}\frac{\partial \tau_{r\phi}}{\partial r} - \frac{1}{r^2}\frac{\partial^2 \tau_{r\phi}}{\partial \phi^2}\right] +$$

$$\frac{\delta}{r}\left(\frac{\partial[B^{-1}r(\tau_{r\phi}\cos\phi+(N_1+N_2)\sin\phi)]}{\partial r}-\frac{\partial[B^{-1}(-\tau_{r\phi}\sin\phi-N_1\cos\phi)]}{\partial\phi}\right). \tag{5.18}$$

The equality above suggests two sources of the secondary motion: 1) a combination of normal stress differences and bend curvature expressed by the second bracket on the right-hand side of eq. (5.18); 2) an imbalance of the second normal stress difference N_2 and the shear stress $\tau_{r\phi}$ in the $r-\phi$ plane. In the limiting case of a straight pipe flow, $\delta = 0$ and the stress distribution is axisymmetric, so there exists no secondary motion.

5.2.2 Leading order ($O(1)$) solution

The leading order solution represents the straight pipe limit ($\delta = 0$) and describes major contributions to the director and velocity distributions. The leading order $s-$ and $r-\phi$ components of momentum balance (equations (5.17) and (5.18)) are given by

$$\left(\frac{\partial p}{\partial s}\right)^{(0)}=\frac{\partial\tau_{rs}^{(0)}}{\partial r}+\frac{1}{r}\tau_{rs}^{(0)}, \tag{5.19a}$$

$$(\nabla\times\nabla p^{(0)})_s=0. \tag{5.19b}$$

$\left(\frac{\partial p}{\partial s}\right)^{(0)}$ is the $O(1)$ component of the pressure gradient (eq. (5.13)) while the shear stress depends on both director orientation and the shear rate

$$\tau_{rs}^{(0)}=\frac{\mu_2+4\mu_1(n_r^{(0)})^2(n_s^{(0)})^2+2}{2}\frac{\partial w^{(0)}}{\partial r}. \tag{B.3a}$$

Other components of $\boldsymbol{\tau}^{(0)}$ are not relevant to the leading order solution and are thus listed in the appendix B.2. The stress tensor is computed based on the director orientation, which is calculated form the $O(1)$ components of angular momentum balance equations. The $r-$, $\phi-$ and $s-$ components of the steady-state director balance are given by

$$\left(2\lambda(n_r^{(0)})^2-\lambda+1\right)\frac{\partial w^{(0)}}{\partial r}=0, \tag{5.20a}$$

$$n_r^{(0)}n_p^{(0)}n_s^{(0)}\frac{\partial w^{(0)}}{\partial r}=0, \tag{5.20b}$$

$$\left(2\lambda(n_s^{(0)})^2-\lambda-1\right)\frac{\partial w^{(0)}}{\partial r}=0. \tag{5.20c}$$

The non-trivial solution for the director field reads

$$\boldsymbol{n}^{(\mathbf{0})}(r\neq0,\phi)=[n_r^{(0)},n_\phi^{(0)},n_s^{(0)}]=\left[-\sqrt{\frac{\lambda-1}{2\lambda}},0,\sqrt{\frac{\lambda+1}{2\lambda}}\right], \tag{5.21}$$

where λ is the tumbling parameter; for $|\lambda|>1$, the liquid crystal aligns in the shear plane, while $|\lambda|<1$ describes tumbling materials; in this thesis we focus on the former group. Note that the director balance equation (5.20) is also satisfied for arbitrary director field when

$\nabla \boldsymbol{v} = \mathbf{0}$.

Substituting eq. (B.3a) into the axial momentum balance (eq. (5.19)) and imposing the no-slip boundary condition (eq. (5.16)), the solution is given by

$$w^{(0)}(r,\phi) = 1 - r^2, \tag{5.22}$$

and further details are presented in the appendix B.2. The $O(1)$ solution represents a straight pipe flow with the axisymmetric distribution of stress and velocity. $\tau_{r\phi} = 0$ and N_2 is independent of ϕ (appendix B.2), so the secondary motion vanishes and

$$\psi^{(0)}(r,\phi) = 0. \tag{5.23}$$

The flow rate is found by integrating the velocity profile across the pipe cross section:

$$Q_s = Q^{(0)} = \int_{\phi=0}^{2\pi}\int_{r=0}^{1} w^{(0)} r dr d\phi = \frac{\pi}{2}. \tag{5.24}$$

5.2.3 First order ($O(\delta)$) solution

The leading order solution corresponds to a straight pipe and predicts an axisymmetric velocity and director distributions. We pursue the first order solution to investigate the effect of flow curvature on the configuration of the microstructure and the velocity distribution. Studies of other non-Newtonian fluids in curved pipes [154, 163, 167] indicate that the combination of geometry curvature and normal stresses induces a secondary motion. Secondary flows lead to additional viscous losses, while not contributing to the throughput, thus affecting the power consumption. Hence, a correct estimation of the power expenditure can serve as a guideline when selecting the pumping equipment.

The solution of higher order terms follows the same procedure as for the leading order components. Grouping $O(\delta)$ components in the expansions of linear momentum $s-$ and $r-\phi$ equations gives

$$0 = \frac{\partial p}{\partial s} r\cos\phi + \frac{\partial \tau_{rs}^{(1)}}{\partial r} + \frac{1}{r}\frac{\partial \tau_{\phi s}^{(1)}}{\partial \phi} + \frac{1}{r}\tau_{rs}^{(1)} + 2\left[\tau_{rs}^{(0)}\cos\phi - \tau_{\phi s}^{(0)}\sin\phi\right], \tag{5.25}$$

$$\begin{aligned} 0 = &-\frac{1}{r}\frac{\partial^2 N_2^{(1)}}{\partial r \partial \phi} - \frac{1}{r^2}\frac{\partial N_2^{(1)}}{\partial \phi} + \frac{\partial^2 \tau_{r\phi}^{(1)}}{\partial r^2} + \frac{3}{r}\frac{\partial}{\partial r}\tau_{r\phi}^{(1)} - \frac{1}{r^2}\frac{\partial^2 \tau_{r\phi}^{(1)}}{\partial \phi^2} \\ &+\sin\phi\left(\frac{1}{r}\frac{\partial \tau_{\phi r}^{(0)}}{\partial \phi} + \frac{1}{r}(N_2^{(0)}) + \frac{\partial \tau_{ss}^{(0)}}{\partial r} + \frac{\partial \tau_{\phi\phi}^{(0)}}{\partial r}\right) + \cos\phi\left(\frac{1}{r}\frac{\partial N_1^{(0)}}{\partial \phi} + \frac{2}{r}\partial \tau_{r\phi}^{(0)} + \frac{\partial \tau_{r\phi}^{(0)}}{\partial r}\right), \end{aligned} \tag{5.26}$$

where $\boldsymbol{\tau}^{(1)}$ is the $O(\delta)$ contribution to the stress tensor defined in appendix B.3. Similarly

to the leading order solution, calculation of the stress tensor requires the solution of angular momentum equation, whose $O(\delta)$ components read

$$0 = -4\frac{\partial w^{(0)}}{\partial r} n_r^{(1)} \sqrt{\lambda(\lambda+1)} + \sqrt{2}\frac{\partial u^{(1)}}{\partial r}(\lambda+1), \tag{5.27a}$$

$$\begin{aligned} 0 = &-2n_p^{(1)}\sqrt{\lambda^2+\lambda}\frac{\partial w^{(0)}}{\partial r} \\ &+\sqrt{2}\sqrt{\lambda^2-\lambda}\left[(\lambda-1)\tfrac{\partial u^{(1)}}{\partial \phi} + (\lambda+1)\left(\tfrac{\partial v^{(1)}}{\partial r} r - v^{(1)}\right)\right] - (\lambda-1)\sqrt{\lambda^2+\lambda}\left(w^{(0)} r\sin\phi + \tfrac{\partial w^{(1)}}{\partial \phi}\right), \end{aligned} \tag{5.27b}$$

$$0 = 4n_s^{(1)}\frac{\partial w^{(0)}}{\partial r}\sqrt{\lambda(\lambda-1)} - \sqrt{2}\frac{\partial u^{(1)}}{\partial r}(\lambda-1). \tag{5.27c}$$

Expressing $\boldsymbol{\tau}^{(1)}$ in terms of $w^{(1)}$ and $\psi^{(1)}$ (eq. (B.5)) and substituting into the linear momentum balance equations (5.25) and (5.26) we obtain a pair of differential equations of $w^{(1)}$ and $\psi^{(1)}$ (eq. (B.7) and (B.8) in the appendix B.3). Further algebraic manipulation and implementation of no-slip boundary condition (eq. (5.16)) provides the solutions

$$w^{(1)}(r,\phi) = (k_1 r^3 + k_2 r + k_3 + k_4 r^{b-1})\cos\phi, \tag{5.28}$$

$$\psi^{(1)}(r,\phi) = \left(r^4 + \frac{4-b}{b-1}r - \frac{3}{b-1}r^b\right) a\sin\phi, \tag{5.29}$$

where a, b and k_i are material-dependent parameters. The contribution of $O(\delta)$ solution to the flow rate is given by

$$Q^{(1)} = \int_{\phi=0}^{2\pi}\int_{r=0}^{1} w^{(1)} r\,dr\,d\phi = 0, \tag{5.30}$$

so despite the fact that the first order solution affects the distribution of the axial velocity profile, the flow rate remains unchanged. We can use the definition of the stream function to compute components of the secondary velocity

$$u^{(1)}(r,\phi) = -\frac{1}{r}\frac{\partial \psi^{(1)}}{\partial \phi} = -\left(r^3 + \frac{4-b}{b-1} - \frac{3}{b-1}r^{b-1}\right) a\cos\phi, \tag{5.31}$$

$$v^{(1)}(r,\phi) = \frac{\partial \psi^{(1)}}{\partial r} = \left(4r^3 + \frac{-3r^{b-1}b - b + 4}{b-1}\right) a\sin\phi. \tag{5.32}$$

Components of the director field are found by substituting the velocity components into eq. (5.27) and rearranging:

$$n_r^{(1)}(r,\phi) = -\frac{3\sqrt{2}(r^b - r^4)a\sqrt{\lambda+1}}{8r^3\sqrt{\lambda}}\cos\phi, \tag{5.33a}$$

$$n_\phi^{(1)}(r,\phi) = \Bigg(-\frac{\Big[9a\lambda + 7a + \sqrt{\lambda-1}(k_1+1)\sqrt{\lambda+1}\Big]\sqrt{2}}{4\sqrt{\lambda+1}\sqrt{\lambda}} r - \frac{\sqrt{2}\Big[-3a\Big[(b-1)^2\lambda + b^2 - 2b - 1\Big] + k_4\sqrt{\lambda^2-1}(b-1)\Big]}{\sqrt{\lambda(\lambda+1)}(4b-4)} r^{b-3} - \frac{\sqrt{2}(k_2-1)\sqrt{\lambda-1}}{4\sqrt{\lambda}}\frac{1}{r} + \frac{\sqrt{2}\Big[2a(b-4) + (b-1)k_3\sqrt{\lambda^2-1}\Big]}{4\sqrt{\lambda(\lambda+1)}(b-1)}\frac{1}{r^2}\Bigg) \sin\phi, \tag{5.33b}$$

$$n_s^{(1)}(r,\phi) = -\frac{3\sqrt{2}(r^b - r^4)a\sqrt{\lambda-1}}{8r^3\sqrt{\lambda}} \cos\phi. \tag{5.33c}$$

Material dependent coefficients a, b and k_i representative for some liquid crystalline materials are listed in table 5.1. Since $|a| << 1$, the $O(\delta)$ contribution only marginally affects the radial and axial components of the director field (eq. (5.33a) and (5.33c)). There is however a problem with with $n_\phi^{(1)}$, as the last two fractions on the right-hand side of eq. (5.33b) diverge at the pipe axis ($r \to 0$). The singularity can be avoided when the coefficients of r^{-1} and r^{-2} are zero, which happens when

$$\lambda = 1. \tag{5.34}$$

In this limit $\sqrt{\lambda-1} = a = k_3 = 0$, so the coefficients of r^{-1} and r^{-2} in eq. (5.33b) are zero. The limit represents a liquid crystal, whose molecules align with the flow direction, normal stresses are zero, so the secondary flow disappears. The singularity at $r = 0$ comes from the leading order solution, where the director orientation is indeterminate at the pipe axis due to the zero shear rate [168]. That causes problems in calculating the $O(\delta)$ contribution. The $n_\phi^{(1)}$ component is only significant close to the pipe axis (fig. 5.2), where the director field rotates towards the bend axis. The singularity is an artefact of the perturbation approach and violates the requirement $|\boldsymbol{n}|^2 = 1$; however, $n_\phi^{(1)}$ but has little effect on the flow field, as it only contributes to $\boldsymbol{\tau}^{(2)}$, and has therefore no impact on the $O(\delta)$ velocity solution. The problem of an indeterminate director field is eliminated in the Leslie-Ericksen and Beris-Edwards models, where the director director orientation on the pipe axis is such that the Helmholtz free energy is minimised [142, 169].

Table 5.1. Coefficients a and b for different liquid crystals.

Liquid crystal	μ_1	μ_2	λ	a	b	k_1	k_2	k_3	k_4
5CB	1.32	-0.76	1.09	0.012	3.20	0.749	-0.754	0.003	0.003
MBBA	1.16	-0.84	1.02	0.001	3.21	0.749	-0.753	0.002	0.002
PAA	1.73	-0.77	1.06	0.018	3.31	0.750	-0.751	< 0.001	< 0.001
Newtonian fluid [154]	0	0	0	0	0	0.750	-0.750	0	0

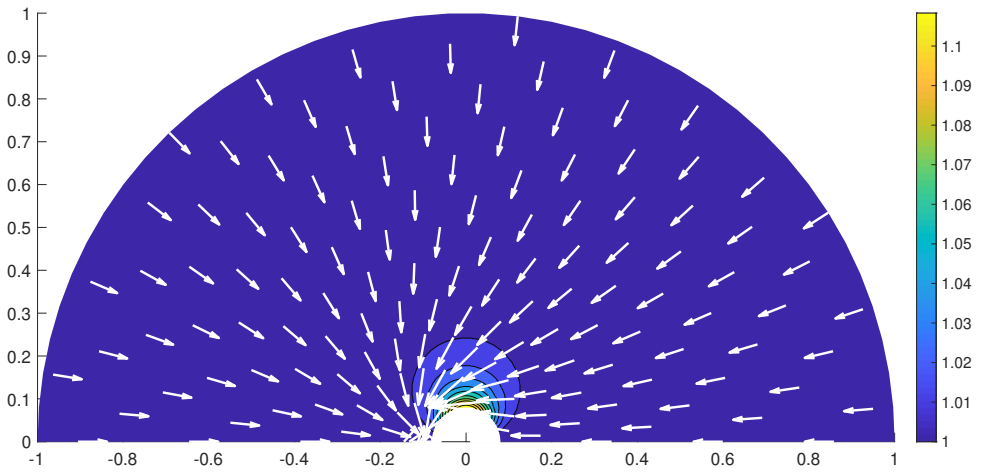

Figure 5.2. Contour of the director magnitude and the projection of the director field onto the $r-\phi$ plane for 5CB, $\delta = 0.2$. Director magnitude increases near the pipe axis, which is caused by a singularity in $n_\phi^{(1)}$. The region of pipe axis is blanked out for visualisation purposes.

5.2.4 Second order ($O(\delta^2)$) solution

We pursue the second order solution to investigate the effect of pipe curvature on the flow rate. Other studies concerned with the fluid motion in curved pipes show that the $O(\delta^2)$ velocity component is of the form [154, 164]

$$w^{(2)}(r,\phi) = w_1^{(2)}(r) + w_2^{(2)}(r)\cos(2\phi), \tag{5.35}$$

where the exact definition of $w_i^{(2)}$ depends on the constitutive equation. The expression is universal and comes from the expansion of axial momentum balance (eq. (5.17)). There cannot be a component proportional to $\sin(2\phi)$, which would violate the symmetry about the centreline. The $O(\delta^2)$ contribution to the flow rate is thus

$$Q^{(2)} = \int_{\phi=0}^{\phi=2\pi}\int_{r=0}^{r=1} w^{(2)}(r,\phi) r dr d\phi = \int_{\phi=0}^{\phi=2\pi}\int_{r=0}^{r=1} w_1^{(2)}(r) r dr d\phi, \tag{5.36}$$

so only solutions for $w_1^{(2)}$ are sought as $w_2^{(2)}$ has no effect on the flow rate. Due to the coordinate induced singularity in $\boldsymbol{n}^{(1)}$, the second-order analytical solution is not realisable for arbitrary μ_i and λ, so we consider the following set of material parameters

$$\mu_1 = -\frac{2\lambda^2\mu_2}{2\lambda^2-\lambda-1}, \qquad \lambda = -\frac{5+\sqrt{17}}{4}, \tag{5.37}$$

which via eq. (B.11b) gives $b = 3$. Fortunately, this is within 10% of the values measured for liquid crystals such as MBBA, 5CB and PAA (table 5.1). λ is negative, which is typical for discotic liquid crystals [158]. Despite that, the calculations are pursued further to observe the effect of pipe curvature on the flow rate. Following the same procedure as with the lower

order contributions, the stream-wise velocity is given by

$$w_1^{(2)}(r) = p_1 r^4 + p_2 r^3 + p_3 r^2 + p_4 r + p_5, \tag{5.38}$$

where $p_i = p_i(\mu_2)$ are constants derived and listed in appendix B.4. The $O(\delta^2)$ contribution to the flow rate is found by integrating the velocity across the pipe and yields

$$Q^{(2)} = \int_{\phi=0}^{2\pi} \int_{r=0}^{1} w^{(2)} r dr d\phi = 2\pi \left(\frac{p_1}{6} + \frac{p_2}{5} + \frac{p_3}{4} + \frac{p_4}{3} + \frac{p_5}{2} \right). \tag{5.39}$$

5.3 Results

5.3.1 Sources of the secondary flow

Curvature induced motion

The role of normal stresses is demonstrated through the $r-$ and $\phi-$ components of the momentum balance (equations (5.6a) and (5.6b), respectively). The effect of $N_1 + N_2$ comes through the ϕ component of the momentum equation (5.6b) and is responsible for propelling the secondary flow in the upper part of the pipe near the wall. Analogously, N_1 appears in the $r-$ component of momentum equation (5.6a) and drives the returning secondary motion at the symmetry plane. The action of normal stresses is schematically depicted in fig. 5.3.

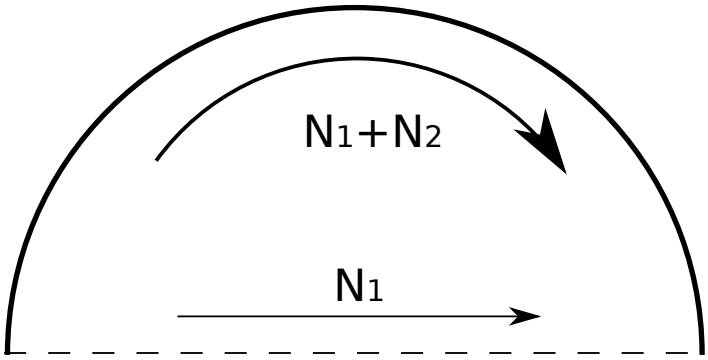

Figure 5.3. Schematic illustration of the action of normal stress differences in the $r - \phi$ plane. Reprinted with permission from [24]. Copyright Elsevier 2022.

Inspecting components of $\boldsymbol{\tau}^{(0)}$ (eq. (B.3) in appendix B.2) we note that

- $\tau_{r\phi}^{(0)} = 0$.
- $N_1^{(0)}$ and $N_2^{(0)}$ are linear in r and independent of ϕ.

Observations above enable us to simplify the $O(\delta)$ contribution of normal stress differences

to the momentum balance in the $r-\phi$ plane (eq. (5.18)):

$$\frac{1}{r}\left\{\frac{\partial[r(\tau_{r\phi}\cos\phi+(N_1+N_2)\sin\phi)]}{\partial r}-\frac{\partial[(-\tau_{r\phi}\sin\phi-N_1\cos\phi)]}{\partial\phi}\right\} = \frac{N_1^{(0)}+2N_2^{(0)}}{r}\sin\phi=(\Psi_1+2\Psi_2)\sin\phi, \quad (5.40)$$

where

$$\Psi_i^{(0)}=-2\frac{N_i^{(0)}}{\frac{\partial w^{(0)}}{\partial r}}, \quad (5.41)$$

is the coefficient of the ith normal stress difference. $\Psi_i^{(0)}$ is undefined on the pipe axis, due to the zero shear rate and indeterminate director orientation. If we neglect the non-Newtonian contribution in $\boldsymbol{\tau}^{(1)}$ (we assume that the first bracket on the right-hand side of eq. (5.18) contains only the Newtonian contribution), the combination of stress imbalance and geometry curvature is the only mechanism driving the secondary flow, and the stream function is given by

$$\psi_{curv}^{(1)}=-\frac{r(r+\frac{1}{2})(1-r)^2}{45}(\Psi_1+2\Psi_2)\sin\phi. \quad (5.42)$$

The derivation of the equation above is presented in appendix B.4.1. A schematic visualisation of the vortex (rotating region of a fluid) is shown in fig. 5.4; its intensity is proportional to $\Psi_1+2\Psi_2$ and the vortex eye has a fixed location $\phi_{cent}=\frac{\pi}{2}$, $r_{cent}\approx 0.42$. The direction of the secondary motion is controlled by the sign of $N_1^{(0)}+2N_2^{(0)}$; if $N_1^{(0)}+2N_2^{(0)}>0$, the stream function is negative and the vortex rotates counter-clockwise in the upper half of the pipe. That is qualitatively similar to the constitutive behaviour represented by the Oldroyd-B and UCM models, where $|N_1|>>|N_2|$ [15], so the rotation is effectively controlled by the sign of N_1. The normal stress differences within liquid crystals can be of any sign [15, 27], hence a flow reversal is possible. Substituting components of $\boldsymbol{\tau}^{(0)}$ defined in eq. (B.3) into eq. (5.40) gives

$$N_1^{(0)}+2N_2^{(0)}=-4(\mu_1+\mu_2)n_r^{(0)}n_s^{(0)}r, \quad (5.43)$$

indicating, that for infinite Ericksen number flows and in the absence of other effects, the sign of $\mu_1+\mu_2$ governs the direction of secondary motion.

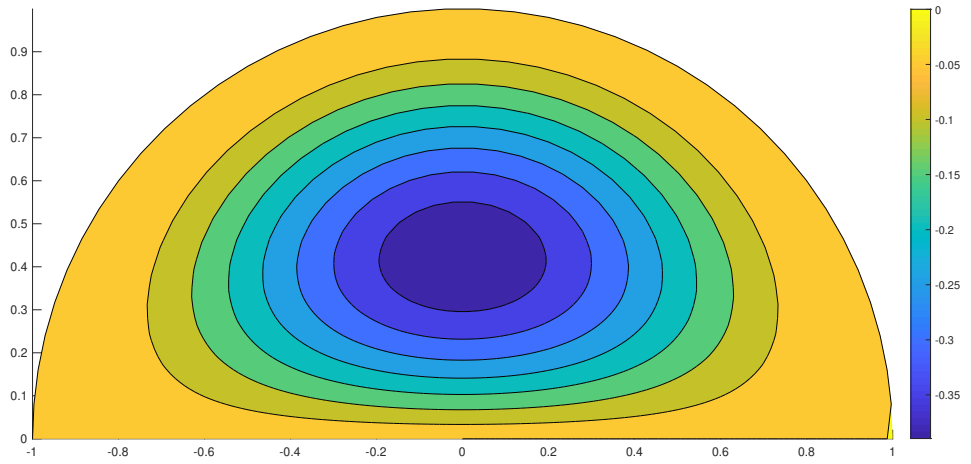

Figure 5.4. Schematic illustration of a vortex driven only by the normal stress difference.

The order of magnitude analysis conducted by Fan et al. [153] show that for zero Reynolds number flows, the pressure gradient and normal stresses balance in the pipe core (fig. 5.5). Therefore, the secondary motion is initiated by the imbalance of normal stresses and ∇p in the near-wall region. When $|N_1| >> |N_2|$, the direction of the secondary motion is governed by the sign of N_1. A positive first normal stress difference represents tension within the microstructure (not within the flow, since $\frac{\partial w}{\partial s} = 0$) [170]. The stress is reduced as the fluid migrates towards the pipe axis, and induces a counter-clockwise motion (fig. 5.6). The mechanism is similar to the rod-climbing effect, where the normal stress reduction occurs when the fluid climbs along the rod [170]. Conversely, when the microstructure is in compression, the fluid reduces its deformation by migrating away from the bend axis, and a clockwise rotation in the upper half of the pipe arises.

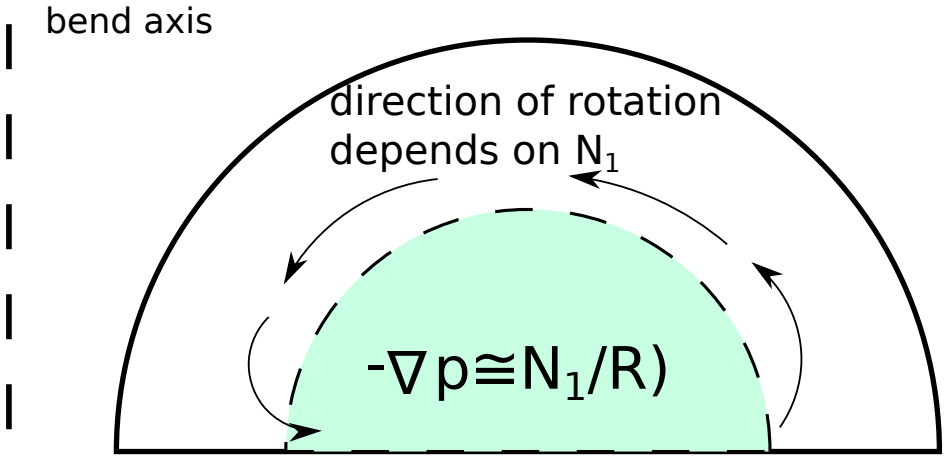

Figure 5.5. The pressure gradient is balanced by normal stresses in the core of a bend.

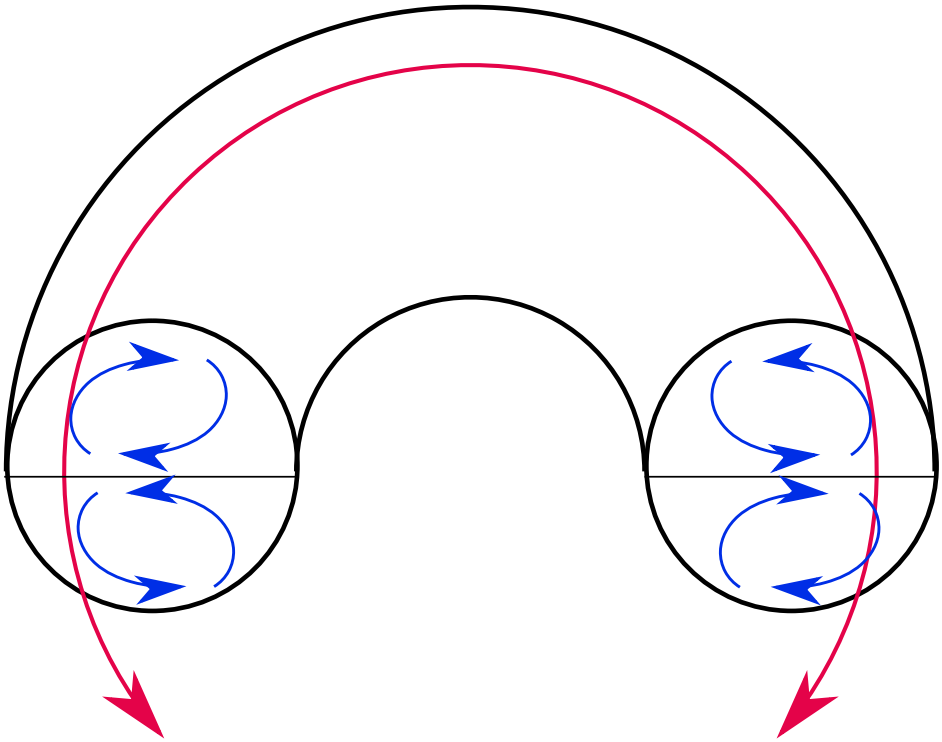

Figure 5.6. Schematic illustration of the effect of microstructure tension on the direction of the secondary motion. The red line represents a flow streamline, whose strain produces a secondary motion. Blue arrows denote the direction of the secondary motion.

In plane stress imbalance

The contribution of stress imbalance to the momentum balance in the $r-\phi$ plane is given by the second term on the right-hand side of eq. (5.18)

$$\left[-\frac{1}{r}\frac{\partial^2 N_2^{(1)}}{\partial r\partial\phi}-\frac{1}{r^2}\frac{\partial N_2^{(1)}}{\partial\phi}+\frac{\partial^2\tau_{r\phi}^{(1)}}{\partial r^2}+\frac{3}{r}\frac{\partial\tau_{r\phi}^{(1)}}{\partial r}-\frac{1}{r^2}\frac{\partial^2\tau_{r\phi}^{(1)}}{\partial\phi^2}\right], \tag{5.44}$$

and indicates that imbalances between $N_2^{(1)}$ and $\tau_{r\phi}^{(1)}$ can produce secondary motion. This mechanism of flow generation was investigated by Ravnik and Yeomans [171], who have shown that the presence of defects in a cylindrical capillary results in stress imbalances, thus inducing a secondary motion; the resultant director and flow fields are schematically depicted in fig. 5.7. The secondary motion is strongest close to the defects, which accelerate the flow [171]. In case of the TIF model, the absence of defects in the steady-state does not allow for secondary flows in a straight pipe. However, due to the combination of flow curvature with microstructure deformation we distinguish other mechanisms that contribute to a flow in the $r-\phi$ plane:

- Shift of the stream-wise velocity field towards the bend axis. The velocity distortion produces additional gradients in the ϕ direction, thus contributing to a stress imbalance;
- Director reorientation caused by a non-axisymmetric flow field;
- Inhomogeneous viscous contribution dependent on the director orientation.

These mechanisms are illustrated in the definition of $\tau_{r\phi}^{(1)}$

$$\tau_{r\phi}^{(1)} = 2n_s^{(0)} \underbrace{n_\phi^{(1)}(\mu_1(n_r^{(0)})^2 + \frac{\mu_2}{4})\frac{\partial w^{(0)}}{\partial r}}_{\text{director reorientation}} + \underbrace{2n_s^{(0)}\frac{\mu_2 n_r^{(0)}\sin\phi}{4}w^{(0)}\frac{\mu_2 n_r^{(0)} n_s^{(0)}\frac{\partial w^{(1)}}{\partial\phi}}{2r}}_{\text{axial velocity shift}}$$
$$+ \underbrace{\frac{\mu_2(n_r^{(0)})^2+2}{2r}\left(\frac{\partial u^{(1)}}{\partial\phi} + \frac{\partial v^{(1)}}{\partial r}r - v^{(1)}\right)}_{\text{inhomogeneous viscous contribution}}. \quad \text{(B.5b)}$$

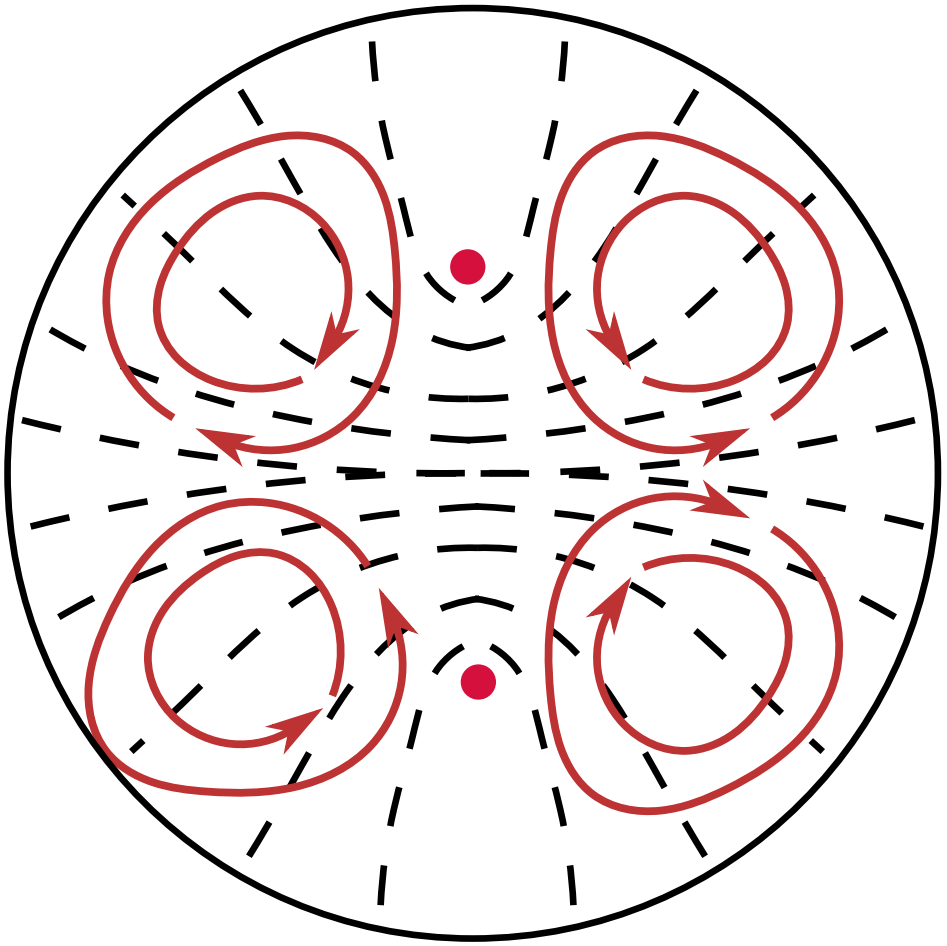

Figure 5.7. Schematic depiction of a secondary flow driven by a pair of defects [171]. Dashed black lines denote director field and the red lines indicate the direction of rotation.

Relative importance of curvature and imbalance effects

The cumulative contribution of the curvature and stress imbalance effects on the secondary flow is described in the expression for the stream function ψ (eq. (5.29). The vortex strength (and thus the secondary flow velocities $u^{(1)}$ and $v^{(1)}$) scale with the parameter a, which is defined as

$$a = -\frac{2\sqrt{\lambda^2-1}(5\lambda\mu_1 + 5\lambda\mu_2 - 3\mu_1)}{9(7\lambda^2\mu_1 + 7\lambda^2\mu_2 + 10\lambda^2 - \lambda\mu_1 - 6\mu_1)}. \quad (5.45)$$

The curvature and imbalance effects can be separated by noting that

- The contribution of $N_1^{(0)} + 2N_2^{(0)}$ depends linearly on $\mu_1 + \mu_2$ irrespective of the value of λ (eq. (5.43)).
- As $\lambda \to 1$, the contribution of μ_1 to the stress imbalance effect vanishes (eq. (5.21), (B.5b)).
- In the limit $\mu_1 = -\mu_2$, curvature effects vanish and for $\lambda \to 1$, the stress imbalance depends only on μ_2.

The above observations enable us to distinguish the separate contributions to the material-dependent constant a:

$$a = -\frac{2\sqrt{\lambda^2-1}\overbrace{[2\lambda(\mu_1+\mu_2)}^{\text{curvature effects}}+\overbrace{3\mu_1(\lambda-1)+3\lambda\mu_2]}^{\text{in plane stress imbalance}}}{9(7\lambda^2\mu_1+7\lambda^2\mu_2+10\lambda^2-\lambda\mu_1-6\mu_1)}, \tag{5.46}$$

with their relative importance described by the factor

$$\chi = \frac{\text{curvature effects}}{\text{stress imbalance}} = \frac{2\lambda(\mu_1+\mu_2)}{3\mu_1(\lambda-1)+3\lambda\mu_2}. \tag{5.47}$$

For the liquid crystals listed in table 5.2, $-1 < \chi < 0$, showing that imbalance effects govern the rotation of the director field; the negative sign of χ implies that curvature effects resist the rotation and thus decrease the magnitude of the secondary flow. In the case of PAA, the ratio χ is closest to -1 (curvature and imbalance effects are of comparable strength), and the secondary flow is the weakest.

Table 5.2. Nematic viscosities converted to match the TIF model [43], the imbalance ratio χ, analytical predictions of horizontal velocities at the pipe axis.

Liquid crystal	μ_1	μ_2	λ	χ	$\frac{u_0}{\delta}$
5CB	1.32	-0.76	1.09	-0.57	$8.9 \cdot 10^{-3}$
MBBA	1.16	-0.84	1.02	-0.26	$10.8 \cdot 10^{-3}$
PAA	1.73	-0.77	1.06	-0.95	$8.7 \cdot 10^{-4}$

5.3.2 Magnitude of the secondary flow at the pipe axis

The secondary flow is generated by the non-Newtonian stresses arising from the flow-director interaction. At $r = 0$, flow is parallel to the symmetry line and the magnitude of the velocity directed towards the bend axis (fig. 5.8) is given by eq. (5.14)

$$\frac{u_0}{\delta} = \frac{u_r\big|_{(r=0,\phi=\pi)}}{\delta} = \frac{u(r=0,\phi=\pi)}{\delta} = \frac{b-4}{b-1}a. \tag{5.48}$$

Velocity predictions are compared in table 5.2. Since u_0 is positive for all materials considered in table 5.2, the fluid rotates clockwise in the upper half of the pipe; the rotation is opposite to inertia [161, 162] and elasticity [154, 164] driven flows. The smallest velocity is predicted for PAA due to the weakest dominance of stress imbalance effects.

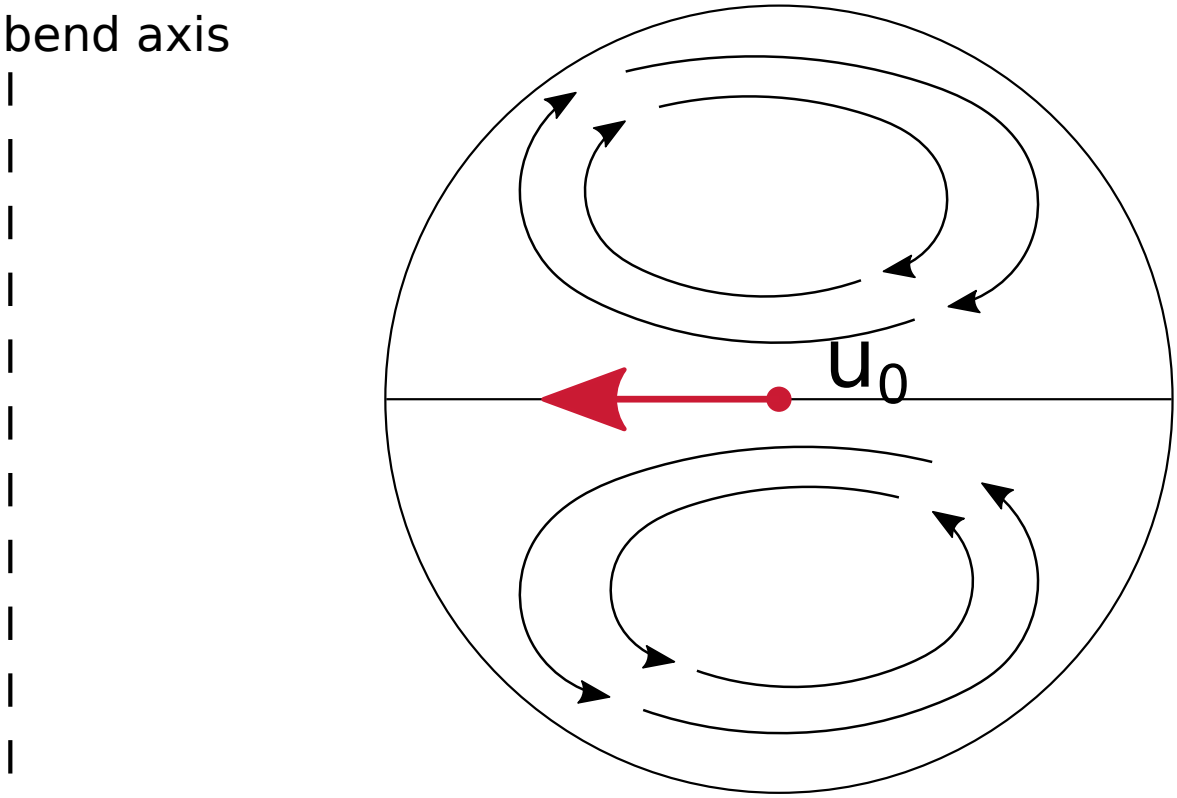

Figure 5.8. Schematic illustration of u_0. When u_0, the secondary flow on the symmetry line is directed towards the bend axis and the fluid rotates in the clockwise direction in the upper half of the pipe.

Based on table 5.2, $|\lambda - 1| << 1$, so choosing this as a basis for a power series expansion of u_0 describes the scaling of the secondary velocity with the tumbling parameter

$$\lim_{\lambda \to 1^+} \frac{(u_0)}{\delta} = -\frac{2(2\mu_1+5\mu_2)\left(-3\mu_2+\sqrt{2}\sqrt{(\mu_2+2)(\mu_2+4)}\right)-6\Big)}{9\sqrt{(\mu_2+2)(\mu_2+4)}(7\mu_2+10)}\sqrt{\lambda-1} + O\left((\lambda-1)^{3/2}\right). \tag{5.49}$$

Above expansion indicates that for λ close to unity the secondary flow scales linearly with $\sqrt{\lambda - 1} \propto n_r^{(0)}$. Therefore, the misalignment between director and stream-wise velocity produces non-zero normal stresses that generate the secondary motion. When $\lambda = 1$, the director perfectly aligns with the stream-wise flow, normal stresses vanish, and the motion in the $r - \phi$ plane ceases. We can extend this result to flows with finite Ericksen numbers: for flows with homeotropic anchoring, the increased misalignment will strengthen the secondary flow. A flow reversal can happen if the curvature and elastic contribution outweigh the stress imbalance. In contrast, the wall-parallel anchoring improves the flow/director alignment and thus weakens the secondary flow.

The intensity of secondary flow on the axis given by eq. (5.48) is plotted in fig. 5.9 as a function of μ_i. Assuming that $\mu_1 > 0$ and $\mu_2 < 0$ (as indicated in table 5.2), u_0 increases as the magnitude of non-Newtonian viscosities increases. In the limit when when $\mu_1 = 0$, $\mu_2 \to -2$, the shear viscosity $\eta_{shear} = 1 + \frac{\mu_2}{2} \to 0$, so even a small normal stress can produce a strong secondary flow.

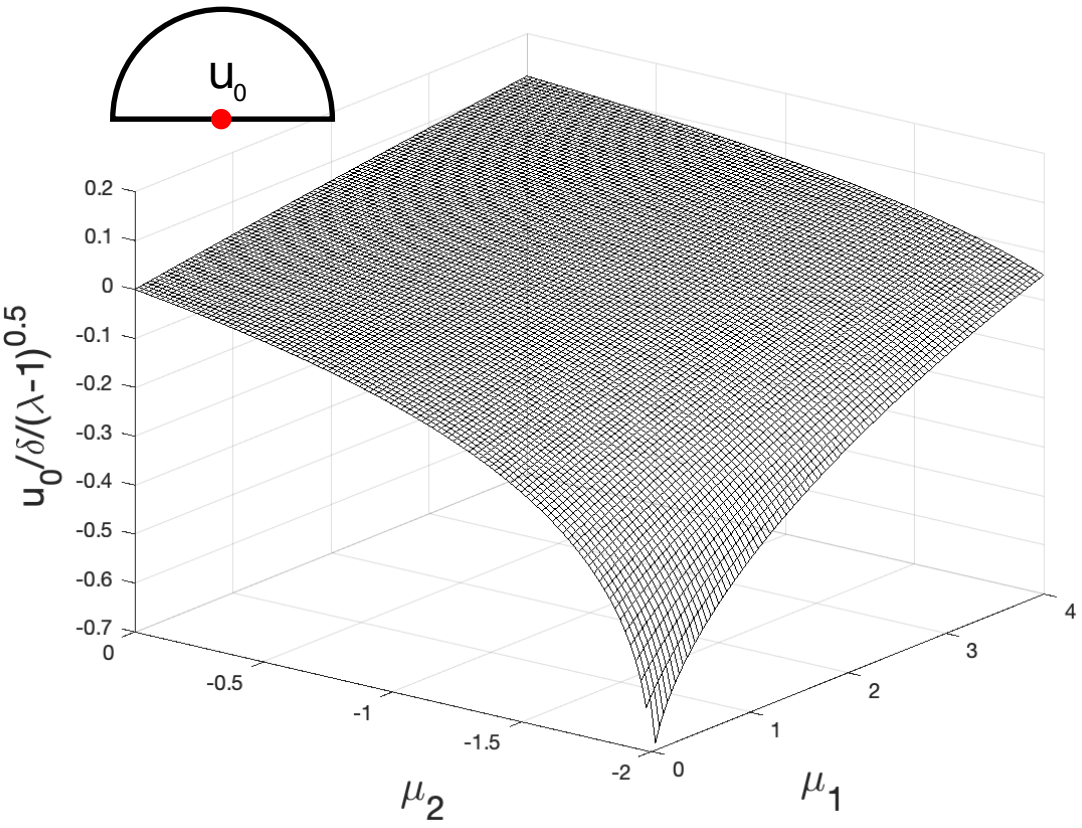

Figure 5.9. Cross-pipe velocity magnitude at the pipe axis as a function of μ_1 and μ_2 for $\lambda \to 1$. Inset: location where u_0 is evaluated. Reprinted with permission from [24]. Copyright Elsevier 2022.

High director/velocity misalignment limit

In this paragraph we consider the effect of significant misalignment between stream-wise flow and the director field on the fluid rheology. The director/velocity misalignment can arise at low Ericksen number flows with homeotropic anchoring and usually varies spatially, depending on the proximity to the wall. Perturbation analysis presented in this chapter cannot account for effects of elasticity and for that reason we consider limit $\lambda \to \pm\infty$ (in which $|n_r^{(0)}| = |n_s^{(0)}| = \frac{\sqrt{2}}{2}$, eq. (5.21)) as a precursor for flows with a significant director/velocity misalignment. When $\lambda \to \pm\infty$, the magnitude of horizontal velocity directed towards the pipe axis is given by

$$\lim_{\lambda\to\infty} \frac{(u_0)}{\delta} = \frac{(\mu_1+\mu_2)\Big[-5\sqrt{2}\sqrt{(\mu_1+\mu_2+2)(\mu_1+\mu_2+4)}+15(\mu_1+\mu_2)+30\Big]\sqrt{2}}{\sqrt{(\mu_1+\mu_2+2)(\mu_1+\mu_2+4)}(63(\mu_1+\mu_2)+90)}. \tag{5.50}$$

The magnitude of secondary flow is a function of $\mu_1+\mu_2$, indicating equal importance of both viscosities. As the μ_i increase, effect of normal stresses becomes more significant, leading to a stronger secondary flow. At the same time, the fluid becomes more viscous, so the magnitude of the secondary motion remains finite for large μ_i, as shown in fig. 5.10.

The effective shear viscosity in the limit of $\lambda = \infty$ is given by

$$\eta_{eff}|_{\lambda=\infty} = 1 + 2\mu_1 \left(n_r^{(0)} n_s^{(0)}\right)^2 + \frac{\mu_2}{2} = 1 + \frac{\mu_1 + \mu_2}{2}, \tag{5.51}$$

and must be greater than zero to avoid violation the second law of thermodynamics [45, 64]. Fig. 5.10 indicates that u_0 strongly increases as $\mu_1 + \mu_2 \to -2$; in this limit the effective viscosity becomes negligible, and even small normal stresses generate secondary flows of large magnitudes.

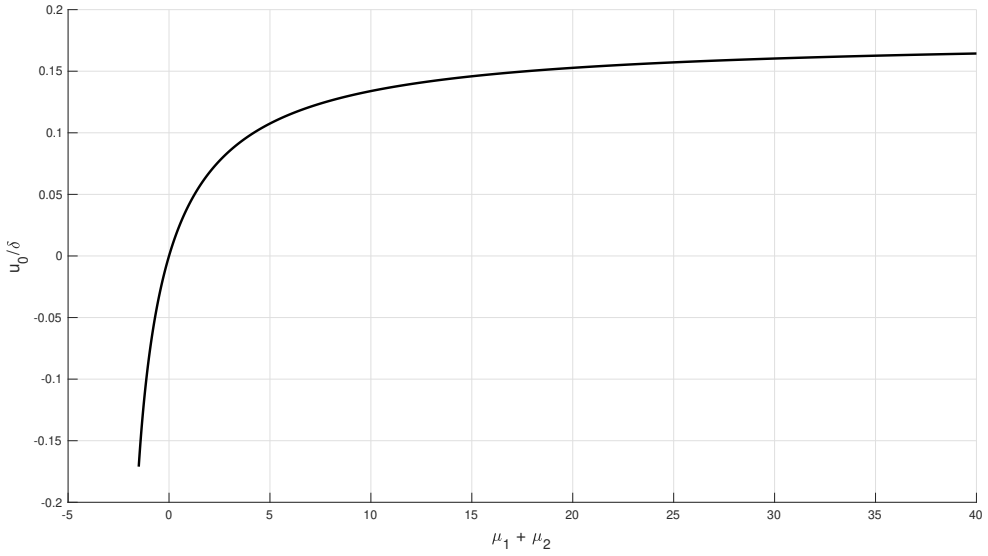

Figure 5.10. Magnitude of the secondary flow as a function of $\mu_1 + \mu_2$.

5.3.3 Structure of the secondary flow

The secondary motion of liquid crystals in a curved pipe consists of a pair of vortices rotating in opposing directions. In the absence of inertial effects, for all liquid crystals considered in this work, the first order contribution to the stream function $\psi^{(1)} > 0$ in the upper half of the pipe, and the fluid rotates counter-clockwise. The stream function distribution is very similar for each of the fluids (PAA, MBBA and 5CB) considered, so only the contour plot of $\psi^{(1)}$ for 5CB is shown in fig. 5.11. Because $|\chi| < 1$, the secondary flow direction is governed by stress imbalance effects, which is unique compared to other viscoelastic models (i.e. Oldroyd-B, UCM). In the latter models, the secondary flow is driven solely by the combination of geometry curvature and normal stresses [154, 164].

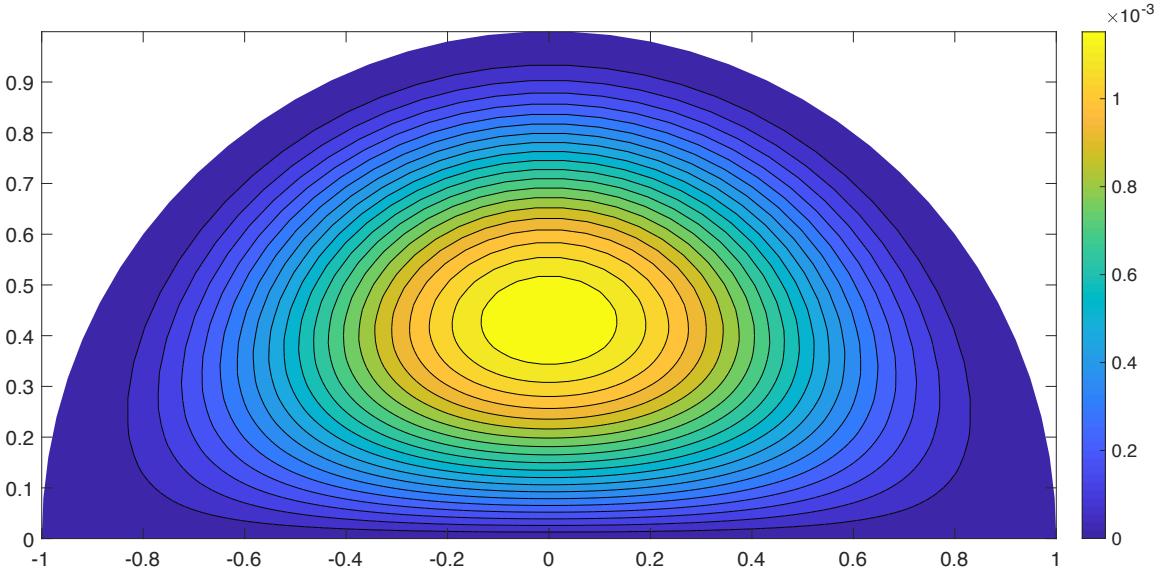

Figure 5.11. Contours of the stream function for 5CB. Positive stream function implies that the flow is rotating clockwise, which is opposite to the direction of a secondary flow driven by inertia. The left side of the plot is closer to the bend axis. Reprinted with permission from [24]. Copyright Elsevier 2022.

5.3.4 Non-uniqueness of the shear viscosity and the effect on the secondary motion

The effective shear viscosity in the TIF model in a straight pipe flow is given by

$$\eta_{eff} = \frac{\tau_{rs}^{(0)}}{\frac{\partial w^{(0)}}{\partial r}} = 1 + 2\mu_1 (n_r^{(0)} n_s^{(0)})^2 + \frac{\mu_2}{2} = 1 + \underbrace{\frac{(\mu_1 + \mu_2)\lambda^2 - \mu_1}{2\lambda^2}}_{\eta_{nN}}. \tag{5.52}$$

A fixed value of η_{nN}, can be composed from an arbitrarily large set of material parameters λ and μ_i. As a result, the normal stress viscosity in materials with fixed η_{eff} need not be constant:

$$\eta_{N1} = \frac{N_1^{(0)}}{\frac{\partial w^{(0)}}{\partial r}} = \frac{-2\eta_{nN} + \mu_2}{\sqrt{\lambda^2 - 1}}. \tag{5.53}$$

The effect is illustrated in fig. 5.12, where η_{eff} varies significantly for a fixed shear viscosity, indicating that materials with similar shear properties can display significantly different extensional behaviour. η_{N1} is particularly sensitive to the value of tumbling parameter in the limit $\lambda \to 1$, as η_{eff} is only weakly affected by λ in this regime (because $n_r^{(0)} \to 0$). Therefore, the intensity and direction of the secondary flow can vary for materials with a fixed shear viscosity (fig. 5.13), indicating that η_{nN} is not sufficient to characterise the complex rheology of liquid crystals. The TIF model contains three material parameters (λ, μ_1, μ_2), so an additional two measurements are required to describe the liquid crystal flow at infinite Ericksen number, e.g. the measurement of the first normal stress difference and the Leslie angle. These, in conjunction with the effective viscosity, enable full characterisation of the material properties of the transversely isotropic fluid.

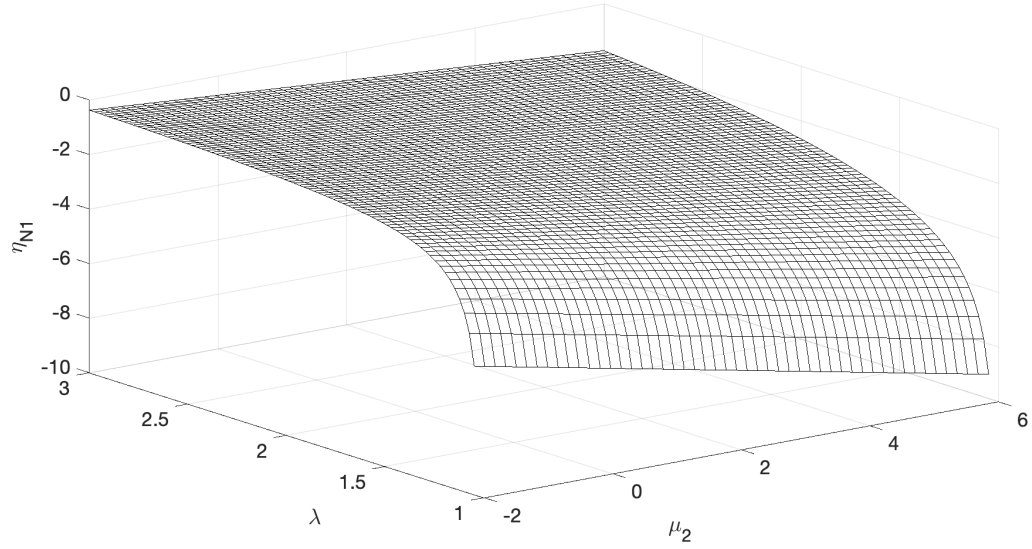

Figure 5.12. The first normal stress viscosity η_{N1} need not be constant for materials with a fixed shear viscosity. Reprinted with permission from [24]. Copyright Elsevier 2022.

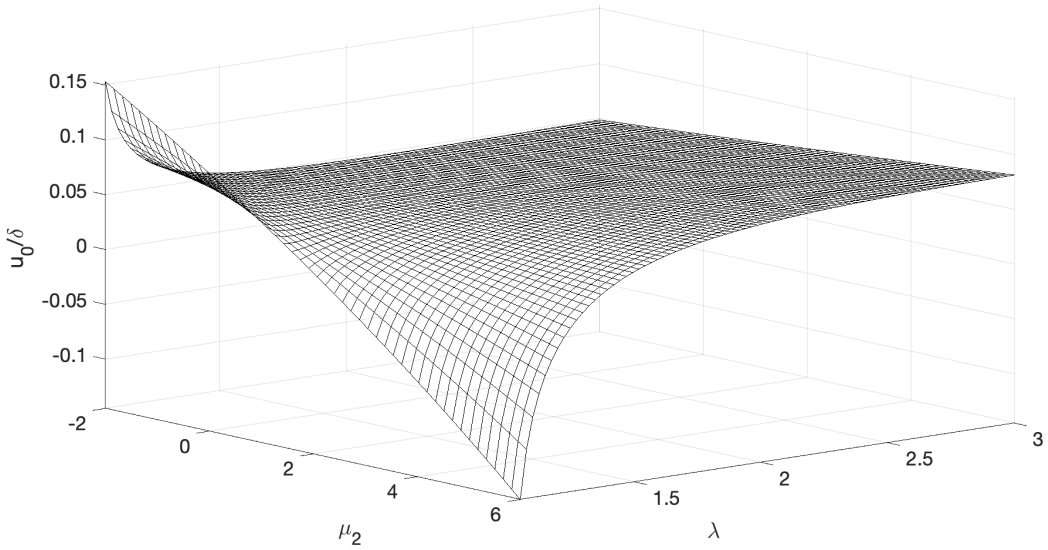

Figure 5.13. The magnitude and direction of the secondary motion in materials with fixed η_{nN} can vary significantly. The plot was obtained for $\eta_{nN} = 1$. Reprinted with permission from [24]. Copyright Elsevier 2022.

5.3.5 Streamwise flow

Curvature effect on the stream-wise velocity and the director

In a straight pipe flow, the axisymmetric velocity profile produces an axisymmetric director distribution, as shown in the inset of fig. 5.14. This is not the case in a curved pipe, where due to the pipe curvature and non-Newtonian contribution the velocity field is given by (eq.

(5.22) and (5.28)):

$$w = w^{(0)} + \delta w^{(1)} + O(\delta^2) = 1 - r^2 + \delta \left[k_1 r^3 + k_2 r + k_3 + k_4 r^{b-1} \right] \cos\phi + O(\delta^2). \quad (5.54)$$

The $O(\delta)$ component shifts the peak axial velocity towards the bend axis (fig. 5.14), which produces velocity and stress gradients in the $\phi-$ direction. The velocity profile on the symmetry line is similar to the Newtonian flow profile (fig. 5.15), indicating that the non-Newtonian stresses have little effect on the stream-wise flow. Compared to the Newtonian fluid, the TIF model introduces new parameters (k_3 and k_4) into the $O(\delta)$ contribution; however, for typical liquid crystals listed in table 5.1, the additional parameters are two orders of magnitude smaller than coefficients k_1 and k_2, and therefore the velocity profile changes only marginally.

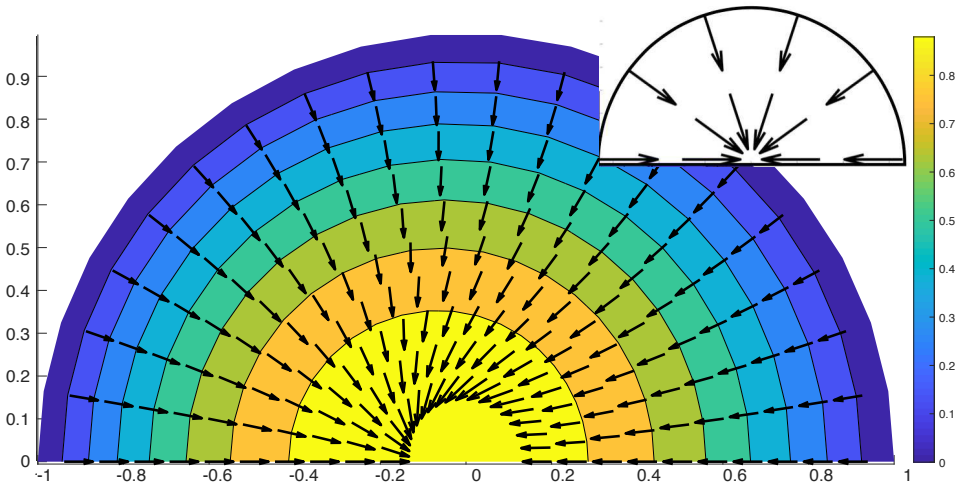

Figure 5.14. Contours of the streamwise velocity field $w = w^{(0)} + \delta w^{(1)}$ and the projection of the director field $\boldsymbol{n} = \boldsymbol{n}^{(0)} + \delta \boldsymbol{n}^{(1)}$ onto the $r - \phi$ plane. A shift in the director field is caused by the shift in the streamwise velocity field. Inset: the director field in a straight pipe. Reprinted with permission from [24]. Copyright Elsevier 2022.

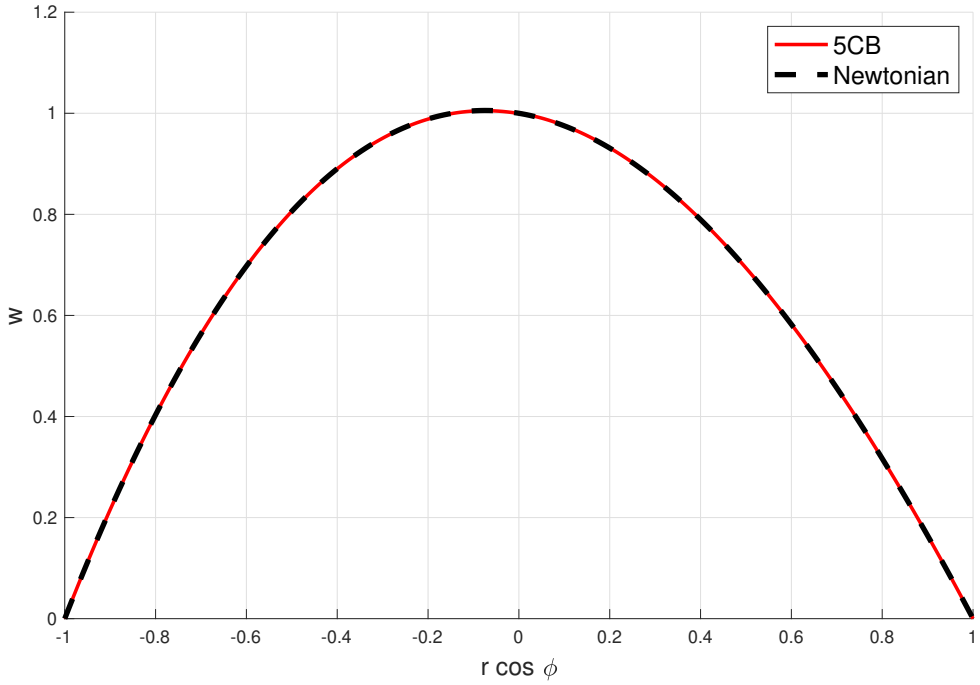

Figure 5.15. Comparison of stream-wise velocity in a curved pipe predicted for a Newtonian and 5CB fluids.

The presence of flow curvature affects the velocity distribution, which in turn distorts the director field: as $r \to 1$, the velocity gradient in the radial direction dominates, and $\boldsymbol{n}$ is confined to the $r - s$ plane, similarly to the straight pipe flow. However, at $r \to 0$, the $O(1)$ component of the velocity gradient vanishes ($\frac{\partial w^{(0)}}{\partial r} = 0$), and the director orientation is governed by $O(\delta)$ effects. As a result, both director and velocity fields shift towards the bend axis, as shown in fig. 5.14.

Power consumption and flow rate

For zero Reynolds number, isothermal flows any pressure work performed on a fluid is balanced by the viscous losses [45, 165]

$$\int \nabla p \cdot \boldsymbol{u} dV = \int \left(\frac{\partial p}{\partial s} w + \underbrace{\frac{\partial p}{\partial r} u + \frac{1}{r} \frac{\partial p}{\partial \phi} v}_{\substack{\text{dissipative contribution of} \\ \text{the secondary motion}}} \right) dV = - \int \Phi dV, \tag{5.55}$$

where $\Phi = \boldsymbol{D} : \boldsymbol{\tau}$ is the dissipation, which represents the work required to overcome resisting stresses. Since the secondary flow is absent in a straight pipe flow, all the pressure work is spent to overcome the viscous losses in the axial direction. The situation is more complex in a curved pipe, where the combination of stream-wise velocity and the secondary flow produce a non-axisymmetric distribution of the dissipation, as shown in fig. 5.16. Smaller dissipation away from the bend axis is only partially compensated for by increased dissipation near the axis.

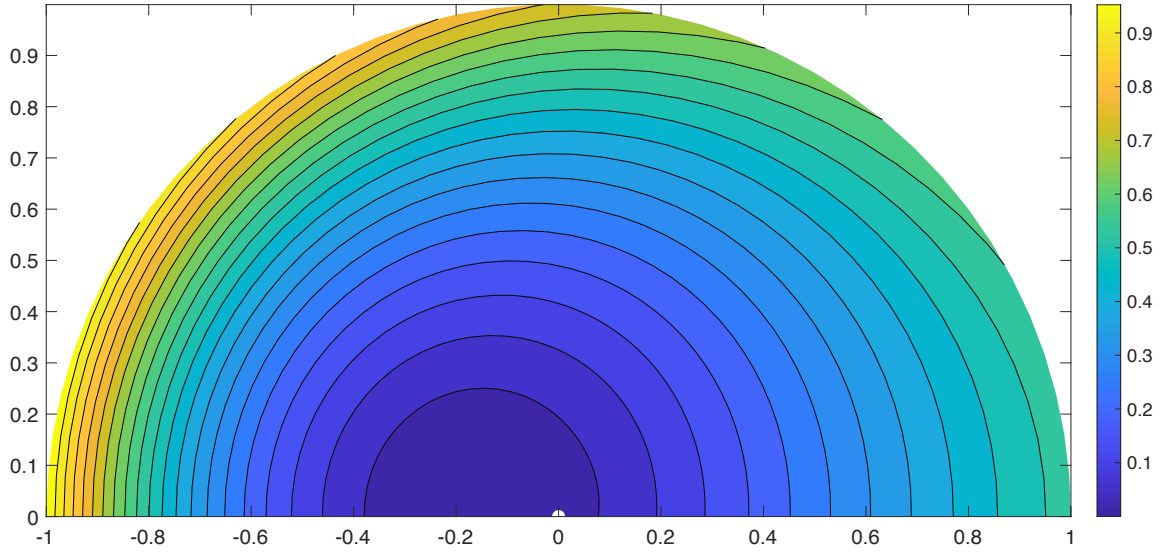

Figure 5.16. Contours of viscous dissipation in the bend cross-section for 5CB. Dissipation is normalised with respect to the maximum value, $\delta = 0.2$. Reprinted with permission from [24]. Copyright Elsevier 2022.

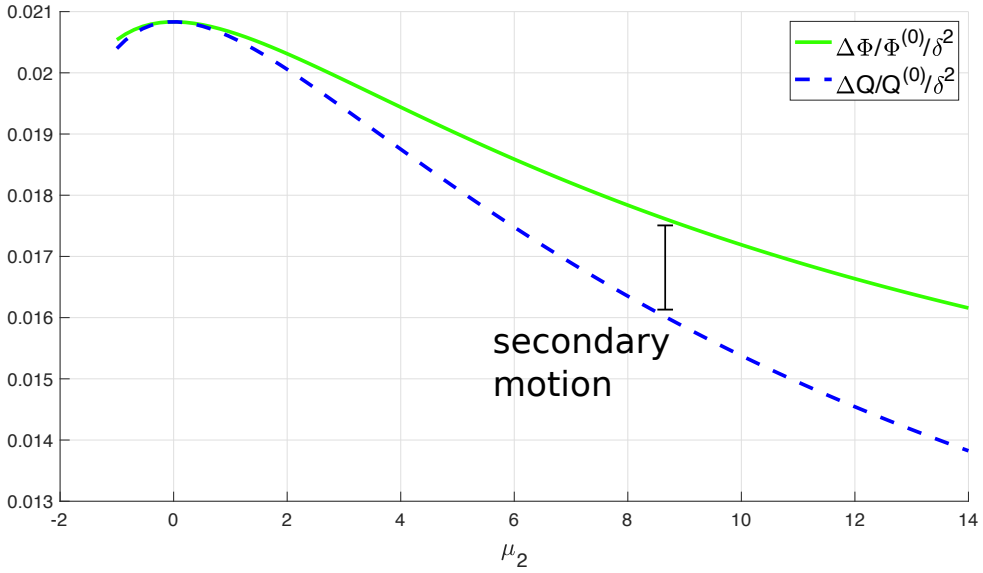

Figure 5.17. Change in the flow rate and the dissipation (at a fixed pressure gradient) compared with the straight pipe flow. The green curve represents dissipation changes, while the blue dashed curve denotes flow rate changes. Reprinted with permission from [24]. Copyright Elsevier 2022.

Compared to a straight pipe flow, the change in the flow rate can be written as

$$\frac{\Delta Q}{Q_s} = \frac{Q_c - Q_s}{Q_s} = \delta^2 \left(\frac{2p_1}{3} + \frac{4p_2}{5} + p_3 + \frac{4p_4}{3} + 2p_5 \right), \tag{5.56}$$

where $Q_c = Q^{(0)} + \delta Q^{(1)} + \delta^2 Q^{(2)}$ is total flow rate in a curved pipe and p_i are defined in appendix B.4. Since $Q^{(1)} = 0$ (eq. (5.30)), the pipe curvature introduces an $O(\delta^2)$ perturbation to the flow rate. For a fixed pressure gradient, the higher flow rate increases the dissipation, as shown in fig. 5.17. The later quantity increases by more due to the secondary motion, which increases the total energy expenditure without contributing to the throughput.

5.3.6 Validity of the perturbation method

The perturbed solutions are valid when higher-order contributions only marginally modify the leading order solution. In the case of Newtonian flows, the Reynolds number and bend curvature δ need to be sufficiently small so that the $O(1)$ solution dominates. In this chapter, we have neglected the inertial contribution to the flow; however, the TIF model introduces additional non-Newtonian stresses that interacts with the flow, and for the solution to remain valid, we require the first order contributions to be smaller than the $O(1)$ solution. A comparison of relative magnitude of $O(1)$ and $O(\delta)$ components is made in table 5.3, which shows that the perturbation solutions are valid for $\mu_1, \mu_2, \lambda > -1$. The case $\mu_1 = -1, \mu_2 = -1.5, \lambda = 2$ is unphysical, which manifests in the excessively large contribution of the $O(\delta)$ director components. The shear viscosity $\frac{(\mu_1+\mu_2+2)\lambda^2-\mu_1}{2\lambda^2}$ in a shear flow becomes negative, which produces in a complex coefficient b. As the magnitude of the TIF parameters increases, the relative importance of the first order solution also increases, reducing the solution accuracy. Therefore, in order to avoid excessive, leading order contributions, it is recommended to use material parameters in the range $-1 < \mu_1, \mu_2 < 7$, $1 \leq |\lambda| < 7$ (well within the range of material parameters presented in table 5.2).

Table 5.3. The relative magnitude of first order terms with respect to the leading order solution for $\delta = 0.2$. Red values indicate a singular behaviour, where radial and axial director components diverge.

μ_1	μ_2	λ	max $\left(\left\|w^{(1)}/w^{(0)}\right\|\right)$	max $\left(\left\|n_r^{(1)}/n_r^{(0)}\right\|\right)$	max $\left(\left\|n_s^{(1)}/n_s^{(0)}\right\|\right)$
-1	-1	2	0.21	0.05	0.19
-1	-1.5	2	0.53	642	208
-1	-1.5	1.1	0.16	0.08	<0.01
2	-1.5	2	0.13	<0.01	<0.01
3	5	2	0.14	0.19	0.06
7	7	7	0.14	0.21	0.16
10	10	10	0.14	0.23	0.19
15	15	15	0.14	0.26	0.23

5.4 Summary

The creeping flow of a transversely isotropic fluid in a curved pipe is analytically described through a perturbation expansion. We show that the secondary motion arises as a consequence of the misalignment between stream-wise flow and director, which leads to generation of non-Newtonian stresses. In the limit of $|\lambda - 1| << 1$, the magnitude of secondary flow in the $r - \phi$ plane scales with $n_r^{(0)}$, while for flows with a large director/velocity misalignment, μ_1 and μ_2 are equally important, and the intensity of the secondary flow depends on $\mu_1 + \mu_2$.

We distinguish two different effects responsible for the secondary flow: 1) a combination of the normal stresses with the pipe curvature; 2) an imbalance of the second normal stress difference and the shear stress in the $r-\phi$ plane. The latter effect can also be present in straight

pipe flows of active nematics, where an imbalance of elastic stress caused by defects produces a secondary flow. In typical liquid crystalline fluids (5CB, PAA, MBBA), the curvature and stress imbalance effects work against each other, the latter of which is dominant. For that reason, the secondary flow rotates in the direction opposite to inertially and elastically driven flows [154, 161]. There are two possibilities to tune the secondary flow: 1) by controlling the magnitude of the parameter a (defined in eq. (B.11)), the strength of the secondary motion can be effected; 2) by applying an external field (electric, magnetic), the director field can be rotated, which would alter the non-Newtonian stress tensor, and therefor influence both the secondary and streamwise motions.

A fixed effective shear viscosity of a transversely isotropic fluid can be constructed in infinitely many ways from the material parameters λ, μ_i. That does not guarantee a fixed extensional characteristics, and η_{N_i} can be orders of magnitude different from the shear viscosity, depending on the choice of material parameters. As a result, materials with a fixed effective viscosity can induce secondary flows of different intensities and directions. Hence, an accurate characterisation of transversely isotropic fluids requires other flow characteristics, such as first and second normal stress differences.

The geometry curvature affects the stream-wise velocity profile, which, compared to the straight pipe solution, is shifted towards the bend axis. The perturbed velocity profile deforms the director field, whose orientation is governed by the $O(1)$ components at the wall and $O(\delta)$ contribution near the pipe axis. For a fixed pressure gradient, the flow curvature increases both the flow rate and the dissipation. The increase in the latter quantity is more significant, which is a manifestation of additional losses induced by the secondary flow. Therefore, it is necessary to use stronger pumps to overcome additional viscous losses.

The next chapter provides an extension of the analysis made in this chapter by considering the effect of wall anchoring in the finite Ericksen number regime and assessing the flow and director development upstream/downstream of the bend.

Chapter 6

Flow of Leslie-Ericksen fluids through 90^o bends

This chapter investigates the flow of Leslie-Ericksen fluids through bends at finite Ericksen numbers. Simulations are conducted to: 1) examine the effect of elasticity on the director and flow fields; 2) assess the effect of bend entrance and exit on the velocity and director field; 3) estimate the additional pressure drop due to the presence of a bend.

6.1 Geometry

The geometry considered in this chapter is schematically depicted in fig. 6.1 and consists of two straight pipes with a radius r_0^* connected by a 90^o bend. The outlet pipe has a length of $30r_0^*$ to provide enough space for flow and microstructure to reach a fully developed state after leaving the bend. R_0^* denotes the bend radius, and bend curvature has the same definition as in the previous chapter ($\delta = \frac{r_0^*}{R_0^*}$). The flow is laminar, which enables us to assume that it is symmetric about the $z = 0$ plane [161, 172]; thus, in order to reduce the computational cost of simulation, we only consider flow above the symmetry plane.

6.2 Methodology

6.2.1 Governing equations

The motion of a Leslie-Ericksen fluid in a bend is described by a set of Navier-Stokes equations. Numerical solutions are obtained in OpenFOAM and we have used our new solver *rheoFoam2* (introduced in section 3.1) to model the director and stress evolution. The linear momentum balance is supplemented with a viscoelastic stress tensor describing the microstructure contribution

$$\boldsymbol{\tau}^* = \alpha_1^* \boldsymbol{nnnn} : \boldsymbol{D}^* + \alpha_2^* \boldsymbol{nN^*} + \alpha_3^* \boldsymbol{N}^* \boldsymbol{n} + \alpha_4^* \boldsymbol{D}^* + \alpha_5^* \boldsymbol{nn} \cdot \boldsymbol{D}^* + \alpha_6^* \boldsymbol{D}^* \cdot \boldsymbol{nn} - \frac{\partial f_d^*}{\partial \nabla^* \boldsymbol{n}} \cdot (\nabla^* \boldsymbol{n})^T, \tag{2.52}$$

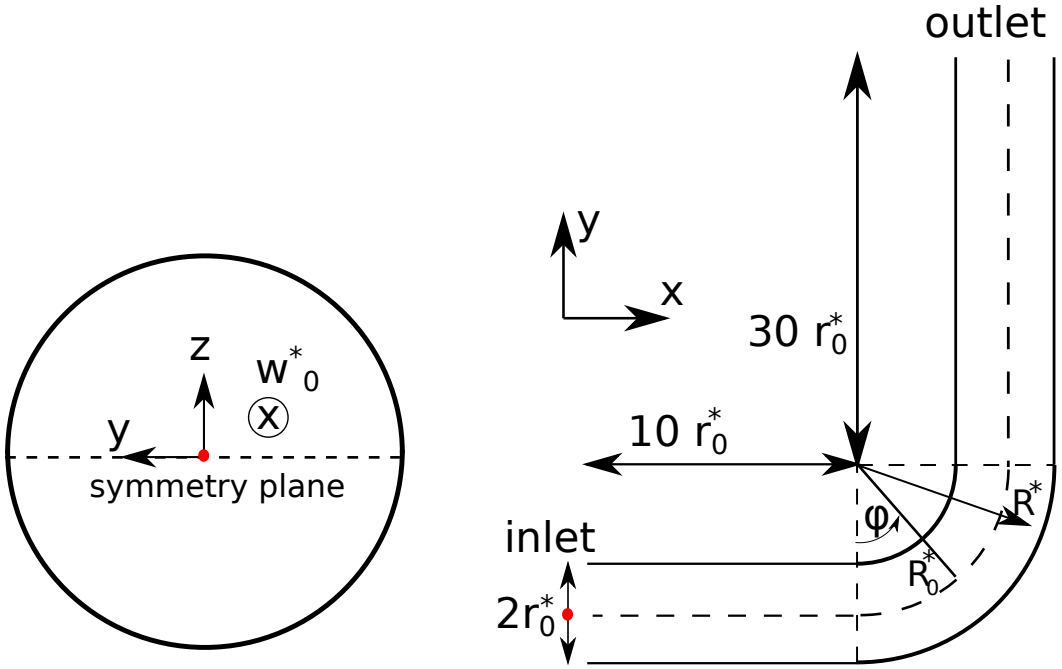

Figure 6.1. Schematic depiction of a 90^o pipe bend and the pipe cross-section at the inlet. The red dot denotes the centre of the coordinate system, which is located at the axis of inlet.

where the starred variables refer to dimensional quantities; α_i^* are Leslie viscosities, $\boldsymbol{N}^*$ denotes the co-rotational time derivative of the director field and f_d^* is the Helmholtz free energy, for which the one-constant approximation (eq. (2.44)) is used. Dimensionless variables appear without stars and are non-dimensionalised in the same fashion as in the previous chapter (eq. (5.5)). The stress is computed based on the director orientation, whose evolution is described by the angular momentum balance

$$\boldsymbol{h}^* - \boldsymbol{nn}\cdot\boldsymbol{h}^* - \gamma_2^*(\boldsymbol{n}\cdot\boldsymbol{D}^* - \boldsymbol{nnn}:\boldsymbol{D}^*) - \gamma_1^*\boldsymbol{N}^* = 0, \tag{2.53}$$

where the molecular field $\boldsymbol{h}^* = -\frac{\delta f_d^*}{\delta \boldsymbol{n}}$ quantifies system's departure from the minimum Helmholtz free energy.

6.2.2 Boundary conditions

Boundary conditions employed in simulations are summarised in table 6.1; we impose a uniform velocity distribution at the inlet, with the director aligned in the flow direction. The outlet is located far enough downstream the bend exit, so the flow is fully developed; hence, we prescribe a zero-gradient boundary condition for velocity and director.

Results of chapter 4 suggest that the fluid rheology significantly depends on the Ericksen number and the type of wall anchoring. Director orientation not only affects the velocity profile but also controls the magnitude of normal stresses, which were shown to have a significant impact on the flow in a curved pipe [24, 167]. Therefore, we consider configurations with both homeotropic and wall-parallel anchoring; details on the implementation of director boundary conditions in OpenFOAM are given in appendix C.1.

Table 6.1. Boundary conditions for the velocity, director and pressure fields.

location	velocity	director	pressure
inlet	uniform, fixed value $w^* = \bar{w}_0^*$	flow-aligned, $\boldsymbol{n} = [1, 0, 0]$	zero-gradient
outlet	zero gradient	zero gradient	fixed value $p = 0$
wall	no-slip	homeotropic/wall parallel	zero-gradient
symmetry plane	symmetry	symmetry	symmetry

The Ericksen number is defined based on the inlet flow properties, in the same manner as in chapter 4:

$$Er = \frac{\bar{w}_0^* r_0^* \alpha_4^*}{K^*}, \tag{6.1}$$

where $\bar{w}_0^*$ is the uniform inlet velocity, r_0^* is the pipe radius, α_4^* represents a viscosity scale and K^* is the Frank constant.

6.2.3 Material parameters

We consider three different fluids whose material properties are listed in table 6.2. Parameters of fluid 1 are identical to 5CB [43]; it has a small Leslie angle and $-1 < \chi < 0$ (χ and describes the relative importance of curvature and imbalance effects (section 5.3.1)). Parameters for fluids 2 and 3 are selected to investigate the effect of higher Leslie angles and positive χ (curvature and stress imbalance effects are additive in the limit of infinite Ericksen number) on the flow behaviour.

Table 6.2. Nematic viscosities of the fluids considered in this chapter.

α_i(Pa · s)	α_1	α_2	α_3	α_4	α_5	α_6	θ_L	χ
Fluid 1	-0.0060	-0.0812	-0.0036	0.0652	0.064	-0.0208	12^o	-0.57
Fluid 2	-0.01	-0.30	-0.05	0.200	0.400	0.050	22^o	3.02
Fluid 3	-0.01	-0.091	-0.046	0.200	0.173	0.037	35^o	2.03

6.2.4 Computational domain and solution details

Simulations are conducted on a bend with curvature $\delta = 0.2$ using three differently refined meshes: $M_1 = 118\ 200$ cells (coarse), $M_2 = 799\ 600$ cells (fine), $M_3 = 2\ 007\ 500$ cells (refined). Cross sections of the coarse mesh on the inlet and symmetry plane are shown in fig. 6.2.

Simulation on the coarse grid is initialised with a stationary fluid and a horizontal director field. Spatial gradients are computed with the least squares method [107] and the convergence criteria for all variables are set to 10^{-8}. All simulations are run using four cores. The

numerical solution is first obtained on a coarse grid; we then use the *mapFields* utility to map the coarse grid solution as an initial condition for the fine mesh M_2 and reduce the computational cost. The procedure is repeated on the refined M_3 mesh. The calculation requires about $10 \cdot 10^{15}$ floating point operations on the M_1 mesh and takes about six times longer than the laminar, Newtonian solution.

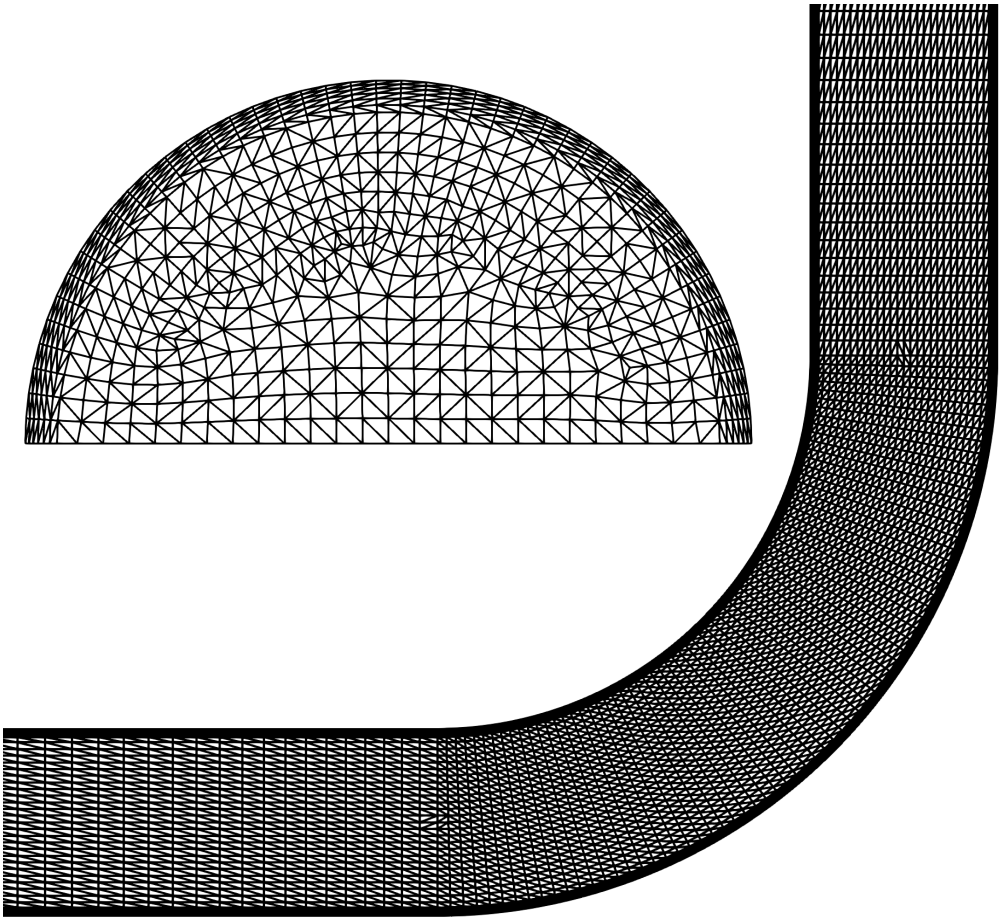

Figure 6.2. Computational domain of the bend used for simulations. For visualisation purposes only the coarse grid M_1 is shown. The grid is refined in the near-wall region to capture sharp gradients of the director field, as the size of flow-elastic layer scales with $Er^{-0.5}$.

6.3 Results

6.3.1 Director field in a bend

The distribution of the director field in a bend shares characteristics with the flows already analysed in previous chapters (flow at finite Er in a straight pipe and flow at infinite Er in a curved pipe). The main features of the microstructure distribution are:

- Shift of the director field towards the bend axis
  - At high Ericksen numbers, a displacement of the director field is caused by the distortion of the velocity profile, whose peak moves closer to the bend axis. Due to a small elastic contribution, the director field nearly aligns with the flow, and the

stream-wise velocity profile resembles the Newtonian solution, for which the peak velocity occurs at [154] $\frac{R^*-R_0^*}{r_0^*} \approx -0.074$ when $\delta = 0.2$; the location coincides with the location where the director aligns with the flow direction ($\theta = 0$), as shown in fig. 6.3.

– For small Ericksen number flows, the director orientation is governed by elastic effects, which act to minimise the Helmholtz free energy. The curved pipe geometry is too complex to obtain analytical solutions for the director orientation even at zero Ericksen number; however, analytical solutions in a curved duct can provide a qualitative explanation. Calculations performed in appendix C.2 indicate that for flows with the homeotropic anchoring, in the limit of one-constant approximation, the Helmholtz free energy in a curved duct is minimised by the angle θ (shown in fig. 6.3) that measures the director deviation from the stream-wise direction

$$\theta(r) = \pi \frac{\ln\left(\frac{r}{r_1}\right) + \ln\left(\frac{r}{r_2}\right)}{\ln\left(\frac{r_2}{r_1}\right)}, \tag{C.5}$$

where r_1 and r_2 are inner and outer radii of the duct. Therefore, the location where the director aligns with the axial flow $r^*(\theta = 0) = R_0^*\sqrt{(1+\delta)(1-\delta)} \leq R_0^*$ moves towards the bend axis as the bend curvature increases. The solution is schematically visualised in fig. 6.4.

• Wall anchoring governs the director orientation in the near-wall region (director boundary layer), whose size is determined by the Ericksen number, as shown in fig. 6.3. For configurations with homeotropic anchoring, the director field escapes from the radial into the axial direction. In contrast, there is little change in director orientation in configurations with wall-parallel anchoring due to small Leslie angles.

Distribution of the director field with homeotropic and wall-parallel boundary conditions is schematically illustrated in fig. 6.5.

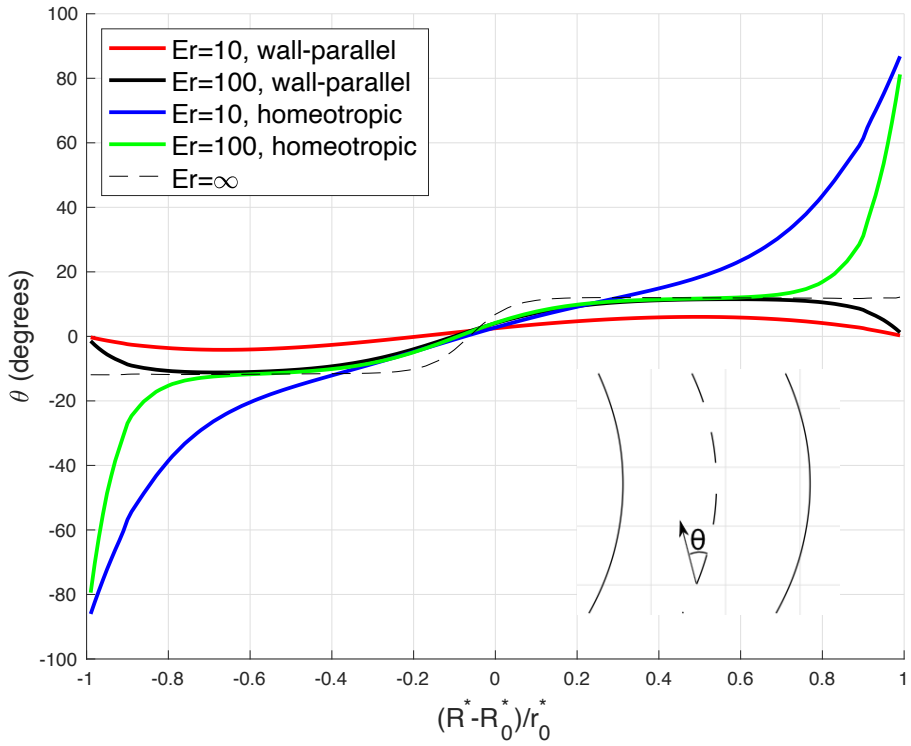

Figure 6.3. Variation of the director orientation at the centre of the bend predicted for fluid 1; distributions for fluids 2 and 3 are similar and therefore not shown. θ denotes an angle between director and flow direction.

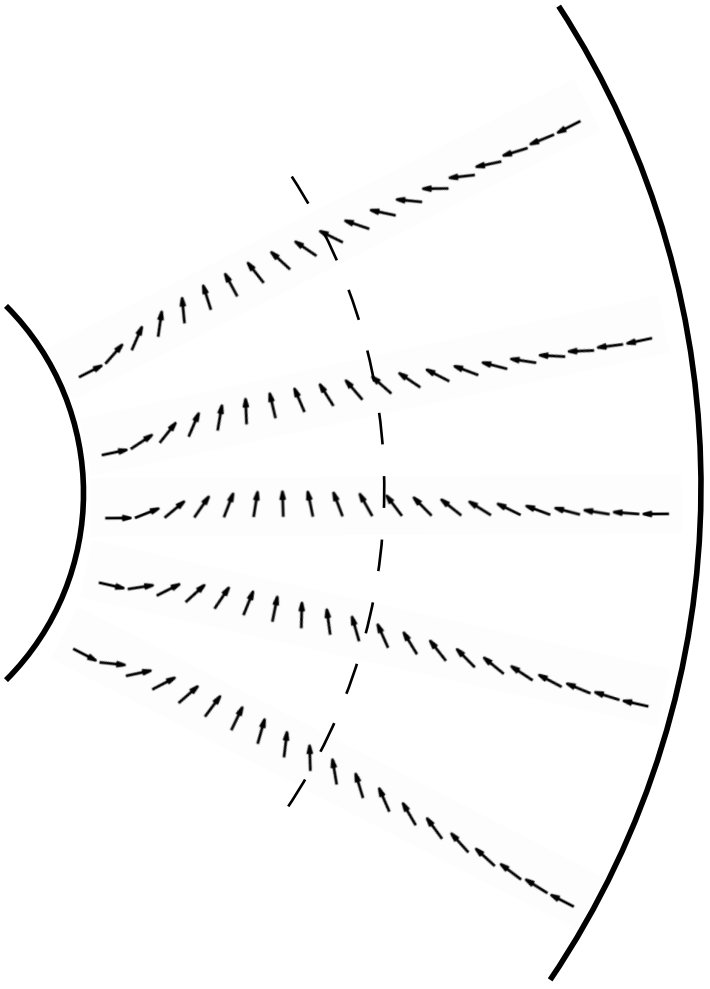

Figure 6.4. Due to the geometry curvature, the director field at $Er = 0$ moves towards the bend axis to minimise the Helmholtz free energy.

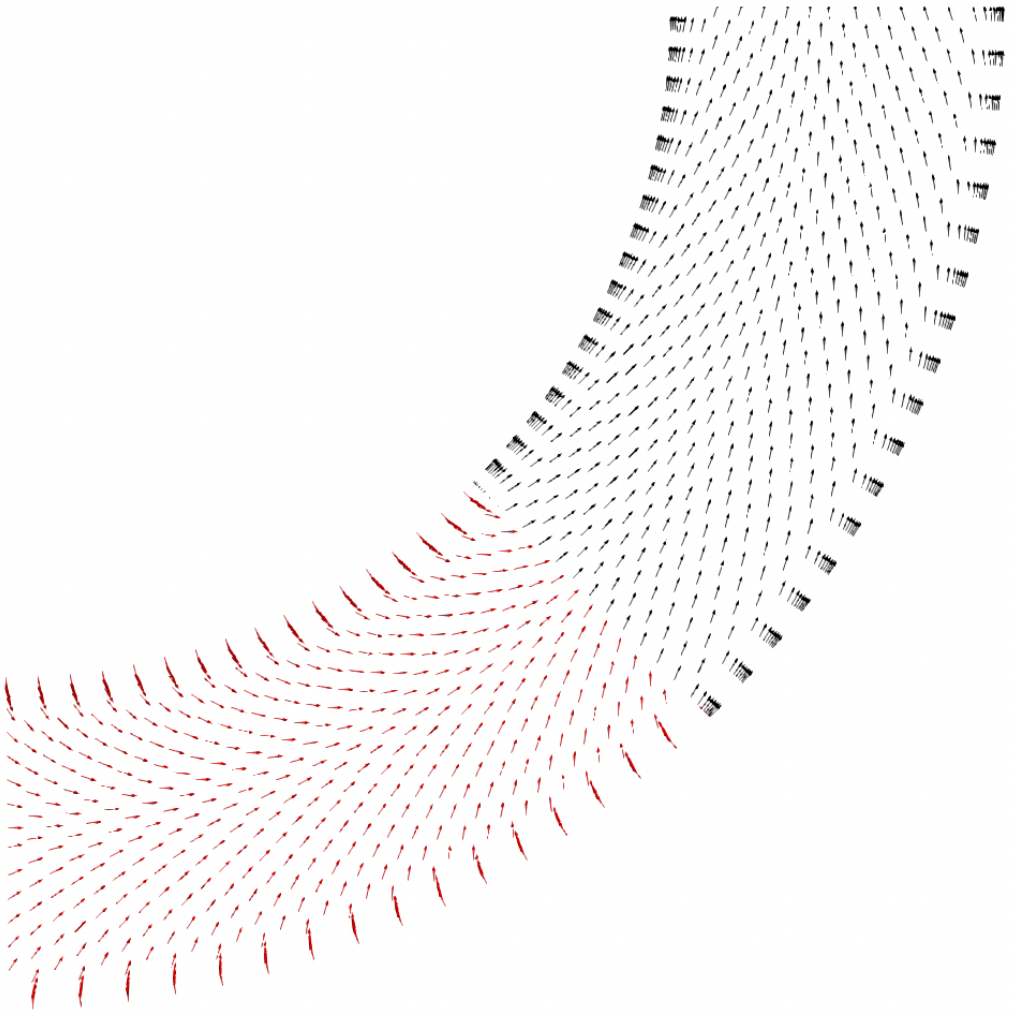

Figure 6.5. Director profile for $Er = 10$ at the symmetry plane of the bend for fluid 3. The red colour represents orientation for homeotropic anchoring and the black colour is the result for a wall-parallel anchoring.

6.3.2 Stream-wise velocity

The geometry curvature has a similar effect on the stream-wise velocity profile as on the director field, and the velocity peak shifts towards the bend axis, as shown in fig. 6.6. For configurations with homeotropic anchoring, the near-wall director-velocity alignment produces a high viscosity layer; wall-parallel anchoring results in a nearly uniform viscosity distribution with a Newtonian-like velocity profile.

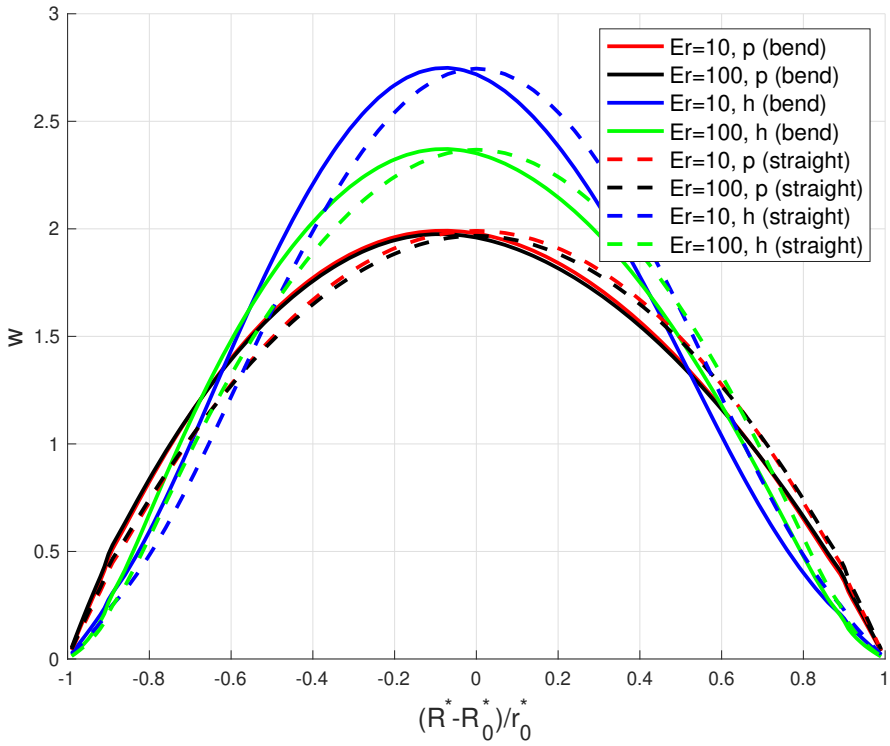

Figure 6.6. Stream-wise velocity profile in the bend centre predicted for 5CB. Letters h and p refer to homeotropic and wall-parallel respectively.

6.3.3 Secondary flow

Analyses made in the previous chapter describe two independent mechanisms that generate the secondary flow: 1) the combination of normal stresses with geometry curvature, whose strength scales with $N_1 + 2N_2$ and; 2) the imbalance of $N_2^{(1)}$ and $\tau_{r\phi}^{(1)}$ in the $r - \phi$ plane, ($N_2^{(1)} = N_2^{bend} - N_2^{straight}$ is the change in the second normal stress difference due to the geometry curvature, $\tau_{r\phi}^{(1)}$ has an analogous meaning). $\boldsymbol{\tau}$ is the dimensionless stress tensor non-dimensionalised through eq. (5.5) and N_i are dimensionless normal stress differences. The relative importance of these effects in the limit of infinite Ericksen number (no elasticity) is quantified through $\chi = \frac{\text{curvature effects}}{\text{imbalance effects}}$. For liquid crystals considered in the previous chapter $-1 < \chi < 0$, suggesting that imbalance effects control the direction of the secondary motion; negativity of χ indicates that curvature and imbalance effects oppose each other ($\chi > 0$ for fluids 2 and 3, so these effects are additive, which results in stronger secondary flows). The situation becomes more complex when elastic effects are present as the sign and magnitude of χ depend on Ericksen number and wall anchoring.

Fig. 6.7 and 6.8 show that the distribution of normal stresses in the bend centre is significantly affected by the Ericksen number and type of wall anchoring. In order to measure the relative change of a given effect ($N_1 + 2N_2$ or $N_2^{(1)}$) with respect to the infinite Ericksen number limit we use the following expression

$$\%(E) = \frac{E(Er)}{E(Er=\infty)} = \sqrt{\frac{\sum [E(Er)^2]}{\sum [E(Er=\infty)^2]}}, \tag{6.2}$$

where $E = N_1 + 2N_2$ or $E = N_2^{(1)}$. The relative changes are compared in table 6.3 and indicate that the reduction of Ericksen number in flows with the wall-parallel anchoring decreases the contribution of curvature effects more significantly than the contribution of flow imbalance effects. As a result there is a small increase in the intensity of the secondary motion, as shown in fig. 6.9. That is not the case for configurations with homeotropic anchoring, where the increased contribution of curvature effects surpasses the strength of stress imbalance effects and a flow reversal occurs at lower Ericksen numbers (fig. 6.9).

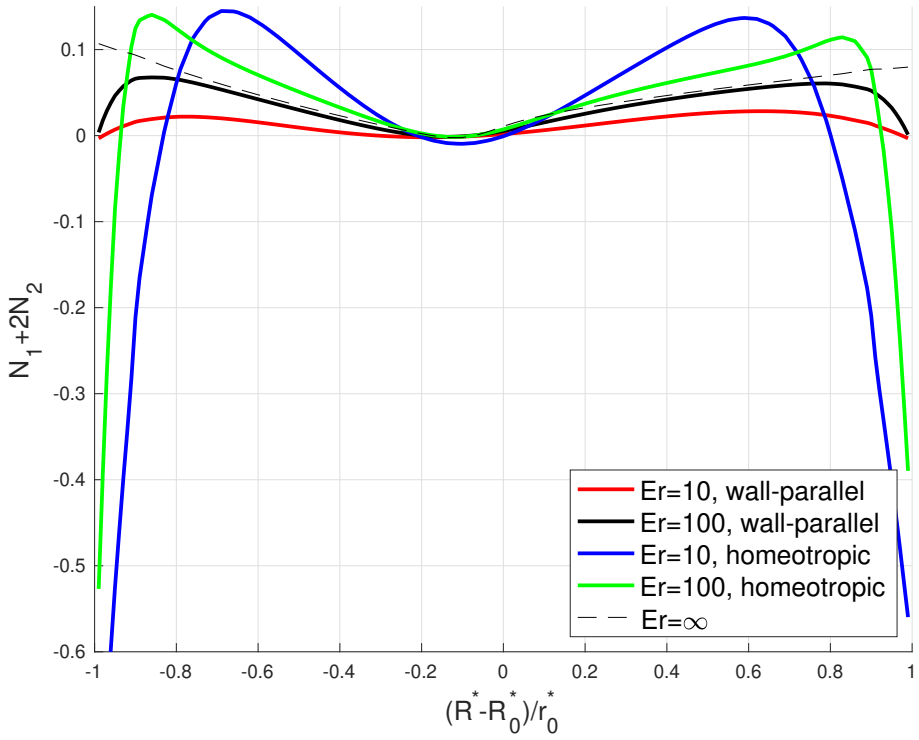

Figure 6.7. Variation of the curvature effect (dimensionless) at the symmetry line for the fluid 1. Stresses are normalised by the shear scale $\frac{w_0\alpha_4}{r_0^*}$.

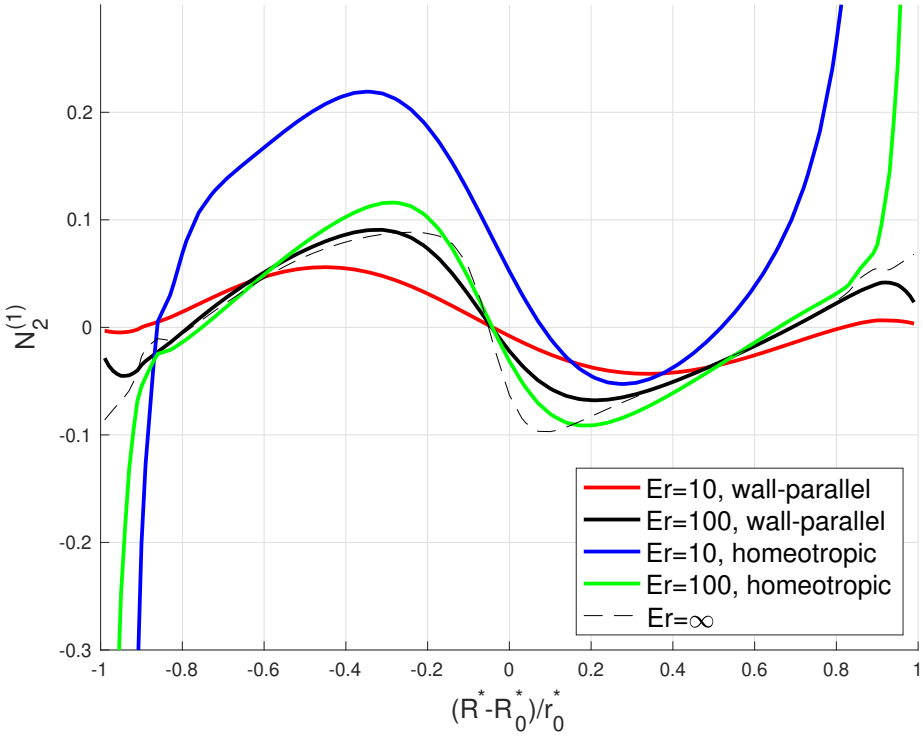

Figure 6.8. Variation of the imbalance effect (dimensionless) at the symmetry line for the fluid 1.

Table 6.3. Change in the strength of a given effect with respect to the infinite Ericksen number limit for fluid 1.

	$\%(N_1+2N_2)$	$\%(N_2^{(1)})$
10p	0.42	0.57
100p	0.87	0.88
10h	2.28	1.93
100h	1.35	1.11

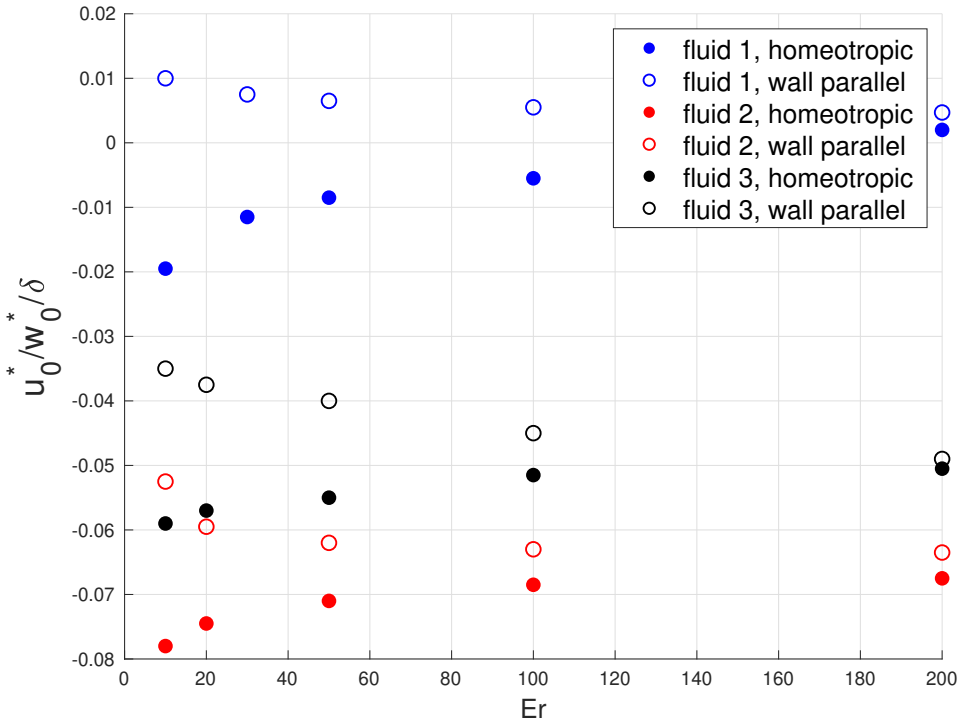

Figure 6.9. Effect of the Ericksen number on the magnitude of the secondary flow. For $u^*_{sec} > 0$ the secondary velocity at the symmetry line is directed towards the bend axis, similarly to fig. 5.8.

Noticeably different behaviour is observed for fluids 2 and 3, where $\chi > 0$, meaning that the curvature and imbalance effects are additive. In flows with homeotropic wall anchoring, a decrease of Ericksen number increases the director/velocity misalignment, leading to an increase in normal stresses, as shown in fig. 6.10 and 6.11; as a result, the intensity of the secondary motion increases (fig. 6.9). In contrast, the wall-parallel anchoring decreases the director/velocity misalignment, so the non-Newtonian stresses decrease, resulting in a weaker secondary flow. It should also be noted that fluids 2 and 3 are characterised by a considerably larger Leslie angle than fluid 1 (table 6.3). A large θ_L imposes a significant director/velocity misalignment even in the infinite Ericksen number limit, and therefore the magnitude of secondary motion is less sensitive to the Ericksen number and wall anchoring compared with fluids where $\lambda \to 1$.

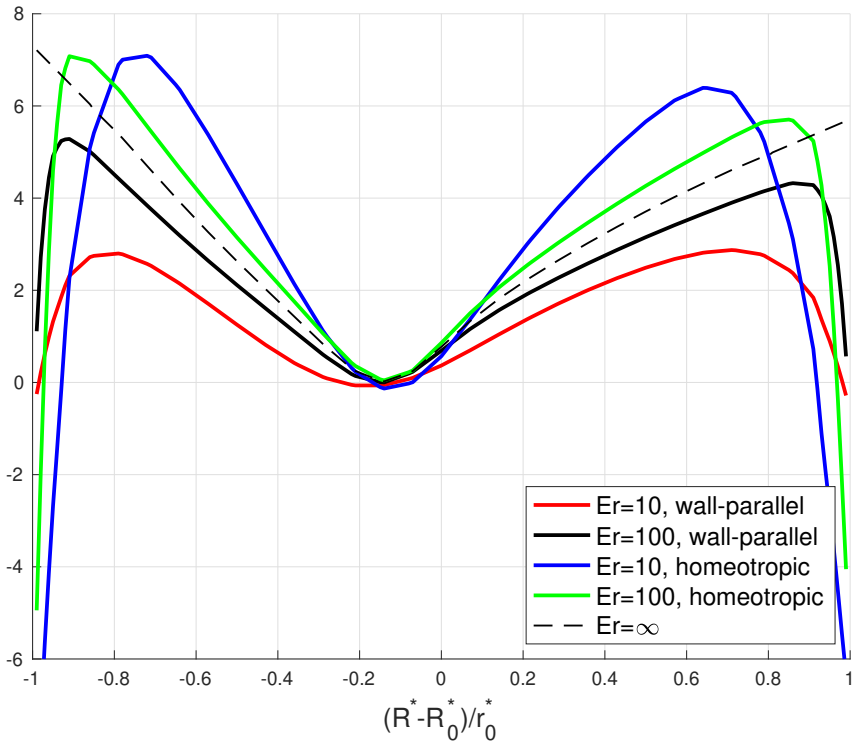

Figure 6.10. Variation of the curvature effect at the symmetry line for fluid 2.

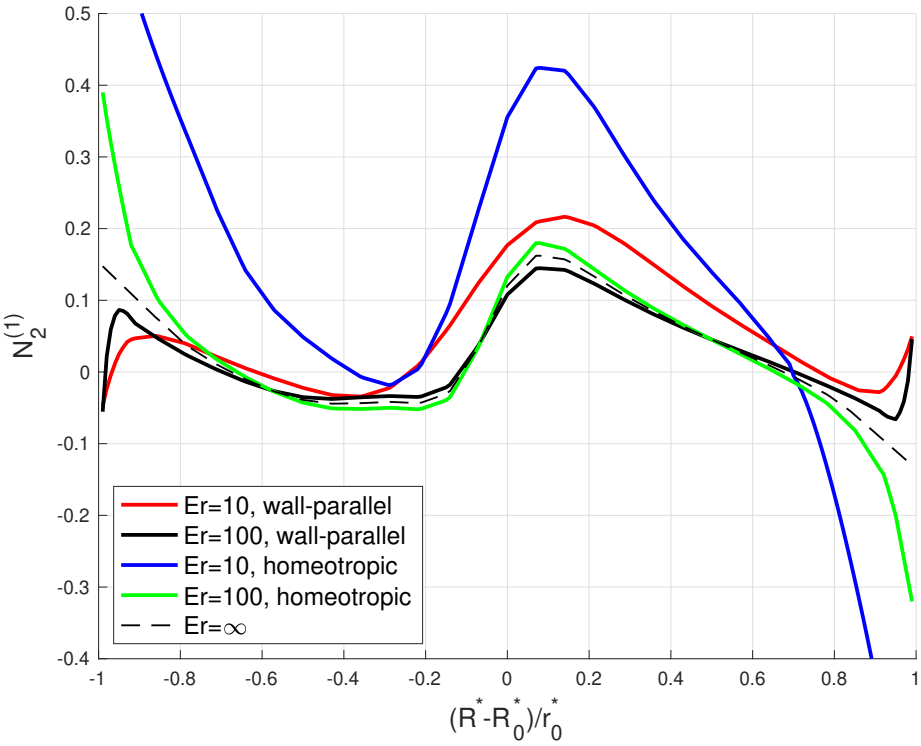

Figure 6.11. Variation of the imbalance effect at the symmetry line for fluid 2.

6.3.4 Entrance and exit velocity effects

The fully developed velocity profile in a bend is shifted towards the bend axis compared to the straight pipe flow, as shown in fig. 6.12. Therefore, as the flow transitions between

straight and curved pipe solutions, there is a stress gradient in the axial direction, which is responsible for a spike in the transverse velocity (velocity component directed towards the bend axis) as the fluid enters/leaves the bend (fig. 6.13). In the case of a creeping Newtonian flow, the entrance and exit spikes are of the same magnitude because of zero normal stresses [24, 154]. Further quantitative details on the origins of the spike are provided in appendix C.3.

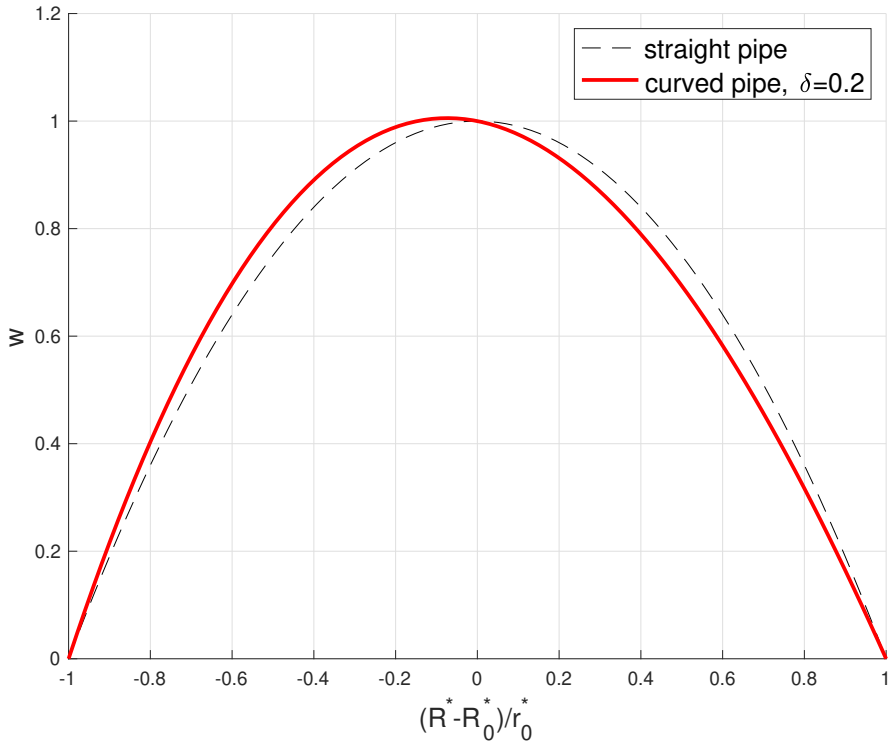

Figure 6.12. Comparison of Newtonian velocity profiles in a straight pipe and a bend.

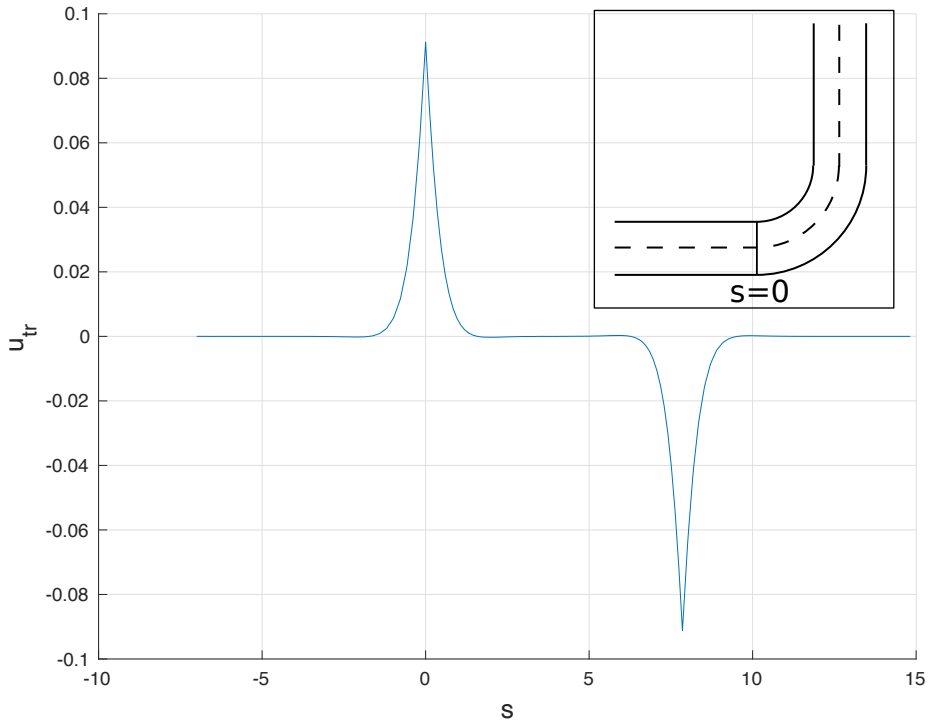

Figure 6.13. Transverse velocity of a Newtonian fluid as it travels across the bend for $\delta = \frac{r_0^*}{R_0^*} = 0.2$. s denotes the distance downstream the bend entrance and is schematically illustrated in the inset.

The analysis of entrance/exit effects in the case of liquid crystals is more complex due to their non-Newtonian nature. Calculations conducted in appendix C.3 indicate two contributions to the velocity spike:

- Gradients of the shear stress in the axial direction (also present in a Newtonian flow). In the case of liquid crystals, the shear stress has both Newtonian and non-Newtonian contributions.
- Non-Newtonian stresses that drive the secondary motion in a fully developed curved pipe.

Since there is a non-zero secondary motion in a fully developed curved pipe flow, spikes are not of the same magnitude at bend entrance and exit, as shown in fig. 6.14 and 6.15. A comparison of τ_{sr} with $N_2^{(1)}$ indicates that the shear stress and its gradients are significantly larger in magnitude than the second normal stress difference (fig. 6.16 and 6.17). For the purpose of scaling analysis, let us assume that the spike magnitude is solely controlled by τ_{sr}, which in the steady-state, fully developed straight pipe flow is given by

$$\tau_{sr} = \frac{1}{2}\Big[\alpha_4 + 2\alpha_1 n_s^2 n_r^2 + (-\alpha_3 + \alpha_6) n_r^2 + (\alpha_2 + \alpha_5) n_s^2\Big] \frac{\partial w}{\partial r}, \tag{C.15d}$$

where subscripts r and s denote radial and stream-wise components of the director field respectively. If we consider the flow close to the pipe axis, where $n_r \to 0$, τ_{sr} (and thus the spike magnitude) is proportional to $\alpha_2 + \alpha_4 + \alpha_5$. The effect is confirmed in fig. 6.18, where

the stress-velocity dependence for fluids with different material properties collapse onto a single line.

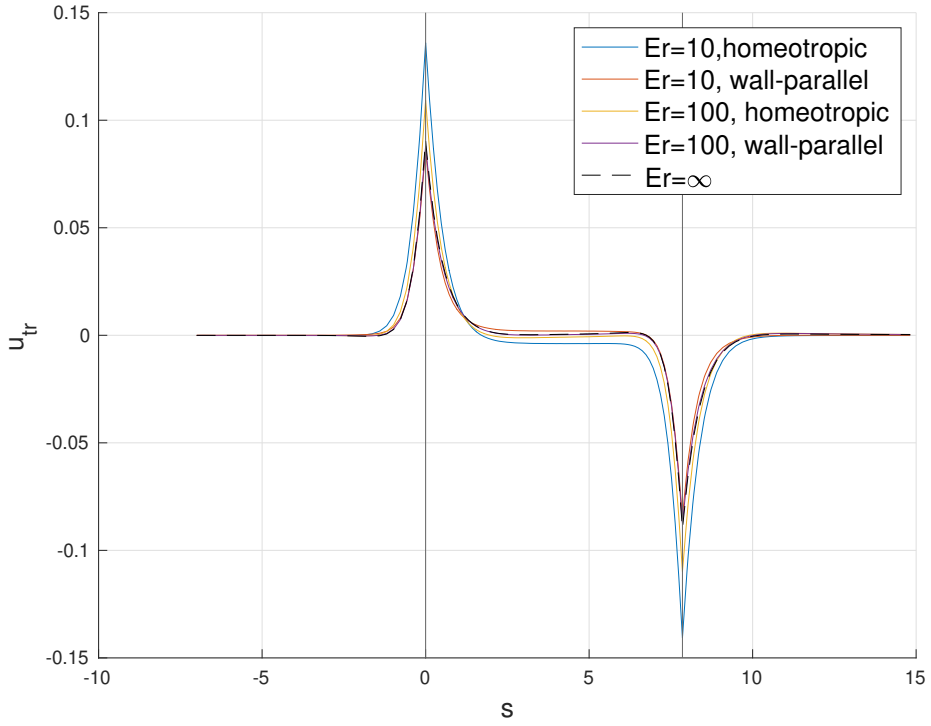

Figure 6.14. Transverse velocity of fluid 1 across the bend. $s = 0$ corresponds to the location of the bend entrance. $\delta = \frac{r_0}{R} = 0.2$. Vertical black lines denote the location of bend inlet and outlet.

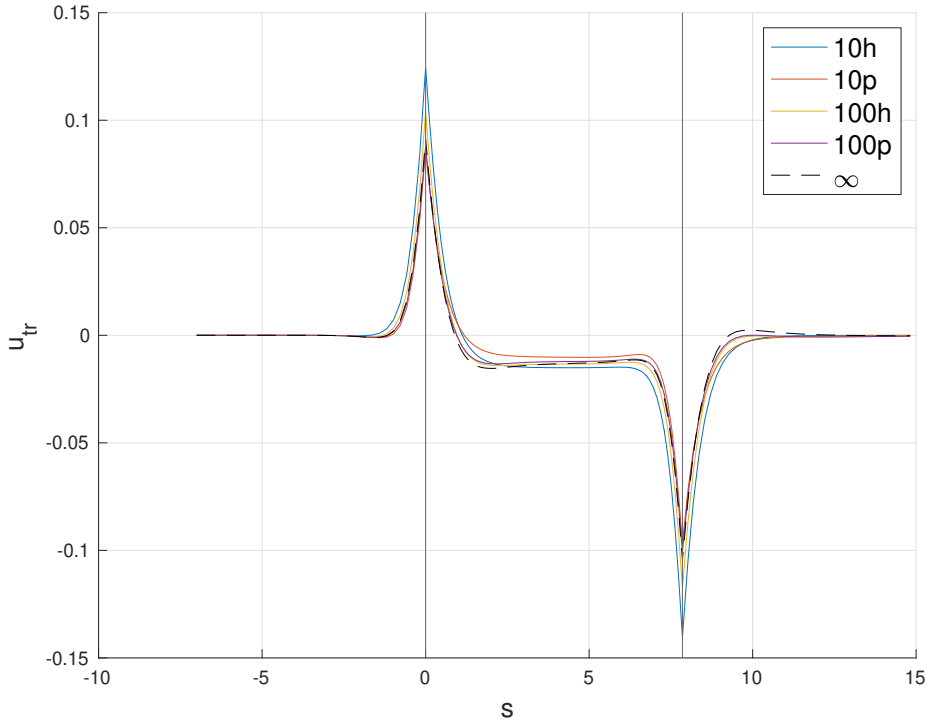

Figure 6.15. Transverse velocity of fluid 2 across the bend. $s = 0$ corresponds to the location of the bend entrance. $\delta = \frac{r_0^*}{R^*} = 0.2$. Vertical black lines denote the location of bend inlet and outlet. The variation of u_{tr} for fluid 3 is qualitatively the same and thus not shown.

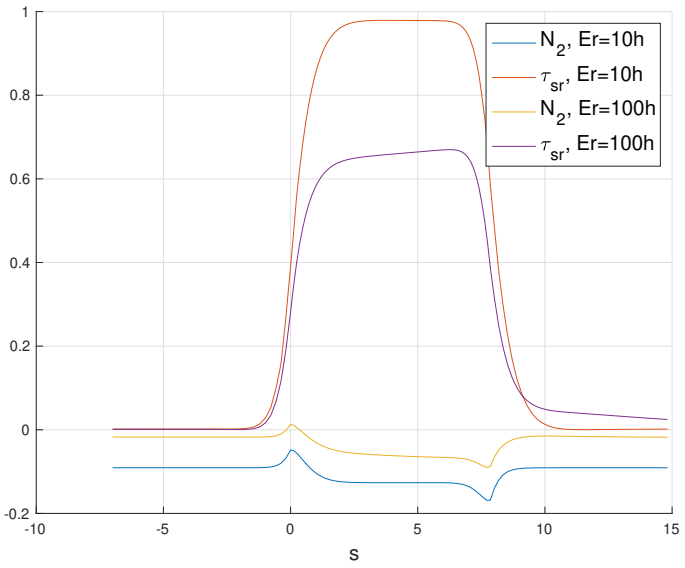

Figure 6.16. Streamwise variation of normal and shear stresses for fluid 1. N_2 is small in comparison to τ_{sr} and thus have a limited impact on the velocity spike.

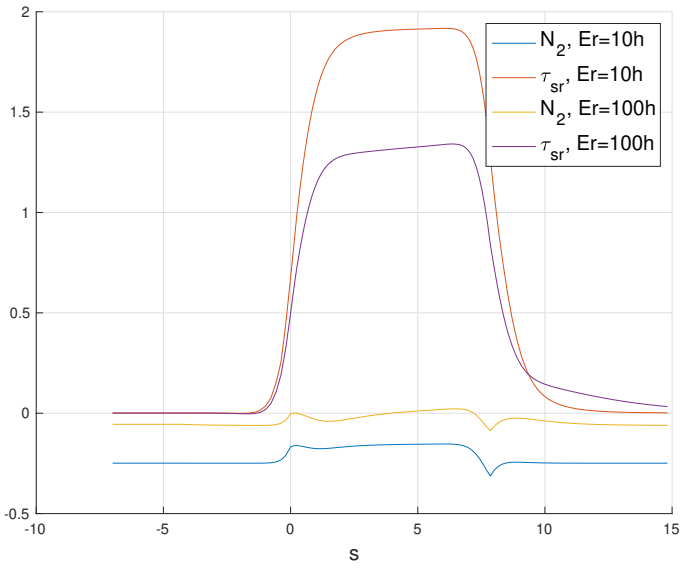

Figure 6.17. Streamwise variation of normal and shear stresses for fluid 2. N_2 is small in comparison to τ_{sr} and thus have a limited impact on the velocity spike.

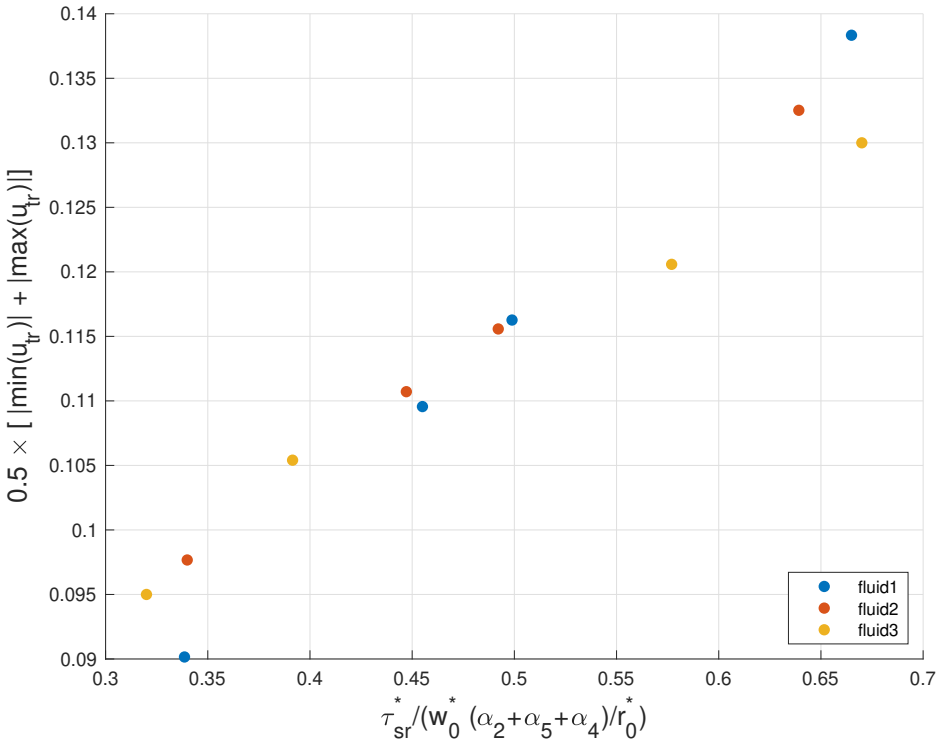

Figure 6.18. Mean spike magnitude vs the shear stress τ_{sr} normalised by $(\alpha_2 + \alpha_4 + \alpha_5)\frac{w_0^*}{r_0^*}$.

6.3.5 Director development downstream of the bend

In a straight pipe flow with finite Ericksen number, the director on the axis is oriented in the stream-wise direction as this orientation minimises the distortion energy. That is not the case at the bend exit (fig. 6.5), where the velocity and director fields are shifted towards the bend axis. Thus, as the flow leaves the bend, there is a transition region with an intermediate director distribution. We first present a qualitative estimation of the development length and use the findings to interpret numerical results.

Analytical estimation of director development

Consider a distorted director field entering a straight channel as shown in fig. 6.19. For two-dimensional flows, the director orientation can be expressed in terms of the polar angle θ that the director makes with the horizontal direction ($[n_x \; n_y] = [\cos\theta \;\; \sin\theta]$), and the dimensionless momentum balance equation (2.53) simplifies to [151]

$$\frac{\partial\theta}{\partial t} + u\frac{\partial\theta}{\partial x} + v\frac{\partial\theta}{\partial y} = \frac{1}{Er\gamma_1}\left[\frac{\partial^2\theta}{\partial x^2} + \frac{\partial^2\theta}{\partial y^2}\right] - \frac{1}{2}\frac{\gamma_2}{\gamma_1}\left[\left(\frac{\partial u}{\partial y} + \frac{\partial v}{\partial x}\right)\cos(2\theta) + \left(\frac{\partial v}{\partial y} - \frac{\partial u}{\partial x}\right)\sin(2\theta)\right] - \frac{1}{2}\left(\frac{\partial u}{\partial y} - \frac{\partial v}{\partial x}\right), \quad (6.3)$$

where u and v are $x-$ and $y-$ dimensionless velocities. Let us make the following assumptions in order to simplify the evolution equation (6.3):

- The system is in a steady state, so the time derivative $\frac{\partial}{\partial t}$ vanishes.
- Director convection takes place predominantly in the flow direction $|v\frac{\partial \theta}{\partial y}| << |u\frac{\partial \theta}{\partial x}|$.
- Flow velocity is maximum at the channel centerline, so flow effects are significantly smaller than elastic effects.
- Director gradients in the $y-$ direction dominate: $|\frac{\partial^2 \theta}{\partial y^2}| >> |\frac{\partial^2 \theta}{\partial x^2}|$.

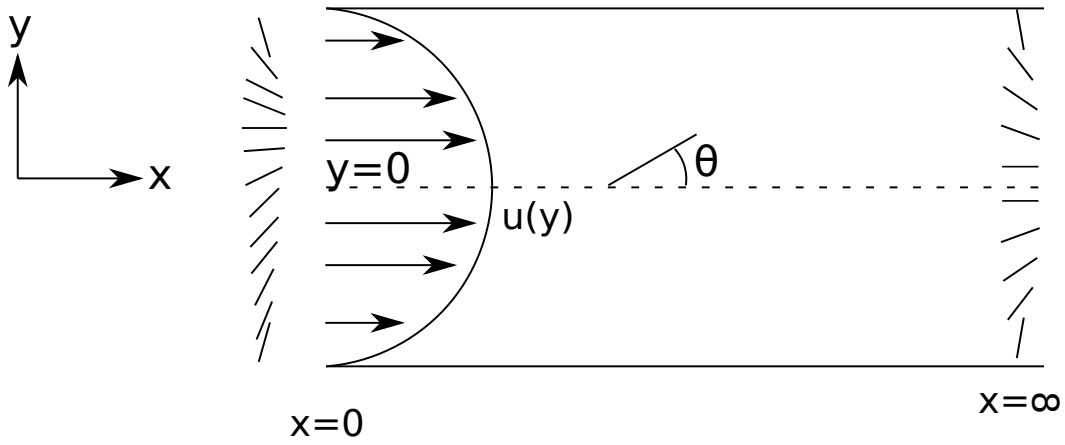

Figure 6.19. Distorted director field entering a straight channel.

With the assumptions above, the director transport equation (6.3) simplifies to

$$u\frac{\partial \theta}{\partial x} = \frac{1}{Er\gamma_1}\frac{\partial^2 \theta}{\partial y^2}, \tag{6.4}$$

which indicates a competition between convective and elastic contributions. Convective effects act to propagate director distortions downstream, while elasticity drives the system towards the straight channel configuration with $\theta(y = 0) = 0$. Calculations performed in appendix C.5 indicate that for small θ we can make the following approximation

$$\frac{\partial^2 \theta}{\partial y^2}|_{\theta \to 0} \approx -\frac{\theta}{2}, \tag{6.5}$$

indicating that in a fully developed flow ($\frac{\partial \theta}{\partial x} = 0$), the system tends to the straight channel solution with $\theta = 0$. Substituting eq. (6.4) into eq. (6.5) and assuming a fixed director angle at the channel entrance $\theta(x = 0) = \theta_0$, the director director evolution is described by

$$\theta(x) = \theta_0 e^{-\frac{x}{2uEr\gamma_1}}, \tag{6.6}$$

the solution is visualised in fig. 6.20 and indicates that the director development length is a function of $\gamma_1 Er$, which measures the relative strength of convective to elastic effects acting on the director. Convection propagates the director distortion, which is resisted by material elasticity acting to recover the straight channel solution.

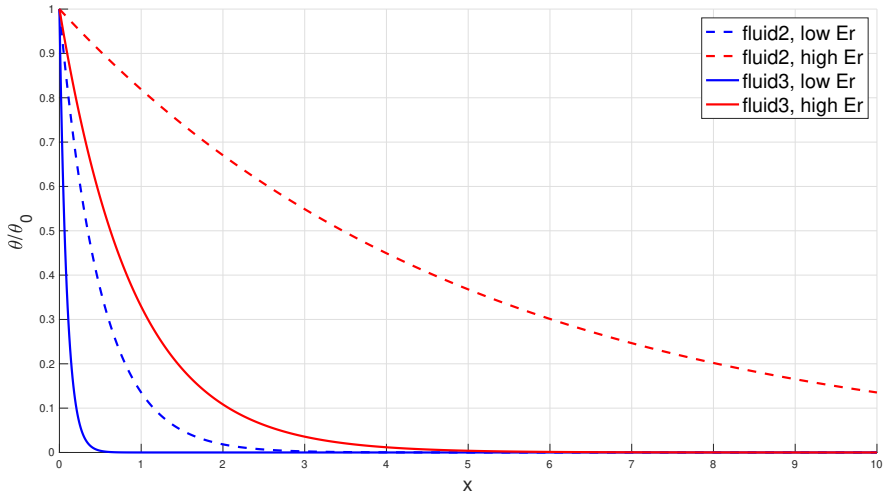

Figure 6.20. Evolution of the director angle downstream the bend exit for fluids 2 and 3 according to eq. (6.6).

Numerical results

The numerical predictions of the director development for fluids 2 and 3 are shown in fig. 6.21 and 6.22 and indicate that the development length can be $O(10r_0^*)$ in the limit of high Ericksen number. Analytical predictions agree with simulations in the following aspects:

- The director development length increases with the Ericksen number.
- Director development is also affected by γ_1, so the transition to the straight flow solution takes longer for fluid 2 (larger γ_1) than fluid 3.

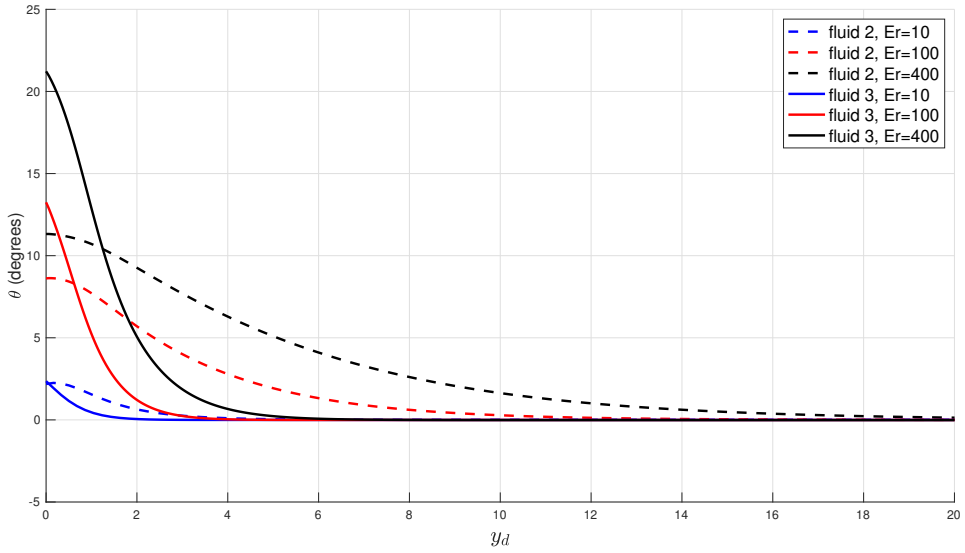

Figure 6.21. Director development on the centerline with homeotropic anchoring for $\delta = \frac{r_0}{R} = 0.2$. y_d denotes the distance downstream the bend exit. Results for wall-parallel anchoring are qualitatively similar and hence not shown.

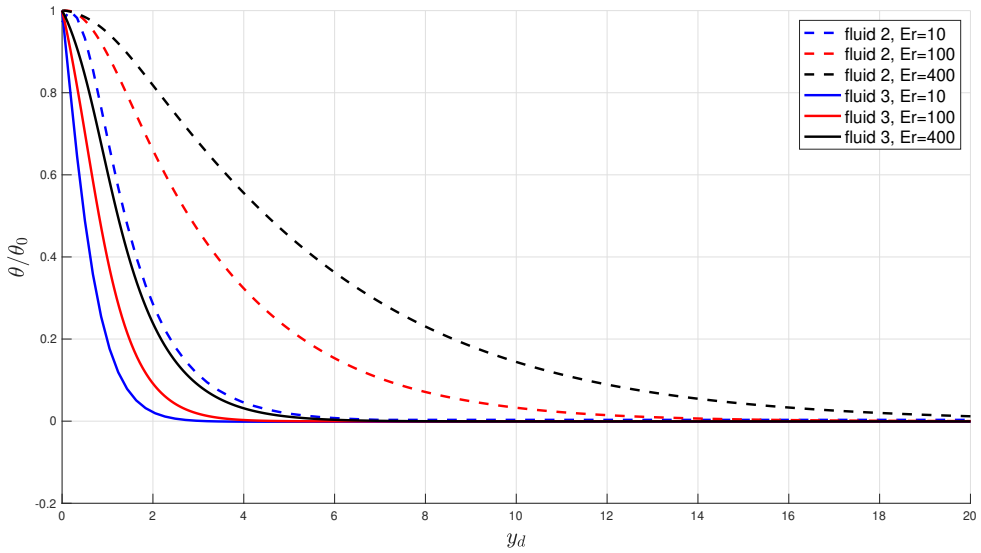

Figure 6.22. Director variation normalised by the entrance director angle.

Simulations also indicate that the director angle at the bend exit increases with the Ericksen number, which is caused by the propagation of the distorted director field. The director field in a bend is schematically illustrated in fig. 6.23 and indicates that there is a thin layer Δw, where elastic effects govern director orientation and $\boldsymbol{n}$ aligns with the axial flow. The size of the layer depends on the relative importance of elastic contribution, so for low Er flows, Δw is significant, and the director angle at the bend exit is small; in contrast, Δw is small at high Er , so the director/velocity misalignment is larger.

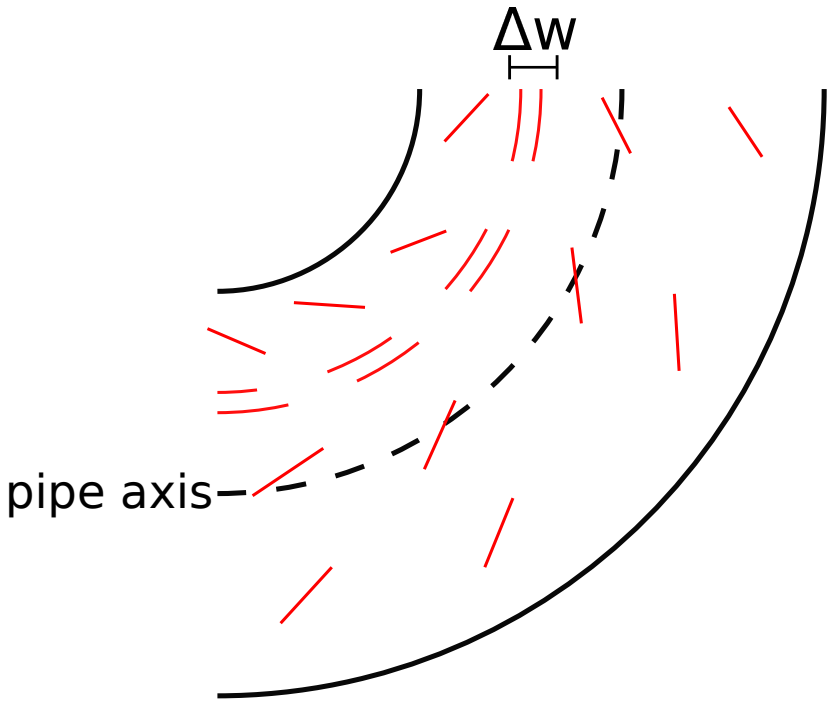

Figure 6.23. Schematic visualisation of a director (red rods) layer Δw with a uniform director orientation. The layer size increases as the Ericksen number decreases.

6.3.6 Pressure drop

Compared to a straight pipe flow, the geometry curvature affects both velocity and director field; their distribution is not axisymmetric anymore, and the combination of normal stresses and flow curvature produces a secondary motion. These effects affect the pressure drop, which, as indicated in fig. 6.24 can be up to 3% higher than in a straight pipe of the same length. The similarity of fig. 6.24 and 6.9 suggests that the excess pressure drop is predominantly caused by the secondary motion; hence the increase is more severe for fluids 2 and 3, which produce stronger secondary flows.

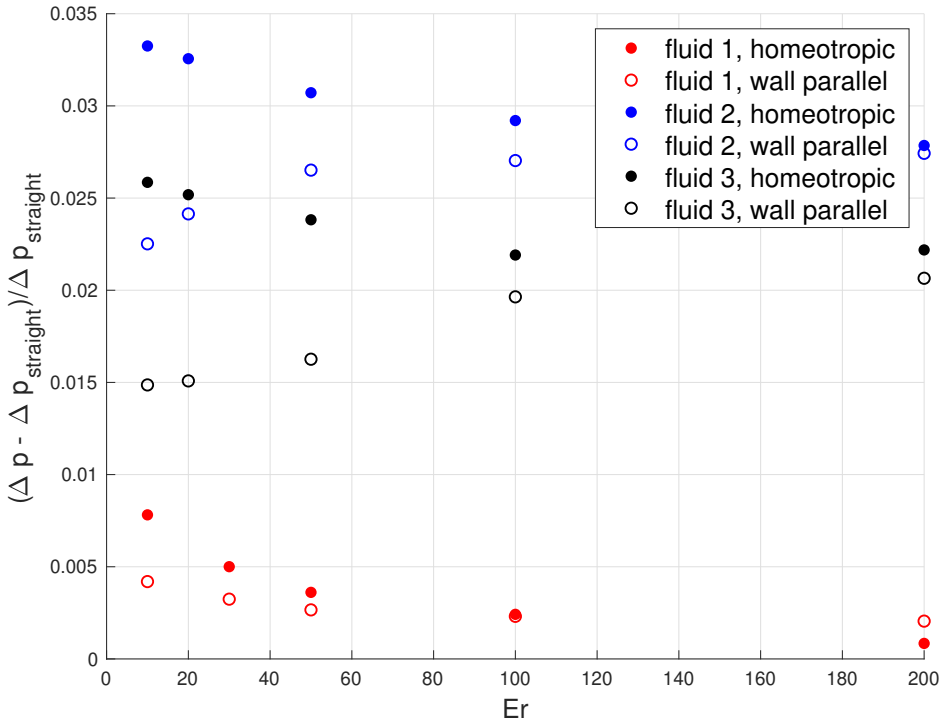

Figure 6.24. Additional pressure gradient relative to the straight pipe solution $\delta = 0.2$.

6.4 Summary

The flow of Leslie-Ericksen fluids through a 90^o pipe is qualitatively similar to both finite Ericksen number, straight pipe flows and infinite Ericksen number curved pipe flows. The bend curvature induces a shift of velocity and director field towards the bend axis, while elastic effects govern the director orientation near the wall. Similarly to the infinite Ericksen number flows, the magnitude of the secondary flow is governed by curvature and stress imbalance effects; however, their relative importance depends on the Ericksen number and anchoring type. A flow reversal is possible for materials where curvature and stress imbalance effects oppose each other. On the other hand, when these effects are additive (fluid 2 and 3), the magnitude of the secondary motion increases in the case of homeotropic anchoring due to the increased director/velocity misalignment; conversely, an improved alignment caused by homeotropic anchoring decreases the strength of the secondary flow.

We find that the transition between fully developed straight and curved pipe flows produces additional stresses responsible for spikes in the transverse velocity. The spike need not be of the same size on the inlet and outlet and depends on the direction and strength of the secondary flow in a fully developed curved pipe. Finally, we have examined director variation downstream the bend exit and find that the development length depends on $\gamma_1 Er$, which can be understood as a measure of the relative strength of convection to elasticity.

Chapter 7

Flow of liquid crystals through a 4:1 planar contraction

This chapter investigates the behaviour of nematic liquid crystals flowing through a planar contraction (fig. 7.1). The flow evolves from the fully developed state in a large (inlet) channel through a transition phase near the contraction walls (where lip vortices and secondary flows occur) and returns to a fully developed state in the smaller (outlet) channel. Contraction flows are of industrial relevance for several reasons:

- Extensional flow generates an additional pressure drop [173].
- A large corner vortex is created upstream of the contraction entrance [174].
- The presence of a contraction introduces a flow distortion; the development length for the flow to reach a fully developed state is of practical importance in pipework design [175, 176].
- Flow near the contraction is dominated by the extensional component, so the effective viscosity need not be the same as in shear flows [177].
- Extensional flows in viscoelastic materials may generate instabilities even at low Reynolds numbers [20, 177].

The flow of the Leslie-Ericksen fluid with the wall-parallel boundary condition was analysed by Cruz et al. [151], who found that the velocity field (size of the corner vortex) and director orientation are strongly affected by the Ericksen number. This chapter aims to extend these analyses by considering the flow of Leslie-Ericksen and Beris-Edwards models subject to both wall-parallel and homeotropic boundary conditions. The polar nature of the director field is taken into account, and we examine the effect of variable director anchoring on the flow and microstructure distribution.

7.1 Geometry

We consider flows in a 4:1 contraction geometry (fig. 7.1), which is frequently used as a benchmark case for examining the performance of viscoelastic constitutive equations [178,

179]. The dimension of the outlet channel $2h = 10^{-3}m$ is a typical length-scale used in the industrial equipment [39]. The length of the inlet channel is chosen to allow the flow to reach a fully developed state before being deformed by corner effects. Similarly, the length of the outlet channel allows the flow and microstructure to reach a fully developed state. The centre of the coordinate system is located on the symmetry line at the contraction (fig. 7.1).

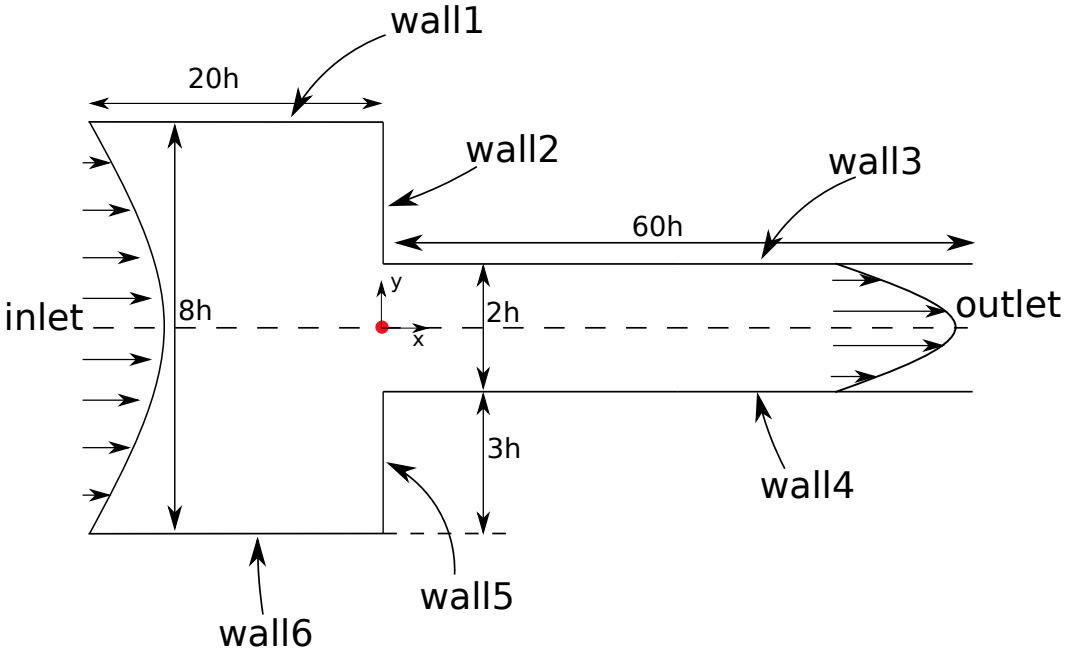

Figure 7.1. Schematic illustration of the contraction geometry considered in this chapter.

7.2 Methodology

7.2.1 Governing equations

Simulations are conducted in OpenFOAM, using the solver *rheoFoam2*, which was introduced in chapter 3. The linear momentum balance is supplemented with a model-dependent viscoelastic stress

$$\begin{aligned}\boldsymbol{\tau}^{LE} = \alpha_1 \boldsymbol{nnnn} : \boldsymbol{D} + \alpha_2 \boldsymbol{nN} + \alpha_3 \boldsymbol{Nn} + \alpha_4 \boldsymbol{D} + \alpha_5 \boldsymbol{nn} \cdot \boldsymbol{D} + \alpha_6 \boldsymbol{D} \cdot \boldsymbol{nn} \\ - \frac{\partial f_d}{\partial \boldsymbol{\nabla n}} \cdot (\boldsymbol{\nabla n})^T,\end{aligned} \tag{2.52}$$

$$\begin{aligned}\boldsymbol{\tau}^{BE} = \mu \boldsymbol{D} - \xi \left[(\boldsymbol{Q} + \frac{\boldsymbol{I}}{3}) \cdot \boldsymbol{H} + \boldsymbol{H} \cdot (\boldsymbol{Q} + \frac{\boldsymbol{I}}{3}) - 2(\boldsymbol{Q} + \frac{\boldsymbol{I}}{3})(\boldsymbol{H} : \boldsymbol{Q}) \right] \\ + \boldsymbol{H} \cdot \boldsymbol{Q} - \boldsymbol{Q} \cdot \boldsymbol{H} - \frac{\partial f_{LdG}}{\partial Q_{ij,\alpha}} Q_{ij,\beta},\end{aligned} \tag{2.69}$$

where $\boldsymbol{\tau}^{LE}$ and $\boldsymbol{\tau}^{BE}$ are the stress contributions in the Leslie-Ericksen and Beris-Edwards models respectively. α_i are Leslie viscosities in the Leslie-Ericksen theory; μ in eq. (2.69) can be understood as a Newtonian viscosity and ξ is the tumbling parameter that controls the flow/director alignment [126, 142]. Computation of the stress tensor requires knowledge of the distribution of microstructure configuration, which is calculated from the angular mo-

mentum balance

$$\frac{\boldsymbol{h}-\boldsymbol{n}\boldsymbol{n}\cdot\boldsymbol{h}}{\gamma_1}-\frac{\gamma_2}{\gamma_1}(\boldsymbol{n}\cdot\boldsymbol{D}-\boldsymbol{n}\boldsymbol{n}\boldsymbol{n}:\boldsymbol{D})-\boldsymbol{N}=0, \tag{2.53}$$

$$\frac{D\boldsymbol{Q}}{Dt}=\boldsymbol{S}+\Gamma\boldsymbol{H}, \tag{2.71}$$

where the molecular field $\boldsymbol{h}$ in the LE model ($=-\frac{\delta f_d}{\delta \boldsymbol{n}}$) or $\boldsymbol{H}$ in the BE model $=-\frac{\delta f_{LdG}}{\delta \boldsymbol{Q}}+\underline{\frac{1}{3}\,\mathrm{tr}\,\frac{\delta f_{LdG}}{\delta \boldsymbol{Q}}}$ measures the deviation of the microstructure from the minimum Helmholtz free energy; the underlined term in the definition of $\boldsymbol{H}$ ensures that $\boldsymbol{Q}$ remains traceless. The Helmholtz free energy in the Leslie-Ericksen framework has only an elastic component that depends on the distortion of the director field; for simplicity we use the one-constant approximation [43]

$$f_d=\frac{1}{2}K(\boldsymbol{\nabla n}):(\boldsymbol{\nabla n})^T, \tag{2.44}$$

where K is the Frank constant that quantifies the resistance to director distortions. In the $\boldsymbol{Q}$-tensor models, the elastic energy is supplemented with an order parameter-dependent bulk free-energy density

$$\begin{aligned} f_{LdG}&=f_d^Q+f_{nematic}\\ &=\underbrace{\frac{1}{2}K^Q Q_{ik,j}Q_{ik,j}}_{\text{elastic}}+\underbrace{\frac{a}{2}\,\mathrm{tr}(\boldsymbol{Q}\cdot\boldsymbol{Q})-\frac{b}{3}\,\mathrm{tr}(\boldsymbol{Q}\cdot\boldsymbol{Q}\cdot\boldsymbol{Q})+\frac{c}{4}\,\mathrm{tr}^2(\boldsymbol{Q}\cdot\boldsymbol{Q})}_{\text{bulk free-energy}}, \end{aligned} \tag{2.68}$$

where K^Q is the Frank constant in the tensorial framework. The tensor $\boldsymbol{S}$ in eq. (2.71) expresses the action of hydrodynamic effects acting on the $\boldsymbol{Q}$-tensor field

$$\boldsymbol{S}=(\xi\boldsymbol{D}-\boldsymbol{\Omega})(\boldsymbol{Q}+\frac{\boldsymbol{\delta}}{3})+(\boldsymbol{Q}+\frac{\boldsymbol{\delta}}{3})(\xi\boldsymbol{D}+\boldsymbol{\Omega})-\underline{2\xi(\boldsymbol{Q}+\frac{\boldsymbol{\delta}}{3})\,\mathrm{tr}(\boldsymbol{Q}\cdot\boldsymbol{\nabla u})}, \tag{2.72}$$

where the underlined term ensures that $\boldsymbol{Q}$ remains traceless.

We consider the same set of parameters as in chapter 4, similar to material properties measured for pentylcyanobiphenyl (5CB) [155]:

- In the BE model: $K^Q=40pN$, $\xi=1.02$, $\Gamma=7.29(\text{Pa}\cdot\text{s})^{-1}$, $\mu=0.2\text{Pa}\cdot\text{s}$, $a=-2\cdot10^{-3}\frac{\text{MJ}}{\text{m}^3}$, $b=4\cdot10^{-2}\frac{\text{MJ}}{\text{m}^3}$, $c=4\cdot10^{-2}\frac{\text{MJ}}{\text{m}^3}$; the equilibrium order parameter is then given by eq. (2.67b): $S_{eq}=0.6208$.
- The Leslie-Ericksen parameters are obtained by assuming a uniaxial director field with a fixed order parameter ($S=0.6208$); the mapping provided by equation (2.75) gives: $\alpha_1=-0.1446\text{Pa}\cdot\text{s}$, $\alpha_2=-0.1288\text{Pa}\cdot\text{s}$, $\alpha_3=-0.023\text{Pa}\cdot\text{s}$, $\alpha_4=0.2091\text{Pa}\cdot\text{s}$, $\alpha_5=0.1757\text{Pa}\cdot\text{s}$, $\alpha_6=0.0239\text{Pa}\cdot\text{s}$. The Frank constant in the Leslie-Ericksen theory is mapped via eq. (2.61) and yields $K=2S_{eq}^2K^Q=30.8$ pN.

7.2.2 Boundary conditions

We prescribe a parabolic velocity profile [45] at the inlet corresponding to a fully-developed, Newtonian flow

$$u(y) = u_{max}\left(1 - \left(\frac{y}{4h}\right)^2\right), \tag{7.1}$$

where u_{max} is the peak velocity. The channel outlet is expected to be located far enough downstream to enable flow to fully develop; therefore we employ a zero-gradient boundary condition for velocity, director and $\boldsymbol{Q}$-tensor. The zero-gradient boundary condition for the pressure in the wall-normal direction is employed at all walls. Flows with both wall-parallel and homeotropic anchoring are considered. In the tensorial framework, the microstructure configuration can be unambiguously described through $\boldsymbol{Q}$, whose boundary conditions are specified in table 7.1 (wall-parallel) and 7.2 (homeotropic).

The vectorial description of the microstructure suffers from the non-orientability issue. The problem in the context of a pressure-driven channel flow was discussed by Anderson [169], who found that the energy-minimising director configuration depends on the Ericksen number; at low Er, the director points in the same direction on both boundaries, while as Er increases, the configuration with opposing director field is preferred, as shown in fig. 7.2. Denniston [142] has shown that the issue does not occur in the Beris-Edwards model, where a horizontal-vertical transition occurs at a sufficiently large Ericksen number. Results of Batista et al. [180] show that the horizontal-vertical transition depends on the strength of wall anchoring, and decreasing the strength of wall anchoring promotes the horizontal director orientation at lower Ericksen numbers. The orientability problem is also present in more complex geometries, where director distribution with minimum energy may be different in vectorial and tensorial frameworks [132]. In the case of a contraction geometry, the sign of $\boldsymbol{n}$ cannot be unambiguously defined due to the discontinuity at the corners. The problem is mitigated by $\boldsymbol{Q}$-tensor models, which are invariant upon $\boldsymbol{n} \rightarrow -\boldsymbol{n}$ transformation and the presence of geometry discontinuity results only in a local decrease in the order parameter [181].

Although the director field is invariant upon $\boldsymbol{n} \rightarrow -\boldsymbol{n}$ transformation on the walls [35], $\boldsymbol{n}$ must change the sign across the whole domain for the set of boundary conditions to produce an identical result. Hence, in a planar contraction consisting of six walls, there are 32 different ways in which a fixed boundary orientation (wall-parallel or homeotropic) can be prescribed. In the case of the wall-parallel anchoring, we analyse boundary configurations schematically visualised in fig. 7.3; configuration A was employed in a similar study by Cruz et al. [151], and we also examine configuration B in order to investigate the sensitivity of flow behaviour to the choice of boundary condition. Components of the director field are given in table 7.1. There is no literature, which investigates the flow of liquid crystals in a planar contraction with homeotropic anchoring, so we consider four different configurations, schematically depicted in fig. 7.4 with components of the director field listed in table 7.2.

Table 7.1. Boundary conditions for the velocity, pressure, $\boldsymbol{Q}$-tensor and director fields in the wall-parallel anchoring configuration. Superscripts A, B refer to configurations shown in fig. 7.3. The off-diagonal components of $\boldsymbol{Q}$ on the boundaries are zero.

location	$\boldsymbol{u}$	p	$\boldsymbol{Q} = [Q_{xx}, Q_{yy}, Q_{zz}]$	$\boldsymbol{n}^A = [n_x, n_y]$	$\boldsymbol{n}^B = [n_x, n_y]$
inlet	eq. (7.1)	$\frac{\partial p}{\partial x} = 0$	$\frac{\partial \boldsymbol{Q}}{\partial x} = 0$	$\frac{\partial \boldsymbol{n}}{\partial x} = \boldsymbol{0}$	$\frac{\partial \boldsymbol{n}}{\partial x} = \boldsymbol{0}$
outlet	$\frac{\partial \boldsymbol{u}}{\partial x} = \boldsymbol{0}$	$p = 0$	$\frac{\partial \boldsymbol{Q}}{\partial x} = 0$	$\frac{\partial \boldsymbol{n}}{\partial x} = \boldsymbol{0}$	$\frac{\partial \boldsymbol{n}}{\partial x} = \boldsymbol{0}$
wall 1	$\boldsymbol{u} = \boldsymbol{0}$	$\frac{\partial p}{\partial y} = 0$	$\left[\frac{2}{3}, -\frac{1}{3}, -\frac{1}{3}\right]$	$[1, 0]$	$[-1, 0]$
wall 2	$\boldsymbol{u} = \boldsymbol{0}$	$\frac{\partial p}{\partial x} = 0$	$\left[-\frac{1}{3}, \frac{2}{3}, -\frac{1}{3}\right]$	$[0, -1]$	$[0, -1]$
wall 3	$\boldsymbol{u} = \boldsymbol{0}$	$\frac{\partial p}{\partial y} = 0$	$\left[\frac{2}{3}, -\frac{1}{3}, -\frac{1}{3}\right]$	$[1, 0]$	$[-1, 0]$
wall 4	$\boldsymbol{u} = \boldsymbol{0}$	$\frac{\partial p}{\partial y} = 0$	$\left[\frac{2}{3}, -\frac{1}{3}, -\frac{1}{3}\right]$	$[1, 0]$	$[-1, 0]$
wall 5	$\boldsymbol{u} = \boldsymbol{0}$	$\frac{\partial p}{\partial x} = 0$	$\left[-\frac{1}{3}, \frac{2}{3}, -\frac{1}{3}\right]$	$[0, 1]$	$[0, 1]$
wall 6	$\boldsymbol{u} = \boldsymbol{0}$	$\frac{\partial p}{\partial y} = 0$	$\left[\frac{2}{3}, -\frac{1}{3}, -\frac{1}{3}\right]$	$[1, 0]$	$[-1, 0]$

Table 7.2. Boundary conditions for the velocity, pressure, $\boldsymbol{Q}$-tensor and director fields in the homeotropic configuration. The off-diagonal components of $\boldsymbol{Q}$ on the boundaries are zero. Superscripts A-D refer to configurations shown in fig. 7.4.

location	$\boldsymbol{u}$	p	$\boldsymbol{Q}$	$\boldsymbol{n}^A$	$\boldsymbol{n}^B$	$\boldsymbol{n}^C$	$\boldsymbol{n}^D$
inlet	eq. (7.1)	$\frac{\partial p}{\partial x} = 0$	$\frac{\partial \boldsymbol{Q}}{\partial x} = 0$	$\frac{\partial \boldsymbol{n}}{\partial x} = \boldsymbol{0}$	$\frac{\partial \boldsymbol{n}}{\partial x} = \boldsymbol{0}$	$\frac{\partial \boldsymbol{n}}{\partial x} = \boldsymbol{0}$	$\frac{\partial \boldsymbol{n}}{\partial x} = \boldsymbol{0}$
outlet	$\frac{\partial \boldsymbol{u}}{\partial x} = \boldsymbol{0}$	$p = 0$	$\frac{\partial \boldsymbol{Q}}{\partial x} = 0$	$\frac{\partial \boldsymbol{n}}{\partial x} = \boldsymbol{0}$	$\frac{\partial \boldsymbol{n}}{\partial x} = \boldsymbol{0}$	$\frac{\partial \boldsymbol{n}}{\partial x} = \boldsymbol{0}$	$\frac{\partial \boldsymbol{n}}{\partial x} = \boldsymbol{0}$
wall 1	$\boldsymbol{u} = \boldsymbol{0}$	$\frac{\partial p}{\partial y} = 0$	$\left[-\frac{1}{3}, \frac{2}{3}, -\frac{1}{3}\right]$	$[0, -1]$	$[0, -1]$	$[0, -1]$	$[0, -1]$
wall 2	$\boldsymbol{u} = \boldsymbol{0}$	$\frac{\partial p}{\partial x} = 0$	$\left[\frac{2}{3}, -\frac{1}{3}, -\frac{1}{3}\right]$	$[1, 0]$	$[-1, 0]$	$[1, 0]$	$[1, 0]$
wall 3	$\boldsymbol{u} = \boldsymbol{0}$	$\frac{\partial p}{\partial y} = 0$	$\left[-\frac{1}{3}, \frac{2}{3}, -\frac{1}{3}\right]$	$[0, -1]$	$[0, -1]$	$[0, 1]$	$[0, 1]$
wall 4	$\boldsymbol{u} = \boldsymbol{0}$	$\frac{\partial p}{\partial y} = 0$	$\left[-\frac{1}{3}, \frac{2}{3}, -\frac{1}{3}\right]$	$[0, 1]$	$[0, 1]$	$[0, 1]$	$[0, 1]$
wall 5	$\boldsymbol{u} = \boldsymbol{0}$	$\frac{\partial p}{\partial x} = 0$	$\left[\frac{2}{3}, -\frac{1}{3}, -\frac{1}{3}\right]$	$[1, 0]$	$[-1, 0]$	$[1, 0]$	$[1, 0]$
wall 6	$\boldsymbol{u} = \boldsymbol{0}$	$\frac{\partial p}{\partial y} = 0$	$\left[-\frac{1}{3}, \frac{2}{3}, -\frac{1}{3}\right]$	$[0, 1]$	$[0, 1]$	$[0, 1]$	$[0, 1]$

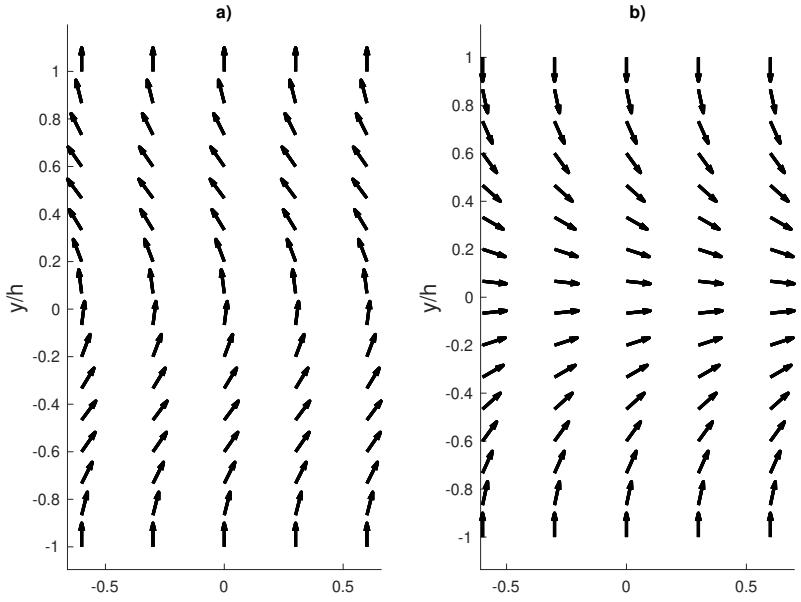

Figure 7.2. Director orientation in a channel flow when a) $\boldsymbol{n}$ points in the same direction on both boundaries; b) $\boldsymbol{n}$ points in the opposite direction on both boundaries. Anderson [169] found that at low Er configuration a) is preferred and configuration b) is favourable at higher Er.

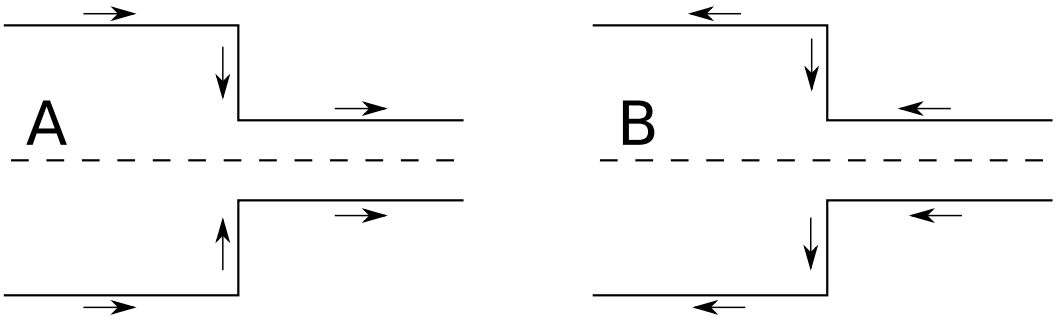

Figure 7.3. Some examples of wall-parallel boundary conditions in the vectorial framework, each representing notionally the same physical state.

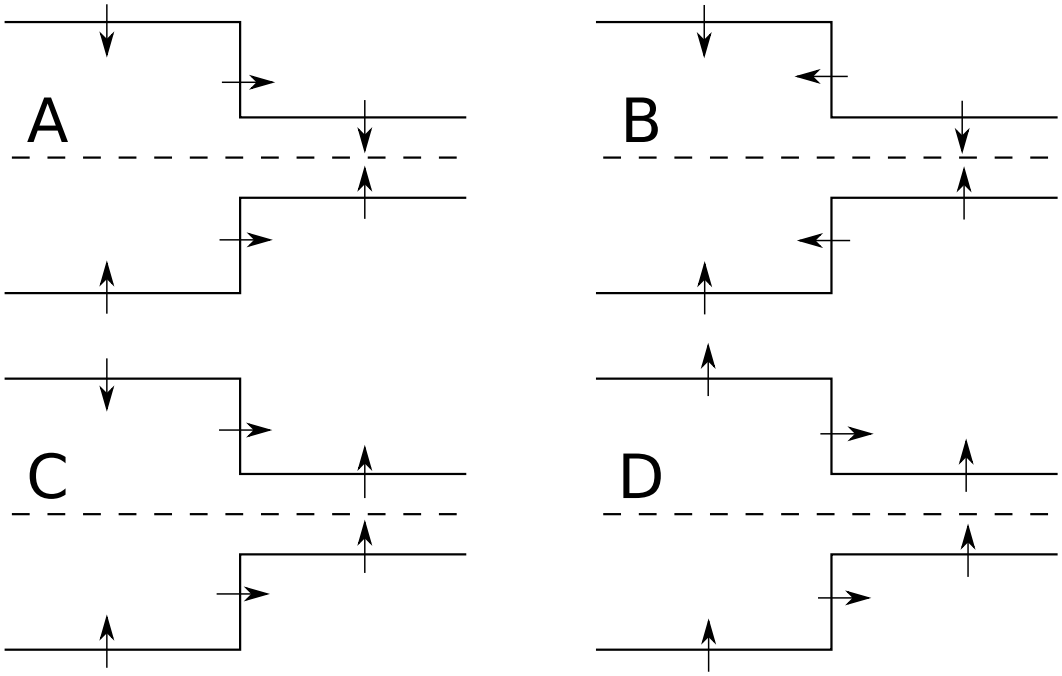

Figure 7.4. Some examples of homeotropic anchoring in the vectorial framework, each representing the same notional physical state.

The Ericksen number is defined based on the inlet conditions:

$$Er = \frac{4hu_0\alpha_4}{K}, \tag{7.2}$$

where $u_0 = \frac{2}{3}u_{max}$ is the mean velocity at the inlet and $4h$ is half of the inlet channel width. The Ericksen number in the Beris-Edwards model is defined as

$$Er_{BE} = \left[\mu + \frac{4}{9}(1-S^2)^2\xi^2\frac{1}{\Gamma}\right]\frac{4hu_0}{2K^Q S_{eq}^2}, \tag{7.3}$$

to ensure that in the uniaxial, constant order parameter limit, equal Ericksen numbers in both frameworks represent an identical partitioning of hydrodynamic and elastic effects,

Finally, the relative importance of hydrodynamic and bulk effects acting on the order-parameter tensor is quantified through the Deborah number

$$De = \frac{3u_0^{out}}{(a+b+c)h\Gamma}, \tag{7.4}$$

where $u_0^{out} = 4u_0$ is the mean flow velocity in the outlet pipe and a, b, c are material parameters in the Beris-Edwards model.

7.2.3 Computational domain and solution details

We use a two-dimensional structured mesh with square elements, as shown in fig. 7.5. The mesh is refined enough to resolve the smallest length-scales that appear in the constitutive equation: 1) the flow-elastic length-scale $\left(\frac{H}{\sqrt{Er}}\right)$, which quantifies the distance over which

the director transitions between wall-induced and flow-induced orientations [21] and; 2) the defect size $\left(\xi_N \approx \sqrt{\frac{3K}{a+b+c}}\right)$ that provides the length-scale over which the order parameter varies significantly [140].

We use three different meshes with different refinement, each of them consists of square elements with a side length $\Delta x = \Delta y$. The mesh density is controlled through the *blockMesh* utility [107] to produce grids of the following densities:

- M_1: $\frac{h}{\Delta x} = \frac{h}{\Delta y} = 10$; the mesh has 28 000 cells in total.
- M_2: $\frac{h}{\Delta x} = \frac{h}{\Delta y} = 20$; the mesh has 112 000 cells in total.
- M_3: $\frac{h}{\Delta x} = \frac{h}{\Delta y} = 40$; the mesh has 448 000 cells in total.

The code used to generate the refined mesh M_3 is given in appendix D, while other meshes can be reproduced by changing the cell density.

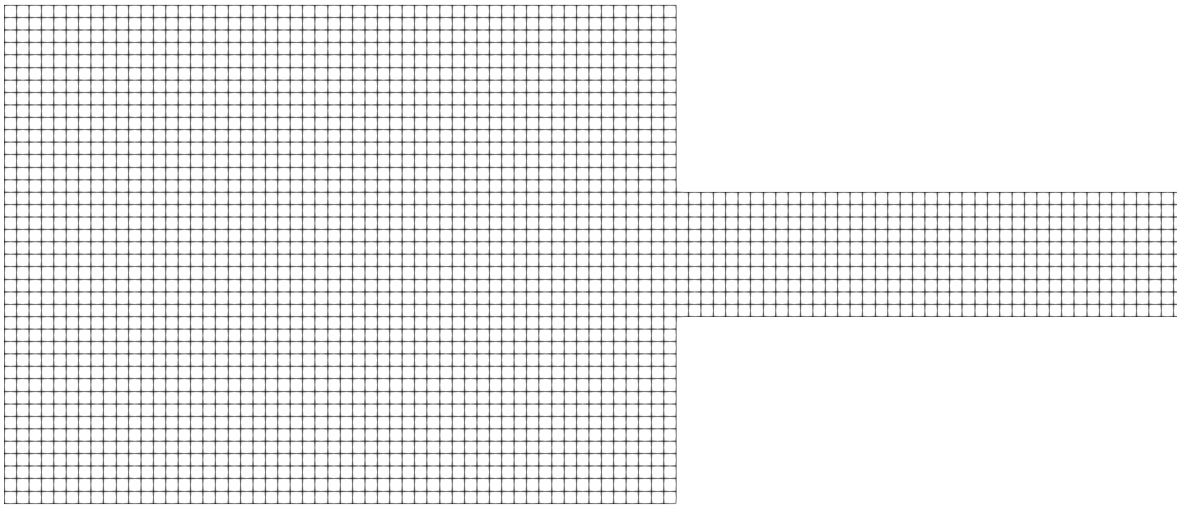

Figure 7.5. Mesh M_1 used in this study. The figure shows a coarsened (by a factor of 2) version of the M_1 grid for presentation purposes. Only a part of the inlet and outlet channel is included.

We consider a creeping flow limit, which enables us to neglect the convective term $\boldsymbol{u} \cdot \nabla \boldsymbol{u}$ from the momentum balance equation (2.8). Spatial gradients are discretised through the second-order central differencing scheme with absolute tolerances for pressure, velocity and director/$\boldsymbol{Q}$ tensor set to 10^{-8}. The SIMPLEC scheme is used for the pressure-velocity coupling.

We initialise the simulation with a horizontal director field and zero velocity throughout the whole domain. Simulations on the coarse mesh are run first until the calculation reaches a steady state. The coarse solution is then mapped onto the fine mesh as an initial condition in order to reduce the calculation time. The procedure is repeated on the refined mesh. The

calculation requires about $200 \cdot 10^{12}$ floating point operations on the coarse grid; the completion time (2 hours) is about five times longer than the analogous simulation of a Newtonian, creeping flow on the same mesh.

7.3 Results

7.3.1 Wall-parallel anchoring

Director orientation

Numerical predictions of the director fields obtained with different forms of the wall-parallel boundary condition are shown in fig. 7.6 ($Er = 1.73$) and 7.7 ($Er = 173$). The LE theory with configuration A better agrees with the benchmark BE model result than configuration B, irrespective of the Ericksen number. The disagreement is particularly significant at low Ericksen numbers (where elastic effects are stronger) (fig. 7.6), as configuration B predicts considerably larger microstructure distortions in the corner. The orientability issue of the vectorial framework is also clear in the outlet pipe, where the director rotates by 180^o between the horizontal outlet wall and the centerline (fig. 7.6c and 7.7c). The rotation is unphysical, since $\boldsymbol{n}$ and $-\boldsymbol{n}$ are equivalent. As the Ericksen number increases, the near-wall region of a sudden director transition shrinks and predictions made by configurations A and B become more similar (fig. 7.7).

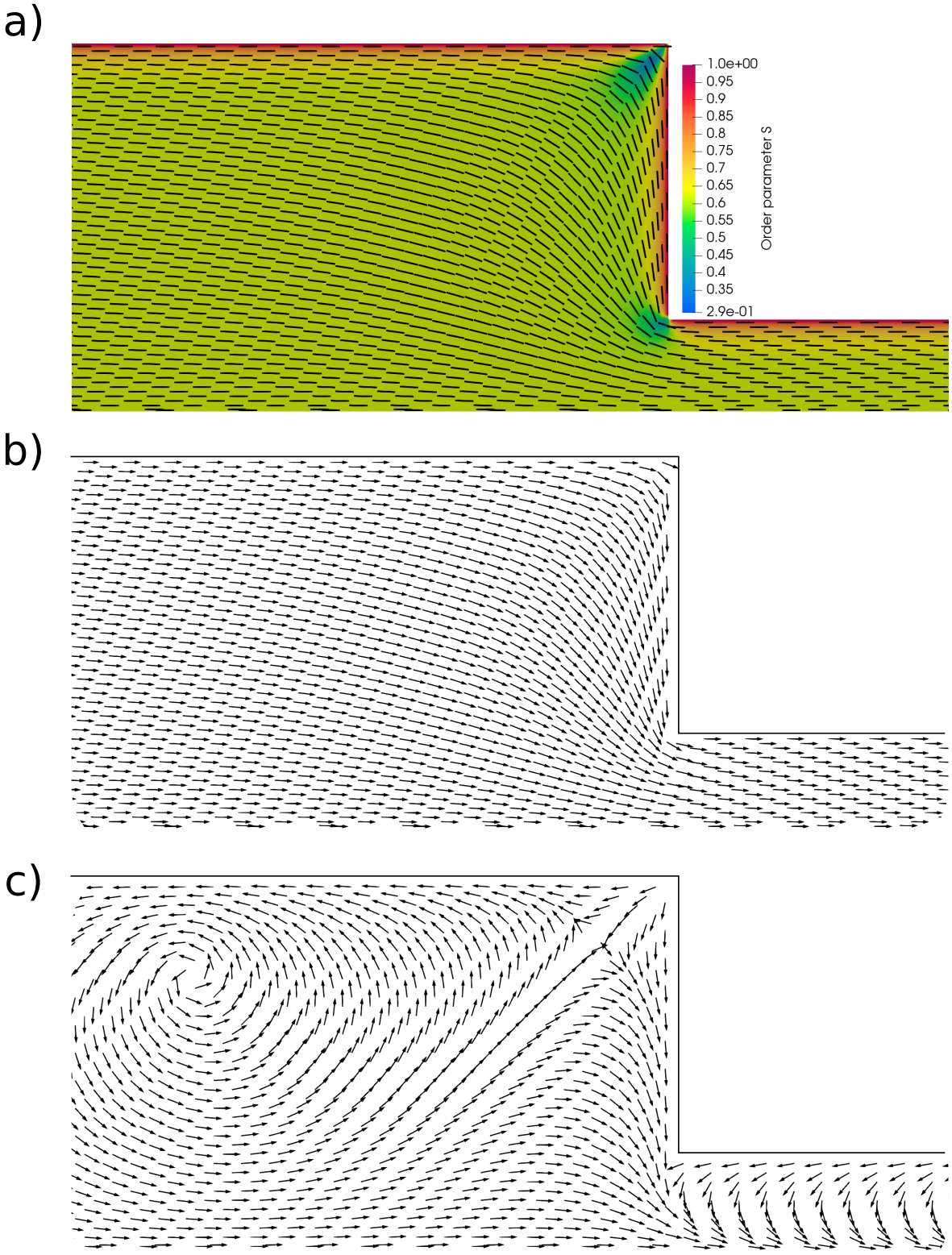

Figure 7.6. Director field with wall-parallel boundary conditions at $Er = 1.73$ a) Beris-Edwards model, b) Leslie-Ericksen model, configuration A, c) Leslie-Ericksen model, configuration B.

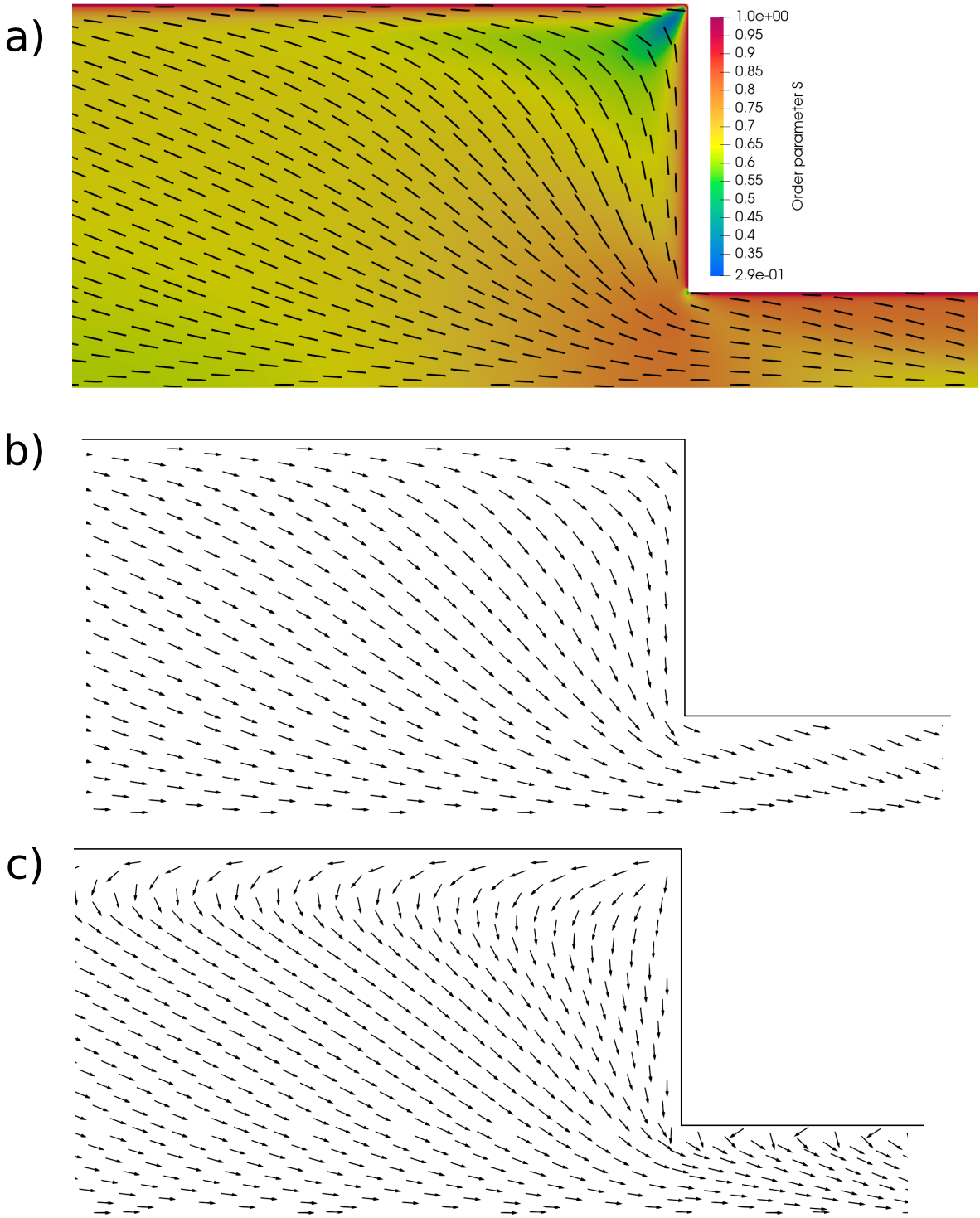

Figure 7.7. Director field with wall-parallel boundary conditions at $Er = 173$ a) Beris-Edwards model, b) Leslie-Ericksen model, configuration A, c) Leslie-Ericksen model, configuration B.

Velocity and stress profiles

A comparison of velocity and stress profiles at a distance $2h$ upstream of the contraction at $Er = 1.73$ is shown in fig. 7.8 and 7.9 and indicates the key effect of wall anchoring on the velocity and stress distribution. Results obtained in configuration A with the Leslie-Ericksen theory match well the BE result (table 7.3); variations in the order parameter affect only the stress distribution in the near-wall region and have little effect on the flow field. In

contrast, results from the configuration B suggest that a different choice of director orientation produces additional (and spurious) normal and shear stresses, which can be of opposite sign and different magnitudes than the benchmark result from the BE model. The difference in the stress distribution is manifested in the pressure drop (discussed later in the chapter), which ultimately governs the selection of the pipework equipment. As the Ericksen number increases, the director orientation is more dominated by hydrodynamic effects, so the orientability issue has less effect on the director field. The prediction of velocity and stress distribution in the BE model is still better matched by configuration A in the LE theory (fig. 7.10 and 7.11); however, the difference is significantly smaller than in the low Ericksen number regime (table 7.3). We thus conclude that the Leslie-Ericksen theory can match the prediction of the BE model provided that the boundary conditions are chosen appropriately. Therefore, we find that the velocity and stress profiles of the BE model are best matched with the LE model when the director fields are similar, which happens when the director points in the flow direction on horizontal walls and towards the symmetry line on vertical walls. That produces a bending director distortion near the corners, also observed in the Beris-Edwards model.

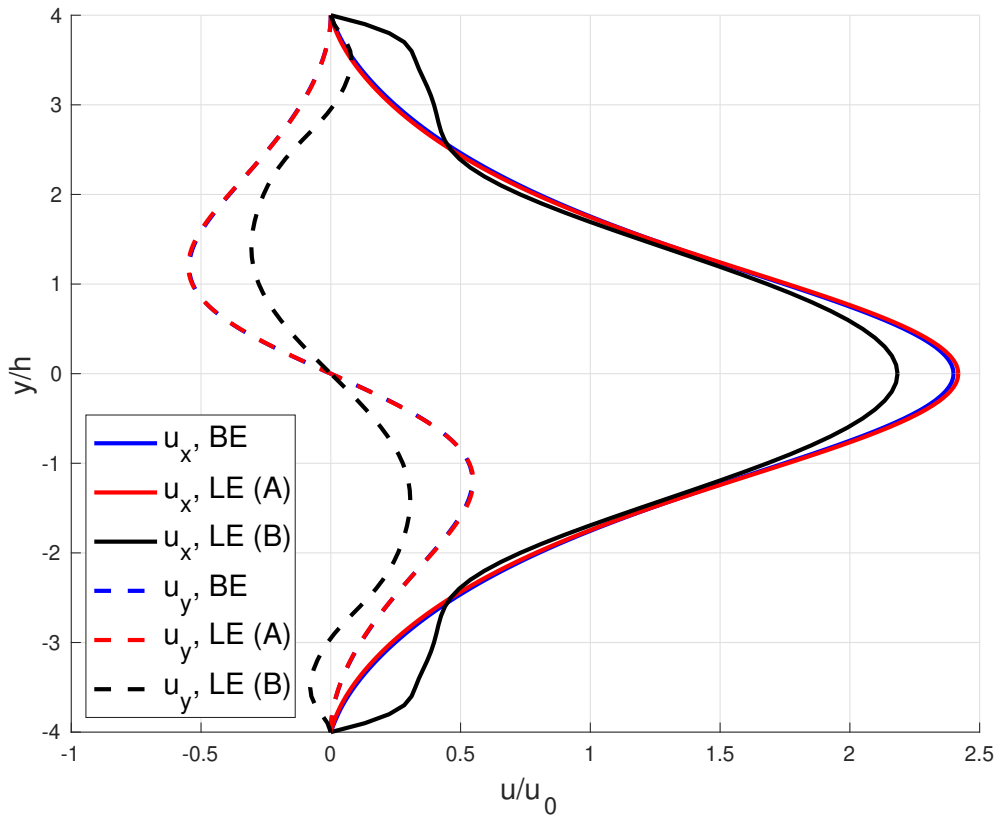

Figure 7.8. Comparison of the velocity fields predicted by BE and LE models at a distance $2h$ upstream of the contraction for the wall-parallel anchoring at $Er = 1.73$.

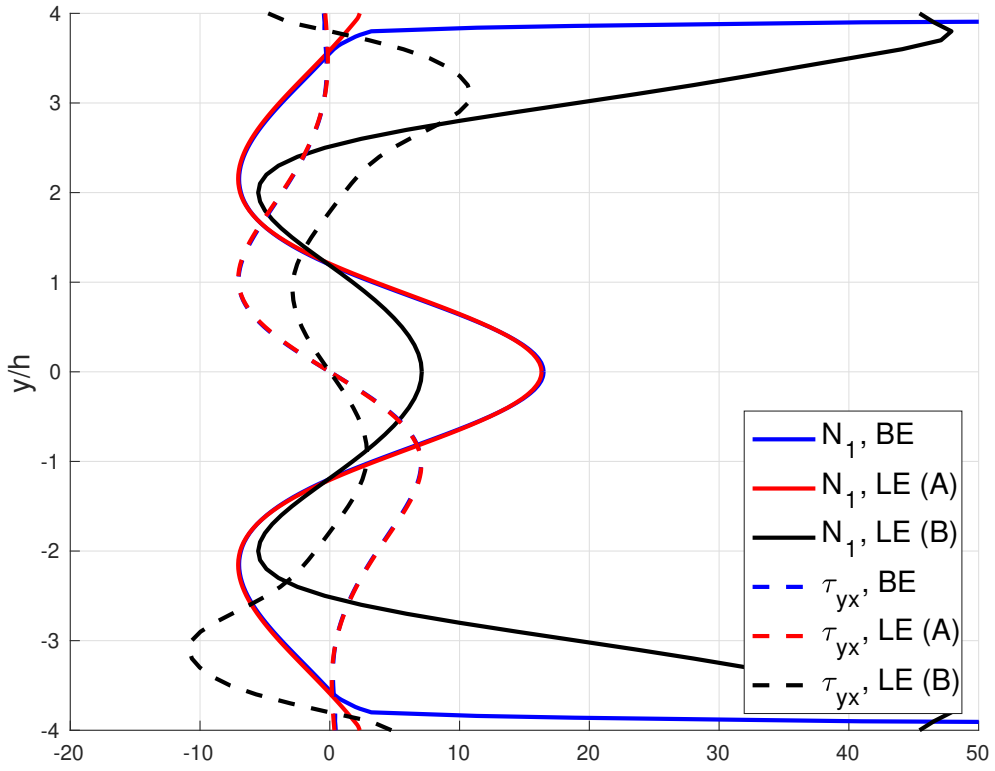

Figure 7.9. Distribution of N_1 and τ_{yx} predicted by BE and LE models at at a distance $2h$ upstream of the contraction for the wall-parallel anchoring at $Er = 1.73$. All stresses are normalised by the stress scale $\frac{\alpha_4 u_0}{H}$.

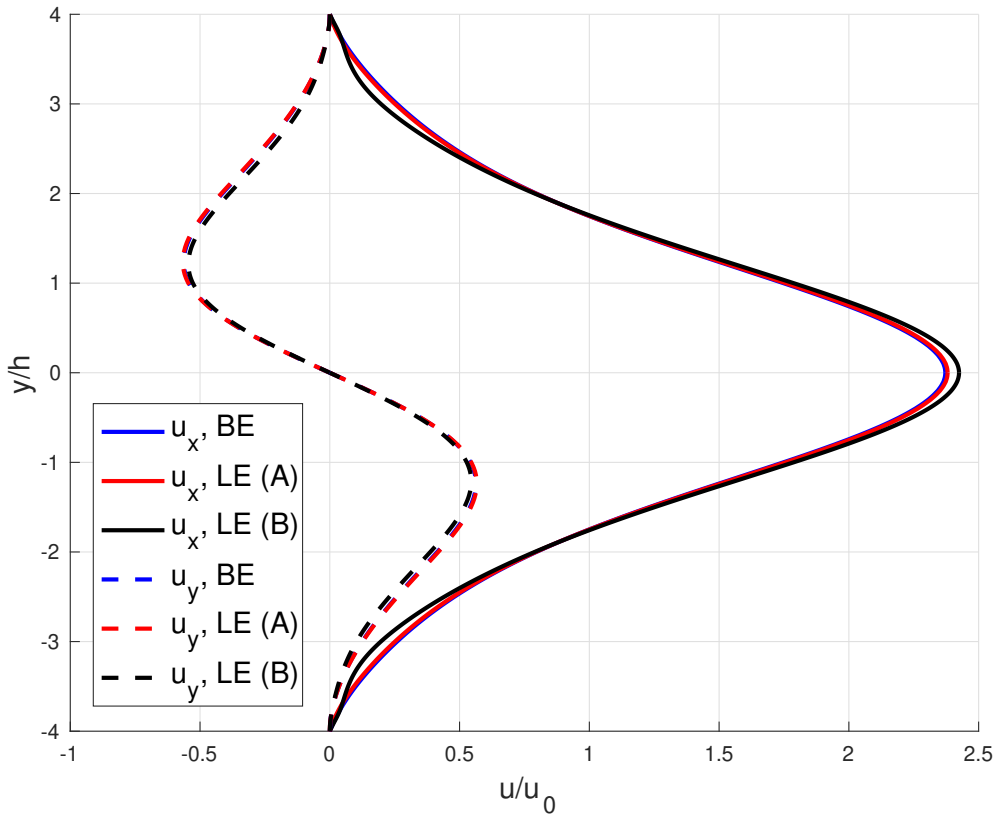

Figure 7.10. Comparison of the velocity fields predicted by BE and LE models at a distance $2h$ upstream of the contraction for the wall-parallel anchoring at $Er = 173$.

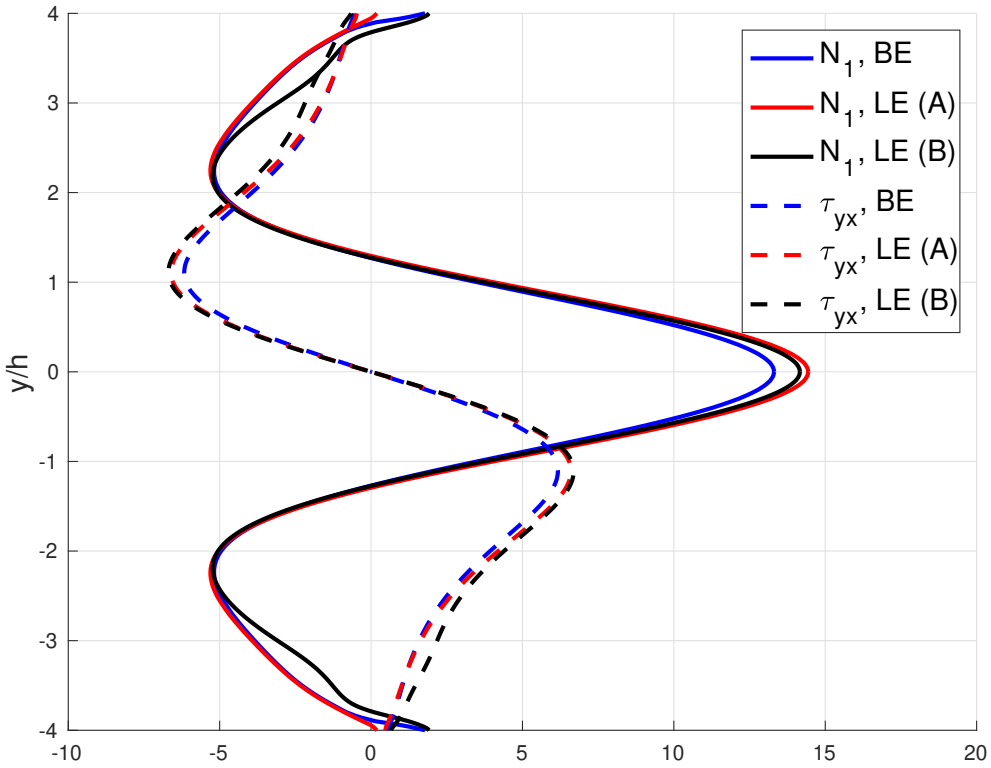

Figure 7.11. Distribution of N_1 and τ_{yx} predicted by BE and LE models at at a distance $2h$ upstream of the contraction for the wall-parallel anchoring at $Er = 173$. All stresses are normalised by the stress scale $\frac{\alpha_4 u_0}{H}$.

Table 7.3. Normalised 2-norm of the LE prediction with respect to the BE result $\frac{||N_{LE}-N_{BE}||_2}{||N_{BE}||_2}$ for flows with the wall-parallel anchoring. N represents either the velocity or stress component.

	$Er = 1.73$, A	$Er = 1.73$, B	$Er = 173$, A	$Er = 173$, B
u_x	$1.3 \cdot 10^{-2}$	10^{-1}	$5.1 \cdot 10^{-3}$	$7.2 \cdot 10^{-2}$
u_y	$5.8 \cdot 10^{-3}$	$4.7 \cdot 10^{-1}$	$2.9 \cdot 10^{-2}$	$5.4 \cdot 10^{-2}$
N_1	$1.8 \cdot 10^{-2}$	$1.8 \cdot 10^{0}$	$8.2 \cdot 10^{-2}$	$8.7 \cdot 10^{-2}$
τ_{yx}	$1.2 \cdot 10^{-2}$	$1.5 \cdot 10^{0}$	$6.7 \cdot 10^{-2}$	$1.2 \cdot 10^{-1}$

Director development

Figure 7.12 compares the director development around the contraction predicted by different models at high and low Ericksen numbers and confirms an agreement between LE and BE theories. The agreement is particularly good for configuration A when $Er = 1.73$, $De = 0.006$; the order parameter is nearly constant and equal to S_{eq} (fig. 7.6). On the other hand, at higher Ericksen and Deborah numbers ($Er = 173$, $De = 0.6$), flow effects are strong enough to introduce significant variations in the order parameter, which in turn affects the Leslie angle [142]

$$\theta_L = \frac{1}{2}\cos^{-1}\left(\frac{3S}{\xi(2+S)}\right). \tag{7.5}$$

The material constants in the Leslie-Ericksen model are calculated based on the equilibrium order parameter S_{eq} (eq. (2.75)), and since $S = const$ in the LE theory, the Leslie angle is independent of the strength of flow effects. In contrast, as the flow effects become stronger, the order parameter in the BE model increases, leading to larger discrepancies between the BE and LE models in the prediction of the Leslie angle. The sensitivity of order parameter to flow effects is governed by the Deborah number, whose value (for a fixed Ericksen number) can be controlled by adjusting material parameters a, b, c in eq. (2.68). In the limit $|a|, |b|, |c| \to \infty$, $De = 0$, which recovers the constant order parameter limit of the Leslie-Ericksen theory.

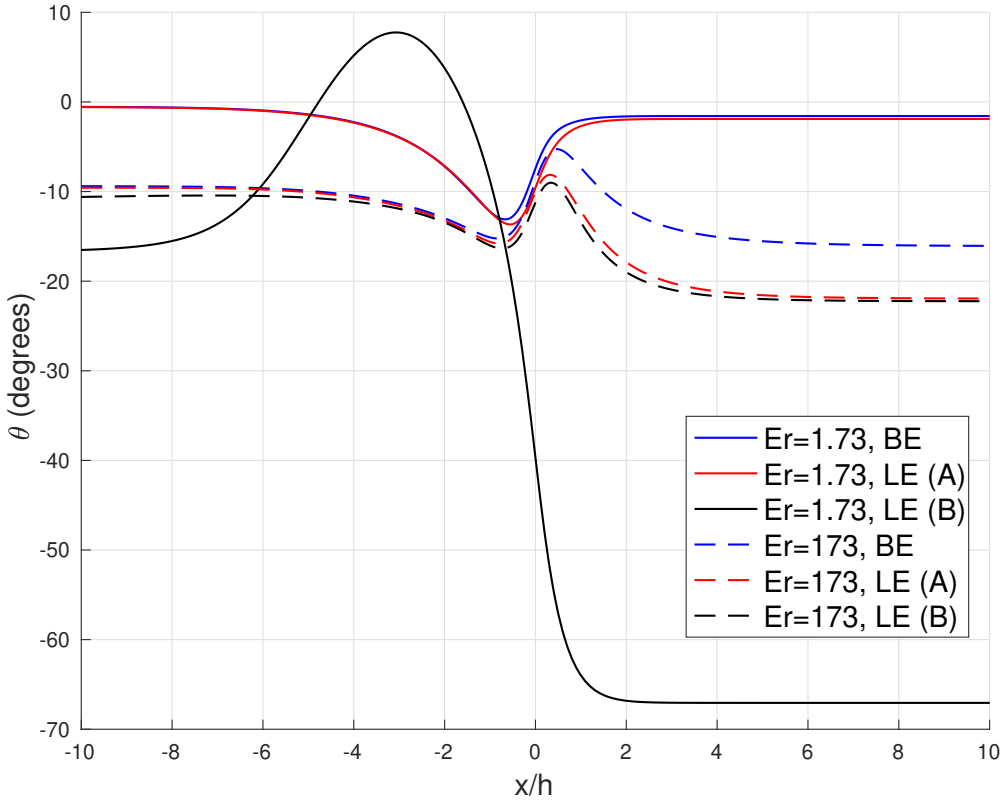

Figure 7.12. Variation of the director angle at $y = 0.4h$, wall-parallel anchoring. At $Er = 1.73$, the prediction of the LE theory (config. A) nearly coincides with the prediction of the BE model.

7.3.2 Homeotropic anchoring

Low Ericksen number

The Beris-Edwards model predicts that there is an orientational transition in the director orientation from the horizontal state at the centerline upstream of the contraction to the vertical state downstream the contraction (fig. 7.13a). Vertical walls induce a bending distortion in the corner; at low Ericksen numbers, the elastic boundary layer is large enough so that the wall anchoring significantly affects the director distribution at the centerline. As a result, $\boldsymbol{n}$ is parallel to the flow direction at $y = 0$, $x < 0$. Downstream the contraction, the director behaviour is also governed by elasticity since the viscous torques are not strong enough to introduce director distortion. In the fully developed state, the director orientation in the outlet

channel is such that the Helmholtz free energy is minimised, which happens when the director is parallel to the velocity gradient direction [142, 169]. The horizontal and vertical states are separated by a low order-parameter region (defect), which appears on the centerline at a distance h downstream the contraction (fig 7.13a). An additional simulation conducted for the Beris-Edwards model with a vertical director state as an initial condition produces and identical director distribution as the simulation with a horizontal director field (fig. 7.13a). Therefore, we conclude that the appearance of the defect is independent of initial director orientation.

The complex director behaviour at low Ericksen numbers predicted by the BE model cannot be replicated by the Leslie-Ericksen theory, as shown in fig. 7.13b-d. Configuration C (fig. 7.13d) reproduces the horizontal-vertical transition, however, the asymmetry of the director field about $y = 0$ results in an uneven (and unphysical) distribution of velocity (fig. 7.14) and stress (fig. 7.15) in the upper and lower part of the contraction. On the other hand, configuration B (fig. 7.13c) incorrectly predicts a splay mode of director distortion in the corner. This results in a differently distributed stress field (fig. 7.15) and a noticeably smaller vortex size (fig. 7.16). Finally, the distribution of the first normal stress difference in the BE model is best replicated by configuration A (table 7.4). Configuration B fails as there is a large director gradient in the vertical direction near the contraction because $\boldsymbol{n}$ rotates by 180^o to accommodate the sharply changing boundary conditions (fig. 7.13c). In the case of configuration C (fig. 7.13d), there is a significant director gradient in the flow direction due to the horizontal-vertical transition. The transition in the BE model occurs further downstream than predicted by configuration C, which is the reason for the lower stress magnitude in the Beris-Edwards model prediction.

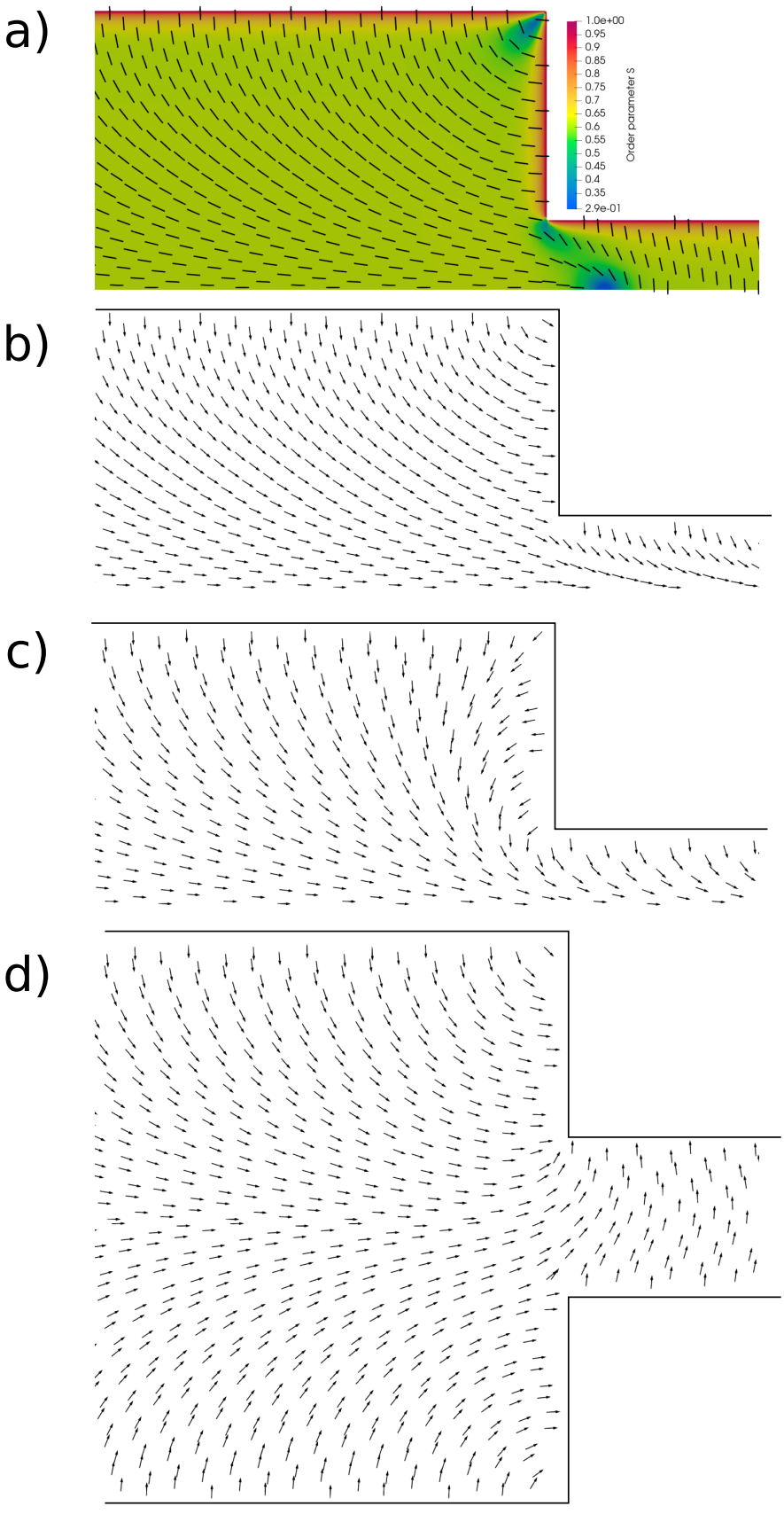

Figure 7.13. Director field with homeotropic boundary conditions at $Er = 1.73$ a) Beris-Edwards model, b) Leslie-Ericksen model, configuration A, c) Leslie-Ericksen model, configuration B, d) Leslie-Ericksen model, configuration D (due to the asymmetry of the director field, a whole contraction is shown).

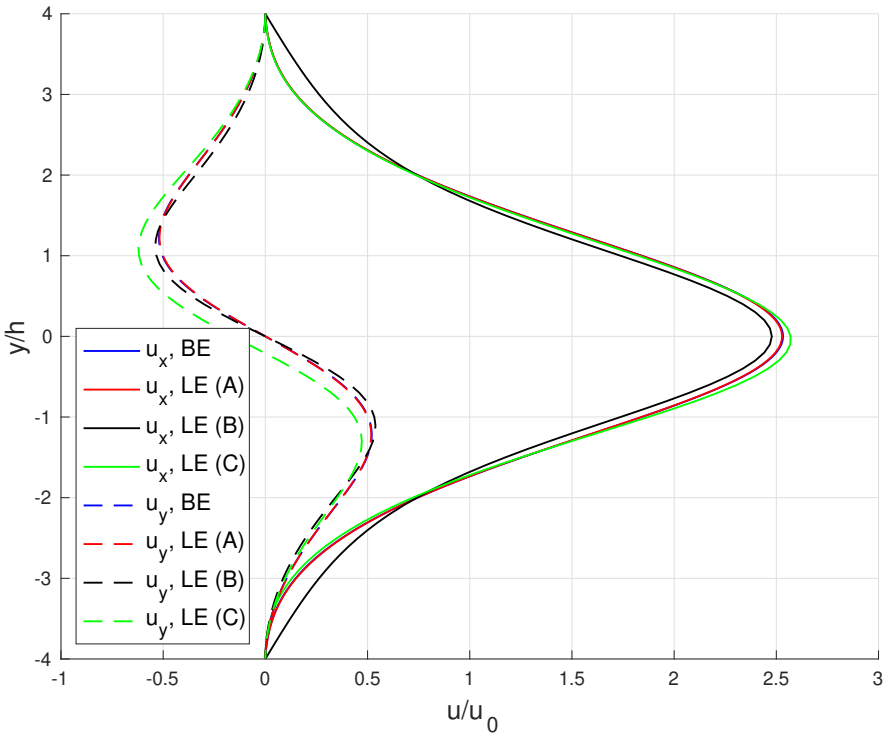

Figure 7.14. Comparison of the velocity fields predicted by BE and LE models at a distance $2h$ upstream of the contraction with the homeotropic anchoring at $Er = 1.73$. Note that the velocity distribution for configuration C is not symmetric about the centreline.

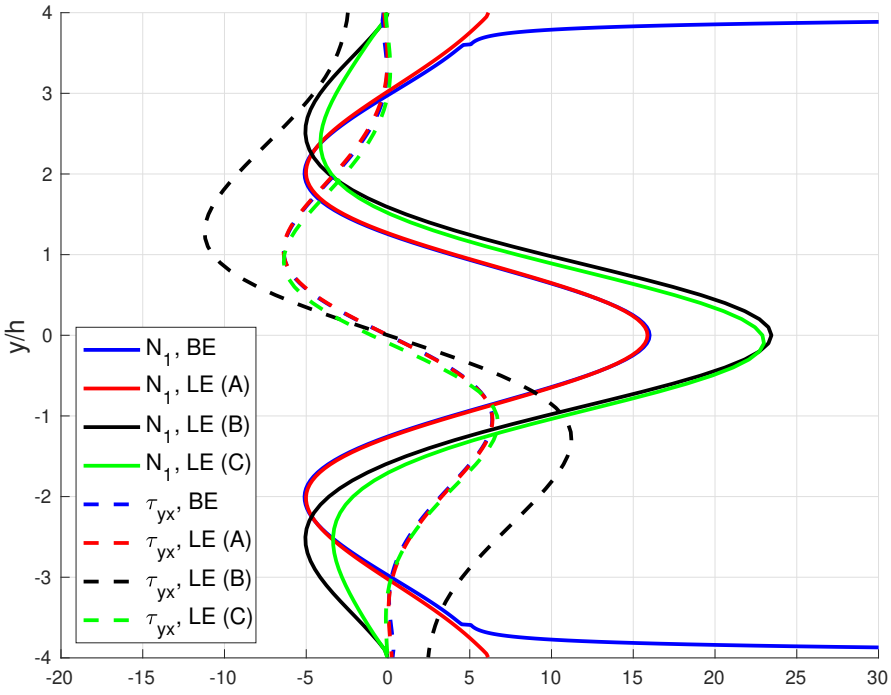

Figure 7.15. Distribution of N_1 and τ_{yx} predicted by BE and LE models at at a distance $2h$ upstream of the contraction with the homeotropic anchoring at $Er = 1.73$. Note that the stress distribution for configuration C is not symmetric about the centreline. All stresses are normalised by the stress scale $\frac{\alpha_4 u_0}{H}$. The shear stress in the BE model (blue dashed line) is falls onto τ_{yx} predicted by the LE theory (red dashed line) and hence the former is hardly visible.

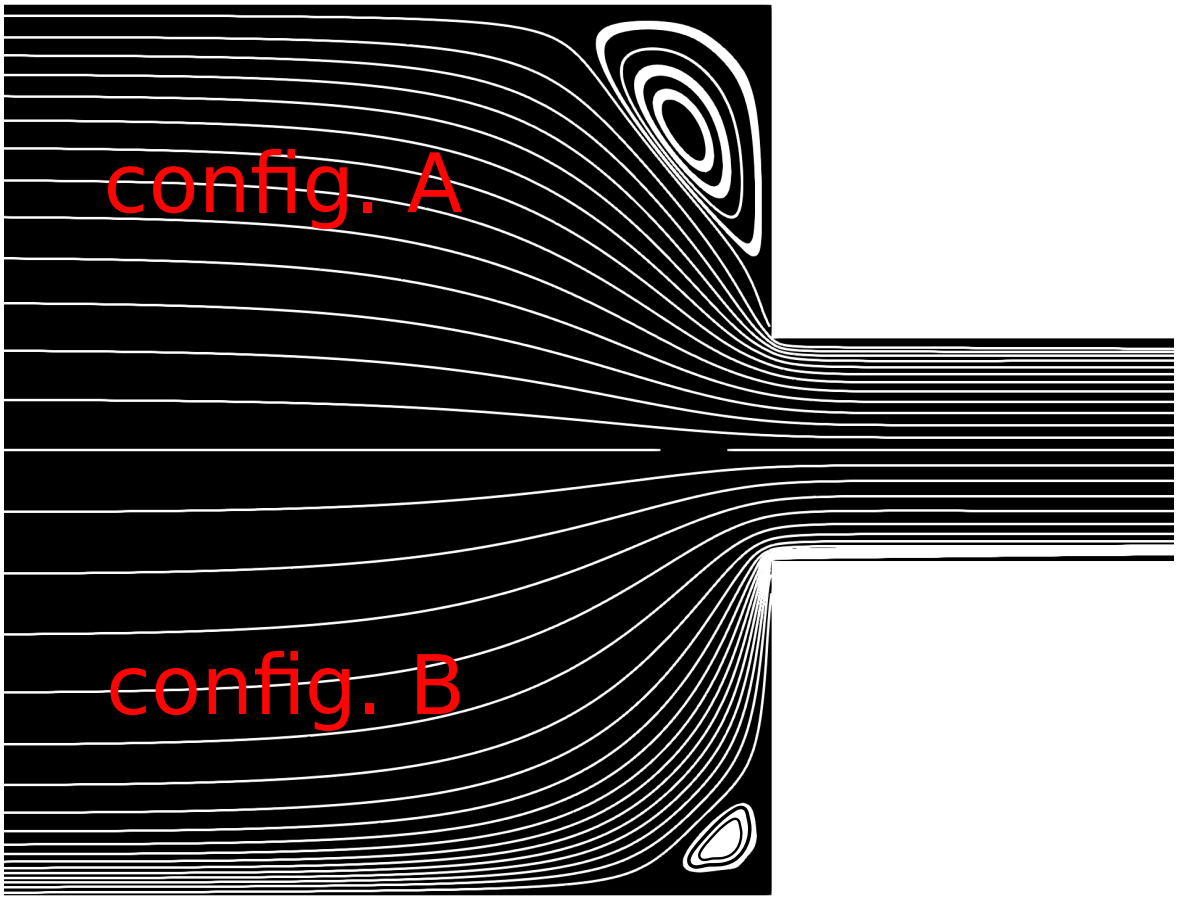

Figure 7.16. Comparison of vortex sizes obtained with configurations A and B ($Er = 1.73$).

Table 7.4. Normalised 2-norm of the LE prediction with respect to the BE result $\frac{||N_{LE}-N_{BE}||_2}{||N_{BE}||_2}$ for flows with the homeotropic anchoring. N represents either the velocity or stress component.

	$Er = 1.73$, A	$Er = 1.73$, B	$Er = 1.73$, C	$Er = 173$, A	$Er = 173$, B	$Er = 173$, C
u_x	$1.8 \cdot 10^{-3}$	$6 \cdot 10^{-2}$	$1.6 \cdot 10^{-2}$	$3.5 \cdot 10^{-3}$	$4.5 \cdot 10^{-3}$	$3.8 \cdot 10^{-3}$
u_y	$5.9 \cdot 10^{-3}$	$7.4 \cdot 10^{-2}$	$2.4 \cdot 10^{-1}$	$1.7 \cdot 10^{-2}$	$7 \cdot 10^{-3}$	$1.5 \cdot 10^{-2}$
N_1	$3 \cdot 10^{-2}$	$6.9 \cdot 10^{-1}$	$6.4 \cdot 10^{-1}$	$9.2 \cdot 10^{-2}$	$8.1 \cdot 10^{-2}$	$8.2 \cdot 10^{-2}$
τ_{yx}	$1.6 \cdot 10^{-2}$	$1.19 \cdot 10^{0}$	$1.2 \cdot 10^{-2}$	$6.6 \cdot 10^{-2}$	$5.3 \cdot 10^{-2}$	$5.5 \cdot 10^{-2}$

Intermediate and high Ericksen numbers

The director distribution predicted by the Beris-Edwards model changes significantly at higher Ericksen numbers. Hydrodynamic torques are strong enough to align the director parallel to the flow direction in the outlet channel, as shown in fig. 7.17a. The Beris-Edwards result is best matched with the configuration A (fig. 7.17b) of the Leslie-Ericksen model; configuration B fails due to the splay distortion mode in the corner (fig. 7.17c). Configuration C is not symmetric, and due to the incorrectly prescribed director orientation at the upper wall of the outlet channel, there is a region of rapid orientational transition (fig. 7.17d).

Similarly to the wall-parallel anchoring at high Ericksen number, the distribution of ve-

locity and stresses at $x = 2h$ upstream of the contraction is similar irrespective of the model considered (fig. 7.18 and 7.19). The difference between LE and BE models appears only in the near-wall region, where a significant change in the order parameter results in additional stress.

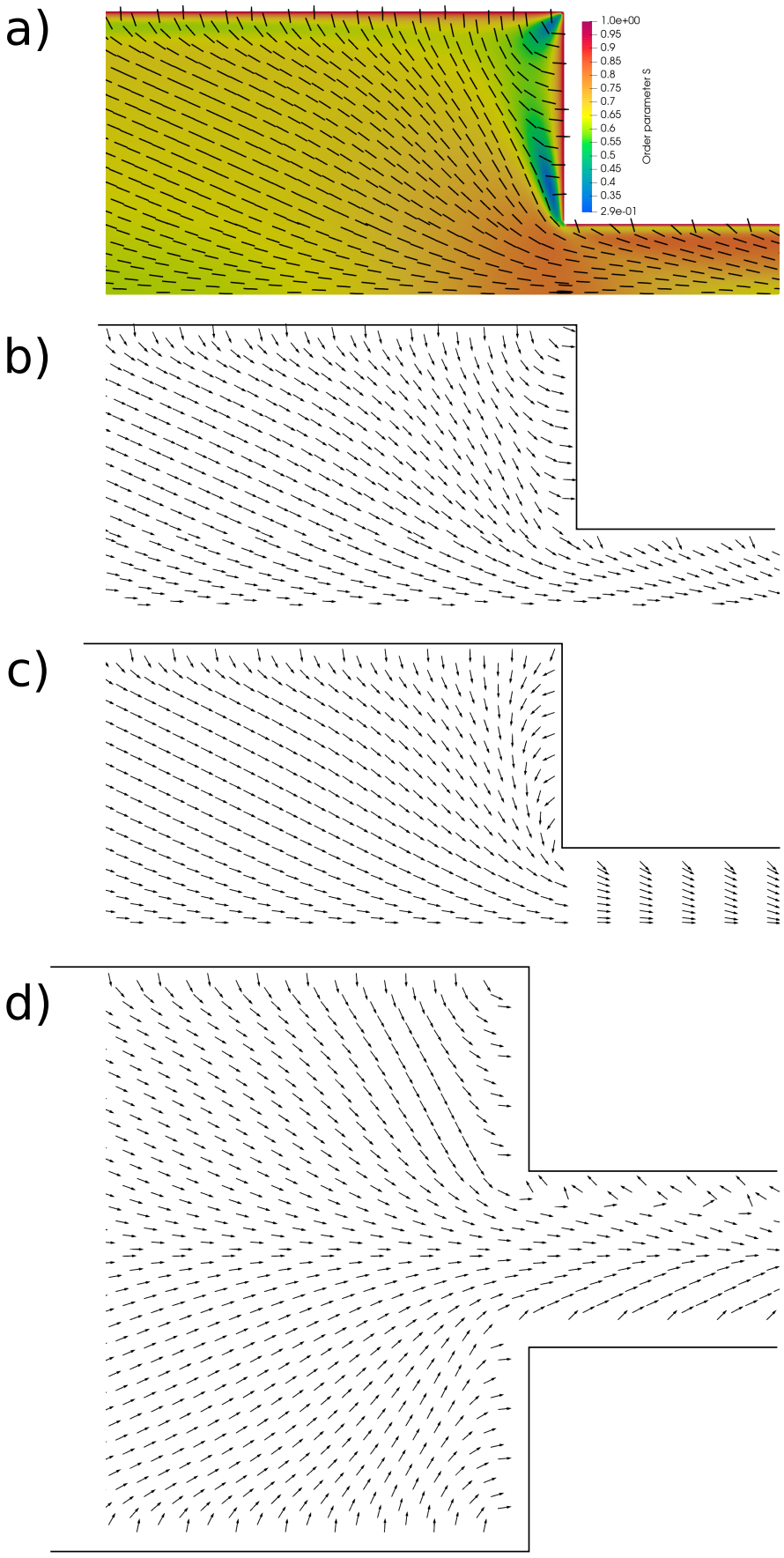

Figure 7.17. Director field with homeotropic boundary conditions at $Er = 173$ a) Beris-Edwards model, b) Leslie-Ericksen model, configuration A, c) Leslie-Ericksen model, configuration B, d) Leslie-Ericksen model, configuration D (due to the asymmetry of the director field, a whole contraction is shown).

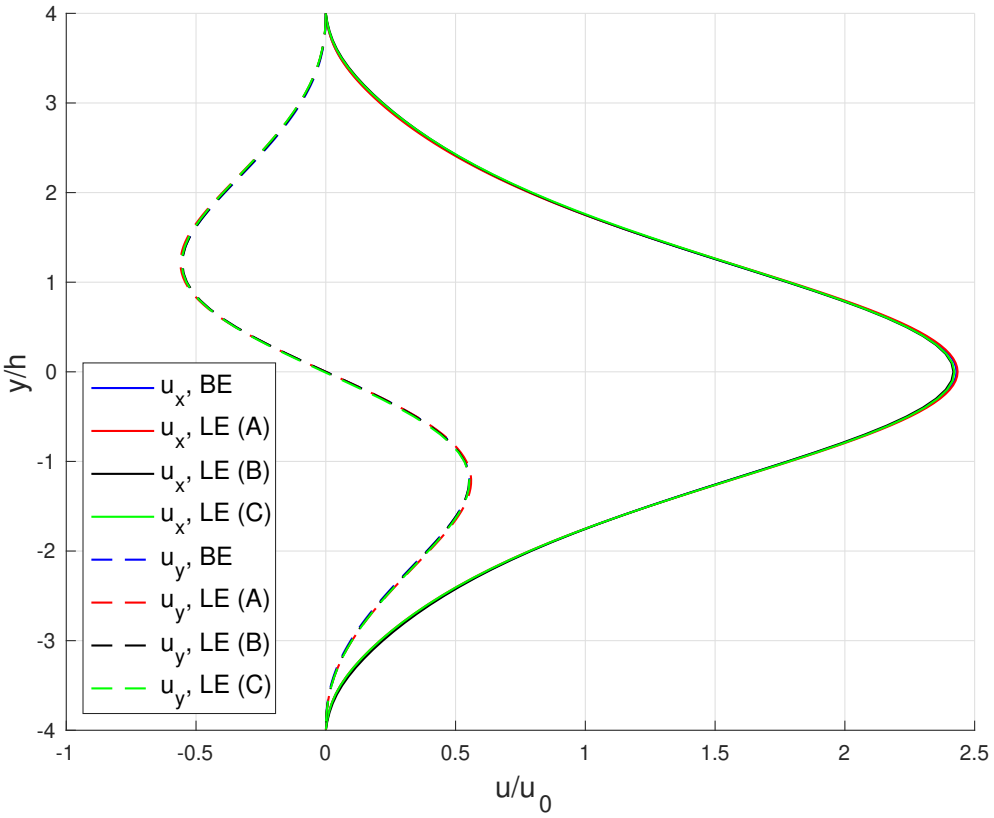

Figure 7.18. Comparison of the velocity fields predicted by BE and LE models at a distance $2h$ upstream of the contraction ($Er = 173$).

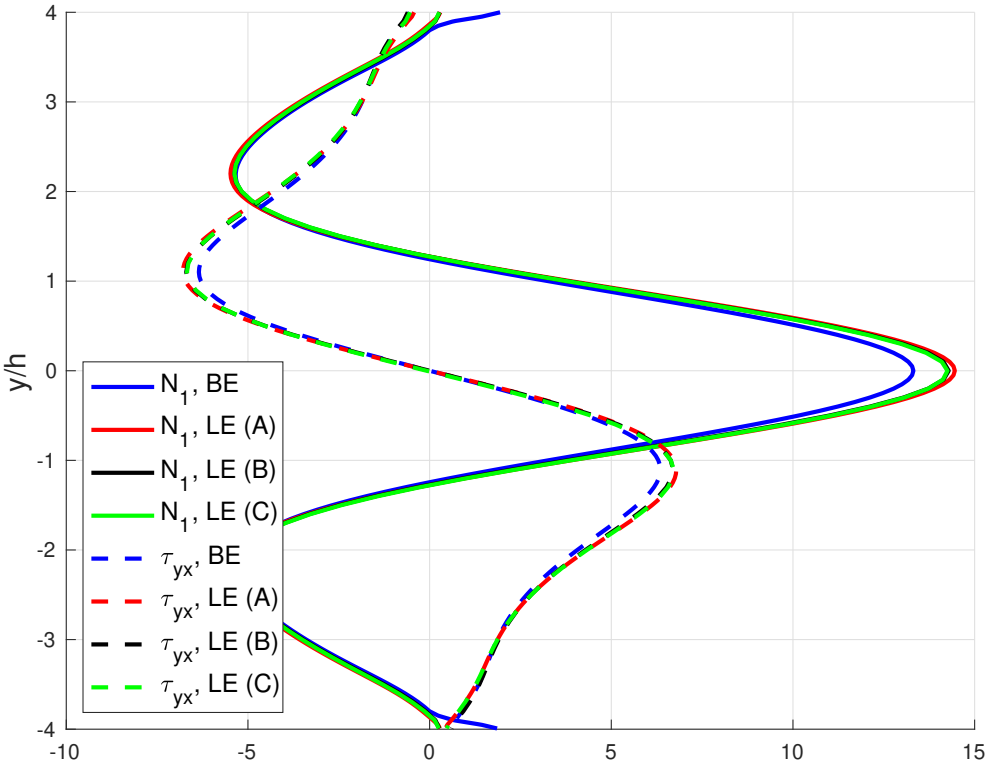

Figure 7.19. Distribution of N_1 and τ_{yx} predicted by BE and LE models at at a distance $2h$ upstream of the contraction ($Er = 173$). All stresses are normalised by the stress scale $\frac{\alpha_4 u_0}{H}$.

Director development

Fig. 7.20 compares the director development profiles obtained from different configurations at $Er = 1.73$ and $Er = 173$. Similarly to the wall-parallel anchoring, the development length increases with the Ericksen number, and the flow reaches a fully developed state at a distance of $5h$ downstream the contraction. Unusual behaviour is predicted for (an unphysical) configuration C at high Ericksen numbers, where the corner distortion propagates in the outlet pipe (fig. 7.21) and reaches the fully developed state at a distance around $20h$ downstream the contraction.

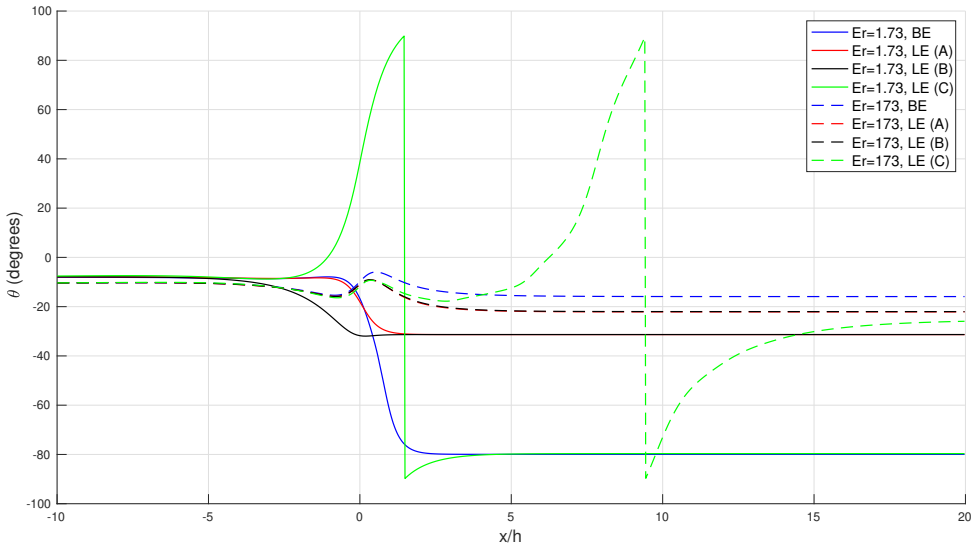

Figure 7.20. Variation of the director angle at $y = 0.4h$, homeotropic anchoring.

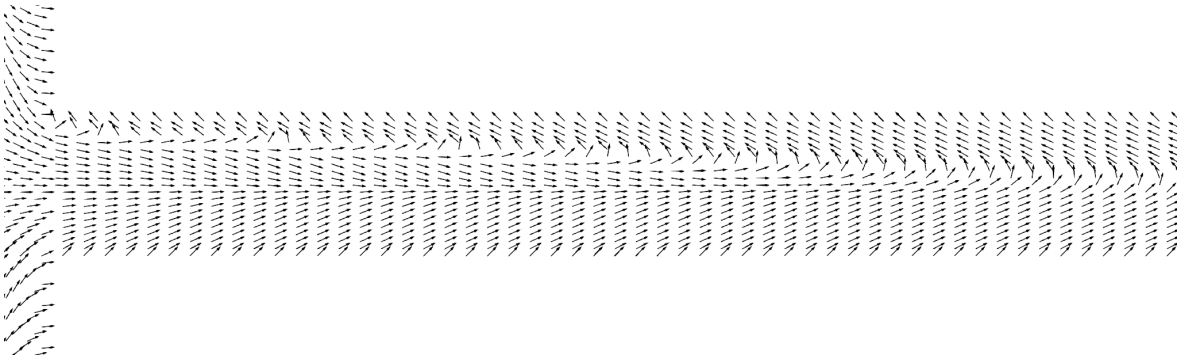

Figure 7.21. Director development at $Er = 173$ for configuration C.

7.3.3 Pressure losses

In order to quantify the effect of contraction on the pressure losses we introduce the Couette correction factor [182]

$$c_c = \frac{\Delta p - \Delta p_{FD}}{2\tau_w}, \tag{7.6}$$

where τ_w is the wall shear stress in the fully developed flow in the outlet channel, Δp is the pressure drop between inlet and outlet locations with fully developed flow, and

$$\Delta p_{FD} = \left(\frac{\partial p}{\partial x}\right)^{inlet} L_i + \left(\frac{\partial p}{\partial x}\right)^{outlet} L_o, \tag{7.7}$$

measures the pressure drop over the same distance due to the fully developed flow only (fig. 7.22). Therefore, we can understand $\Delta p - \Delta p_{FD}$ as the excess pressure drop caused by the presence of contraction.

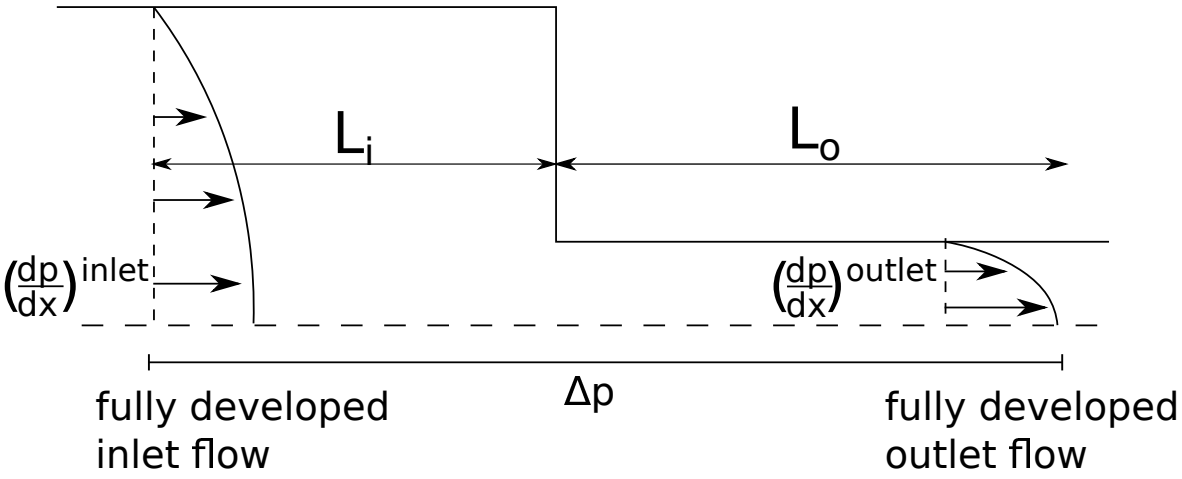

Figure 7.22. Pressure drop across a contraction.

Figure 7.23 compares the Couette correction factor obtained with different configurations considered in the previous sections and suggests the following conclusions on the choice of boundary conditions in the vectorial framework:

- For flows with the wall-parallel anchoring, configuration A provides not only the best agreement in terms of the director field but also matches the prediction of Couette correction factor in the BE model better than configuration B. The choice of boundary condition is particularly significant at low Ericksen numbers, where c_c can be significantly overestimated (c_c predicted for configuration B with the wall-parallel anchoring is larger than the BE model prediction by a factor of two). As Er increases, the director orientation is governed by the flow effects, and the discrepancy between configurations A and B decreases.

- For flows with the homeotropic anchoring, the director distribution predicted by the BE model is best matched by configuration C at low Ericksen numbers and configuration A at higher Ericksen numbers. This preference is also replicated in the estimation of c_c as configurations C and A replicate the BE prediction at low and high Ericksen numbers, respectively.

- In the case of flows with homeotropic anchoring, the 'correct' director configuration in the LE model minimises the value of c_c (config. C at low Er and config. A at higher). A similar result was presented by Anderson [169] in the context of channel flow, where at low Er, the distortion energy is minimised with the director pointing in the vertical

direction at the centerline (fig. 7.2a). In contrast, at higher Er, the director prefers the flow-aligned orientation at the centerline (fig. 7.2b).

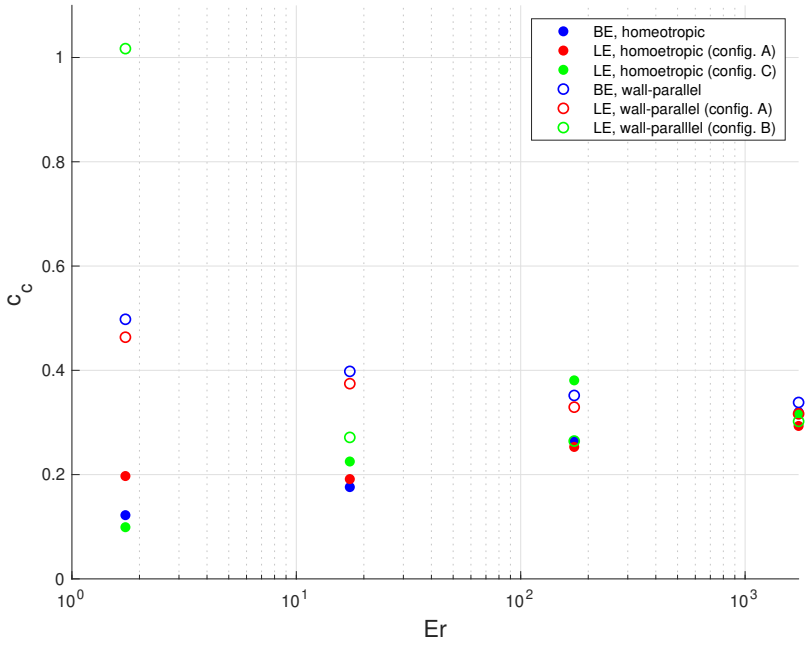

Figure 7.23. Couette criterion for the BE and LE models with homeotropic and wall-parallel boundary conditions.

Figure 7.23 indicates that c_c is larger in flows with wall-parallel boundary conditions, so the presence of contraction has a more profound effect there. Two factors contribute to this effect:

- The dissipation near the contraction entrance (at a distance h upstream) is higher in flows with the wall-parallel anchoring, as shown in fig. 7.24. The budget of dissipation in the case of wall-parallel (fig. 7.25) and homeotropic (fig. 7.26) boundary conditions suggests that the excess dissipation is predominantly caused by the extensional flow near the centerline and shearing close to the re-entrant corner ($y \approx h$). The former of which is absent in a fully developed channel flow.
- τ_w is larger in configurations with homeotropic anchoring, so a fixed excess pressure drop $\Delta p - \Delta p_{FD}$ increases c_c by less than in flows with wall-parallel anchoring (smaller τ_w).

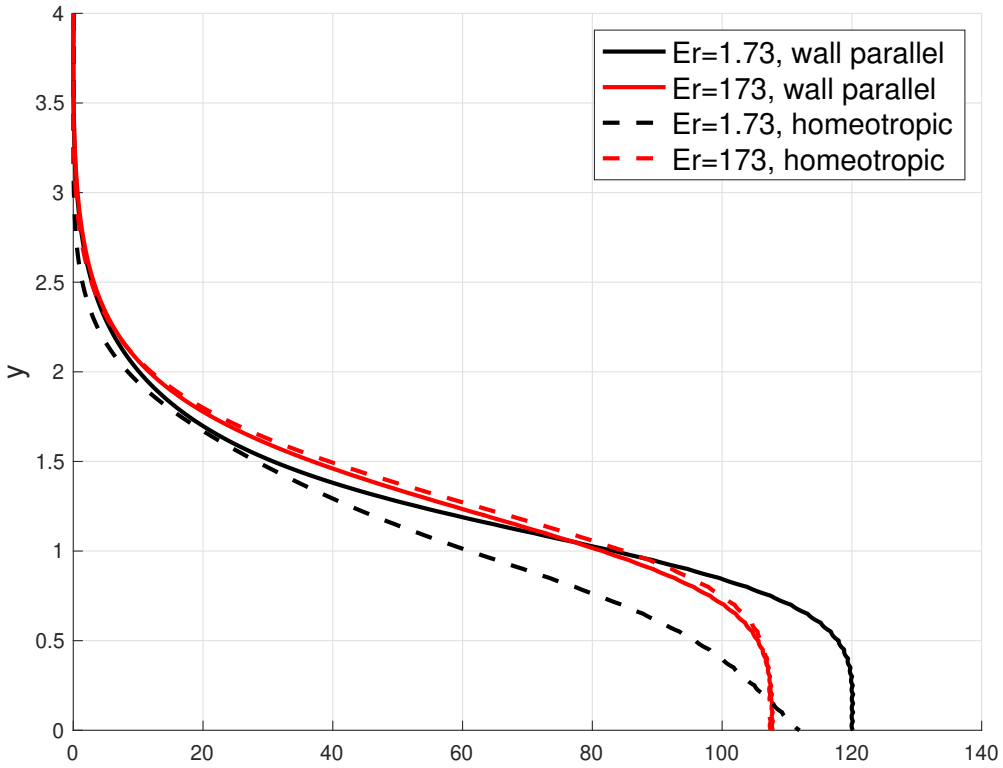

Figure 7.24. Distribution of dissipation at a distance h upstream of the contraction.

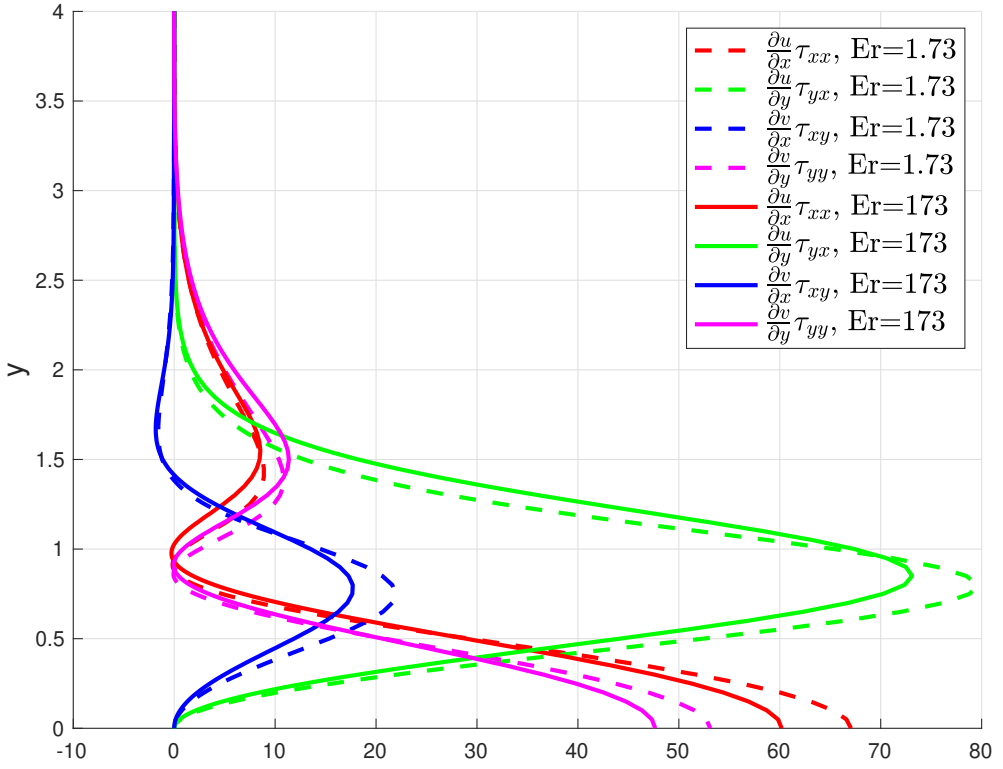

Figure 7.25. Budget of dissipation in configurations with wall-parallel anchoring.

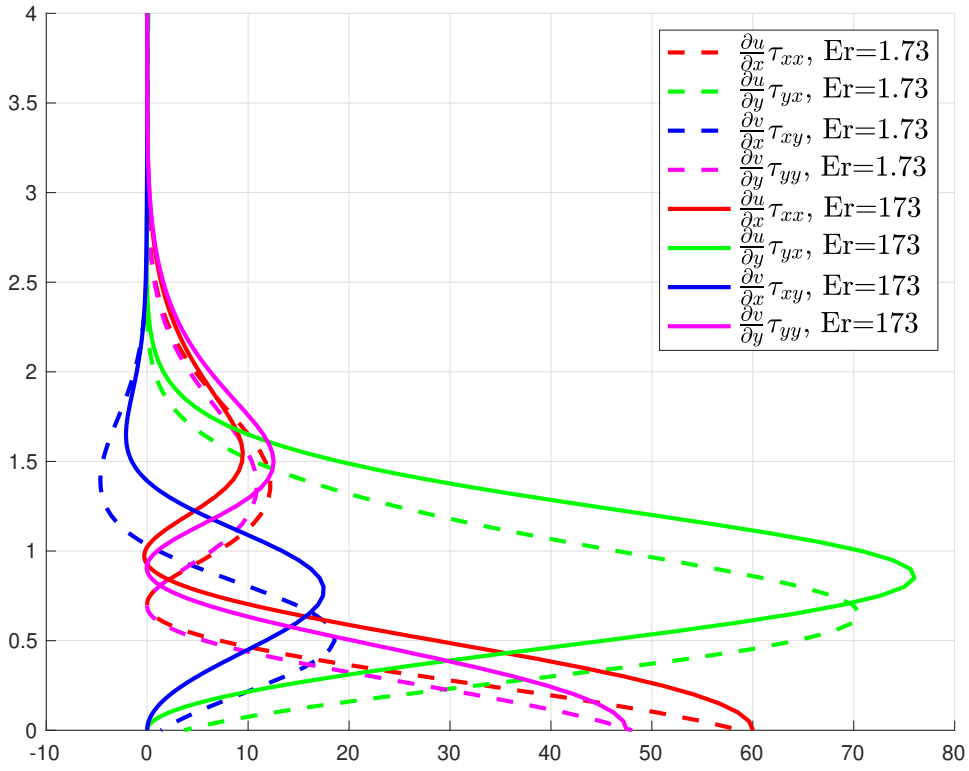

Figure 7.26. Budget of dissipation in configurations with homeotropic anchoring.

Interpretation of the Couette correction

In the outlet channel, the $x-$ component of momentum balance (eq. (2.8)) in a fully developed flow is given by

$$\frac{\partial p}{\partial x} = \frac{\partial \tau_{yx}}{\partial y}, \tag{7.8}$$

where τ_{yx} and $\frac{\partial p}{\partial x}$ are the shear stress and the pressure gradient respectively. The pressure gradient is constant and independent of y, so by manipulating eq. (7.8) we obtain the solution for τ_{yx}:

$$\tau_{yx} = \frac{\partial p}{\partial x} y + C, \tag{7.9}$$

where the integration constant $C = 0$ because the flow is symmetric about $y = 0$. Therefore, the wall shear stress is given by

$$\tau_w = \tau_{yx}(y = h) = \frac{\partial p}{\partial x} h. \tag{7.10}$$

Substituting above into the definition of the Couette correction factor (eq. (7.6)) and rearranging gives

$$\Delta p - \Delta p_{FD} = 2c_c h \frac{\partial p}{\partial x}, \tag{7.11}$$

which shows that the presence of contraction effectively increases the length of the outlet channel by $2c_c h$; the result is schematically illustrated in fig. 7.27. The relative importance of the pressure loss due to the contraction is predicated on length of the outlet channel. Based on the results shown in fig. 7.23, $0.1 < c_c < 0.5$, so the contraction effectively increases the length of the outlet channel by $O(h)$. For an outlet channel with a length of $5h$ (fig. 7.12 and 7.20 suggest that the flow reaches a fully developed state up to $5h$ downstream the contraction), the presence of contraction increases the total pressure drop by up to 20%.

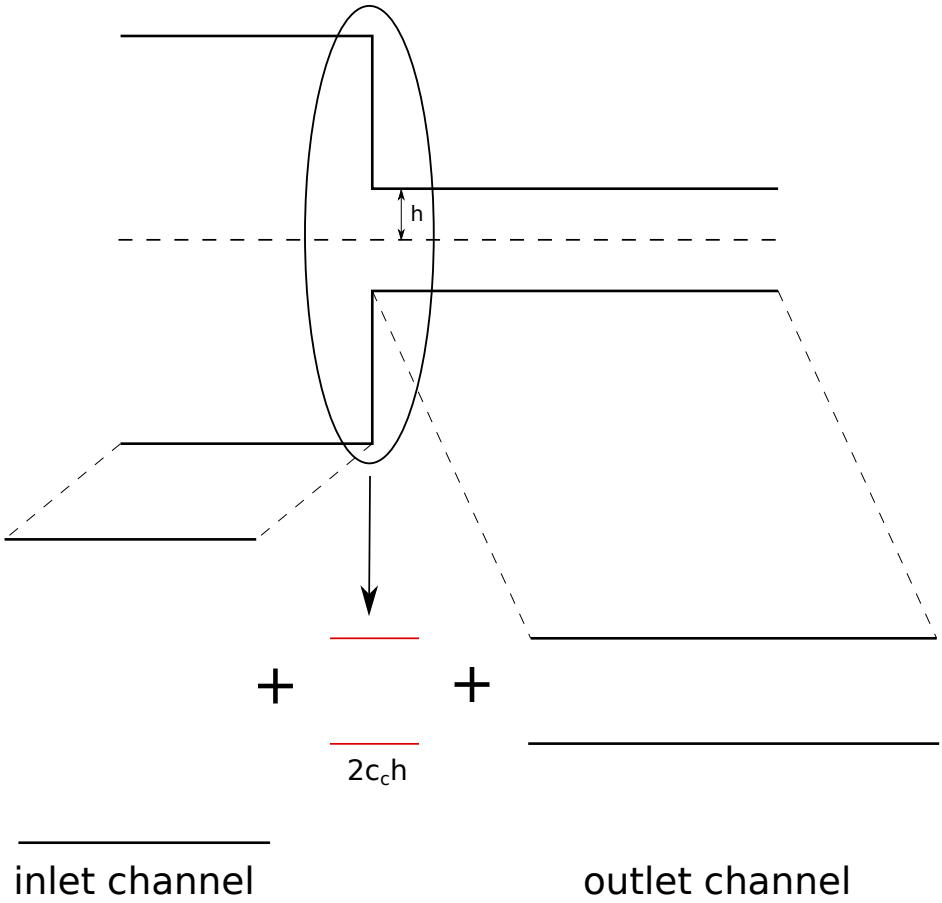

Figure 7.27. Graphical interpretation of the Couette correction.

7.4 Summary

This chapter compared the predictions of vectorial and tensorial frameworks of microstructure representation. Due to the orientational ambiguity in the former approach, a director field with the same physical meaning can be represented in several different ways; each of them produces distinct director and flow distributions. The choice of boundary conditions is simpler in flows with the wall-parallel anchoring, as the same configuration can well match the Beris-Edwards model's prediction irrespective of the Ericksen number. In contrast, results

from the BE model in flows with homeotropic anchoring are best matched either by configuration C (low Er) or A (high Er). At low Ericksen number, the Beris-Edwards model predicts an appearance of a defect, which is likely to increase the additional pressure drop due to an increased director/velocity misalignment; that is qualitatively confirmed in fig. 7.23, where for similar director fields, the BE model predicts a higher Couette criterion.

Due to a varying director orientation, the velocity and stress distribution near the contraction may vary and are particularly sensitive to the selection of configuration at low Ericksen numbers. The choice of boundary conditions also has implications on the pressure drop; we find that configurations whose director distribution is similar to the BE prediction also give the best agreement in the prediction of the Couette factor. The difference is particularly significant at low Ericksen numbers, where the selection of boundary conditions results in an over-prediction of c_c by a factor of two. As the Ericksen number increases, the director orientation is governed by hydrodynamic effects, so the choice of boundary condition has a smaller effect on the pressure drop.

Chapter 8

Conclusions and future work

8.1 Conclusions

This thesis has investigated the predictions of constitutive equations dedicated to liquid crystals in complex geometries relevant to the FMCG industry: bends and contractions. For that reason, we have developed an OpenFOAM solver dedicated to solving linear and angular momentum equations supplemented with a non-Newtonian stress tensor. All results indicate a key role of wall anchoring and director orientation in controlling flow and microstructure behaviour.

The main conclusions drawn from the studies presented in the previous chapters are outlined below.

8.1.1 Flow of liquid crystals in curved pipes

Firstly, we have considered flows of Leslie-Ericksen fluids at an infinite Ericksen number. In this limit, the motion of liquid crystals can be described by the transversely isotropic fluid model, and the wall anchoring does not affect the director distribution. Analytical solutions are obtained by perturbing the linear and angular momentum equation in the limit of small geometry curvature $\delta \to 0$. We find that the non-Newtonian behaviour in the transversely isotropic fluid model (normal stresses, orientation-dependent viscosity) arises due to the flow/director misalignment. These effects influence the distribution of axial and secondary flows. The latter is driven by two different mechanisms 1) a combination of normal stresses and geometry curvature 2) asymmetry of the stress distribution. In the case of nematic liquid crystals (5CB, PAA, MBBA), these effects oppose each other with the latter dominant. For materials, where the tumbling parameter $\lambda \to 1$, the strength of the secondary flow depends on the director/velocity misalignment. The pipe curvature also affects the stream-wise velocity profile, which is shifted towards the bend axis, similarly to a Newtonian, creeping flow. The distorted velocity field influences the director distribution; the effect is most significant near the pipe axis (where the $O(1)$ flow contribution vanishes), and as a result, the director field moves towards the bend axis.

Perturbation analysis was extended with numerical simulations to investigate the effect of wall anchoring at finite Ericksen numbers. Results show that the flow and director dis-

tributions are similar to those at infinite Er. The exception is the near-wall region, where elastic effects rotate the director towards the wall-imposed orientation. We find that the director boundary conditions significantly affect the distribution of normal stresses. That can lead to the reversal of the secondary motion in materials where $\chi < 0$ (the ratio of curvature and stress imbalance effects) with homeotropic wall anchoring. In contrast, in materials with positive χ, a decrease in Ericksen number in configurations with homeotropic anchoring increases the magnitude of the secondary motion. On the other hand, the wall-parallel anchoring improves director/velocity alignment, reducing stresses and weakening the strength of the secondary motion.

Numerical simulations also enabled to explore of the flow behaviour as the fluid enters/leaves the bend and reveal spikes in the transverse velocity field. These are predominantly caused by the stream-wise variation in the shear stress as the flow transforms between fully developed states in straight and curved pipes. In the case of liquid crystals, the spike magnitude depends on material properties and scales with $\alpha_2 + \alpha_4 + \alpha_5$. The flow curvature also affects the development of the director field. Analytical considerations show that the development length is a function of $\gamma_1 Er$, which expresses the relative importance of convective to elastic effects governing the director orientation.

8.1.2 Flow of liquid crystals through a planar contraction

We have used the planar contraction as a benchmark geometry to compare the flow and director predictions obtained from tensorial and vectorial frameworks. Due to the ambiguity in the vectorial description, a boundary condition with the same physical meaning can be defined in several distinct ways. The discrepancy in the flow and director fields is reflected in the prediction of the Couette factor, which quantifies an excess pressure drop caused by the presence of contraction. As a result, selecting appropriate boundary conditions that can match predictions of the BE model is not trivial; for flows with the wall-parallel anchoring, the same set of boundary conditions matches the tensorial predictions at both low and high Ericksen numbers. In contrast, the choice of director orientation in flows with homeotropic anchoring depends on the Ericksen number. Therefore, to eliminate ambiguity in the selection of director orientation in complex geometries (mixers), it is recommended to use a tensorial framework.

8.2 Future work

In this thesis, we have analysed the behaviour of non-Newtonian, viscoelastic fluids, which are suitable to describe the liquid crystal properties in the lower viscosity, regions II and III of the Asada flow curve. One of the major problems in soap extrusion is the presence of the yield stress, whose physics in the context of soap flow is not fully understood [41]. Therefore, as a part of future work, we consider exploring different approaches to account for the solid-like behaviour.

8.2.1 Addition of yield stress term

In the original derivation of the TIF model [110], the stress tensor contains a yield-stress component $\mu_Y \boldsymbol{nn}$, which is usually omitted, as the majority of liquid nematics do not experience a solid-like behaviour [15]. The orientation-dependent yield stress depends on the mode of material deformation (shearing/extension), which controls director alignment. As a result, the yield stresses in shearing and extensional flows need not be of the same value, which qualitatively agrees with experimental measurements [5]. This feature is advantageous over the Bingham or Herschel-Bulkley models and can improve in-silico predictions of the pressure drop in geometries, where both shearing and elongation are present, e.g. contractions.

8.2.2 Defect dynamics

In the case of nematic liquid crystals, the solid-like behaviour in the region I of the Onogi-Asada curve is explained by the presence of defects [27]. Hence, we could account for the yield stress by modelling the evolution and transport of defect structures. Their presence controls the relaxation behaviour at low shear rates [183, 184]. Defects are destroyed at higher shear rates [185] when the hydrodynamic effects are strong enough to induce a uniform director orientation in the whole domain.

8.2.3 Smectic liquid crystals

Micellar systems at moderate concentrations form nematic-like structures. As the micelle concentration increases, the system arrives at a more ordered, smectic phase, consisting of layers of nematic liquid crystals. The layered structure is more resistant to material distortion, and this concept can help to explain the existence of the yield stress. Numerous constitutive equations were proposed [62, 63, 186, 187]; the simplest relations only focus on modelling the layer deformation.

References

[1] P. Helo, K. Phusavat, and P. Anussornnitisarn, "Fast moving consumer goods - a productivity perspective on supply chains," *International Journal of Productivity and Quality Management*, vol. 5, no. 3, pp. 269–285, 2010.

[2] K. Sable, "FMCG Market by Type (Food & Beverage, Personal Care, Health Care, and Home Care) and Distribution Channel (Supermarkets & Hypermarkets, Grocery Stores, Specialty Stores, E-commerce, and Others): Global Opportunity Analysis and Industry Forecast, 2018 - 2025," Allied Market Research, Tech. Rep., Jan. 2019, Accessed: 2021-08-30.

[3] "Cleaning Products Industry Impact Report: COVID-19," American Cleaning Institute, Tech. Rep., Aug. 2020.

[4] J. Hague, *INDUSTRY 4.0. A view from Research and Developement in FMCG.* University Lecture, 2017.

[5] G. McFann, *Project Report Part 1: Measurement of Rheological Parameters of 82/18 Soap Using Kalyon's Method*, Internal report, 1999.

[6] W. de Paula Ferreira, F. Armellini, and L. A. De Santa-Eulalia, "Simulation in industry 4.0: A state-of-the-art review," *Computers & Industrial Engineering*, vol. 149, p. 106 868, 2020.

[7] L. Silvestri, "CFD modeling in Industry 4.0: New perspectives for smart factories," *Procedia Computer Science*, vol. 180, pp. 381–387, 2021, Proceedings of the 2nd International Conference on Industry 4.0 and Smart Manufacturing (ISM 2020).

[8] R. Prosser, *Concurrent product-process design challenges presented by the process dependent microstructures. 2017*, 2nd Edwards Symposium, 2017.

[9] B. McKenna and D. Kilcast, *Texture in Food: Semi-Solid Foods*, ser. Texture in Food. Elsevier Science, 2003.

[10] P. Coussot, "Yield stress fluid flows: A review of experimental data," *Journal of Non-Newtonian Fluid Mechanics*, vol. 211, pp. 31–49, 2014.

[11] H. A. Ardakani, E. Mitsoulis, and S. G. Hatzikiriakos, "Thixotropic flow of toothpaste through extrusion dies," *Journal of Non-Newtonian Fluid Mechanics*, vol. 166, no. 21, pp. 1262–1271, 2011.

[12] P. A. Cornwell, “A review of shampoo surfactant technology: Consumer benefits, raw materials and recent developments,” *International Journal of Cosmetic Science*, vol. 40, no. 1, pp. 16–30,

[13] Z. Ren, A. Kowalski, and T. Rodgers, “Measuring inline velocity profile of shampoo by electrical resistance tomography (ERT),” *Flow Measurement and Instrumentation*, vol. 58, pp. 31–37, 2017.

[14] H. Wildmoser, J. Scheiwiller, and E. J. Windhab, “Impact of disperse microstructure on rheology and quality aspects of ice cream,” *LWT - Food Science and Technology*, vol. 37, no. 8, pp. 881–891, 2004.

[15] R. G. Larson, *The Structure and Rheology of Complex Fluids*. Oxford University Press, New York, 1999.

[16] E. Zondervan, C. Almeida-Rivera, and K. V. Camarda, *Product-Driven Process Design: From Molecule to Enterprise*. De Gruyter, 2020.

[17] A. Morozov and S. Spagnolie, “Introduction to complex fluids,” in *Complex Fluids in Biological Systems*. Springer, 2015.

[18] F. Morrison, *Understanding rheology.* Oxford University Press, 2001.

[19] K. Lissant, *Emulsions and Emulsion Technology.* CRC Press, 1974.

[20] R. G. Larson, “Introduction to Constitutive Equations for Viscoelastic Fluids,” in *Constitutive Equations for Polymer Melts and Solutions*, ser. Butterworths Series in Chemical Engineering, R. G. Larson, Ed., Butterworth-Heinemann, 1988.

[21] P. de Gennes and J. Prost, *The Physics of Liquid Crystals*. Oxford Science Publications, 1993.

[22] G. W. Gray, “Introduction and historical development,” in *Handbook of Liquid Crystals*. John Wiley & Sons, Ltd, 1998.

[23] R. Astolfi, J. L. Basso, S. R. Leopoldino, L. F. C. Vidigal, V. Vijayakrishnan, and Y. K. Yarovoy, *Process for making soap bar having separate regions of specifically selected components*, WO2017064141A1, Apr. 2017. [Online]. Available: `https://patents.google.com/patent/WO2017064141A1/en`.

[24] K. Fedorowicz and R. Prosser, “Flow of transversely isotropic fluid in curved pipes,” *Journal of Non-Newtonian Fluid Mechanics*, vol. 300, p. 104 716, 2022.

[25] A. Dukhin, S. Parlia, and P. Somasundaran, “Rheology of non-newtonian liquid mixtures and the role of molecular chain length,” *Journal of Colloid and Interface Science*, vol. 560, pp. 492–501, 2020.

[26] Y. Shi and G. Tang, "Simulation of Newtonian and non-Newtonian rheology behavior of viscous fingering in channels by the lattice Boltzmann method," *Computers & Mathematics with Applications*, vol. 68, no. 10, pp. 1279–1291, 2014.

[27] K. F. Wissbrun, "Rheology of Rod-like Polymers in the Liquid Crystalline State," *Journal of Rheology*, vol. 25, no. 6, pp. 619–662, 1981.

[28] N. Yavuz and K. Sandeep, "Scale-Up of Shear Thinning Fluid Mixing in an Unbaffled Stirred Vessel with Eccentrically Located and Modified Impellers:" *International Journal of Chemical Reactor Engineering*, vol. 17, no. 4, p. 20 180 205, 2019.

[29] F. X. McConville and S. B. Kessler, "Chemical engineering in the pharmaceutical industry," in John Wiley & Sons, Ltd, 2019.

[30] W. H. Herschel and R. Bulkley, "Konsistenzmessungen von Gummi-Benzollösungen," *Kolloid-Zeitschrift*, vol. 39, no. 4, pp. 291–300, 1926.

[31] A. Metzner, "Non-Newtonian Technology: Fluid Mechanics, Mixing, and Heat Transfer," in ser. Advances in Chemical Engineering, T. B. Drew and J. W. Hoopes, Eds., vol. 1, Academic Press, 1956, pp. 77–153.

[32] A. E. Likhtman and R. S. Graham, "Simple constitutive equation for linear polymer melts derived from molecular theory: Rolie-poly equation," *Journal of Non-Newtonian Fluid Mechanics*, vol. 114, no. 1, pp. 1–12, 2003.

[33] H. Giesekus, "A unified approach to a variety of constitutive models for polymer fluids based on the concept of configuration-dependent molecular mobility," *Rheologica Acta*, vol. 21, pp. 366–375, Jul. 1982.

[34] F. M. Leslie, "Some constitutive equations for anisotropic fluids," *The Quarterly Journal of Mechanics and Applied Mathematics*, vol. 19, no. 3, pp. 357–370, 1966.

[35] F. Frank, "Liquid crystals. On the theory of liquid crystals," *Discussions of the Faraday Society*, vol. 25, pp. 19–29, 1958.

[36] J. H. Ferziger and M. Perić, *Computational Methods for Fluid Dynamics*, 2nd. Berlin: Springer, 1999.

[37] H. K. Versteeg and W. Malalasekera, *An Introduction to Computational Fluid Dynamics: The Finite Volume Method.* Addison-Wesley-Longman, 1995, pp. I–X, 1–257.

[38] M. Bryan, S. Rough, and D. Wilson, "Flow visualisation and modelling of solid soap extrusion," *Chemical Engineering Science*, vol. 173, pp. 110–120, 2017.

[39] Y. Yarovoy, *private communication*.

[40] S. Aktas, D. M. Kalyon, B. M. Marin-Santibanez, and J. Perez-Gonozalez, "Shear viscosity and wall slip behavior of a viscoplastic hydrogel," *Journal of Rheology*, vol. 58, no. 2, pp. 513–535, 2014.

[41] Y. Yarovoy and S. Watson, *private communication*.

[42] Siemens Digital Industries Software, *Simcenter STAR-CCM+, version 2021.1*, version 2021.1, Siemens 2021.

[43] I. Stewart, *The Static and Dynamic Continuum Theory of Liquid Crystals: A Mathematical Introduction*. Taylor and Francis, London, 2004.

[44] C. Kittel, *Introduction to Solid State Physics*, 8th ed. Wiley, 2004.

[45] F. White, *Fluid Mechanics*, ser. McGraw-Hill series in mechanical engineering. McGraw-Hill Education, 2016.

[46] F. Pimenta and M. Alves, "Stabilization of an open-source finite-volume solver for viscoelastic fluid flows," *Journal of Non-Newtonian Fluid Mechanics*, vol. 239, pp. 85–104, 2017.

[47] R. Williams, "Domains in liquid crystals," *The Journal of Chemical Physics*, vol. 39, no. 2, pp. 384–388, 1963.

[48] G. Heilmeier, L. Zanoni, and L. Barton, "Dynamic scattering: A new electrooptic effect in certain classes of nematic liquid crystals," *Proceedings of the IEEE*, vol. 56, no. 7, pp. 1162–1171, 1968.

[49] A. Yoshizawa, "Material design for blue phase liquid crystals and their electro-optical effects," *RSC Adv.*, vol. 3, pp. 25 475–25 497, 48 2013.

[50] D. J. Mulder, A. P. H. J. Schenning, and C. W. M. Bastiaansen, "Chiral-nematic liquid crystals as one dimensional photonic materials in optical sensors," *Journal of Materials Chemistry C*, vol. 2, pp. 6695–6705, 33 2014.

[51] Y. Yamamoto, "Lcd processing and testing," in *Handbook of Visual Display Technology*, J. Chen, W. Cranton, and M. Fihn, Eds. Berlin, Heidelberg: Springer Berlin Heidelberg, 2012, pp. 1649–1671.

[52] K.-C. Fan, J.-Y. Chen, C.-H. Wang, and W.-C. Pan, "Development of a drop-on-demand droplet generator for one-drop-fill technology," *Sensors and Actuators A: Physical*, vol. 147, no. 2, pp. 649–655, 2008.

[53] J. R. L. Cousins, S. K. Wilson, N. J. Mottram, D. Wilkes, and L. Weegels, "Transient flow-driven distortion of a nematic liquid crystal in channel flow with dissipative weak planar anchoring," *Phys. Rev. E*, vol. 102, p. 062 703, 6 Dec. 2020.

[54] H. Mundoor, S. Park, B. Senyuk, H. H. Wensink, and I. I. Smalyukh, "Hybrid molecular-colloidal liquid crystals," *Science*, vol. 360, no. 6390, pp. 768–771, 2018.

[55] M. E. Cates and S. M. Fielding, "Rheology of giant micelles," *Advances in Physics*, vol. 55, no. 7-8, pp. 799–879, 2006.

[56] G. A. DiLisi, "Mesophases of matter," in *An Introduction to Liquid Crystals*, ser. 2053-2571, Morgan & Claypool Publishers, 2019, 2-1 to 2–4.

[57] N. J. Mottram and C. J. P. Newton, *Introduction to Q-tensor theory*, 2014. arXiv: 1409.3542.

[58] T. J. Sluckin, D. A. Dunmur, and H. Stegemeyer, *Crystals that flow: classic papers from the history of liquid crystals*. Taylor and Francis, 2004.

[59] L. A. Madsen, T. J. Dingemans, M. Nakata, and E. T. Samulski, "Thermotropic biaxial nematic liquid crystals," *Physical Review Letters*, vol. 92, p. 145 505, 14 Apr. 2004.

[60] V. Prasad, S.-W. Kang, K. A. Suresh, L. Joshi, Q. Wang, and S. Kumar, "Thermotropic biaxial nematic liquid crystals," *Journal of the American Chemical Society*, vol. 127, pp. 17 224–17 227, 49 Dec. 2005.

[61] M. J. Freiser, "Ordered States of a Nematic Liquid," *Physical Review Letters*, vol. 24, pp. 1041–1043, 19 May 1970.

[62] F. M. Leslie, I. W. Stewart, and M. Nakagawa, "A Continuum Theory for Smectic C Liquid Crystals," *Molecular Crystals and Liquid Crystals*, vol. 198, no. 1, pp. 443–454, 1991.

[63] I. W. Stewart, "Dynamic theory for smectic A liquid crystals," *Continuum Mechanics and Thermodynamics*, vol. 18, no. 6, pp. 343–360, 2007.

[64] A. Beris and B. Edwards, *Thermodynamics of Flowing Systems with an Internal Microstructure*. Oxford University Press, 1994.

[65] B. Outram, "Discotic and columnar liquid crystals," in *Liquid Crystals*, ser. 2053-2563, IOP Publishing, 2018, 8-1 to 8–11.

[66] T. Tsuji and A. D. Rey, "Effect of long range order on sheared liquid crystalline materials Part 1: compatibility between tumbling behavior and fixed anchoring," *Journal of Non-Newtonian Fluid Mechanics*, vol. 73, no. 1, pp. 127–152, 1997.

[67] E. G. Virga, *Variational Theories for Liquid Crystals*. Chapman & Hall, 1994.

[68] K. Rijeesh, H. Higuchi, Y. Okumura, J. Yamamoto, and H. Kikuchi, "Liquid crystal anchoring transitions and weak anchoring interface formation at surfaces created by uniquely designed acrylate copolymers," *Polymer*, vol. 116, pp. 447–451, 2017.

[69] J. A. Castellano, “Surface Anchoring of Liquid Crystal Molecules on Various Substrates,” *Molecular Crystals and Liquid Crystals*, vol. 94, no. 1-2, pp. 33–41, 1983.

[70] G. Haas, M. Fritsch, H. WÃ¶hler, and D. A. Mlynski, “Polar anchoring energy and order parameter at a nematic liquid crystal-wall interface,” *Liquid Crystals*, vol. 5, no. 2, pp. 673–681, 1989.

[71] A. Rapini and M. Papoular, “Polar anchoring energy and order parameter at a nematic liquid crystal-wall interface,” *Journal de Physique Colloques*, vol. 30, pp. C4–54, 1969.

[72] G. T. Park, J.-H. Chang, and A. R. Lim, “Thermotropic Liquid Crystalline Polymers with Various Alkoxy Side Groups: Thermal Properties and Molecular Dynamics,” *Polymers*, vol. 11, no. 6, 2019.

[73] J. L. W. H. Aoki and J. F. Fellers, “A Rheological and Optical Properties Investigation of Aliphatic (Nylon 66, P(gamma)BLG) and Aromatic (Kevlar, Nomex) Polyamide Solutions,” *Journal of Applied Polymer Science*, vol. 23, pp. 2293–2314, 1979.

[74] S. Sarman, “Chapter 9 - transport properties of liquid crystals via molecular dynamics simulation,” in *Molecular Dynamics*, ser. Theoretical and Computational Chemistry, P. B. Balbuena and J. M. Seminario, Eds., vol. 7, Elsevier, 1999, pp. 325–361.

[75] R. S. Porter and J. F. Johnson, “Chapter 5 - the rheology of liquid crystals,” in *Rheology*, F. R. Eirich, Ed., Academic Press, 1967, pp. 317–345.

[76] S. Onogi and T. Asada, “Rheology and Rheo-Optics of Polymer Liquid Crystals,” in *Rheology*, F. R. Eirich, Ed., Springer, Boston, 1980.

[77] R. J. Fox, W.-R. Chen, C. Do, S. J. Picken, M. G. Forest, and T. J. Dingemans, “Fingerprinting the nonlinear rheology of a liquid crystalline polyelectrolyte,” *Rheologica Acta*, vol. 59, pp. 727–743, 2020.

[78] E. Glowinska, P. Parcheta, and J. Datta, “Chapter 10 - Rheology of liquid crystalline polymers,” in *Rheology of Polymer Blends and Nanocomposites*, ser. Micro and Nano Technologies, S. Thomas, C. Sarathchandran, and N. Chandran, Eds., Elsevier, 2020, pp. 205–224.

[79] J. Ericksen, “The Mechanics of Nematic Liquid Crystals,” in *The Mechanics of Viscoelastic Fluids*, R. Rivlin, Ed., ASME, New York, 1977.

[80] O. Henrich, K. Stratford, D. Marenduzzo, P. V. Coveney, and M. E. Cates, “Rheology of lamellar liquid crystals in two and three dimensions: A simulation study,” *Soft Matter*, vol. 8, pp. 3817–3831, 14 2012.

[81] K. F. Wissbrun, "Observations on the Melt Rheology of Thermotropic Aromatic Polyesters," *British Polymer Journal*, vol. 12, no. 4, pp. 163–169, 1980.

[82] S. P. Papkov, V. G. Kulichikhin, V. D. Kalmykova, and A. Y. Malkin, "Rheological properties of anisotropic poly(para-benzamide) solutions," *Journal of Polymer Science: Polymer Physics Edition*, vol. 12, no. 9, pp. 1753–1770, 1974.

[83] M. Doi, "Molecular dynamics and rheological properties of concentrated solutions of rodlike polymers in isotropic and liquid crystalline phases," *Journal of Polymer Science: Polymer Physics Edition*, vol. 19, no. 2, pp. 229–243, 1981.

[84] G. Kiss and R. S. Porter, "Rheology of concentrated solutions of helical polypeptides," *Journal of Polymer Science: Polymer Physics Edition*, vol. 18, no. 2, pp. 361–388, 1980.

[85] A. Okagawa, R. Cox, and S. Mason, "The kinetics of flowing dispersions. VI. Transient orientation and rheological phenomena of rods and discs in shear flow," *Journal of Colloid and Interface Science*, vol. 45, no. 2, pp. 303–329, 1973.

[86] J. Fishers and A. G. Fredrickson, "Interfacial effects on the viscosity of a nematic mesophase," *Molecular Crystals*, vol. 8, no. 1, pp. 267–284, 1969.

[87] N. P., "Shear rheology of semidilute poly(methyl methacrylate) solutions," *Macromolecules*, vol. 26, p. 7095, 1993.

[88] R. G. Larson and D. W. Mead, "Time and Shear-Rate Scaling Laws for Liquid Crystal Polymers," *Journal of Rheology*, vol. 33, no. 8, pp. 1251–1281, 1989.

[89] P. Moldenaers and J. Mewis, "Transient Behavior of Liquid Crystalline Solutions of Poly(benzylglutamate)," *Journal of Rheology*, vol. 30, no. 3, pp. 567–584, 1986.

[90] I. Fisher, *Statistical Theory of Liquids*. University of Chicago Press, 1961.

[91] W. Tian, B. Song, J. H. VanZwieten, P. Pyakurel, and Y. Li, "Numerical simulations of a horizontal axis water turbine designed for underwater mooring platforms," *International Journal of Naval Architecture and Ocean Engineering*, vol. 8, no. 1, pp. 73–82, 2016.

[92] P. He, T. Katayama, T. Hayashi, J.-i. Tsutsumi, J. Tanimoto, and I. Hosooka, "Numerical simulation of air flow in an urban area with regularly aligned blocks," *Journal of Wind Engineering and Industrial Aerodynamics*, vol. 67-68, pp. 281–291, 1997, Computational Wind Engineering.

[93] V. Michael, R. Prosser, and A. Kowalski, "CFD-PBM simulation of dense emulsion flows in a high-shear rotor-stator mixer," *Chemical Engineering Research and Design*, vol. 125, pp. 494–510, 2017.

[94] H. Barnes, "Bubbles, drops and particles in non-newtonian fluids," *Journal of Non-Newtonian Fluid Mechanics*, vol. 56, pp. 363–364, 1995.

[95] R. Huilgol, *Fluid Mechanics of Viscoplasticity*. Springer Berlin Heidelberg, 2015.

[96] P. Cheng, M. C. Burroughs, L. G. Leal, and M. E. Helgeson, "Distinguishing shear banding from shear thinning in flows with a shear stress gradient," English, *Rheologica Acta*, vol. 56, no. 12, pp. 1007–1032, 2017.

[97] T. Divoux, M.-A. Fardin, S. Manneville, and S. Lerouge, "Shear banding of complex fluids," *Annual Review of Fluid Mechanics*, vol. 48, 2015.

[98] T. Sochi, "Analytical solutions for the flow of Carreau and Cross fluids in circular pipes and thin slits," *Rheologica Acta*, 2015.

[99] J. Boyd, J. M. Buick, and S. Green, "Analysis of the Casson and Carreau-Yasuda non-Newtonian blood models in steady and oscillatory flows using the lattice Boltzmann method," *Physics of Fluids*, vol. 19, no. 9, 2007.

[100] A. Keshmiri, A. Ruiz-Soler, M. McElroy, and F. Kabinejadian, "Numerical Investigation on the Geometrical Effects of Novel Graft Designs for Peripheral Artery Bypass Surgery," *Procedia CIRP*, vol. 49, pp. 147–152, 2016, The Second CIRP Conference on Biomanufacturing.

[101] A. Shamloo, M. Mirzakhanloo, and M. R. Dabirzadeh, "Numerical Simulation for efficient mixing of Newtonian and non-Newtonian fluids in an electro-osmotic micro-mixer," *Chemical Engineering and Processing: Process Intensification*, vol. 107, pp. 11–20, 2016.

[102] A. Afzal and K.-Y. Kim, "Flow and mixing analysis of non-Newtonian fluids in straight and serpentine microchannels," *Chemical Engineering Science*, vol. 116, pp. 263–274, 2014.

[103] C. Bălan, D. Broboana, and C. Balan, "Mixing process of immiscible fluids in microchannels," *International Journal of Heat and Fluid Flow*, vol. 31, pp. 1125–1133, 2010.

[104] A. Sun and S. Gunasekaran, "Yield Stress in Foods: Measurements and Applications," *International Journal of Food Properties*, vol. 12, no. 1, pp. 70–101, 2009.

[105] E. Bingham, *Fluidity and plasticity.* McGraw-Hill, New York, 1922.

[106] Thohura,S. and Molla,Md. M. and Sarker,M. M. A., "Numerical simulation of Bingham fluid flows in a lid-driven skewed cavity," *AIP Conference Proceedings*, vol. 1980, no. 1, p. 040 022, 2018.

[107] The OpenFOAM Foundation, *OpenFOAM v6 User Guide*.

[108] Z. Tadmor and C. G. Gogos, "Principles of Polymer Processing," in John Wiley & Sons, Ltd.

[109] M. Miesowicz, "The Three Coefficients of Viscosity of Anisotropic Liquids," *Nature*, vol. 4001, pp. 27–27, Jul. 1946.

[110] J. L. Ericksen, "Transversely isotropic fluids," *Kolloid-Zeitschrift*, vol. 173, p. 117, 1960.

[111] J. E. R. Rivlin, "Stress-Deformation Relations for Isotropic Materials," *Archive for Rational Mechanics and Analysis*, vol. 4, pp. 323–425, 1955.

[112] C. R. Holloway, G. Cupples, D. J. Smith, J. E. F. Green, R. J. Clarke, and R. J. Dyson, "Influences of transversely isotropic rheology and translational diffusion on the stability of active suspensions," *Royal Society Open Science*, vol. 5, no. 8, p. 180 456, 2018.

[113] G. B. Jeffery and L. N. G. Filon, "The motion of ellipsoidal particles immersed in a viscous fluid," *Proceedings of the Royal Society of London. Series A, Containing Papers of a Mathematical and Physical Character*, vol. 102, no. 715, pp. 161–179, 1922.

[114] Y. Cengel and M. Boles, *Thermodynamics: An Engineering Approach*. McGraw-Hill, 2015.

[115] D. Kondepudi and I. Prigogine, *Modern Thermodynamics: From Heat Engines to Dissipative Structures*. John Wiley & Sons, Ltd, 1998.

[116] D. Andrienko, "Introduction to liquid crystals," *Journal of Molecular Liquids*, vol. 267, pp. 520–541, 2018, Special Issue Dedicated to the Memory of Professor Y. Reznikov.

[117] C. W. Oseen, "The theory of liquid crystals," *Transactions of the Faraday Society*, vol. 29, pp. 883–899, 140 1933.

[118] I. Haller, "Elastic Constants of the Nematic Liquid Crystalline Phase of p-Methoxybenzylidene-p-n-Butylaniline (MBBA)," *The Journal of Chemical Physics*, vol. 57, no. 4, pp. 1400–1405, 1972.

[119] W. H. D. Jeu, "Physical Properties of Liquid Crystalline Materials in Relation to Their Applications," *Molecular Crystals and Liquid Crystals*, vol. 63, no. 1, pp. 83–109, 1981.

[120] H. Mattoussi and M. Veyssie, "Frank elastic constants and rotational viscosity for nematic solutions of main-chain polymers," *Journal de Physique*, vol. 50, no. 1, pp. 99–106, 1989. [Online]. Available: `https://hal.archives-ouvertes.fr/jpa-00210903`.

[121] L. Susskind and A. Friedman, *Quantum Mechanics: The Theoretical Minimum*. Penguin Books Limited, 2014.

[122] H. D. I. Abarbanel, R. Brown, and Y. M. Yang, "Hamiltonian formulation of inviscid flows with free boundaries," *The Physics of Fluids*, vol. 31, no. 10, pp. 2802–2809, 1988.

[123] W. van Saarloos, "A canonical transformation relating the Lagrangian and Eulerian description of ideal hydrodynamics," *Physica A-statistical Mechanics and Its Applications*, vol. 108, pp. 557–566, 1981.

[124] A. N. Beris and B. J. Edwards, "Poisson bracket formulation of incompressible flow equations in continuum mechanics," *Journal of Rheology*, vol. 34, no. 1, pp. 55–78, 1990.

[125] O. Parodi, "Stress tensor for a nematic liquid crystal," *Journal de Physique*, vol. 31, no. 7, pp. 581–584, 1970.

[126] Ž. Kos, J. Aplinc, U. Mur, and M. Ravnik, "Mesoscopic Approach to Nematic Fluids," in *Flowing Matter*, F. Toschi and M. Sega, Eds. Cham: Springer International Publishing, 2019, pp. 51–93.

[127] A. Sonnet and E. Virga, *Dissipative Ordered Fluids: Theories for Liquid Crystals*, English. Springer, 2012.

[128] J. R. L. Cousins, S. K. Wilson, N. J. Mottram, D. Wilkes, and L. Weegels, "Squeezing a drop of nematic liquid crystal with strong elasticity effects," *Physics of Fluids*, vol. 31, no. 8, p. 083 107, 2019. DOI: 10.1063/1.5110878.

[129] F. Brochard, "Backflow effects in nematic liquid crystals," *Molecular Crystals and Liquid Crystals*, vol. 23, no. 1-2, pp. 51–58, 1973.

[130] Y. Mieda and K. Furutani, "Microsphere manipulation using ferroelectric liquid crystals," *Physical Review Letters*, vol. 95, p. 177 801, 17 Oct. 2005.

[131] Ž. Kos and M. Ravnik, "Field generated nematic microflows via backflow mechanism," *Scientific Reports*, vol. 10, no. 1, p. 1446, 2020.

[132] J. M. Ball, "Mathematics and liquid crystals," *Molecular Crystals and Liquid Crystals*, vol. 647, no. 1, pp. 1–27, 2017.

[133] M. Doi, T. Shimada, and K. Okano, "Concentration fluctuation of stiff polymers. II. Dynamical structure factor of rod-like polymers in the isotropic phase," *The Journal of Chemical Physics*, vol. 88, no. 6, pp. 4070–4075, 1988.

[134] M. Kleman and O. D. Lavrentovich, "Topological point defects in nematic liquid crystals," *Philosophical Magazine*, vol. 86, no. 25-26, pp. 4117–4137, 2006.

[135] A. Sonnet, A. Kilian, and S. Hess, "Alignment tensor versus director: Description of defects in nematic liquid crystals," *Physical Review E*, vol. 52, pp. 718–722, 1 Jul. 1995.

[136] M. Reichenstein, T. Seitz, and H.-R. Trebin, "Numerical Simulations of Three Dimensional Liquid Crystal Cells," *Molecular Crystals and Liquid Crystals Science and Technology. Section A. Molecular Crystals and Liquid Crystals*, vol. 330, no. 1, pp. 549–555, 1999.

[137] L. A. Parry-Jones, R. B. Meyer, and S. J. Elston, "Mechanisms of flexoelectric switching in a zenithally bistable nematic device," *Journal of Applied Physics*, vol. 106, no. 1, p. 014 510, 2009.

[138] B. J. Edwards and A. N. Beris, "Note: Order Parameter Representation of Spatial Inhomogeneities of Polymeric Liquid Crystals," *Journal of Rheology*, vol. 33, no. 7, pp. 1189–1193, 1989.

[139] L. Landau and E. Lifshitz, *Statistical Physics*, 2nd. Pergamon, Oxford, 1969.

[140] M. Ravnik and S. Åœumer, "Landau-de Gennes modelling of nematic liquid crystal colloids," *Liquid Crystals*, vol. 36, no. 10-11, pp. 1201–1214, 2009.

[141] B. J. Edwards, A. N. Beris, and M. Grmela, "Generalized constitutive equation for polymeric liquid crystals Part 1. Model formulation using the Hamiltonian (Poisson bracket) formulation," *Journal of Non-Newtonian Fluid Mechanics*, vol. 35, no. 1, pp. 51–72, 1990.

[142] C. Denniston, E. Orlandini, and J. M. Yeomans, "Lattice Boltzmann simulations of liquid crystal hydrodynamics," *Physical Review E*, vol. 63, p. 056 702, 5 Apr. 2001.

[143] A. D. Rey, "Capillary models for liquid crystal fibers, membranes, films, and drops," *Soft Matter*, vol. 3, pp. 1349–1368, 11 2007.

[144] J. Ericksen, "Liquid crystals with variable degree of orientation," *Archive for Rational Mechanics and Analysis*, vol. 113, pp. 97–120, 1991.

[145] F. Pimenta and M. Alves, *rheoTool*, `https://github.com/fppimenta/rheoTool`, 2016.

[146] R. Comminal, F. Pimenta, J. H. Hattel, M. A. Alves, and J. Spangenberg, "Numerical simulation of the planar extrudate swell of pseudoplastic and viscoelastic fluids with the streamfunction and the VOF methods," *Journal of Non-Newtonian Fluid Mechanics*, vol. 252, pp. 1–18, 2018.

[147] M. Alves, P. Oliveira, and F. Pinho, "Numerical methods for viscoelastic fluid flows," *Annual Review of Fluid Mechanics*, vol. 53, no. 1, pp. 509–541, 2021.

[148] P. Moin, *Fundamentals of Engineering Numerical Analysis*. Cambridge University Press, 2010. [Online]. Available: https://books.google.pl/books?id=uvpwKK7ZVwMC.

[149] Cladis, P.E. and Kléman, M., "Non-singular disclinations of strength S = + 1 in nematics," *Journal de Physique*, vol. 33, pp. 591–598, 1972.

[150] R. B. Meyer, "On the existence of even indexed disclinations in nematic liquid crystals," *The Philosophical Magazine: A Journal of Theoretical Experimental and Applied Physics*, vol. 27, no. 2, pp. 405–424, 1973.

[151] P. A. Cruz, M. F. Tome, I. W. Stewart, and S. McKee, "Numerical solution of the Ericksen-Leslie dynamic equations for two-dimensional nematic liquid crystal flows," *Journal of Computational Physics*, vol. 247, pp. 109–136, 2013.

[152] R. H. Nochetto, S. W. Walker, and W. Zhang, "A finite element method for nematic liquid crystals with variable degree of orientation," *SIAM Journal on Numerical Analysis*, vol. 55, no. 3, pp. 1357–1386, 2017. DOI: 10.1137/15M103844X.

[153] Y. Fan, R. I. Tanner, and N. Phan-Thien, "Fully developed viscous and viscoelastic flows in curved pipes," *Journal of Fluid Mechanics*, vol. 440, pp. 327–357, 2001.

[154] A. Robertson and S. Muller, "Flow of Oldroyd-B fluids in curved pipes of circular and annular cross-section," *International Journal of Non-Linear Mechanics*, vol. 31, no. 1, pp. 1–20, 1996.

[155] A. Sengupta, U. š. Tkalec, M. Ravnik, J. M. Yeomans, C. Bahr, and S. Herminghaus, "Liquid Crystal Microfluidics for Tunable Flow Shaping," *Physical Review Letters*, vol. 110, p. 048 303, 4 Jan. 2013.

[156] G. De Luca and A. D. Rey, "Ringlike cores of cylindrically confined nematic point defects," *The Journal of Chemical Physics*, vol. 126, no. 9, p. 094 907, 2007.

[157] P. Steffen, E. Stellamanns, and A. Sengupta, "Surface anchoring mediates bifurcation in nematic microflows within cylindrical capillaries," *Physics of Fluids*, vol. 33, no. 7, p. 072 005, 2021.

[158] L.R.P. de Andrade Lima and A.D. Rey, "Poiseuille flow of Leslie-Ericksen discotic liquid crystals: solution multiplicity, multistability, and non-Newtonian rheology," *Journal of Non-Newtonian Fluid Mechanics*, vol. 110, no. 2, pp. 103–142, 2003.

[159] P. A. Cruz, M. F. Tome, S. McKee, and I. W. Stewart, "Numerical solution of the Ericksen-Leslie model for liquid crystalline polymers free surface flows," *Journal of Non-Newtonian Fluid Mechanics*, vol. 268, pp. 30–45, 2019.

[160] Z. Kos, M. Ravnik, and S. Åœumer, "Nematodynamics and structures in junctions of cylindrical micropores," *Liquid Crystals*, vol. 44, no. 12-13, pp. 2161–2171, 2017.

[161] W. Dean, " XVI. Note on the motion of fluid in a curved pipe," *The London, Edinburgh, and Dublin Philosophical Magazine and Journal of Science*, vol. 4, no. 20, pp. 208–223, 1927.

[162] ——, " LXXII. The stream-line motion of fluid in a curved pipe (Second paper)," *The London, Edinburgh, and Dublin Philosophical Magazine and Journal of Science*, vol. 5, no. 30, pp. 673–695, 1928.

[163] L. Ducloue *et al.*, "Secondary flows of viscoelastic fluids in serpentine microchannels," *Microfluid. Nanofluidics*, vol. 23, p. 33, 3 2019.

[164] P. Bowen, A. Davies, and K. Walters, "On viscoelastic effects in swirling flows," *Journal of Non-Newtonian Fluid Mechanics*, vol. 38, no. 2, pp. 113–126, 1991.

[165] G. K. Batchelor, "Kinematics of the flow field," in *An Introduction to Fluid Dynamics*, ser. Cambridge Mathematical Library. Cambridge University Press, 2000, pp. 71–130.

[166] Maple 2020. Maplesoft, a division of Waterloo Maple Inc., Waterloo, Ontario.

[167] W. Jitchote and A. Robertson, "Flow of second order fluids in curved pipes," *Journal of Non-Newtonian Fluid Mechanics*, vol. 90, no. 1, pp. 91–116, 2000.

[168] F. M. Leslie, "Some constitutive equations for liquid crystals," *Archive for Rational Mechanics and Analysis*, vol. 28, pp. 265–283, 4 1968.

[169] T. Anderson, E. Mema, L. Kondic, and L. Cummings, "Transitions in poiseuille flow of nematic liquid crystal," *International Journal of Non-Linear Mechanics*, vol. 75, pp. 15–21, 2015, Instabilities and Nonlinearities in Soft Systems: From Fluids to Biomaterials.

[170] O. Maklad and R. Poole, "A review of the second normal-stress difference; its importance in various flows, measurement techniques, results for various complex fluids and theoretical predictions," *Journal of Non-Newtonian Fluid Mechanics*, vol. 292, p. 104 522, 2021.

[171] M. Ravnik and J. M. Yeomans, "Confined Active Nematic Flow in Cylindrical Capillaries," *Physical Review Letters*, vol. 110, p. 026 001, 2 Jan. 2013.

[172] M. J. Tunstall and J. K. Harvey, "On the effect of a sharp bend in a fully developed turbulent pipe-flow," *Journal of Fluid Mechanics*, vol. 34, no. 3, pp. 595–608, 1968.

[173] F. N. Cogswell, "Converging flow of polymer melts in extrusion dies," *Polymer Engineering & Science*, vol. 12, no. 1, pp. 64–73, 1972.

[174] E. B. Bagley and A. M. Birks, "Flow of polyethylene into a capillary," *Journal of Applied Physics*, vol. 31, no. 3, pp. 556–561, 1960.

[175] S. Hooshyar and N. Germann, "Shear banding in 4:1 planar contraction," *Polymers*, vol. 11, no. 3, 2019.

[176] L. Prandtl, "Ueber flussigkeitsbewegung bei sehr kleiner reibung," *Verhandl. III, Internat. Math.-Kong., Heidelberg, Teubner, Leipzig, 1904*, pp. 484–491, 1904.

[177] J. P. Tordella, "Fracture in the extrusion of amorphous polymers through capillaries," *Journal of Applied Physics*, vol. 27, no. 5, pp. 454–458, 1956.

[178] S. Hooshyar and N. Germann, "Shear banding in 4:1 planar contraction," *Polymers*, vol. 11, no. 3, 2019.

[179] M. A. Alves, P. J. Oliveira, and F. T. Pinho, "Benchmark solutions for the flow of oldroyd-b and ptt fluids in planar contractions," *Journal of Non-Newtonian Fluid Mechanics*, vol. 110, no. 1, pp. 45–75, 2003.

[180] V. M. O. Batista, M. L. Blow, and M. M. Telo da Gama, "The effect of anchoring on the nematic flow in channels," *Soft Matter*, vol. 11, pp. 4674–4685, 23 2015.

[181] J. P. Hernandez-Ortiz, B. T. Gettelfinger, J. Moreno-Razo, and J. J. de Pablo, "Modeling flows of confined nematic liquid crystals," *The Journal of Chemical Physics*, vol. 134, no. 13, p. 134 905, 2011.

[182] M. Aboubacar, H. Matallah, H. Tamaddon-Jahromi, and M. Webster, "Numerical prediction of extensional flows in contraction geometries: Hybrid finite volume/element method," *Journal of Non-Newtonian Fluid Mechanics*, vol. 104, no. 2, pp. 125–164, 2002.

[183] G. Marrucci and F. Greco, "A molecular approach to the polydomain structure of lcps in weak shear flows," *Journal of Non-Newtonian Fluid Mechanics*, vol. 44, pp. 1–13, 1992.

[184] G. Marrucci, "Rheology of liquid crystalline polymers," *Pure and Applied Chemistry*, vol. 57, no. 11, pp. 1545–1552, 1985.

[185] R. G. Larson and D. W. Mead, "Development of orientation and texture during shearing of liquid-crystalline polymers," *Liquid Crystals*, vol. 12, no. 5, pp. 751–768, 1992.

[186] P. C. Martin, O. Parodi, and P. S. Pershan, "Unified hydrodynamic theory for crystals, liquid crystals, and normal fluids," *Physical Review A*, vol. 6, pp. 2401–2420, 6 Dec. 1972.

[187] G. Ahmadi, "A continuum theory of smectic a liquid crystals," *Journal of Rheology*, vol. 26, no. 6, pp. 535–556, 1982.

Appendices

Appendix A

Source codes

The fundamental features of the new solver and constitutive equations are outlined below

1. The solution procedure is contained by the file `rheoFoam2.C` listed in the appendix A. The code starts by initialising the relevant variables, e.g. velocity, pressure, director or order parameter tensor through the `createFields.H` file. Based on that, momentum and continuity equations are solved, then followed by the angular momentum balance. Details of the selected nematodynamic model with the relevant parameters are stored in the object *constEq2* belonging to the class *constitutiveModel2*. If required, the transport equation of a passive scalar is solved. The stress tensor field is updated, and the procedure repeats until the solution converges.

2. All the models are stored in the *constitutiveEqs* directory, each having its sub-folder where the differential form of the governing equation, variables, constants and stress definitions are specified. Nematodynamic relations are similar to log-conformation tensor models: the transport equation for the conformation tensor (director) is solved and then used to compute the stress tensor via an algebraic expression. Thus, the directory containing the log-conformation Oldroyd-B model was copied and appropriately modified to solve the director equation, later used to compute the stress tensor. The stress tensor in the Leslie-Ericksen and Beris-Edwards models (eq. (2.52) and (2.69)) is not symmetric, so *rheoFoam* is not appropriate for nematodynamic simulations. The new solver *rheoFoam2* allows for a non-symmetric stress tensor through the modified class *constitutiveEq2*, which defines the operations that can be performed on $\boldsymbol{\tau}$, such as stress divergence *divTau()*, velocity gradient decomposition *decomposeGradU* or the calculation of eigenvalues *calcEig()*. Member functions of *constitutiveEq2* are defined in the file `constitutiveEq2.C`.

A.1 Solver codes

A.1.1 `rheoFoam2.C`

```
1  #include "fvCFD.H"
2  #include "dynamicFvMesh.H"
3  #include "simpleControl.H"
4  #include "CorrectPhi.H"
5  #include "fvOptions.H"
6
7  #include "adjustCorrPhi.H"
8  #include "ppUtilInterface.H"
9  #include "constitutiveModel2.H"
10
11 // * * * * * * * * * * * * * * * * * * * * * * * * * * * * * * * * * * * * * //
12 int main(int argc, char *argv[])
13 {
14     #include "postProcess.H"
15
16     #include "setRootCaseLists.H"
17     #include "createTime.H"
```

```
18      #include "createDynamicFvMesh.H"
19      #include "initContinuityErrs.H"
20      #include "createFields.H"
21      #include "createControls.H"
22      #include "createPPutil.H"
23      #include "createUfIfPresent.H"
24      #include "CourantNo.H"
25      #include "setInitialDeltaT.H"
26
27      // * * * * * * * * * * * * * * * * * * * * * * * * * * * * * * * * * * * * * * * * * * * * //
28
29      Info<< "\nStarting time loop\n" << endl;
30
31      while (simple.loop(runTime))
32      {
33          #include "readDyMControls.H"
34          #include "CourantNo.H"
35          #include "setDeltaT.H"
36
37          Info<< "Time = " << runTime.timeName() << nl << endl;
38
39          // --- Inner loop iterations ---
40          for (int i=0; i<nInIter; i++)
41          {
42              Info << "Inner iteration:  " << i << nl << endl;
43
44              if (i==0 || moveMeshOuterCorrectors)
45              {
46                  mesh.update();
47
48                  if (mesh.changing())
49                  {
50                      MRF.update();
51
52                      if (correctPhi)
53                      {
54                          // Calculate absolute flux
55                          // from the mapped surface velocity
56                          phi = mesh.Sf() & Uf();
57
58                          #include "correctPhi.H"
59
60                          // Make the flux relative to the mesh motion
61                          fvc::makeRelative(phi, U);
62                      }
63
64                      if (checkMeshCourantNo)
65                      {
66                          #include "meshCourantNo.H"
67                      }
68                  }
69              }
70
71              // --- Pressure-velocity SIMPLEC corrector
72              {
73                 // ---- Solve U and p ----
74                 #include "UEqn.H"
75                 #include "pEqn.H"
76              }
77
78              // ---- Solve constitutive equation ----
79              constEq2.correct();
80
81              // --- Passive Scalar transport
82              if (sPS)
83               {
84                 #include "CEqn.H"
85               }
86          }
87
88          postProc.update();
89          runTime.write();
90
91          Info<< "ExecutionTime = " << runTime.elapsedCpuTime() << " s"
92              << "  ClockTime = " << runTime.elapsedClockTime() << " s"
93              << nl << endl;
94      }
95
96      Info<< "End\n" << endl;
97
98      return 0;
99  }
100
101
102 // ************************************************************************* //
```

A.1.2 createFields.H

```
1   Info<< "Reading field p\n" << endl;
2   volScalarField p
3   (
4       IOobject
5       (
6           "p",
7           runTime.timeName(),
8           mesh,
9           IOobject::MUST_READ,
10          IOobject::AUTO_WRITE
11      ),
12      mesh
13  );
14
15  Info<< "Reading field U\n" << endl;
16  volVectorField U
17  (
18      IOobject
19      (
20          "U",
21          runTime.timeName(),
22          mesh,
23          IOobject::MUST_READ,
24          IOobject::AUTO_WRITE
25      ),
26      mesh
27  );
28
29  #include "createPhi.H"
30
31
32  label pRefCell = 0;
33  scalar pRefValue = 0.0;
34  setRefCell(p, mesh.solutionDict().subDict("SIMPLE"), pRefCell, pRefValue);
35  mesh.setFluxRequired(p.name());
36
37
38  #include "createMRF.H"
39  #include "createFvOptions.H"
40
41  // Create constitutive equation
42  constitutiveModel2 constEq2(U, phi);
43
44  IOdictionary cttProperties
45  (
46      IOobject
47      (
48          "constitutiveProperties",
49          runTime.constant(),
```

```
            mesh,
            IOobject::MUST_READ_IF_MODIFIED,
            IOobject::NO_WRITE,
            false
        )
    );

    bool    sPS = cttProperties.subDict("passiveScalarProperties").
    lookupOrDefault<Switch>("solvePassiveScalar", false);

    autoPtr<volScalarField>  C
    (
      sPS != true
      ?
      NULL
      :
      new volScalarField
      (
        IOobject
        (
          "C",
          runTime.timeName(),
          mesh,
          IOobject::MUST_READ,
          IOobject::AUTO_WRITE
        ),
        mesh
     )
    );
```

A.1.3 Libraries

A.1.4 constitutiveModel2.C

```
#include "constitutiveModel2.H"

// * * * * * * * * * * * * * * * * * * * * * * * * * * * * * * * * * * * * * * * * * * * * //

namespace Foam
{

// * * * * * * * * * * * * * * * * * * * * * * * * * * * * * * * * * * * * * * * * * * * * //

defineTypeNameAndDebug(constitutiveModel2, 0);


// * * * * * * * * * * * * * * * * * Constructors  * * * * * * * * * * * * * * * * * * * * //

constitutiveModel2::constitutiveModel2
(
    const volVectorField& U,
    const surfaceScalarField& phi
)
:
    IOdictionary
    (
        IOobject
        (
            "constitutiveProperties",
            U.time().constant(),
            U.db(),
            IOobject::MUST_READ,
            IOobject::NO_WRITE
        )
    ),
    eqPtr_(constitutiveEq2::New(word::null, U, phi, subDict("parameters")))
{}


// * * * * * * * * * * * * * * * * Member Functions  * * * * * * * * * * * * * * * * * * * //

tmp<volTensorField> constitutiveModel2::tau() const
{
    return eqPtr_->tau();
}

tmp<volTensorField> constitutiveModel2::tauTotal() const
{
    return eqPtr_->tauTotal();
}

const dimensionedScalar constitutiveModel2::rho() const
{
    return eqPtr_->rho();
}

tmp<fvVectorMatrix> constitutiveModel2::divTau(volVectorField& U) const
{
    return eqPtr_->divTau(U);
}

bool constitutiveModel2::isGNF() const
{
    return eqPtr_->isGNF();
}

void constitutiveModel2::correct()
{
    eqPtr_->correct();
}


bool constitutiveModel2::read()
{
    if (regIOobject::read())
    {
        return true;
    }
    else
    {
        return false;
    }
}


// * * * * * * * * * * * * * * * * * * * * * * * * * * * * * * * * * * * * * * * * * * * * //

} // End namespace Foam

// ************************************************************************* //
```

A.1.5 constitutiveModel2.H

```
#ifndef constitutiveModel2_H
#define constitutiveModel2_H

#include "constitutiveEq2.H"
#include "autoPtr.H"

// * * * * * * * * * * * * * * * * * * * * * * * * * * * * * * * * * * * * * * * * * * * * //

namespace Foam
```

```
{

/*---------------------------------------------------------------------------*\
                        Class constitutiveModel2 Declaration
\*---------------------------------------------------------------------------*/

class constitutiveModel2
:
    public IOdictionary
{
private:

    // Private data

        //- Constitutive Eq
        autoPtr<constitutiveEq2> eqPtr_;


    // Private Member Functions

        //- Disallow default bitwise copy construct
        constitutiveModel2(const constitutiveModel2&);

        //- Disallow default bitwise assignment
        void operator=(const constitutiveModel2&);


public:

    //- Runtime type information
    TypeName("constitutiveModel2");


    // Constructors


        //- Construct from components
        constitutiveModel2
        (
            const volVectorField& U,
            const surfaceScalarField& phi
        );

    // Destructor

        virtual ~constitutiveModel2()
        {}


    // Member Functions

        //- Return the viscoelastic stress tensor
        virtual tmp<volTensorField> tau() const;

        //- Return the total stress tensor (solvent + polymeric)
        virtual tmp<volTensorField> tauTotal() const;

        //- Return the density
        virtual const dimensionedScalar rho() const;

        //- Return the coupling term for the momentum equation
        virtual tmp<fvVectorMatrix> divTau(volVectorField& U) const;

        //- Is GNF or VE
        virtual bool isGNF() const;

        //- Correct the viscoelastic stress
        virtual void correct();

        //- Read constitutiveProperties dictionary
        virtual bool read();


};


// ************************************************************************* //

} // End namespace Foam

// ************************************************************************* //

#endif

// ************************************************************************* //
```

A.1.6 LE_1constant.C

```
#include "LE_1constant.H"
#include "addToRunTimeSelectionTable.H"

// * * * * * * * * * * * * * * * Static Data Members * * * * * * * * * * * * * * //

namespace Foam
{
namespace constitutiveEqs
{
    defineTypeNameAndDebug(LE_1constant, 0);
    addToRunTimeSelectionTable(constitutiveEq2, LE_1constant, dictionary);
}
}

// * * * * * * * * * * * * * * * * * Constructors  * * * * * * * * * * * * * * * //

Foam::constitutiveEqs::LE_1constant::LE_1constant
(
    const word& name,
    const volVectorField& U,
    const surfaceScalarField& phi,
    const dictionary& dict
)
:
    constitutiveEq2(name, U, phi),
    tau_
    (
        IOobject
        (
            "tau" + name,
            U.time().timeName(),
            U.mesh(),
            IOobject::MUST_READ,
            IOobject::AUTO_WRITE
        ),
        U.mesh()
    ),

    n_
    (
        IOobject
        (
            "n" + name,
            U.time().timeName(),
            U.mesh(),
            IOobject::MUST_READ,
            IOobject::AUTO_WRITE
        ),
        U.mesh()
    ),
```

```
51
52
53          tauTotal_
54          (
55              IOobject
56              (
57                  "tauTotal" + name,
58                  U.time().timeName(),
59                  U.mesh(),
60                  IOobject::MUST_READ,
61                  IOobject::AUTO_WRITE
62              ),
63              U.mesh()
64          ),
65
66      //etaS=alpha4, eta1=alpha1, eta2=alpha2, eta3=alpha3, eta5=alpha5, eta6=alpha6
67          rho_(dict.lookup("rho")),
68          etaS_(dict.lookup("etaS")),
69          eta1_(dict.lookup("eta1")),
70          eta2_(dict.lookup("eta2")),
71          eta3_(dict.lookup("eta3")),
72          eta5_(dict.lookup("eta5")),
73          eta6_(dict.lookup("eta6")),
74          K_(dict.lookup("K"))
75
76
77      {
78       checkForStab(dict);
79      }
80
81
82      // * * * * * * * * * * * * * * * * Member Functions  * * * * * * * * * * * * * * //
83
84      void Foam::constitutiveEqs::LE_1constant::correct()
85      {
86        // Velocity gradient tensor
87          volTensorField L = fvc::grad(U());
88
89          // Symmetric velocity gradient tensor
90          volTensorField D = ( L+T(L) )/2;
91
92          // Antisymmetric velocity gradient tensor
93          volTensorField omega = skew(L);
94
95
96      //director equation
97          fvVectorMatrix nEqn
98          (
99              (eta3_ - eta2_)*(fvm::ddt(n_) + fvm::div(phi(), n_) - (n_ & omega) )
100
101
102             - K_*fvc::laplacian(n_)
103
104             + ( (n_ *n_) &   K_*fvc::laplacian(n_)     )
105     ==
106             -(eta6_ - eta5_)*( (n_ & D) - n_*tr(n_*n_ & D)  )
107
108
109
110         );
111
112
113             nEqn.relax();
114             nEqn.solve();
115             n_=n_/mag(n_);
116
117
118     volVectorField N=(  fvc::ddt(n_) + fvc::div(phi(), n_)  - (n_ & omega)  );
119
120
121             // stress tensor in the Leslie-Ericksen model
122             tau_ = (
123             eta1_ *tr(D & n_ * n_)*(n_*n_)
124             + eta2_ * (      n_ *N   )
125             + eta3_ * (      N *n_   )
126             + eta5_ * (      (n_*n_) & D )
127             + eta6_ * (D & (n_*n_)  )
128             - K_ * (         fvc::grad(n_) & T(fvc::grad(n_))         )
129             );
130
131             // total stress tensor
132     tauTotal_=tau_+2*etaS_*D;
133
134       tau_.correctBoundaryConditions();
135
136     }
137
138
139     // ************************************************************************* //
```

A.1.7 LE_1constant.H

```
1   #ifndef LE_1constant_H
2   #define LE_1constant_H
3
4   #include "constitutiveEq2.H"
5
6   // * * * * * * * * * * * * * * * * * * * * * * * * * * * * * * * * * * * * * * * * //
7
8   namespace Foam
9   {
10  namespace constitutiveEqs
11  {
12
13  /*---------------------------------------------------------------------------*\
14                             Class LE_1constant Declaration
15  \*---------------------------------------------------------------------------*/
16
17  class LE_1constant
18  :
19      public constitutiveEq2
20  {
21      // Private data
22
23
24          //- Transported nematic stress
25          volTensorField tau_;
26          //- director field
27          volVectorField n_;
28          //- Transported nematic stress
29          volTensorField tauTotal_;
30
31
32          // Model constants
33
34              //- Density
35              dimensionedScalar rho_;
36
37              //- Newtonian viscosity alpha4/2
38              dimensionedScalar etaS_;
39              //- eta1
40              dimensionedScalar eta1_;
41              //- eta2
42              dimensionedScalar eta2_;
43              //- eta3
44              dimensionedScalar eta3_;
45              //- eta5
46              dimensionedScalar eta5_;
```

```
47              //- eta6
48              dimensionedScalar eta6_;
49              //- tumbling parameter
50  //            dimensionedScalar lambda_;
51
52              //- K
53              dimensionedScalar K_;
54
55      // Private Member Functions
56          //- Disallow default bitwise copy construct
57          LE_1constant(const LE_1constant&);
58          //- Disallow default bitwise assignment
59          void operator=(const LE_1constant&);
60
61  protected:
62
63          //- Return the solvent viscosity
64          virtual const dimensionedScalar etaS() const
65          {
66              return etaS_;
67          }
68          //- Return eta1
69          virtual const dimensionedScalar eta1() const
70          {
71              return eta1_;
72          }
73          //- Return eta2
74          virtual const dimensionedScalar eta2() const
75          {
76              return eta2_;
77          }
78          //- Return eta3
79          virtual const dimensionedScalar eta3() const
80          {
81              return eta3_;
82          }
83          //- Return eta5
84          virtual const dimensionedScalar eta5() const
85          {
86              return eta5_;
87          }
88          //- Return eta6
89          virtual const dimensionedScalar eta6() const
90          {
91              return eta6_;
92          }
93
94  public:
95
96      //- Runtime type information
97      TypeName("LE_1constant");
98
99      // Constructors
100
101         //- Construct from components
102         LE_1constant
103         (
104             const word& name,
105             const volVectorField& U,
106             const surfaceScalarField& phi,
107             const dictionary& dict
108         );
109
110
111     // Destructor
112
113         virtual ~LE_1constant()
114         {}
115
116
117     // Member Functions
118
119        //- Return the viscoelastic stress tensor
120         virtual tmp<volTensorField> tau() const
121         {
122             return tau_;
123         }
124
125         //- Return the density
126         virtual const dimensionedScalar rho() const
127         {
128             return rho_;
129         }
130
131         //- Return true if GNF (non-elastic)
132         virtual bool isGNF() const
133         {
134           return false;
135         };
136
137         //- Correct the viscoelastic stress
138         virtual void correct();
139 };
140
141
142 // * * * * * * * * * * * * * * * * * * * * * * * * * * * * * * * * * * * * * * * * * * * * //
143
144 } // End namespace constitutiveEqs
145 } // End namespace Foam
146
147 // * * * * * * * * * * * * * * * * * * * * * * * * * * * * * * * * * * * * * * * * * * * * //
148
149 #endif
150
151 // ************************************************************************* //
```

A.1.8 BerisEdwards.C

```
1   #include "BerisEdwards.H"
2   #include "addToRunTimeSelectionTable.H"
3
4   // * * * * * * * * * * * * * * * Static Data Members * * * * * * * * * * * * * * * //
5
6   namespace Foam
7   {
8   namespace constitutiveEqs
9   {
10      defineTypeNameAndDebug(BerisEdwards, 0);
11      addToRunTimeSelectionTable(constitutiveEq2, BerisEdwards, dictionary);
12  }
13  }
14
15  // * * * * * * * * * * * * * * * * * Constructors  * * * * * * * * * * * * * * * //
16
17  Foam::constitutiveEqs::BerisEdwards::BerisEdwards
18  (
19      const word& name,
20      const volVectorField& U,
21      const surfaceScalarField& phi,
22      const dictionary& dict
23  )
24  :
25      constitutiveEq2(name, U, phi),
26      tau_
27      (
28          IOobject
29          (
30              "tau" + name,
```

```
31                  U.time().timeName(),
32                  U.mesh(),
33                  IOobject::MUST_READ,
34                  IOobject::AUTO_WRITE
35              ),
36              U.mesh()
37      ),
38
39      Q_
40      (
41          IOobject
42          (
43              "Q" + name,
44              U.time().timeName(),
45              U.mesh(),
46              IOobject::MUST_READ,
47              IOobject::AUTO_WRITE
48          ),
49          U.mesh()
50      ),
51
52      sigma2_
53      (
54          IOobject
55          (
56              "sigma2" + name,
57              U.time().timeName(),
58              U.mesh(),
59              IOobject::MUST_READ,
60              IOobject::AUTO_WRITE
61          ),
62          U.mesh()
63      ),
64
65
66      tauTotal_
67      (
68          IOobject
69          (
70              "tauTotal" + name,
71              U.time().timeName(),
72              U.mesh(),
73              IOobject::MUST_READ,
74              IOobject::AUTO_WRITE
75          ),
76          U.mesh()
77      ),
78
79
80      rho_(dict.lookup("rho")),
81      etaS_(dict.lookup("etaS")),
82      a_(dict.lookup("a")),
83      b_(dict.lookup("b")),
84      c_(dict.lookup("c")),
85      L_(dict.lookup("L")),
86      xi_(dict.lookup("xi")),
87      gamma_(dict.lookup("gamma"))
88
89  {
90   checkForStab(dict);
91  }
92
93
94  // * * * * * * * * * * * * * * * * Member Functions  * * * * * * * * * * * * * * * //
95
96  void Foam::constitutiveEqs::BerisEdwards::correct()
97  {
98    // Velocity gradient tensor
99      volTensorField gradU = fvc::grad(U());
100
101     // Symmetric velocity gradient tensor
102     volTensorField D = ( gradU+T(gradU) )/2;
103
104     // Antisymmetric velocity gradient tensor
105     volTensorField omega = skew(gradU);
106
107 tensor I(1,0,0,0,1,0,0,0,1);
108
109         volTensorField S=( (xi_*D - omega) & (Q_ + I/3 ) )
110                         + ( (Q_ + I/3 ) & (xi_*D + omega) )
111                         - ( 2*xi_ *  (Q_ + I/3 )*tr(Q_ & gradU) );
112
113
114         volTensorField H=fvc::laplacian(L_, Q_) - a_*Q_
115                                 + b_*( (Q_ & Q_) - (tr(Q_ & Q_ ) )* I/3 ) - c_ * Q_ * ( tr(Q_ & Q_) );
116
117
118
119 //Q-tensor transport equation
120     fvTensorMatrix QEqn
121     (
122         fvm::ddt(Q_)
123         + fvm::div(phi(), Q_)
124         ==
125
126         S + gamma_ * H
127
128     );
129
130         QEqn.relax();
131         QEqn.solve();
132
133
134         Q_=( Q_ + T(Q_) )/2;
135
136 forAll(Q_, cellI)
137 {
138 Q_[cellI][8]=-Q_[cellI][0]-Q_[cellI][4];
139 }
140
141
142 // calculate gradients of Q
143
144
145         volScalarField Q11=Q_.component(0);
146         volScalarField Q12=Q_.component(1);
147         volScalarField Q13=Q_.component(2);
148         volScalarField Q21=Q_.component(3);
149         volScalarField Q22=Q_.component(4);
150         volScalarField Q23=Q_.component(5);
151         volScalarField Q31=Q_.component(6);
152         volScalarField Q32=Q_.component(7);
153         volScalarField Q33=Q_.component(8);
154
155
156
157         volVectorField gradQ11=fvc::grad(Q11);
158         volVectorField gradQ12=fvc::grad(Q12);
159         volVectorField gradQ13=fvc::grad(Q13);
160         volVectorField gradQ21=fvc::grad(Q21);
161         volVectorField gradQ22=fvc::grad(Q22);
162         volVectorField gradQ23=fvc::grad(Q23);
163         volVectorField gradQ31=fvc::grad(Q31);
164         volVectorField gradQ32=fvc::grad(Q32);
165         volVectorField gradQ33=fvc::grad(Q33);
166
167
168
169 tensor Ixx(1,0,0,0,0,0,0,0,0);
170 tensor Ixy(0,1,0,0,0,0,0,0,0);
```

```
171     tensor Ixz(0,0,1,0,0,0,0,0,0);
172     tensor Iyx(0,0,0,1,0,0,0,0,0);
173     tensor Iyy(0,0,0,0,1,0,0,0,0);
174     tensor Iyz(0,0,0,0,0,1,0,0,0);
175     tensor Izx(0,0,0,0,0,0,1,0,0);
176     tensor Izy(0,0,0,0,0,0,0,1,0);
177     tensor Izz(0,0,0,0,0,0,0,0,1);
178
179     //elastic stress tensor
180
181             volScalarField sigmaExx=
182                             gradQ11.component(0)*gradQ11.component(0)
183                             +gradQ12.component(0)*gradQ12.component(0)
184                             +gradQ13.component(0)*gradQ13.component(0)
185                             +gradQ21.component(0)*gradQ21.component(0)
186                             +gradQ22.component(0)*gradQ22.component(0)
187                             +gradQ23.component(0)*gradQ23.component(0)
188                             +gradQ31.component(0)*gradQ31.component(0)
189                             +gradQ32.component(0)*gradQ32.component(0)
190                             +gradQ33.component(0)*gradQ33.component(0)       ;
191
192     volScalarField  sigmaExy=
193                             gradQ11.component(0)*gradQ11.component(1)
194                             +gradQ12.component(0)*gradQ12.component(1)
195                             +gradQ13.component(0)*gradQ13.component(1)
196                             +gradQ21.component(0)*gradQ21.component(1)
197                             +gradQ22.component(0)*gradQ22.component(1)
198                             +gradQ23.component(0)*gradQ23.component(1)
199                             +gradQ31.component(0)*gradQ31.component(1)
200                             +gradQ32.component(0)*gradQ32.component(1)
201                             +gradQ33.component(0)*gradQ33.component(1)       ;
202
203     volScalarField  sigmaExz=
204                             gradQ11.component(0)*gradQ11.component(2)
205                             +gradQ12.component(0)*gradQ12.component(2)
206                             +gradQ13.component(0)*gradQ13.component(2)
207                             +gradQ21.component(0)*gradQ21.component(2)
208                             +gradQ22.component(0)*gradQ22.component(2)
209                             +gradQ23.component(0)*gradQ23.component(2)
210                             +gradQ31.component(0)*gradQ31.component(2)
211                             +gradQ32.component(0)*gradQ32.component(2)
212                             +gradQ33.component(0)*gradQ33.component(2)       ;
213
214     volScalarField  sigmaEyx=
215                             gradQ11.component(1)*gradQ11.component(0)
216                             +gradQ12.component(1)*gradQ12.component(0)
217                             +gradQ13.component(1)*gradQ13.component(0)
218                             +gradQ21.component(1)*gradQ21.component(0)
219                             +gradQ22.component(1)*gradQ22.component(0)
220                             +gradQ23.component(1)*gradQ23.component(0)
221                             +gradQ31.component(1)*gradQ31.component(0)
222                             +gradQ32.component(1)*gradQ32.component(0)
223                             +gradQ33.component(1)*gradQ33.component(0)       ;
224
225
226     volScalarField  sigmaEyy=
227                             gradQ11.component(1)*gradQ11.component(1)
228                             +gradQ12.component(1)*gradQ12.component(1)
229                             +gradQ13.component(1)*gradQ13.component(1)
230                             +gradQ21.component(1)*gradQ21.component(1)
231                             +gradQ22.component(1)*gradQ22.component(1)
232                             +gradQ23.component(1)*gradQ23.component(1)
233                             +gradQ31.component(1)*gradQ31.component(1)
234                             +gradQ32.component(1)*gradQ32.component(1)
235                             +gradQ33.component(1)*gradQ33.component(1)       ;
236
237     volScalarField  sigmaEyz=
238                             gradQ11.component(1)*gradQ11.component(2)
239                             +gradQ12.component(1)*gradQ12.component(2)
240                             +gradQ13.component(1)*gradQ13.component(2)
241                             +gradQ21.component(1)*gradQ21.component(2)
242                             +gradQ22.component(1)*gradQ22.component(2)
243                             +gradQ23.component(1)*gradQ23.component(2)
244                             +gradQ31.component(1)*gradQ31.component(2)
245                             +gradQ32.component(1)*gradQ32.component(2)
246                             +gradQ33.component(1)*gradQ33.component(2)       ;
247
248     volScalarField  sigmaEzx=
249                             gradQ11.component(2)*gradQ11.component(0)
250                             +gradQ12.component(2)*gradQ12.component(0)
251                             +gradQ13.component(2)*gradQ13.component(0)
252                             +gradQ21.component(2)*gradQ21.component(0)
253                             +gradQ22.component(2)*gradQ22.component(0)
254                             +gradQ23.component(2)*gradQ23.component(0)
255                             +gradQ31.component(2)*gradQ31.component(0)
256                             +gradQ32.component(2)*gradQ32.component(0)
257                             +gradQ33.component(2)*gradQ33.component(0)       ;
258
259     volScalarField  sigmaEzy=
260                             gradQ11.component(2)*gradQ11.component(1)
261                             +gradQ12.component(2)*gradQ12.component(1)
262                             +gradQ13.component(2)*gradQ13.component(1)
263                             +gradQ21.component(2)*gradQ21.component(1)
264                             +gradQ22.component(2)*gradQ22.component(1)
265                             +gradQ23.component(2)*gradQ23.component(1)
266                             +gradQ31.component(2)*gradQ31.component(1)
267                             +gradQ32.component(2)*gradQ32.component(1)
268                             +gradQ33.component(2)*gradQ33.component(1)       ;
269
270
271     volScalarField  sigmaEzz=
272                             gradQ11.component(2)*gradQ11.component(2)
273                             +gradQ12.component(2)*gradQ12.component(2)
274                             +gradQ13.component(2)*gradQ13.component(2)
275                             +gradQ21.component(2)*gradQ21.component(2)
276                             +gradQ22.component(2)*gradQ22.component(2)
277                             +gradQ23.component(2)*gradQ23.component(2)
278                             +gradQ31.component(2)*gradQ31.component(2)
279                             +gradQ32.component(2)*gradQ32.component(2)
280                             +gradQ33.component(2)*gradQ33.component(2)       ;
281
282
283     sigma2_= Ixx*sigmaExx + Ixy*sigmaExy + Ixz*sigmaExz +
284             Iyx*sigmaEyx + Iyy*sigmaEyy + Iyz*sigmaEyz +
285             Izx*sigmaEzx + Izy*sigmaEzy + Izz*sigmaEzz       ;
286
287     //viscous stress tensor
288             volTensorField sigma_= (H & Q_) - (Q_ & H)
289                                     - xi_ * ( (Q_ + I/3 ) & H ) - xi_ * ( H & (Q_ + I/3 ) )
290                                     + 2 * xi_ * ( (Q_ + I/3 ) * (Q_ && H ) ) ;
291
292     // elastic+viscous non-Newtonian stresses
293
294             tau_ = ( -L_* sigma2_ + sigma_ );
295
296
297     // total stress
298     tauTotal_=tau_+2*etaS_*D;
299
300       tau_.correctBoundaryConditions();
301
302     }
303
304
305     // ************************************************************************* //
```

A.1.9 BerisEdwards.H

```
1
2
3   #ifndef BerisEdwards_H
4   #define BerisEdwards_H
5
6   #include "constitutiveEq2.H"
7
8   // * * * * * * * * * * * * * * * * * * * * * * * * * * * * * * * * * * * * * * * * * * * * //
9
10  namespace Foam
11  {
12  namespace constitutiveEqs
13  {
14
15  /*---------------------------------------------------------------------------*\
16                              Class BerisEdwards Declaration
17  \*---------------------------------------------------------------------------*/
18
19  class BerisEdwards
20  :
21      public constitutiveEq2
22  {
23      // Private data
24
25
26          //- Transported nematic stress
27          volTensorField tau_;
28          volTensorField Q_;
29          volTensorField sigma2_;
30          //- Transported nematic stress
31          volTensorField tauTotal_;
32
33          // Model constants
34              //- Density
35              dimensionedScalar rho_;
36              //- Newtnoian viscosity
37              dimensionedScalar etaS_;
38
39              dimensionedScalar a_;
40
41              dimensionedScalar b_;
42
43              dimensionedScalar c_;
44
45              dimensionedScalar L_;
46
47              dimensionedScalar xi_;
48
49              dimensionedScalar gamma_;
50
51      // Private Member Functions
52
53          //- Disallow default bitwise copy construct
54          BerisEdwards(const BerisEdwards&);
55
56          //- Disallow default bitwise assignment
57          void operator=(const BerisEdwards&);
58
59  protected:
60
61         //- Return the solvent viscosity
62         virtual const dimensionedScalar etaS() const
63         {
64            return etaS_;
65         }
66
67
68
69  public:
70
71      //- Runtime type information
72      TypeName("BerisEdwards");
73
74      // Constructors
75
76          //- Construct from components
77          BerisEdwards
78          (
79              const word& name,
80              const volVectorField& U,
81              const surfaceScalarField& phi,
82              const dictionary& dict
83          );
84
85
86      // Destructor
87
88          virtual ~BerisEdwards()
89          {}
90
91
92      // Member Functions
93
94         //- Return the viscoelastic stress tensor
95          virtual tmp<volTensorField> tau() const
96          {
97              return tau_;
98          }
99
100         //- Return the density
101         virtual const dimensionedScalar rho() const
102         {
103             return rho_;
104         }
105
106         //- Return true if GNF (non-elastic)
107         virtual bool isGNF() const
108         {
109           return false;
110         };
111
112         //- Correct the viscoelastic stress
113         virtual void correct();
114 };
115
116
117 // * * * * * * * * * * * * * * * * * * * * * * * * * * * * * * * * * * * * * * * * * * * * //
118
119 } // End namespace constitutiveEqs
120 } // End namespace Foam
121
122 // * * * * * * * * * * * * * * * * * * * * * * * * * * * * * * * * * * * * * * * * * * * * //
123
124 #endif
125
126 // ************************************************************************* //
```

A.2 Analytical solution of nematic flow in a capillary

The fluid motion is described by the linear momentum equation (2.8), whose dimensional form in cylindrical coordinates reads [18]

$$\frac{\partial p^*}{\partial r^*} = \frac{\partial \tau^*_{rr}}{\partial r^*} + \frac{1}{r^*}\frac{\partial \tau_{r^*\phi}}{\partial \phi} + \frac{1}{r^*}N^*_2, \tag{A.1a}$$

$$\frac{1}{r^*}\frac{\partial p^*}{\partial \phi} = \frac{\partial \tau_{r^*\phi}}{\partial r^*} + \frac{1}{r^*}\frac{\partial \tau^*_{\phi\phi}}{\partial \phi} + \frac{2}{r^*}\tau_{r\phi}, \tag{A.1b}$$

$$\frac{\partial p^*}{\partial s^*} = \frac{\partial \tau^*_{rs}}{\partial r^*} + \frac{1}{r^*}\frac{\partial \tau^*_{\phi s}}{\partial \phi} + \frac{1}{r^*}\tau^*_{rs}, \tag{A.1c}$$

where N^*_i are normal stress differences and τ^*_{ij} are components of the stress tensor

$$\boldsymbol{\tau}^* = \alpha^*_1 \boldsymbol{nnnn} : \boldsymbol{D}^* + \alpha^*_2 \boldsymbol{nN}^* + \alpha^*_3 \boldsymbol{N}^*\boldsymbol{n} + \alpha_4 \boldsymbol{D}^* + \alpha^*_5 \boldsymbol{nn}\cdot\boldsymbol{D}^* + \alpha^*_6 \boldsymbol{D}\cdot\boldsymbol{nn} - \tfrac{1}{Er}\boldsymbol{\nabla}^*\boldsymbol{n}\cdot(\boldsymbol{\nabla}^*\boldsymbol{n})^T. \tag{2.81}$$

Let us introduce the following scaling

$$r = \frac{r^*}{R^*}, \qquad v_s = v^*_s/v^*_0, \qquad \boldsymbol{\tau} = \frac{r^*_0}{\frac{\alpha_4}{2}v^*_0}\boldsymbol{\tau^*} \qquad \alpha_i = \frac{\alpha^*_i}{\frac{\alpha^*_4}{2}}, \tag{A.2}$$

where starred variables refer to dimensional quantities, v^*_0 is the peak velocity. We are interested only in the $s-$component of the momentum equation, as there is no motion in the $r-\phi$ plane due to the steady-state, fully developed flow assumption. Hence, eq. (A.2) into the s-component of the momentum equation (A.1c) yields

$$\frac{2R^{*2}}{v^*_0\alpha^*_4}\frac{\partial p^*}{\partial s^*} = \frac{\partial \tau_{rs}}{\partial r} + \frac{1}{r}\tau_{rs}. \tag{A.3}$$

The $r-s$ component of the stress tensor is given by

$$\tau_{rs} = \frac{(2\alpha_1 n^2_s - \alpha_2 + \alpha_5)n^2_r + (\alpha_3+\alpha_6)n^2_s + 2}{2}\frac{\partial v_s}{\partial r}. \tag{A.4}$$

In order to obtain the analytical solution, τ_{rs} is simplified further by assuming that $\alpha_1 = \alpha_3 = 0$, $\alpha_5 = -\alpha_2$, which gives $\alpha_6 = 0$ [125]. The simplification is based on the inspection of liquid crystal viscosities, which shows that [21, 43]

$$|\alpha_1| \approx |\alpha_3| \approx |\alpha_6| << |\alpha_2| \approx |\alpha_5| = O(1). \tag{A.5}$$

Hence, the $r-s$ component of the stress tensor simplifies to

$$\tau_{rs} = \frac{1 + r^4 + (2-4\alpha_2)r^2}{(r^2+1)^2}\frac{\partial v_s}{\partial r}, \tag{A.6}$$

which upon substitution into eq. (A.3) and implementation of the no-slip boundary condition ($v_s(r=1)=0$) yields the velocity solution

$$\frac{v_s^*}{2\frac{\partial p^*}{\partial s^*}\frac{(r_0^*)^2}{\alpha_4^*}} = \frac{1-r^2}{4} - \frac{1}{2}\alpha_2 \ln\left(1 + r^4 + (-4\alpha_2 + 2)r^2\right)$$
$$+ \tanh^{-1}\left(\frac{r^2 - 2\alpha_2 + 1}{2\sqrt{\alpha_2(\alpha_2 - 1)}}\right)\frac{\alpha_2^2 - \frac{1}{2}\alpha_2}{\sqrt{\alpha_2(\alpha_2 - 1)}}$$
$$+ \tanh^{-1}\left(\frac{\alpha_2 - 1}{\sqrt{\alpha_2(\alpha_2 - 1)}}\right)\frac{\alpha_2^2 - \frac{1}{2}\alpha_2}{\sqrt{\alpha_2(\alpha_2 - 1)}} + \frac{\alpha_2[2\ln(2) + \ln(-\alpha_2 + 1)]}{2} \quad \text{(A.7)}$$

Hence, the viscous component of the normal stress can be calculated from eq. (2.81) and is given by

$$N_1 = -\alpha_2 n_r n_s \frac{\partial v_s}{\partial r}. \quad \text{(A.8)}$$

Appendix B

Supplementary material of chapter 5

B.1 Components of the velocity gradient tensor

Components of the velocity gradient tensor $\nabla \boldsymbol{u} = \frac{\partial v_i}{\partial x_j} \boldsymbol{e}_j \boldsymbol{e}_i$ are given by

$$
\begin{aligned}
[\nabla \boldsymbol{u}]_{r,r} &= \frac{\partial u}{\partial r}, \qquad [\nabla \boldsymbol{u}]_{r,\phi} = \frac{1}{r}\frac{\partial u}{\partial \phi} - \frac{u}{r} \qquad [\nabla \boldsymbol{u}]_{r,s} = -\frac{\delta}{B} w \cos\phi, \\
[\nabla \boldsymbol{u}]_{\phi,r} &= \frac{\partial v}{\partial r}, \qquad [\nabla \boldsymbol{u}]_{\phi,\phi} = \frac{1}{r}\frac{\partial v}{\partial \phi} + \frac{u}{r}, \qquad [\nabla \boldsymbol{u}]_{\phi,s} = \frac{\delta}{B} w \sin\phi, \\
[\nabla \boldsymbol{u}]_{s,r} &= \frac{\partial w}{\partial r}, \qquad [\nabla \boldsymbol{u}]_{s,\phi} = \frac{1}{r}\frac{\partial w}{\partial \phi}, \qquad [\nabla \boldsymbol{u}]_{s,s} = \frac{\delta}{B}(u\cos\phi - v\sin\phi).
\end{aligned}
\tag{B.1}
$$

B.2 Leading order solution

Neglecting terms $O(\delta)$ and higher from the angular momentum equation (2.29) reduces the problem to a fully developed, axisymmetric straight pipe flow with $r-$, $\phi-$ and $s-$ components given by

$$
\left(2\lambda (n_r^{(0)})^2 - \lambda + 1\right) \frac{\partial w^{(0)}}{\partial r} = 0, \tag{5.20a}
$$

$$
n_r^{(0)} n_p^{(0)} n_s^{(0)} \frac{\partial w^{(0)}}{\partial r} = 0, \tag{5.20b}
$$

$$
\left(2\lambda (n_s^{(0)})^2 - \lambda - 1\right) \frac{\partial w^{(0)}}{\partial r} = 0. \tag{5.20c}
$$

while the $O(1)$ component of the linear momentum balance in the axial direction (5.17) has the same form as in the cylindrical coordinate system

$$
0 = \underbrace{4\left(1 + 2\mu_1 \left(n_r^{(0)} n_s^{(0)}\right)^2 + \frac{\mu_2}{2}\right)}_{\text{pressure gradient}} + \frac{\partial \tau_{rs}^{(0)}}{\partial r} + \frac{1}{r}\tau_{rs}^{(0)}. \tag{5.19}
$$

In a straight pipe the axial symmetry prevents the appearance of a steady state flow and the momentum balance in the $r-\phi$ plane (5.18) reads

$$
(\nabla \times \nabla p^{(0)})_s = 0. \tag{5.19b}
$$

The non-zero components the of $\boldsymbol{\tau}^0$ are given by

$$\tau_{rs}^{(0)} = \frac{\mu_2 + 4\mu_1 (n_r^{(0)})^2 (n_s^{(0)})^2 + 2}{2} \frac{\partial w^{(0)}}{\partial r}, \tag{B.3a}$$

$$\tau_{rr}^{(0)} = \frac{\partial w^{(0)}}{\partial r} n_r^{(0)} n_s^{(0)} \left(2\mu_1 (n_r^{(0)})^2 + \mu_2\right), \tag{B.3b}$$

$$\tau_{ss}^{(0)} = n_r^{(0)} n_r^{(0)} [2\mu_1 (n_s^{(0)})^2 + \mu_2] \frac{\partial w^{(0)}}{\partial r}, \tag{B.3c}$$

Substituting eq. (B.3a) into the axial momentum balance (5.19) gives the second order differential equation for $w^{(0)}$:

$$\frac{\partial^2 w^{(0)}}{\partial r^2} + \frac{1}{r} \frac{\partial w^{(0)}}{\partial r} = -4. \tag{B.4}$$

Imposing the no-slip boundary condition gives the solution

$$w^{(0)}(r, \phi) = 1 - r^2. \tag{5.22}$$

B.3 First order $O(\delta)$ solution

The $O(\delta)$ components of the linear momentum equations (5.17) and (5.18) are given by

$$0 = \frac{\partial p}{\partial s} r \cos\phi + \frac{\partial \tau_{rs}^{(1)}}{\partial r} + \frac{1}{r} \frac{\partial \tau_{\phi s}^{(1)}}{\partial \phi} + \frac{1}{r} \tau_{rs}^{(1)} + 2 \left[\tau_{rs}^{(0)} \cos\phi - \tau_{\phi s}^{(0)} \sin\phi\right], \tag{5.25}$$

$$\begin{aligned} 0 = &-\frac{1}{r} \frac{\partial^2 N_2^{(1)}}{\partial r \partial \phi} - \frac{1}{r^2} \frac{\partial N_2^{(1)}}{\partial \phi} + \frac{\partial^2 \tau_{r\phi}^{(1)}}{\partial r^2} + \frac{3}{r} \frac{\partial}{\partial r} \tau_{r\phi}^{(1)} - \frac{1}{r^2} \frac{\partial^2 \tau_{r\phi}^{(1)}}{\partial \phi^2} \\ &+ \sin\phi \left(\frac{1}{r} \frac{\partial \tau_{\phi r}^{(0)}}{\partial \phi} + \frac{1}{r} (N_2^{(0)}) + \frac{\partial \tau_{ss}^{(0)}}{\partial r} + \frac{\partial \tau_{\phi\phi}^{(0)}}{\partial r}\right) + \cos\phi \left(\frac{1}{r} \frac{\partial N_1^{(0)}}{\partial \phi} + \frac{2}{r} \partial \tau_{r\phi}^{(0)} + \frac{\partial \tau_{r\phi}^{(0)}}{\partial r}\right), \end{aligned} \tag{5.26}$$

where $\boldsymbol{\tau}^{(1)}$ denotes the first order stress tensor and its components read

$$\begin{aligned} \tau_{rr}^{(1)} = &\underbrace{\left(6 n_s^{(0)} \left[\mu_1 (n_r^{(0)})^2 + \frac{\mu_2}{6}\right] n_r^{(1)} + 2 n_s^{(1)} \left[\mu_1 (n_r^{(0)})^2 + \frac{\mu_2}{2}\right] n_r^{(0)}\right) \frac{\partial w^{(0)}}{\partial r}}_{\text{non-axisymmetric distortion of the director field}} \\ &+ \underbrace{n_s^{(0)} n_r^{(0)} \left(2\mu_1 (n_r^{(0)})^2 + \mu_2\right) \left(-w^{(0)} \cos\phi + \frac{\partial w^{(1)}}{\partial r}\right)}_{\text{axial velocity shift}} \\ &+ \underbrace{2 \left(\mu_1 (n_r^{(0)})^4 + \mu_2 (n_r^{(0)})^2 + 1\right) \frac{\partial u^{(1)}}{\partial r}}_{\text{homogeneous viscous contribution}} \end{aligned} \tag{B.5a}$$

$$\tau_{r\phi}^{(1)} = 2n_s^{(0)} \underbrace{n_\phi^{(1)}(\mu_1(n_r^{(0)})^2 + \frac{\mu_2}{4})\frac{\partial w^{(0)}}{\partial r}}_{\text{director reorientation}} + \underbrace{2n_s^{(0)}\frac{\mu_2 n_r^{(0)}\sin\phi}{4}w^{(0)}\frac{\mu_2 n_r^{(0)} n_s^{(0)}\frac{\partial w^{(1)}}{\partial\phi}}{2r}}_{\text{axial velocity shift}}$$
$$+ \underbrace{\frac{\mu_2(n_r^{(0)})^2+2}{2r}\left(\frac{\partial u^{(1)}}{\partial\phi} + \frac{\partial v^{(1)}}{\partial r}r - v^{(1)}\right)}_{\text{inhomogeneous viscous contribution}}$$
$$= -\left[\left((n_r^{(0)})^2\mu_1 + \frac{(n_r^{(0)})^2\mu_2}{2} + \frac{\mu_2}{4} + 1\right)\lambda - (n_r^{(0)})^2\mu_1 - \frac{\mu_2}{2}\right]\frac{\partial^2\psi^{(1)}}{\partial\phi^2} +$$
$$\frac{\left((\mu_1 + \frac{\mu_2}{2})(n_r^{(0)})^2 + \frac{\mu_2}{4}\right)\lambda - (n_r^{(0)})^2\mu_1 - \frac{\mu_2}{4}}{n_r^{(0)}\lambda}w^{(0)}n_s^{(0)}\sin\phi +$$
$$\frac{\left((n_r^{(0)})^2\mu_1 + \frac{(n_r^{(0)})^2\mu_2}{2} + \frac{\mu_2}{4} + 1\right)\lambda + (n_r^{(0)})^2\mu_1 + \frac{\mu_2}{4}}{\lambda}\left(\frac{\partial v^{(1)}}{\partial r} - \frac{v^{(1)}}{r}\right), \quad \text{(B.5b)}$$

$$\tau_{rs}^{(1)} = 2\cos\phi((\mu_1(n_s^{(0)})^2 + \mu_2/4)(n_r^{(0)})^2 + \mu_2(n_s^{(0)})^2/4 + 1/2)r^2$$
$$+ (-8n_r^{(0)}(\mu_1(n_s^{(0)})^2 + \mu_2/4)n_r^{(1)} - 8n_s^{(0)}(\mu_1(n_r^{(0)})^2 + \mu_2/4)n_s^{(1)})r$$
$$+ 2((\mu_1(n_s^{(0)})^2 + \mu_2/4)(n_r^{(0)})^2 + \mu_2(n_s^{(0)})^2/4 + 1/2)\frac{\partial w^{(1)}}{\partial r}$$
$$- 2\cos\phi((\mu_1(n_s^{(0)})^2 + \mu_2/4)(n_r^{(0)})^2 + \mu_2(n_s^{(0)})^2/4 + 1/2)$$
$$+ 2n_r^{(0)}n_s^{(0)}(\mu_1(n_r^{(0)})^2 + \frac{\mu_2}{2})\left(\frac{1}{r^2}\frac{\partial\psi^{(1)}}{\partial\phi} - \frac{1}{r}\frac{\partial^2\psi^{(1)}}{\partial r\partial\phi}\right), \quad \text{(B.5c)}$$

$$\tau_{\phi s}^{(1)} = -\sin\phi(\mu_2(n_s^{(0)})^2 + 2)r^2/2 - 4n_r^{(0)}(\mu_1(n_s^{(0)})^2 + \mu_2/4)rn_p^{(1)} + \frac{\mu_2}{2}n_r^{(0)}n_s^{(0)}\frac{\partial^2\psi^{(1)}}{\partial r^2} +$$
$$\frac{1}{2}\sin\phi(\mu_2(n_s^{(0)})^2 + 2) - \frac{(-\mu_2(n_s^{(0)})^2 - 2)\frac{\partial w^{(1)}}{\partial\phi} + \mu_2 n_r^{(0)}n_s^{(0)}\frac{\partial\psi^{(1)}}{\partial r}}{2r} - \frac{\mu_2\frac{\partial^2\psi^{(1)}}{\partial\phi^2}n_r^{(0)}n_s^{(0)}}{2r^2}, \quad \text{(B.5d)}$$

$$\tau_{ss}^{(1)} = 2n_r^{(0)}n_s^{(0)}\cos\phi(\mu_1(n_s^{(0)})^2 + \frac{\mu_2}{2})r^2 + (-4n_s^{(0)}(\mu_1(n_s^{(0)})^2 + \frac{\mu_2}{2})n_r^{(1)}$$
$$- 12n_r^{(0)}(\mu_1(n_s^{(0)})^2 + \frac{\mu_2}{6})n_s^{(1)})r + 2n_r^{(0)}n_s^{(0)}(\mu_1(n_s^{(0)})^2 + \frac{\mu_2}{2})\frac{\partial w^{(1)}}{\partial r}$$
$$- 2n_r^{(0)}n_s^{(0)}\cos\phi(\mu_1(n_s^{(0)})^2 + \frac{\mu_2}{2}) + 2\mu_1(n_r^{(0)})^2(n_s^{(0)})^2\left(\frac{1}{r^2}\frac{\partial\psi^{(1)}}{\partial\phi} - \frac{1}{r}\frac{\partial^2\psi^{(1)}}{\partial r\partial\phi}\right), \quad \text{(B.5e)}$$

$$\tau_{\phi\phi}^{(1)} = -2\left(\frac{1}{r^2}\frac{\partial\psi^{(1)}}{\partial\phi} - \frac{1}{r}\frac{\partial^2\psi^{(1)}}{\partial r\partial\phi}\right). \quad \text{(B.5f)}$$

The first-order director evolution equation is found by collecting $O(\delta)$ terms from eq.

(2.27)

$$0 = -4\frac{\partial w^{(0)}}{\partial r} n_r^{(1)} \sqrt{\lambda(\lambda+1)} + \sqrt{2}\frac{\partial u^{(1)}}{\partial r}(\lambda+1), \tag{5.27a}$$

$$0 = -2n_p^{(1)}\sqrt{\lambda^2+\lambda}\frac{\partial w^{(0)}}{\partial r} + \sqrt{2}\sqrt{\lambda^2-\lambda}\left[(\lambda-1)\tfrac{\partial u^{(1)}}{\partial \phi} + (\lambda+1)\left(\tfrac{\partial v^{(1)}}{\partial r} r - v^{(1)}\right)\right] - (\lambda-1)\sqrt{\lambda^2+\lambda}\left(w^{(0)} r\sin\phi + \tfrac{\partial w^{(1)}}{\partial \phi}\right), \tag{5.27b}$$

$$0 = 4n_s^{(1)}\frac{\partial w^{(0)}}{\partial r}\sqrt{\lambda(\lambda-1)} - \sqrt{2}\frac{\partial u^{(1)}}{\partial r}(\lambda-1). \tag{5.27c}$$

Substituting the relevant components of stress (eq. (B.5)) and director field (eq. (5.27)) into momentum balance equations (5.25) and (5.26) provides a pair of differential equations in terms of $w^{(1)}$ and $\psi^{(1)}$:

$$\sqrt{\lambda+1}\left[-6\cos(\phi)r^3 + r^2\tfrac{\partial^2 w^{(1)}(r,\phi)}{\partial r^2} + r\tfrac{\partial w^{(1)}(r,\phi)}{\partial r} + \tfrac{\partial^2 w^{(1)}(r,\phi)}{\partial \phi^2}\right]\Big((\mu_1+\mu_2+2)\lambda^2 - \mu_1\Big)r + \sqrt{\lambda-1}\left[\Big((\mu_1+\mu_2)\lambda^2-\mu_1\Big)\frac{\partial^3\psi^{(1)}}{\partial\phi^3} + \Big((\mu_1+\mu_2)\lambda+\mu_1\Big)(\lambda+1)\frac{\partial\psi^{(1)}}{\partial\phi}\right] = 0, \tag{B.7}$$

$$\begin{aligned}
&\Bigg\{\Big[(\mu_1+\mu_2+2)\lambda^2-(2\mu_1+\mu_2)\lambda+\mu_1\Big]\frac{\partial^4\psi^{(1)}(r,\phi)}{\partial\phi^4} + \Big[(\mu_1+\mu_2+2)\lambda^2-\mu_1\Big]r^4\frac{\partial^4\psi^{(1)}(r,\phi)}{\partial r^4} \\
&+ r^2(4\lambda^2+\lambda\mu_1-\mu_1)\frac{\partial^2}{\partial\phi^2}\left(\frac{\partial^2\psi^{(1)}(r,\phi)}{\partial r^2}\right) + 2\Big[(\mu_1+\mu_2+2)\lambda^2-\mu_1\Big]r^3\frac{\partial^3\psi^{(1)}(r,\phi)}{\partial r^3} \\
&- r(4\lambda^2+\lambda\mu_1-\mu_1)\frac{\partial}{\partial r}\left(\frac{\partial^2\psi^{(1)}(r,\phi)}{\partial\phi^2}\right) \\
&+ \Big[(2\mu_1+2\mu_2+8)\lambda^2-(\mu_1+\mu_2)\lambda-\mu_1\Big]\frac{\partial^2\psi^{(1)}(r,\phi)}{\partial\phi^2} \\
&- \left(\frac{\partial^2\psi^{(1)}(r,\phi)}{\partial r^2}r - \frac{\partial\psi^{(1)}(r,\phi)}{\partial r}\right)\Big((\mu_1+\mu_2+2)\lambda^2-\mu_1\Big)r\Bigg\}\sqrt{\lambda(\lambda-1)} \\
&+ 10(\lambda-1)r\Bigg[\left(\frac{(\mu_1+\mu_2)\lambda-\mu_1}{10}\right)\frac{\partial^3 w^{(1)}(r,\phi)}{\partial\phi^3} + \left(\frac{(\mu_1+\mu_2)\lambda-\mu_1}{10}\right)\frac{\partial w^{(1)}(r,\phi)}{\partial\phi} \\
&\qquad + r^3\Big[(\mu_1+\mu_2)\lambda - \frac{3\mu_1}{5}\Big]\sin(\phi)\Bigg]\sqrt{\lambda(\lambda+1)} = 0
\end{aligned} \tag{B.8}$$

Inspection of eq. (B.7) and (B.8) suggests the most general forms of $w^{(1)}(r,\phi)$ and $\psi^{(1)}(r,\phi)$:

$$w^{(1)}(r,\phi) = w^{(1)}(r)\cos\phi, \qquad \psi^{(1)}(r,\phi) = \psi^{(1)}(r)\sin\phi, \tag{B.9}$$

hence, by substituting eq. (B.9) into eq. (B.8) we obtain a differential equation with a single variable $\psi^{(1)}(r)$:

$$\Bigg[\Big((\mu_1+\mu_2+2)\lambda^2-\mu_1\Big)r^4\frac{\partial^4\psi^{(1)}(r)}{\partial r^4}+2\Big((\mu_1+\mu_2+2)\lambda^2-\mu_1\Big)r^3\frac{\partial^3\psi^{(1)}(r)}{\partial r^3}$$
$$-\left(r^2\frac{\partial^2\psi^{(1)}(r)}{\partial r^2}-r\frac{\partial\psi^{(1)}(r)}{\partial r}+\psi^{(1)}(r)\right)\Big((\mu_1+\mu_2+6)\lambda^2+\lambda\mu_1-2\mu_1\Big)\Bigg]\sqrt{\lambda(\lambda-1)}$$
$$+10\Big((\mu_1+\mu_2)\lambda-\frac{3\mu_1}{5}\Big)\sqrt{\lambda(\lambda+1)}(\lambda-1)r^4=0 \quad \text{(B.10)}$$

Equation (B.10) is solved with the mathematical manipulation software Maple 2020 [166]; imposing the no-slip boundary condition (eq. (5.16)) gives the solution

$$\psi^{(1)}(r,\phi)=\left(r^4+\frac{4-b}{b-1}r-\frac{3}{b-1}r^b\right)a\sin\phi, \tag{5.29}$$

where $a=a(\mu_i,\lambda)$ and $b=b(\mu_i,\lambda)$ are material-dependent constants

$$a=-\frac{2\sqrt{\lambda^2+\lambda}\sqrt{\lambda^2-\lambda}(5\lambda\mu_1+5\lambda\mu_2-3\mu_1)}{9\lambda(7\lambda^2\mu_1+7\lambda^2\mu_2+10\lambda^2-\lambda\mu_1-6\mu_1)}, \tag{B.11a}$$
$$b=\frac{\lambda^2\mu_1+\lambda^2\mu_2+2\lambda^2+\sqrt{(\lambda^2\mu_1+\lambda^2\mu_2+2\lambda^2-\mu_1)(2\lambda^2\mu_1+2\lambda^2\mu_2+8\lambda^2+\lambda\mu_1-3\mu_1)}-\mu_1}{\lambda^2\mu_1+\lambda^2\mu_2+2\lambda^2-\mu_1}. \tag{B.11b}$$

We can then substitute $\psi^{(1)}$ solution (eq. (5.29)) into eq. (B.7) and by enforcing the no-slip boundary condition (eq. (5.16)), the solution becomes

$$w^{(1)}(r,\phi)=(k_1r^3+k_2r+k_3+k_4r^{b-1})\cos\phi, \tag{5.28}$$

where $k_i=k_i(\mu_i,\lambda)$ are material-dependent constants

$$k_1=-2\frac{(-3\sqrt{\lambda(\lambda+1)}((\mu_1+\mu_2+2)\lambda^2-\mu_1)\sqrt{\lambda(\lambda-1)}+((\mu_1+\frac{\mu_2}{2})\lambda+\mu_1)\lambda(\lambda-1)a)}{(\sqrt{\lambda(\lambda-1)}\sqrt{\lambda(\lambda+1)}((8\mu_1+8\mu_2+16)\lambda^2-8\mu_1))}, \tag{B.12a}$$
$$k_2=-3\frac{(b((\mu_1+\mu_2+2)\lambda^2-\mu_1)(b-2)\sqrt{\lambda(\lambda+1)}\sqrt{\lambda(\lambda-1)}-3(b-\frac{2}{3})((\mu_1+\frac{\mu_2}{2})\lambda+\mu_1)a(\lambda-1)\lambda(b-4))}{(4b((\mu_1+\mu_2+2)\lambda^2-\mu_1)(b-2)\sqrt{\lambda(\lambda+1)}\sqrt{\lambda(\lambda-1)})}, \tag{B.12b}$$
$$k_3=-\frac{2((\mu_1+\frac{\mu_2}{2})\lambda+\mu_1)a(\lambda-1)\lambda(b-4)}{(\sqrt{\lambda(\lambda-1)}\sqrt{\lambda(\lambda+1)}((\mu_1+\mu_2+2)\lambda^2-\mu_1)(b-1))}, \tag{B.12c}$$
$$k_4=\frac{6a\Big((\mu_1+\frac{\mu_2}{2})\lambda+\mu_1\Big)\lambda(\lambda-1)}{(\sqrt{\lambda(\lambda+1)}\sqrt{\lambda(\lambda-1)}(b-1)((\mu_1+\mu_2+2)\lambda^2-\mu_1)b(b-2))}. \tag{B.12d}$$

Finally, by substituting solutions for $w^{(1)}$ (eq. 5.29) and $\psi^{(1)}$ (eq. (5.28)) into the director evolution equations, we can solve for the components of $\boldsymbol{n}^{(1)}$:

$$n_r^{(1)}(r,\phi)=-\frac{3\sqrt{2}(r^b-r^4)a\sqrt{\lambda+1}}{8r^3\sqrt{\lambda}}\cos\phi, \tag{5.33a}$$

$$n_\phi^{(1)}(r,\phi) = \Bigg(-\frac{\Big[9a\lambda + 7a + \sqrt{\lambda-1}(k_1+1)\sqrt{\lambda+1}\Big]\sqrt{2}}{4\sqrt{\lambda+1}\sqrt{\lambda}} r - \frac{\sqrt{2}\Big[-3a\Big[(b-1)^2\lambda + b^2 - 2b - 1\Big] + k_4\sqrt{\lambda^2-1}(b-1)\Big]}{\sqrt{\lambda(\lambda+1)}(4b-4)} r^{b-3} - \frac{\sqrt{2}(k_2-1)\sqrt{\lambda-1}}{4\sqrt{\lambda}}\frac{1}{r} + \frac{\sqrt{2}\Big[2a(b-4) + (b-1)k_3\sqrt{\lambda^2-1}\Big]}{4\sqrt{\lambda(\lambda+1)}(b-1)}\frac{1}{r^2}\Bigg)\sin\phi \tag{5.33b}$$

$$n_s^{(1)}(r,\phi) = -\frac{3\sqrt{2}(r^b - r^4)a\sqrt{\lambda-1}}{8r^3\sqrt{\lambda}}\cos\phi. \tag{5.33c}$$

B.4 Second order $O(\delta^2)$ solution

In order to obtain the second order solutions, we consider a special case with

$$\mu_1 = -\frac{2\lambda^2\mu_2}{2\lambda^2 - \lambda - 1}, \qquad \lambda = -\frac{5+\sqrt{17}}{4}. \tag{5.37}$$

In the most general forms, the second-order contributions of velocity and stream-function ($w^{(2)}(r,\phi)$ and $\psi^{(2)}(r,\phi)$) are given by:

$$w^{(2)}(r,\phi) = w_1^{(2)}(r) + w_2^{(2)}(r)\cos(2\phi), \qquad \psi^{(2)}(r,\phi) = \psi^{(2)}(r)\sin(2\phi). \tag{B.14}$$

Expressing $\boldsymbol{\tau}^{(2)}$ and $\boldsymbol{n}^{(2)}$ in terms of $w^{(2)}(r,\phi)$ and $\psi^{(2)}(r,\phi)$ gives the momentum balance in the general form

$$f_1(w_1^{(2)}(r,\phi)) + f_2(w_2^{(2)}(r,\phi), \psi^{(2)}(r,\phi))\cos(2\phi) = 0. \tag{B.15}$$

We are only interested in the solution for $w_1^{(2)}(r)$, so we focus on f_1, which is given by

$$\begin{aligned}
&-32400r^4\lambda^4(\lambda-1)^2(-4\lambda+\mu_2-2)^4\frac{\partial^2 w_1^{(2)}}{\partial r^2} - 32400r^3\lambda^4(\lambda-1)^2(-4\lambda+\mu_2-2)^4\frac{\partial w_1^{(2)}}{\partial r} \\
&+(-45619200r^6 + 14515200r^4)\lambda^{10} + 45619200\mu_2(r^2 - 7/22)r^4\lambda^9 \\
&-17015040\Big[(\mu_2^2 + \frac{1980}{1477}\mu_2 - \frac{5940}{1477})r^5 + \frac{171\mu_2^2 r^4}{11816} + (-\frac{135}{422}\mu_2^2 - \frac{90}{211}\mu_2 + \frac{270}{211})r^3 - \frac{\mu_2^2 r^2}{211} - \frac{\mu_2^2}{1688}\Big]r\lambda^8 \\
&+2800512\Big[(\mu_2^3 + 1110/187\mu_2^2 - 4500/221\mu_2 + 1800/221)r^5 + 907(\mu_2 + 6615/907)\mu_2^2 r^4/19448 \\
&+(-1579/4862\mu_2^3 - 4725/2431\mu_2^2 + 15750/2431\mu_2 - 6300/2431)r^3 \\
&-(71\mu_2^2(\mu_2 + 435/71)r^2)/4862 - (35\mu_2^2(\mu_2+5))/19448\Big]r\lambda^7 \\
&+\Big[(-171320\mu_2^4 - 3990080\mu_2^3 + 12623040\mu_2^2 + 5702400\mu_2 - 25660800)r^6 \\
&+(-17130\mu_2^4 - 574704\mu_2^3 + 1739880\mu_2^2)r^5
\end{aligned}$$

$$
\begin{aligned}
&+ (57068\mu_2^4 + 1372320\mu_2^3 - 4082400\mu_2^2 - 1814400\mu_2 + 8164800)r^4 \\
&+ (5296\mu_2^4 + 149152\mu_2^3 - 803520\mu_2^2)r^3 + (658\mu_2^4 + 15120\mu_2^3 - 128520\mu_2^2)r - 32\mu_2^3(\mu_2+4)\Big]\lambda^6 \\
&+ \Big[(314544\mu_2^4 + 67712\mu_2^3 - 6946560\mu_2^2 + 22809600\mu_2 - 17107200)r^6 \\
&+ (84417\mu_2^4 - 746316\mu_2^3 - 1462860\mu_2^2)r^5 + (-115528\mu_2^4 + 43776\mu_2^3 + 2721600\mu_2^2 - 7257600\mu_2 + 5443200)r^4 \\
&+ (-22260\mu_2^4 + 333152\mu_2^3 + 66960\mu_2^2)r^3 + (-2345\mu_2^4 + 56700\mu_2^3 - 8820\mu_2^2)r + 192\mu_2^4 + 896\mu_2^3\Big]\lambda^5 \\
&+ \Big[(-177152\mu_2^4 + 329024\mu_2^3 - 4052160\mu_2^2 + 5702400\mu_2 - 2851200)r^6 \\
&+ (66570\mu_2^4 + 1527012\mu_2^3 - 1404540\mu_2^2)r^5 + (51032\mu_2^4 - 609408\mu_2^3 + 1360800\mu_2^2 - 1814400\mu_2 + 907200)r^4 \\
&+ (-33296\mu_2^4 - 230224\mu_2^3 + 619920\mu_2^2)r^3 + (-6482\mu_2^4 - 23940\mu_2^3 + 97020\mu_2^2)r + 328\mu_2^4 + 416\mu_2^3\Big]\lambda^4 \\
&+ \Big[(173504\mu_2^4 - 363648\mu_2^3 - 915840\mu_2^2)r^6 + (-279957\mu_2^4 + 1167804\mu_2^3 + 218700\mu_2^2)r^5 \\
&+ (32192\mu_2^4 - 285984\mu_2^3)r^4 + (54620\mu_2^4 - 253200\mu_2^3 + 261360\mu_2^2)r^3 \\
&+ (7525\mu_2^4 - 36540\mu_2^3 + 49140\mu_2^2)r - 1744\mu_2^4 - 7392\mu_2^3\Big]\lambda^3 \\
&+ 33552\mu_2^2\Big[(\mu_2^2 - 440/699\mu_2 - 2200/233)r^6 + (-34799/11184\mu_2^2 + 8335/932\mu_2 + 5625/932)r^5 \\
&+ (2141/4194\mu_2^2 - 990/233\mu_2)r^4 + (2519/2796\mu_2^2 - 875/699\mu_2 + 175/233)r^3 \\
&+ (5957/33552\mu_2^2 - 175/932\mu_2 + 175/932)r - (22\mu_2^2)/233 - (110\mu_2)/699\Big]\lambda^2 \\
&+ \Big[(23680\mu_2^4 - 51200\mu_2^3)r^6 + (-29880\mu_2^4 + 75600\mu_2^3)r^5 \\
&+ (-1680\mu_2^4 - 21600\mu_2^3)r^4 + (7720\mu_2^4 - 2000\mu_2^3)r^3 + 1680\mu_2^4 r \\
&\qquad - 1520\mu_2^4 - 800\mu_2^3\Big]\lambda - 200(r-1)^2\mu_2^4(r^4 - 17/8r^3 + 5/4r^2 + 9/8r + 1) = 0. \quad \text{(B.16)}
\end{aligned}
$$

Solving for $w_1^{(2)}(r)$ and enforcing the no-slip boundary condition gives the solution of the form

$$w_1^{(2)}(r) = p_1 r^4 + p_2 r^3 + p_3 r^2 + p_4 r + p_5, \tag{5.38}$$

where coefficients $p_i = p_i(\mu_2)$ are are given by

$$p_1 = \frac{(2748\mu_2^5+34037\mu_2^4+72460\mu_2^3-179740\mu_2^2+237600\mu_2-158400)\sqrt{17}-13727\mu_2^5-187109\mu_2^4-561368\mu_2^3+627020\mu_2^2+554400\mu_2-475200}{7200(\mu_2^2+6\mu_2-8)^2(3+\sqrt{17}+\mu_2)}, \tag{B.17a}$$

$$p_2 = -\frac{\mu_2^2(1783\sqrt{17}\mu_2^3+23832\sqrt{17}\mu_2^2-7257\mu_2^3+68540\sqrt{17}\mu_2-97624\mu_2^2-75120\sqrt{17}-284388\mu_2+310800)}{2700(\mu_2^2+6\mu_2-8)^2(3+\sqrt{17}+\mu_2)}, \tag{B.17b}$$

$$p_3 = \frac{(448\mu_2^5+8007\mu_2^4+41780\mu_2^3+31500\mu_2^2-151200\mu_2+100800)\sqrt{17}-297\mu_2^5-2839\mu_2^4-6168\mu_2^3-56700\mu_2^2-352800\mu_2+302400}{3600(\mu_2^2+6\mu_2-8)^2(3+\sqrt{17}+\mu_2)}, \tag{B.17c}$$

$$p_4 = \frac{(37\sqrt{17}\mu_2 + 250\sqrt{17} - 139\mu_2 - 1046)\mu_2^2}{180(3+\sqrt{17}+\mu_2)(\mu_2^2+6\mu_2-8)}, \tag{B.17d}$$

$$p_5 = \frac{(-1108\mu_2^5 - 16137\mu_2^4 - 64220\mu_2^3 - 10740\mu_2^2 + 194400\mu_2 - 129600)\sqrt{17} + 1587\mu_2^5 + 22969\mu_2^4 + 65688\mu_2^3 - 58620\mu_2^2 + 453600\mu_2 - 388800}{21600(\mu_2^2 + 6\mu_2 - 8)^2(3 + \sqrt{17} + \mu_2)}.$$

(B.17e)

B.4.1 Streamfunction solution in the absence of non-Newtonian $O(\delta)$ stress

Neglecting the non-Newtonian contribution to $\boldsymbol{\tau}^{(1)}$, the contribution of stress imbalance effects vanishes and momentum balance in the $r-\phi$ plane (eq. (5.17)) becomes

$$0 = -\frac{1}{r}\frac{\partial^2 \tau_{rr}^{(1)}}{\partial r \partial \phi} - \frac{1}{r^2}\frac{\partial \tau_{rr}^{(1)}}{\partial \phi} + \frac{1}{r}\frac{\partial^2 \tau_{\phi\phi}^{(1)}}{\partial r \partial \phi} + \frac{1}{r^2}\frac{\partial^2 \tau_{\phi\phi}^{(1)}}{\partial \phi} + \frac{\partial^2 \tau_{r\phi}^{(1)}}{\partial r^2} + \frac{3}{r}\frac{\partial}{\partial r}\tau_{r\phi}^{(1)} - \frac{1}{r^2}\frac{\partial^2 \tau_{r\phi}^{(1)}}{\partial \phi^2} + (\Psi_1^{(0)} + 2\Psi_2^{(0)})\sin\phi, \quad \text{(B.18)}$$

where the relevant components of Newtonian stress tensor expressed in terms of the stream function are given by

$$\tau_{r\phi}^{(1)} = \frac{1}{r}\frac{\partial u^{(1)}}{\partial \phi} - \frac{u^{(1)}}{r} + \frac{\partial v^{(1)}}{\partial r} = \frac{\partial^2 \psi^{(1)}}{\partial r^2} - \frac{1}{r}\frac{\partial \psi^{(1)}}{\partial r} - \frac{1}{r^2}\frac{\partial^2 \psi^{(1)}}{\partial \phi^2}, \quad \text{(B.19a)}$$

$$\tau_{rr}^{(1)} = 2\frac{\partial u^{(1)}}{\partial r} = -2\frac{\partial}{\partial r}\left(\frac{1}{r}\frac{\partial \psi^{(1)}}{\partial r}\right), \quad \text{(B.19b)}$$

$$\tau_{\phi\phi}^{(1)} = \frac{1}{r}\frac{\partial v^{(1)}}{\partial \phi} + \frac{u^{(1)}}{r} = 2\frac{\partial}{\partial r}\left(\frac{1}{r}\frac{\partial \psi^{(1)}}{\partial r}\right). \quad \text{(B.19c)}$$

Substituting eq. (B.19) into eq. (B.18) gives

$$(\Psi_1^{(0)} + 2\Psi_2^{(0)})\sin(\phi)r^4 + \frac{\partial^4 \psi^{(1)}(r,\phi)}{\partial r^4}r^4 + 2\frac{\partial^3 \psi^{(1)}(r,\phi)}{\partial r^3}r^3 + 2\frac{\partial^2}{\partial r^2}\left(\frac{\partial^2 \psi^{(1)}(r,\phi)}{\partial \phi^2}\right)r^2 - \frac{\partial^2 \psi^{(1)}(r,\phi)}{\partial r^2}r^2 - 2\frac{\partial}{\partial r}\left(\frac{\partial^2 \psi^{(1)}(r,\phi)}{\partial \phi^2}\right)r + \frac{\partial \psi^{(1)}(r,\phi)}{\partial r}r + 4\frac{\partial^2 \psi^{(1)}(r,\phi)}{\partial \phi^2} + \frac{\partial^4 \psi^{(1)}(r,\phi)}{\partial \phi^4} = 0. \quad \text{(B.20)}$$

Above equation indicates that the stream function can be written in the form

$$\psi^{(1)}(r,\phi) = \psi^{(1)}(r)\sin\phi, \quad \text{(B.21)}$$

which then provides an equation for $\psi^{(1)}(r)$:

$$(\Psi_1^{(0)} + 2\Psi_2^{(0)})\sin(\phi)r^4 + \frac{\partial^4 \psi^{(1)}(r)}{\partial r^4}r^4 + 2\frac{\partial^3 \psi^{(1)}(r)}{\partial r^3}r^3 - 3\frac{\partial^2 \psi^{(1)}(r)}{\partial r^2}r^2 = 0. + 3\frac{\partial \psi^{(1)}(r)}{\partial r}r - 3\psi^{(1)}(r) \quad \text{(B.22)}$$

Using Maple [166] to solve the above equation with imposed no-slip boundary condition (eq. (5.16) gives the final solution

$$\psi^{(1)}(r,\phi) = -\frac{r(r+\frac{1}{2})(1-r)^2}{45}(\Psi_1 + 2\Psi_2)\sin\phi. \quad \text{(B.23)}$$

Appendix C

Supplementary material of chapter 6

C.1 Implementation of boundary conditions

C.1.1 Wall-parallel boundary condition

```
1
2   // wall connected with the inlet
3       wall1
4           {
5           type          fixedValue;
6           value     uniform (1 0 0);
7           }
8
9   // bend
10      wall2
11          {
12                  type            codedMixed;
13                  refValue        uniform (1 0 0);
14                  refGradient     uniform (0 0 0);
15                  valueFraction   uniform 1;
16
17
18          redirectType homeotropicAnchoring2; // name of generated BC
19          code
20                  #{
21      // Get range and orientation
22      boundBox bb(patch().patch().localPoints(), true);
23          const vectorField& c = patch().Cf();
24
25          scalar cx(1e-2); // x coordinate of the bend axis
26          scalar cy(5e-3); // y coordinate of the bend axis
27
28          vector ux(1, 0, 0);
29          vector uy(0, 1, 0);
30          vector uz(0, 0, 1);
31
32  const vectorField normal = patch().nf();
33
34  // function for the wall parallel orientation in the axis direction
35          this -> refValue()=-ux* ( (c&uy)- cy )/sqrt( pow( (c&uy)- cy,2) +
36  pow( (c&ux) - cx,2) ) + uy* ( (c&ux) - cx )/sqrt( pow( (c&uy)- cy,2)
37  + pow( (c&ux) - cx,2) ) ;
38                  #};
39          }
40  // wall connected to the outlet
41      wall3
42          {
43          type          fixedValue;
44          value     uniform (0 1 0);
45          }
46
47      symmetry
48      {
49      type          symmetry;
50      }
51
52
53  }
54
55  // ************************************************************************* //
```

C.1.2 Homeotropic boundary condition

```
1
2   // wall connected to the inlet
3   wall1
4           {
5                   type            codedMixed;
6                   refValue        uniform (1 0 0);
7                   refGradient     uniform (0 0 0);
8                   valueFraction   uniform 1;
9
10
11          redirectType homeotropicAnchoring1; // name of generated BC
12          code
13                  #{
14      // Get range and orientation
15      boundBox bb(patch().patch().localPoints(), true);
16
17          // compute wall-normal vector
18          const vectorField n = patch().nf();
19
20          this -> refValue()=-n;
21
22                  #};
23
24  // wall of the bend      }
25  wall2
26          {
27                  type            codedMixed;
28                  refValue        uniform (1 0 0); //refValue and refGradient DO NOT matter at all
29                  refGradient     uniform (0 0 0);
30                  valueFraction   uniform 1;
31
32
33          redirectType homeotropicAnchoring2; // name of generated BC
34          code
35                  #{
36      // Get range and orientation
37      boundBox bb(patch().patch().localPoints(), true);
38
39          //compute wall-normal vector in the bend
40          const vectorField n = patch().nf();
41
42          this -> refValue()=-n;
43
44                  #};
45          }
46
47  // wall connected to the outlet
48  wall3
49          {
50                  type            codedMixed;
51                  refValue        uniform (1 0 0);
52                  refGradient     uniform (0 0 0);
53                  valueFraction   uniform 1;
54
55
56          redirectType homeotropicAnchoring3; // name of generated BC
57          code
58                  #{
59      // Get range and orientation
60      boundBox bb(patch().patch().localPoints(), true);
61
62          //compute wall-normal vector
63          const vectorField n = patch().nf();
64
65          this -> refValue()=-n;
66
67                  #};
68          }
```

C.2 Equilibrium director distribution in a curved duct

Analytical solutions for the distribution of the director field in a curved pipe cannot be obtained. However, the problem can be simplified to consider a straight duct in the absence of flow with a homeotropic boundary condition as shown in fig. C.1. Conclusions made by studying the director distribution in a duct are also applicable to a curved pipe.

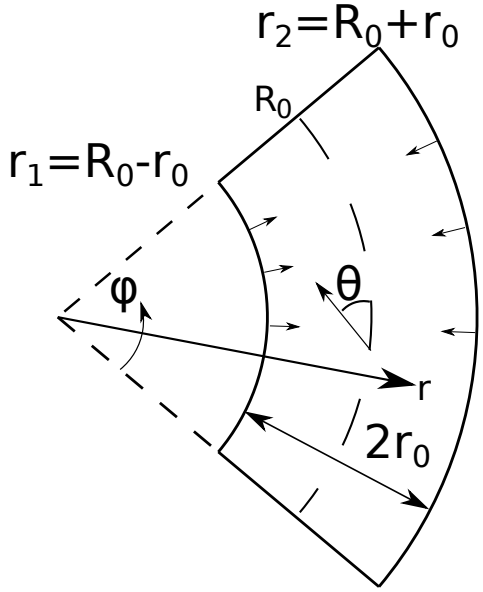

Figure C.1. Schematic illustration of a curved duct. The director is pointing in the opposite direction to mimic the situation in a curved pipe.

In the set-up shown in fig. C.1 the director is constrained to the $r-\phi$ plane and does not change in the ϕ direction. This allows $\boldsymbol{n}$ to be represented as a function of an arbitrary variable $\theta(r)$:

$$\boldsymbol{n} = [n_r(r),\ n_\phi(r),\ n_s(r)] = [-\sin\theta(r),\ \cos\theta(r),\ 0]. \tag{C.1}$$

In the one-constant approximation the distortion energy is given by

$$f_d = \frac{1}{2}K\nabla\boldsymbol{n} : (\nabla\boldsymbol{n})^T, \tag{C.2}$$

where the non-zero components of $\nabla\boldsymbol{n}$ are

$$[\nabla\boldsymbol{n}]_{r,r} = \frac{\partial n_r}{\partial r}, \qquad [\nabla\boldsymbol{n}]_{r,\phi} = -\frac{n_\phi}{r}, \qquad [\nabla\boldsymbol{n}]_{\phi,r} = \frac{\partial n_\phi}{\partial r}, \qquad [\nabla\boldsymbol{n}]_{\phi,\phi} = \frac{n_r}{r}. \tag{C.3}$$

The Euler-Lagrange equilibrium equation is obtained by taking the functional derivative of eq. (C.2) with respect to θ and yields the equilibrium equation

$$\frac{\partial(r\frac{\partial\theta(r))}{\partial r})}{\partial r} = 0, \tag{C.4}$$

with boundary conditions $\theta(r_1) = -\frac{\pi}{2}$, $\theta(r_2) = \frac{\pi}{2}$ the solution is

$$\theta(r) = \pi\frac{\ln\left(\frac{r}{r_1}\right) + \ln\left(\frac{r}{r_2}\right)}{\ln\left(\frac{r_2}{r_1}\right)}, \tag{C.5}$$

with radial and tangential components of the director shown in fig. C.2 and schematically

illustrated in fig. C.3.

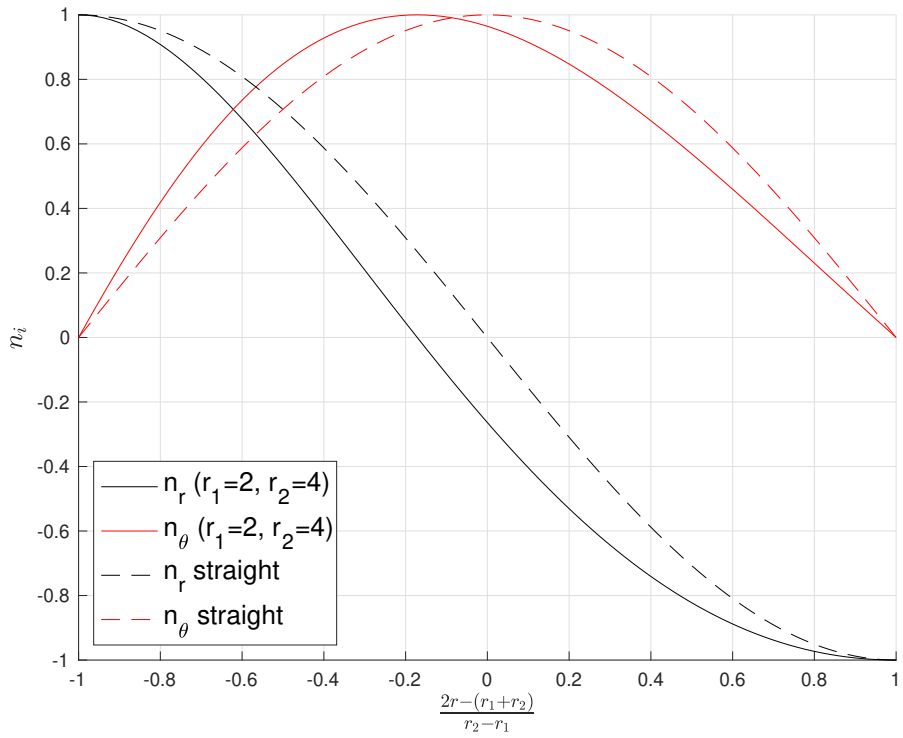

Figure C.2. Comparison of curved and straight duct solutions. Negative x-axis is closer to the centre of curvature.

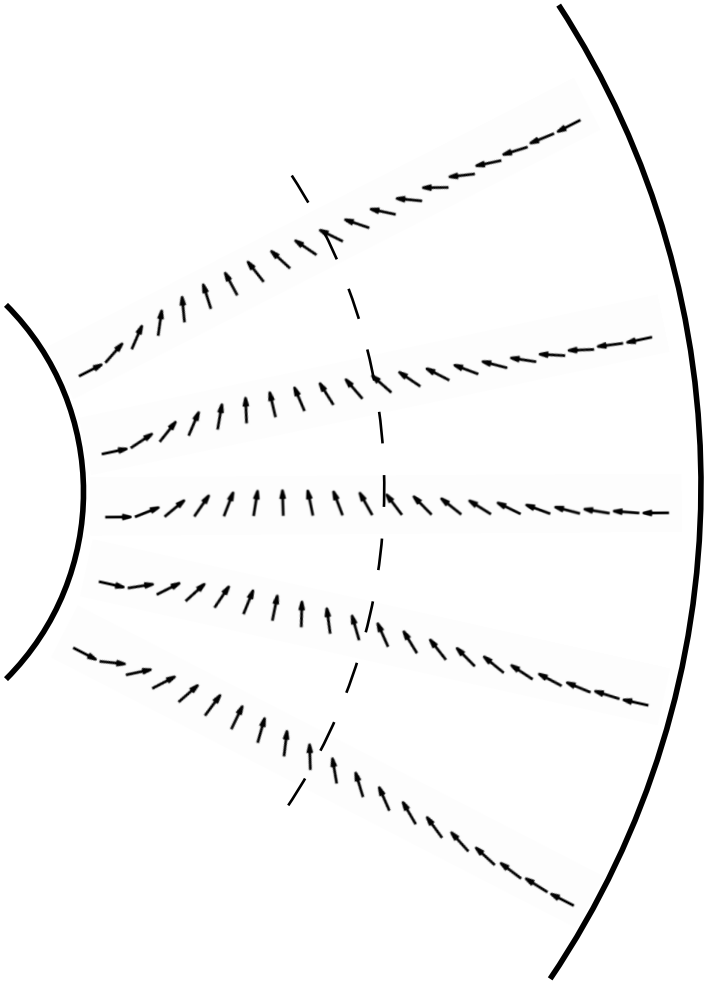

Figure C.3. Due to the geometry curvature, the director field at $Er = 0$ moves towards the bend axis to minimise the Helmholtz free energy.

The location of maximum tangential component of the director occurs where $\theta = 0$, which by solving eq. (C.5) gives

$$r^{max} = \sqrt{r_1 r_2}, \tag{C.6}$$

which is the geometric average of the limiting coordinates. Expressing r_i in terms of $R = \frac{r_1+r_2}{2}$ and $h = \frac{r_2-r_1}{2}$ gives

$$r^{max} = \sqrt{(R-h)(R+h)} = \sqrt{R}\sqrt{(1-\delta)(1+\delta)}, \tag{C.7}$$

where $\delta = \frac{h}{R}$. Thus as the curvature becomes very small the straight duct limit is recovered and the solution becomes symmetric about the centreline.

C.3 Explanation of the sudden velocity perturbations

Newtonian flow

The dimensionless $r-$ and $\phi-$ components of the Navier-Stokes equation in the toroidal coordinates are given by

$$\frac{\partial p}{\partial r} = \frac{\tau_{rr} - \tau_{\phi\phi}}{r} + \frac{\partial \tau_{rr}}{\partial r} + \frac{1}{r}\tau_{r\phi} + \frac{1}{B}\frac{\partial \tau_{rs}}{\partial s} + \frac{\delta}{B}\left(\tau_{rr}\cos\phi - \tau_{r\phi}\sin\phi - \tau_{ss}\cos\phi\right), \tag{C.8a}$$

$$\frac{1}{r}\frac{\partial p}{\partial \phi} = \frac{2\tau_{r\phi}}{r} + \frac{\partial \tau_{r\phi}}{\partial r} + \frac{1}{r}\frac{\partial \tau_{\phi\phi}}{\partial \phi} + \frac{1}{B}\frac{\partial \tau_{\phi s}}{\partial s} + \frac{\delta}{B}\left(\tau_{ss}\sin\phi + \tau_{r\phi}\cos\phi - \tau_{\phi\phi}\sin\phi\right). \tag{C.8b}$$

Note that eq. (C.8a) and (C.8b) contain stream-wise derivatives, which are absent in the fully developed flow analysis presented in chapter 5. The stress is purely Newtonian

$$\boldsymbol{\tau} = 2\mu\boldsymbol{D}, \tag{C.9}$$

where $\boldsymbol{D}$ is the symmetric part of the velocity gradient tensor, whose full form in toroidal coordinates reads

$$\begin{aligned}
[\nabla\boldsymbol{u}]_{r,r} &= \frac{\partial u}{\partial r}, & [\nabla\boldsymbol{u}]_{r,\phi} &= \frac{1}{r}\frac{\partial u}{\partial \phi} - \frac{u}{r} & [\nabla\boldsymbol{u}]_{r,s} &= \frac{1}{B}\frac{\partial u}{\partial s} - \frac{\delta}{B}w\cos\phi,\\
[\nabla\boldsymbol{u}]_{\phi,r} &= \frac{\partial v}{\partial r}, & [\nabla\boldsymbol{u}]_{\phi,\phi} &= \frac{1}{r}\frac{\partial v}{\partial \phi} + \frac{u}{r}, & [\nabla\boldsymbol{u}]_{\phi,s} &= \frac{1}{B}\frac{\partial v}{\partial s} + \frac{\delta}{B}w\sin\phi,\\
[\nabla\boldsymbol{u}]_{s,r} &= \frac{\partial w}{\partial r}, & [\nabla\boldsymbol{u}]_{s,\phi} &= \frac{1}{r}\frac{\partial w}{\partial \phi}, & [\nabla\boldsymbol{u}]_{s,s} &= \frac{1}{B}\frac{\partial w}{\partial s} + \frac{\delta}{B}(u\cos\phi - v\sin\phi).
\end{aligned} \tag{C.10}$$

Substituting combining eq. (C.8), (C.9) and (C.10) to calculate the leading order component of $(\nabla\times\nabla p)_s$ on the symmetry line (where $v=0$) gives

$$\frac{\partial^2 u}{\partial r^2}r^2B^2 + 2\frac{\partial u}{\partial r}rB^2 + B^2\frac{\partial^2 u}{\partial \phi^2} + B\frac{\partial w}{\partial s}r + \frac{\partial^2 u}{\partial s^2}r^2 = 0. \tag{C.11}$$

In a fully developed flows $\frac{\partial w}{\partial s}r = 0$, and eq. (C.11) is satisfied by $u=0$. However, as the flow changes direction (accelerates) due to the geometry curvature $\frac{\partial w}{\partial s}r \neq 0$, must be balanced by a non-zero transverse velocity.

Non-Newtonian fluids

Let us first split the total stress tensor into Newtonian and non-Newtonian contributions:

$$\tau = 2\boldsymbol{D} + \boldsymbol{\sigma}. \tag{C.12}$$

Following the same procedure as for a Newtonian fluid, the momentum balance in the $r-\phi$ plane is given by

$$\underbrace{-\frac{\partial^2\sigma_{r\phi}}{\partial r^2}r^3B^2-2\frac{\partial\sigma_{r\phi}}{\partial r}r^2B^2+\frac{\partial^2\sigma_{rr}}{\partial\phi\partial r}r^2B^2+2B^2r\sigma_{r\phi}+B^2r\frac{\partial\sigma_{rr}}{\partial\phi}-B^2r\frac{\partial\sigma_{\phi\phi}}{\partial\phi}+B^2r\frac{\partial^2\sigma_{r\phi}}{\partial\phi^2}}_{\text{components in the fully developed curved pipe flow}}$$
$$\underbrace{+\frac{\partial^3u}{\partial\phi\partial r^2}r^2B^2+2rB^2\frac{\partial^2u}{\partial r\partial\phi}+B^2\frac{\partial^3u}{\partial\phi^3}+\frac{\partial^3u}{\partial\phi\partial s^2}}_{\text{transverse velocity}}$$
$$+\underbrace{r^2B\frac{\partial^2\sigma_{sr}}{\partial\phi\partial s}+Br\frac{\partial^2w}{\partial s\partial\phi}-r^3B\frac{\partial^2\sigma_{s\phi}}{\partial s\partial r}}_{\text{streamwise gradient}}. \quad \text{(C.13)}$$

Equation above indicates that when the flow is fully developed $\frac{\partial}{\partial s}=0$, and non-zero u is produced by the imbalance of non-Newtonian stresses (terms in the first underbrace). However, eq. (C.13) suggests that the transverse velocity can be also generated not only when the fluid accelerates $\frac{\partial w}{\partial s}r\neq 0$, but also when there are stream-wise gradients of the shear stress $\frac{\partial\sigma_{sr}}{\partial s}$ and $\frac{\partial\sigma_{s\phi}}{\partial s}$.

C.4 Stress coefficients in the LE model in a straight pipe

In the limit of a fully developed, straight pipe flow, all velocity gradients apart from $\nabla\boldsymbol{u}]_{s,r}=\frac{\partial w}{\partial r}$ vanish. The viscous stress is given by

$$\alpha_1\boldsymbol{nnnn}:\boldsymbol{D}+\alpha_2\boldsymbol{nN}+\alpha_3\boldsymbol{Nn}+\alpha_4\boldsymbol{D}+\alpha_5\boldsymbol{nn}\cdot\boldsymbol{D}+\alpha_6\boldsymbol{D}\cdot\boldsymbol{nn}, \quad \text{(C.14)}$$

and its non-zero components read

$$\tau_{rr}=\frac{1}{2}\Big[2\alpha_1n_r^2+\alpha_2+\alpha_3+\alpha_5+\alpha_6\Big]n_rn_s\frac{\partial w}{\partial r}, \quad \text{(C.15a)}$$
$$\tau_{ss}=\frac{1}{2}\Big[2\alpha_1n_s^2-\alpha_2-\alpha_3+\alpha_5+\alpha_6\Big]n_rn_s\frac{\partial w}{\partial r}, \quad \text{(C.15b)}$$
$$\tau_{rs}=\frac{1}{2}\Big[\alpha_4+2\alpha_1n_s^2n_r^2+(-\alpha_2+\alpha_5)n_r^2+(\alpha_3+\alpha_6)n_s^2\Big]\frac{\partial w}{\partial r}, \quad \text{(C.15c)}$$
$$\tau_{sr}=\frac{1}{2}\Big[\alpha_4+2\alpha_1n_s^2n_r^2+(-\alpha_3+\alpha_6)n_r^2+(\alpha_2+\alpha_5)n_s^2\Big]\frac{\partial w}{\partial r}. \quad \text{(C.15d)}$$
$$\quad \text{(C.15e)}$$

Note that $\boldsymbol{\tau}$ is not symmetric. τ_{rs} is the *actual* shear stress that enters the Navier-Stokes equation. When director is aligned in the flow direction ($n_s=1$), the effective viscosity is $\frac{\alpha_3+\alpha_4+\alpha_6}{2}$ (first Miesowicz viscosity [43]) and when director aligns in the velocity gradient direction ($n_r=1$), the effective viscosity is $\frac{-\alpha_2+\alpha_4+\alpha_5}{2}$ (second Miesowicz viscosity [43]).

C.5 Director distortion on the centerline

The steady state distribution of the director angle in a curved channel at low Ericksen numbers was calculated in appendix C.2 and is given by

$$\theta(r) = \pi \frac{\ln\left(\frac{r}{r_1}\right) + \ln\left(\frac{r}{r_1+\delta_r}\right)}{\ln\left(\frac{r_1+\delta_r}{r_1}\right)}, \tag{C.16}$$

where r_1 and $r_2 = r_1 + \delta_r$ are inner and outer radii of the curved channel respectively, δ_r is a gap between channel walls. The solution is schematically visualised in fig. C.2. In order to map between the curved and straight sections of a channel, let us consider an identically distributed director field in a straight channel. For that purpose, we introduce a variable $-1 \leq y \leq 1$

$$y = \frac{2r - (r_1 + r_2)}{r_2 - r_1}, \tag{C.17}$$

So that the director angle is given by

$$\begin{aligned}\theta(y) = \pi \frac{\ln\left(\frac{1}{2}y\frac{\delta_r}{r_1} + \frac{r_1+\frac{1}{2}\delta_r}{r_1}\right) + \ln\left(\frac{1}{2}y\frac{\delta_r}{r_1+\delta_r} + \frac{r_1+\frac{1}{2}\delta_r}{r_1+\delta_r}\right)}{\ln\left(\frac{r_1+\delta r}{r_1}\right)} \\ = \pi \frac{\ln\left(\frac{1}{2}yc_1 + 1 + \frac{1}{2}c_1\right) + \ln\left(\frac{1}{2}y\frac{c_1}{1+c_1} + \frac{1+\frac{1}{2}c_1}{1+c_1}\right)}{\ln(1+c_1)},\end{aligned} \tag{C.18}$$

where $c_1 = \frac{\delta_r}{r_1}$ is a free parameter that controls the deviation from the straight channel solution. We are interested in the relation between $\frac{\partial^2\theta}{\partial y^2}$ and θ at the channel centerline. In the limit of $\delta_r \to 0$, the power series expansion of $\frac{\partial^2\theta}{\partial y^2}$ and θ at the centreline is given by

$$\theta|_{y=0} \approx \frac{\pi}{8}\frac{\delta_r}{r_1} + O(\delta_r^2), \tag{C.19a}$$

$$\frac{\partial^2\theta}{\partial y^2}|_{y=0} \approx -\frac{\pi}{4}\frac{\delta_r}{r_1} + O(\delta_r^2), \tag{C.19b}$$

which shows that $\frac{\partial^2\theta}{\partial y^2}|_{y=0} \propto -\theta|_{y=0}$.

Appendix D

Contraction mesh code

The code used to generate the M3 mesh of the contraction

```
/*--------------------------------*- C++ -*----------------------------------*\
  =========                 |
  \\      /  F ield         | OpenFOAM: The Open Source CFD Toolbox
   \\    /   O peration     | Website:  https://openfoam.org
    \\  /    A nd           | Version:  6
     \\/     M anipulation  |
\*---------------------------------------------------------------------------*/
FoamFile
{
    version     2.0;
    format      ascii;
    class       dictionary;
    object      blockMeshDict;
}
// * * * * * * * * * * * * * * * * * * * * * * * * * * * * * * * * * * * * //

convertToMeters 0.001;

vertices
(
    (0 0 -1) //0
    (  10 0 -1)
    ( 40 0 -1)
    (0 0.5 -1)
    (  10 0.5 -1) //4
    ( 40 0.5 -1)
    (0 2 -1)
    (  10 2 -1)

    (0 0  1)
    (  10 0  1)
    ( 40 0  1)
    (0 0.5  1)
    (  10 0.5  1)
    ( 40 0.5  1)
    (0 2  1)
    (  10 2  1)

    (0 -0.5 -1) //16
    (  10 -0.5 -1)
    ( 40 -0.5 -1)
    (0 -2 -1)
    (  10 -2 -1) //20

    (0 -0.5 1) //21
    (  10 -0.5 1)
    ( 40 -0.5 1)
    (0 -2 1)
    (  10 -2 1) //25



);

xInl 400; // cells in the front in the x direction
yInl 60; // cells along the vertical wall in the contraction
yOut 20;//cells from the centerline to the horizontal wall of the outlet pipe
xOut 1200; //cells in the outlet pipe


blocks
(
    hex (0 1 4 3  8  9 12 11) ($xInl $yOut 1) simpleGrading (1 1 1)
    hex (1 2 5 4  9 10 13 12) ($xOut $yOut 1) simpleGrading (1 1 1)
        //outlet pipe
    hex (3 4 7 6 11 12 15 14) ($xInl $yInl 1) simpleGrading (1 1 1)
        //outside inlet up

    hex (16 17 1 0 21 22 9 8) ($xInl $yOut 1) simpleGrading (1 1 1)
    hex (17 18 2 1 22 23 10 9) ($xOut $yOut 1) simpleGrading (1 1 1)
        //outlet pipe
    hex (19 20 17 16 24 25 22 21) ($xInl $yInl 1) simpleGrading (1 1 1)
        // outside inlet bot

);

edges
(
);

boundary
(
    inlet
    {
        type patch;
        faces
        (
            (0 3 11 8)
            (3 6 14 11)
            (16 0 8 21)
            (19 16 21 24)
        );
    }

    wallsHorTop
    {
        type wall;
        faces
        (

            (4 5 13 12)
            (6 7 15 14)


        );
```

```
107         }
108
109         wallsHorBot
110         {
111             type wall;
112             faces
113             (
114
115                (19 20 25 24)
116                 (17 18 23 22)
117
118             );
119         }
120
121         wallsVertBot
122         {
123             type wall;
124             faces
125             (
126                 (17 20 25 22)
127             );
128         }
129
130         wallsVertTop
131         {
132             type wall;
133             faces
134             (
135                 (7 4 12 15)
136             );
137         }
138
139
140         outlet
141         {
142             type patch;
143             faces
144             (
145                 (2 5 13 10)
146                 (18 2 10 23)
147             );
148         }
149
150
151         frontAndBack
152         {
153             type empty;
154             faces
155             (
156                 (0 1 4 3)
157                 (3 4 7 6)
158                 (1 2 5 4)
159                 (8 9 12 11)
160                 (11 12 15 14)
161                 (9 10 13 12)
162
163                 (16 17 1 0)
164                 (19 20 17 16)
165                 (17 18 2 1)
166                 (21 22 9 8)
167                 (24 25 22 21)
168                 (22 23 10 9)
169
170             );
171         }
172     );
173
174     /*
175     mergePatchPairs
176     (
177     );
178     */
179
180     // ************************************************************************* //
```